IJOER
RESEARCH JOURNAL

International Journal of Engineering Research & Science

ISSN
2395-6992

www.ijoer.com
www.adpublications.org

Volume-3! Issue-8 ! August, 2017 www.ijoer.com ! info@ijoer.com

Preface

We would like to present, with great pleasure, the inaugural volume-3, Issue-8, August 2017, of a scholarly journal, *International Journal of Engineering Research & Science*. This journal is part of the AD Publications series *in the field of Engineering, Mathematics, Physics, Chemistry and science Research Development*, and is devoted to the gamut of Engineering and Science issues, from theoretical aspects to application-dependent studies and the validation of emerging technologies.

This journal was envisioned and founded to represent the growing needs of Engineering and Science as an emerging and increasingly vital field, now widely recognized as an integral part of scientific and technical investigations. Its mission is to become a voice of the Engineering and Science community, addressing researchers and practitioners in below areas

Chemical Engineering	
Biomolecular Engineering	Materials Engineering
Molecular Engineering	Process Engineering
Corrosion Engineering	
Civil Engineering	
Environmental Engineering	Geotechnical Engineering
Structural Engineering	Mining Engineering
Transport Engineering	Water resources Engineering
Electrical Engineering	
Power System Engineering	Optical Engineering
Mechanical Engineering	
Acoustical Engineering	Manufacturing Engineering
Optomechanical Engineering	Thermal Engineering
Power plant Engineering	Energy Engineering
Sports Engineering	Vehicle Engineering
Software Engineering	
Computer-aided Engineering	Cryptographic Engineering
Teletraffic Engineering	Web Engineering
System Engineering	
Mathematics	
Arithmetic	Algebra
Number theory	Field theory and polynomials
Analysis	Combinatorics
Geometry and topology	Topology
Probability and Statistics	Computational Science
Physical Science	Operational Research
Physics	
Nuclear and particle physics	Atomic, molecular, and optical physics
Condensed matter physics	Astrophysics
Applied Physics	Modern physics
Philosophy	Core theories

<table>
<tr><th colspan="2">Chemistry</th></tr>
<tr><td>Analytical chemistry</td><td>Biochemistry</td></tr>
<tr><td>Inorganic chemistry</td><td>Materials chemistry</td></tr>
<tr><td>Neurochemistry</td><td>Nuclear chemistry</td></tr>
<tr><td>Organic chemistry</td><td>Physical chemistry</td></tr>
<tr><th colspan="2">Other Engineering Areas</th></tr>
<tr><td>Aerospace Engineering</td><td>Agricultural Engineering</td></tr>
<tr><td>Applied Engineering</td><td>Biomedical Engineering</td></tr>
<tr><td>Biological Engineering</td><td>Building services Engineering</td></tr>
<tr><td>Energy Engineering</td><td>Railway Engineering</td></tr>
<tr><td>Industrial Engineering</td><td>Mechatronics Engineering</td></tr>
<tr><td>Management Engineering</td><td>Military Engineering</td></tr>
<tr><td>Petroleum Engineering</td><td>Nuclear Engineering</td></tr>
<tr><td>Textile Engineering</td><td>Nano Engineering</td></tr>
<tr><td>Algorithm and Computational Complexity</td><td>Artificial Intelligence</td></tr>
<tr><td>Electronics & Communication Engineering</td><td>Image Processing</td></tr>
<tr><td>Information Retrieval</td><td>Low Power VLSI Design</td></tr>
<tr><td>Neural Networks</td><td>Plastic Engineering</td></tr>
</table>

Each article in this issue provides an example of a concrete industrial application or a case study of the presented methodology to amplify the impact of the contribution. We are very thankful to everybody within that community who supported the idea of creating a new Research with IJOER. We are certain that this issue will be followed by many others, reporting new developments in the Engineering and Science field. This issue would not have been possible without the great support of the Reviewer, Editorial Board members and also with our Advisory Board Members, and we would like to express our sincere thanks to all of them. We would also like to express our gratitude to the editorial staff of AD Publications, who supported us at every stage of the project. It is our hope that this fine collection of articles will be a valuable resource for *IJOER* readers and will stimulate further research into the vibrant area of Engineering and Science Research.

Mukesh Arora

(Chief Editor)

Board Members

Mukesh Arora(Editor-in-Chief)

BE(Electronics & Communication), M.Tech(Digital Communication), currently serving as Assistant Professor in the Department of ECE.

Dr. Omar Abed Elkareem Abu Arqub

Department of Mathematics, Faculty of Science, Al Balqa Applied University, Salt Campus, Salt, Jordan, He received PhD and Msc. in Applied Mathematics, The University of Jordan, Jordan.

Dr. AKPOJARO Jackson

Associate Professor/HOD, Department of Mathematical and Physical Sciences,Samuel Adegboyega University, Ogwa, Edo State.

Dr. Ajoy Chakraborty

Ph.D.(IIT Kharagpur) working as Professor in the department of Electronics & Electrical Communication Engineering in IIT Kharagpur since 1977.

Dr. Ukar W.Soelistijo

Ph D , Mineral and Energy Resource Economics,West Virginia State University, USA, 1984, Retired from the post of Senior Researcher, Mineral and Coal Technology R&D Center, Agency for Energy and Mineral Research, Ministry of Energy and Mineral Resources, Indonesia.

Dr. Heba Mahmoud Mohamed Afify

h.D degree of philosophy in Biomedical Engineering, Cairo University, Egypt worked as Assistant Professor at MTI University.

Dr. Aurora Angela Pisano

Ph.D. in Civil Engineering, Currently Serving as Associate Professor of Solid and Structural Mechanics (scientific discipline area nationally denoted as ICAR/08"–"Scienza delle Costruzioni"), University Mediterranea of Reggio Calabria, Italy.

Dr. Faizullah Mahar

Associate Professor in Department of Electrical Engineering, Balochistan University Engineering & Technology Khuzdar. He is PhD (Electronic Engineering) from IQRA University, Defense View,Karachi, Pakistan.

Dr. S. Kannadhasan

Ph.D (Smart Antennas), M.E (Communication Systems), M.B.A (Human Resources).

Dr. Christo Ananth

Ph.D. Co-operative Networks, M.E. Applied Electronics, B.E Electronics & Communication Engineering Working as Associate Professor, Lecturer and Faculty Advisor/ Department of Electronics & Communication Engineering in Francis Xavier Engineering College, Tirunelveli.

Dr. S.R.Boselin Prabhu

Ph.D, Wireless Sensor Networks, M.E. Network Engineering, Excellent Professional Achievement Award Winner from Society of Professional Engineers Biography Included in Marquis Who's Who in the World (Academic Year 2015 and 2016). Currently Serving as Assistant Professor in the department of ECE in SVS College of Engineering, Coimbatore.

Dr. Maheshwar Shrestha

Postdoctoral Research Fellow in DEPT. OF ELE ENGG & COMP SCI, SDSU, Brookings, SD Ph.D, M.Sc. in Electrical Engineering from SOUTH DAKOTA STATE UNIVERSITY, Brookings, SD.

Zairi Ismael Rizman

Senior Lecturer, Faculty of Electrical Engineering, Universiti Teknologi MARA (UiTM) (Terengganu) Malaysia Master (Science) in Microelectronics (2005), Universiti Kebangsaan Malaysia (UKM), Malaysia. Bachelor (Hons.) and Diploma in Electrical Engineering (Communication) (2002), UiTM Shah Alam, Malaysia

Dr. D. Amaranatha Reddy

Ph.D.(Postdocteral Fellow,Pusan National University, South Korea), M.Sc., B.Sc. : Physics.

Dr. Dibya Prakash Rai

Post Doctoral Fellow (PDF), M.Sc.,B.Sc., Working as Assistant Professor in Department of Physics in Pachhuncga University College, Mizoram, India.

Dr. Pankaj Kumar Pal

Ph.D R/S, ECE Deptt., IIT-Roorkee.

Dr. P. Thangam

BE(Computer Hardware & Software), ME(CSE), PhD in Information & Communication Engineering, currently serving as Associate Professor in the Department of Computer Science and Engineering of Coimbatore Institute of Engineering and Technology.

Dr. Pradeep K. Sharma

PhD., M.Phil, M.Sc, B.Sc, in Physics, MBA in System Management, Presently working as Provost and Associate Professor & Head of Department for Physics in University of Engineering & Management, Jaipur.

Dr. R. Devi Priya

Ph.D (CSE),Anna University Chennai in 2013, M.E, B.E (CSE) from Kongu Engineering College, currently working in the Department of Computer Science and Engineering in Kongu Engineering College, Tamil Nadu, India.

Dr. Sandeep

Post-doctoral fellow, Principal Investigator, Young Scientist Scheme Project (DST-SERB), Department of Physics, Mizoram University, Aizawl Mizoram, India- 796001.

Mr. Abilash

MTech in VLSI, BTech in Electronics & Telecommunication engineering through A.M.I.E.T.E from Central Electronics Engineering Research Institute (C.E.E.R.I) Pilani, Industrial Electronics from ATI-EPI Hyderabad, IEEE course in Mechatronics, CSHAM from Birla Institute Of Professional Studies.

Mr. Varun Shukla

M.Tech in ECE from RGPV (Awarded with silver Medal By President of India), Assistant Professor, Dept. of ECE, PSIT, Kanpur.

Mr. Shrikant Harle

Presently working as a Assistant Professor in Civil Engineering field of Prof. Ram Meghe College of Engineering and Management, Amravati. He was Senior Design Engineer (Larsen & Toubro Limited, India).

Table of Contents

Performance Analysis of Regular and Irregular Structure Under Seismic Effect for RCC and Steel Composite Column Using Response Spectrum

Nethravathi S.M[1], Thouseef.T[2]

Dept. of Civil Engineering, VTU BELGAVI

Abstract**—***Composite construction is a modern method of construction presently holds a wide area of interest. This paper includes performance analysis of regular and irregular structure under seismic effect for RCC and Composite column. Modeling and analysis of structure is done by using ETABS software. Since composite construction is combination of steel section and concrete, which shows the properties of both steel and concrete. The compression efficiency of concrete and high ductile properties of steel together contributes to the structure for its perfect durability.*

Keywords—Composite Column, ETABS.

I. INTRODUCTION

Composite construction has become common technique in the field of construction. Since it is a combination of steel sections and concrete which add ups the properties of structure in its durability as well as strength. It should be noticed that efficiency of tensional property of steel and resisting property against corrosion also adds up the overall behavior of the structure. We all know that steel section is more prone to buckling but concrete resist the buckling, together as a composite unit which contribute high strength for structure, hence composite structure holds a high value of safety.

II. COMPOSITE STRUCTURAL ELEMENTS

2.1 Composite beam

Composite beam is a part which connects slab and column together to form as a single united structure. The load from slab can be equally distributed to the beam. Composite beam can be produced by incorporating steel section in beam mould and reinforcing the same with certain grade of concrete. Shear connectors are main element in composite beam which acts same like shear reinforcement. The steel section can be kept inside the beam mould or filling material can be filled inside the steel section.

2.2 Composite column

These columns are same like RCC columns but instead of steel reinforcement steel sections are inserted. There are different types of steel sections are available, so based on insertion of steel section column name changes. Steel section can be inserted inside the column with filling material as concrete or hollow steel section are filled with filling material like concrete with suitable grades. Examples of different sections that can be encased with concrete are steel hollow pipe, steel tube sections, steel channel section and many more.

2.3 Composite slab

Composite slab, another member of composite structure which connects the beam and column together and forms as a structural unit. A trapezoidal deck is formed over beam with profiled sheets, reinforcement bars are laid and concreting is done above that. It provides a smooth working platform since profiled sheets are laid before concreting. There are mainly 2 types of decks available such as trapezoidal and Re-entrant steel deck.

III. MODELING AND ANALYSIS

ETABS-Regular plan models shown in Fig.1. and ETABS-Irregular plan models shown in Fig.2.

Case I: Regular plan with Rectangular composite column

Case II: Regular plan with Rectangular RCC column

Case III: Irregular plan with Circular Composite column

Case IV: Irregular plan with Circular RCC column

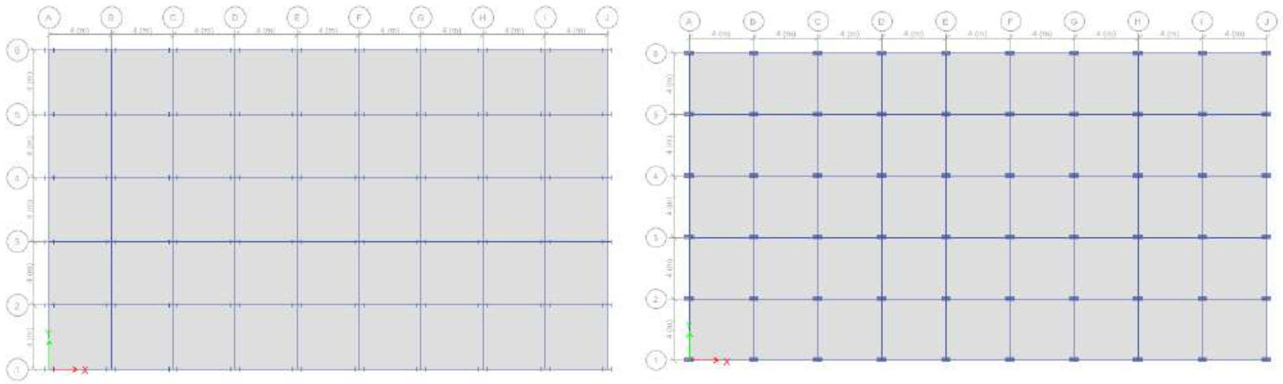

FIG.1: REGULAR PLAN MODELS MODEL FOR CASE I & II

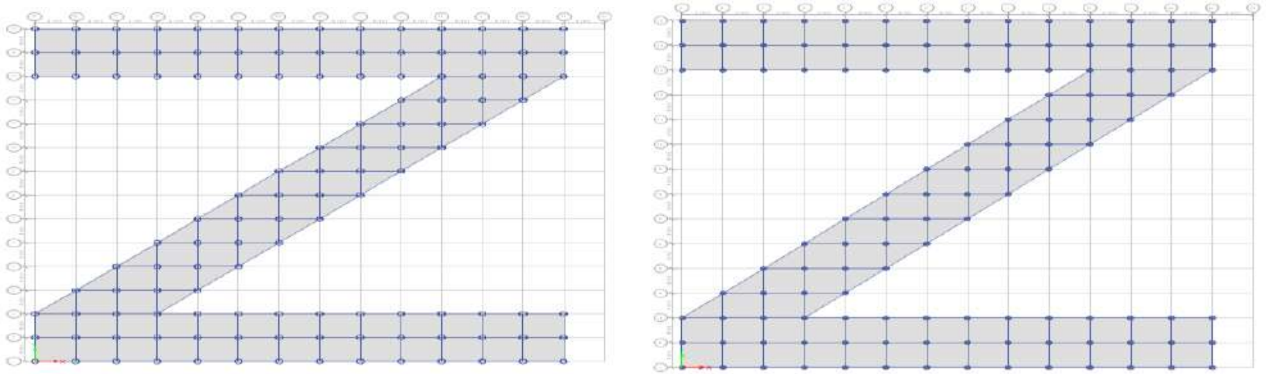

FIG.2: IRREGULAR PLAN MODELS MODEL FOR CASE III & IV

3.1 Model Description

TABLE 1
DETAILS OF MODEL

PLAN	REGULAR PLAN		IRREGULAR PLAN	
Column	RCC	COMPOSITE	RCC	COMPOSITE
Shape of column	Rectangular	Rectangular	Circular	Circular
Shape of plan	Rectangular	Rectangular	Z shape	Z shape
Floor Height(m)	3	3	3	3
Beam Size(mm)	300x600	300x600	300x600	300x600
Column size(mm)	300x600	300x600	600	600
Number of storey	7	7	5	5

TABLE 2
GEOMETRIC DETAILS OF MODEL

Type of structure	Multi storey RC and Composite structure
Grade of concrete column	M30
Grade of concrete Beam	M20
Grade of Reinforcement	Fe415
Floor Height	3m
Slab Thickness	125mm
Slab load	3kN/m^2
Number of storey	7(Regular) and 5(Irregular)
Type of composite column	Concrete encasement column
Embedded steel section	ISWB 550
Density of concrete	25kN/m^2

IV. RESULTS AND ANALYSIS

4.1 Comparison between Rectangular RCC and Composite column in Regular plan

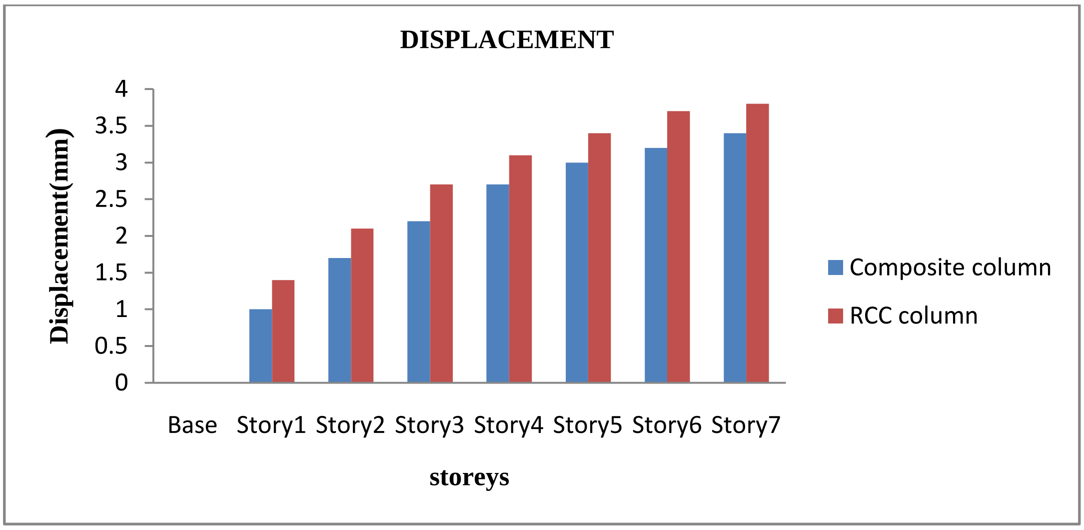

FIG.3: GRAPH OF STOREY VS DISPLACEMENT

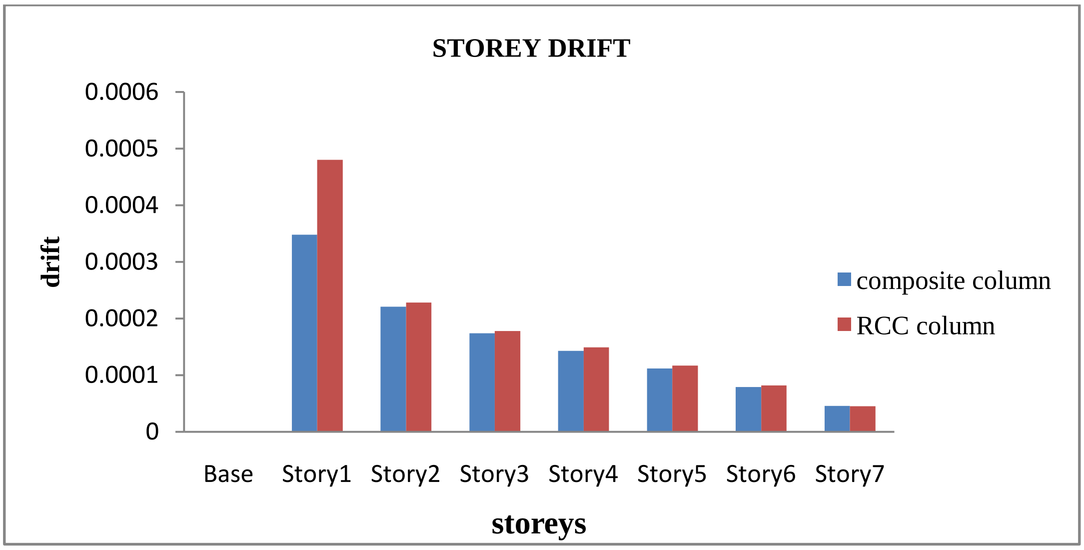

FIG.4: GRAPH OF STOREY VS DRIFT

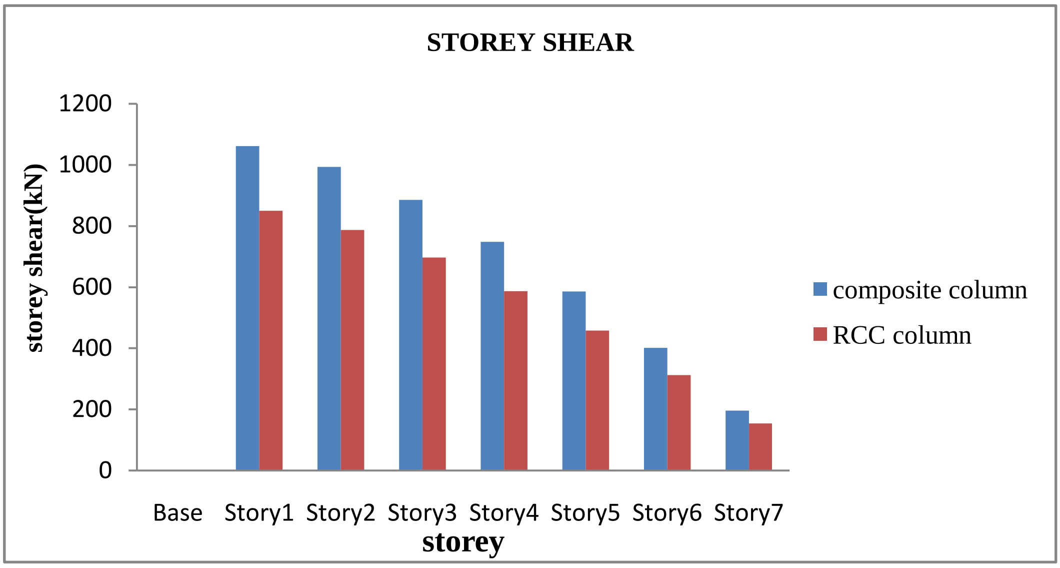

FIG.5: GRAPH OF STOREY VS SHEAR

4.2 Comparison between Circular RCC and Composite column in Irregular plan

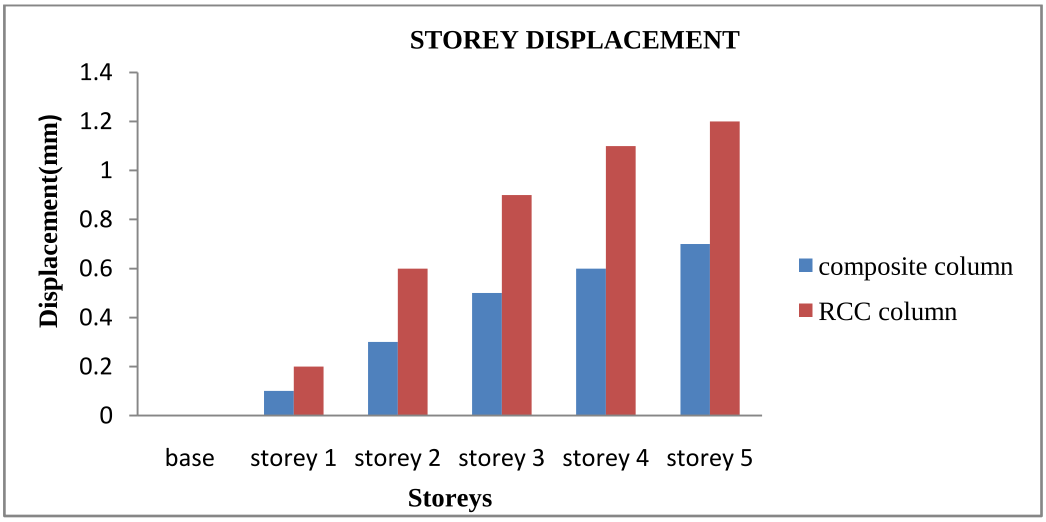

FIG.6: GRAPH OF STOREY VS DISPLACEMENT

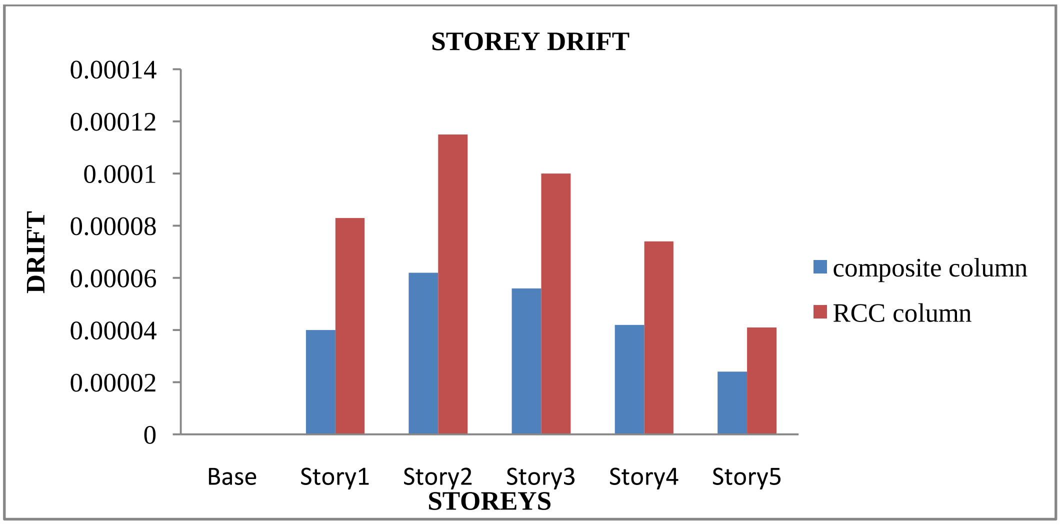

FIG.7:GRAPH OF STOREY VS DRIFT

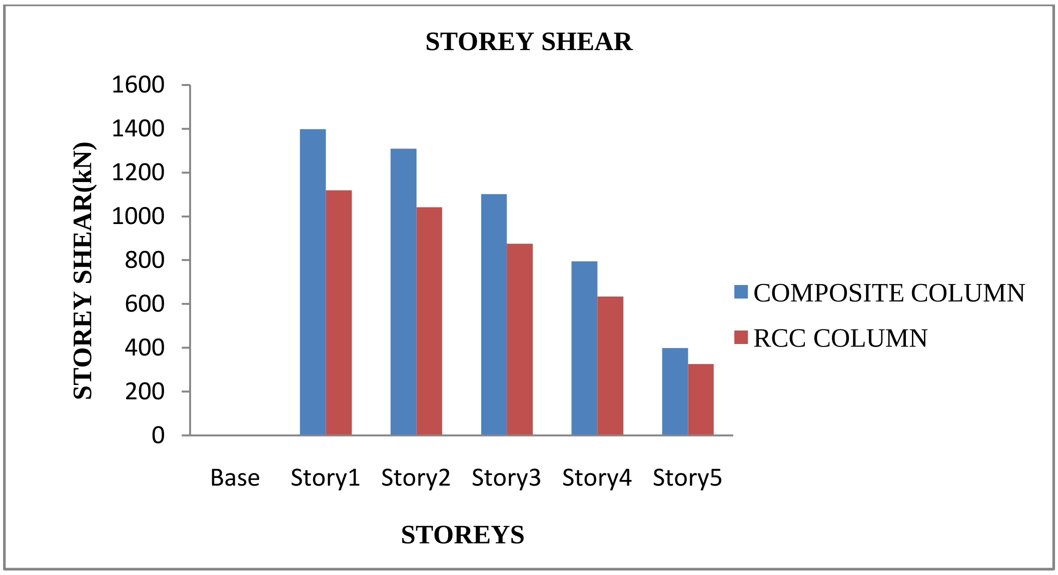

FIG.8:GRAPH OF STOREY VS SHEAR

V. CONCLUSION

- It is observed that displacement in regular structure having rectangular composite column is reduced to 40% to 50% as compared to same structure with rectangular RCC column.
- It is observed that shear in regular structure having rectangular composite column is increased to 60% to 70% as compared to same structure with rectangular RCC column.
- It is observed that drift in regular structure having rectangular composite column is increased to 35% to 40% as compared to same structure with rectangular RCC column.
- It is observed that displacement in irregular structure having circular composite column is reduced to 40% to 50% as compared to same structure with circular RCC column.
- It is observed that shear in irregular structure having circular composite column is increased to 60% to 70% as compared to same structure with circular RCC column.
- It is observed that drift in irregular structure having circular composite column is increased to 35% to 40% as compared to same structure with circular RCC column.

REFERENCES

[1]. Liu Jinbho and Liu Yangbing, “Seismic Behaviour of Analysis of Steel Concrete Composite Frame Structure System”,World Conference on Earthquake Engineering, October, 2008.

[2]. Mahesh Suresh Kumawat and L.G Kalukar, “Analysis and Design of Multistorey Building Using Composite Structure’’,International Journal of Structural and Civil Engineering Research,Vol.3,No.2,May 2014.

[3]. Abhishek Sanjay Mahajana and Laxman.G.Kalukar, “Performance Analysis of RCC and Steel Concrete Composite Structure Under Seismic Effect’’, Intenational Journal of Journal of Research in Engineering and Technology, Vol.05, Issue 04, April 2016.

[4]. Nilesh kumar Ganwani and S.S Jamkar, “Comparitive Study on RCC and Steel Concrete Composite Building using Linear Static Analysis’’ , International Journal for Research and Development,Vol. 04,Issue 02, April 2016.

[5]. IS 1893 (Part 1): 2002 “Indian Standard. Criteria for Earthquake Resistant Design of Structures”.

[6]. IS 11384, “Code of Practice for Composite Construction in Structural Steel and Concrete”.

Comparison of aliphatic hydrocarbon resistant plasticized PVC hoses

Krisztina Roman[1], Gabriella Zsoldos[2], Kalman Marossy[3]

[123]University of Miskolc, B1/214 Miskolc, Hungary, 3515

Abstract: *This paper presents an experimental investigation of two types of aliphatic hydrocarbons resistant soft PVC hoses. A number of tests were performed to determine the internal structures and the difference between the hoses. First tests concerned with pentane resistance, the plasticizer and extender's effects on variations in the structure. The solubility of gas in plasticizer and the changing of morphology determined the applicability. The second analysis of FTIR results can show the internal structure's composition, what the difference is between the two formulations. The weight changes of the hoses can shows the material's gas resistance. The gas diffusion's driving force was the gas evaporation. The gas diffusion can be determined from the decrease of the quantity of the hydrocarbons. The internal structure was also observed by DMA. The measurement was made after a pentane soak of simple samples. The morphology, the material's density, mechanical properties and aliphatic hydrocarbon resistance of samples were determined. After all the measurements, the difference between the products was noticeable during even visual inspection of the samples as well.*

Keywords: PVC hose, FTIR, DMA, gas diffusion, aliphatic hydrocarbon resistant.

I. INTRODUCTION

The use of aliphatic resistant PVC hoses is spreading all across the world, with improved gas safety requirements for industry and public facilities, such as in home hoses. Numerous reasons for this growth include environmental protection, excellent mechanical properties, superior aliphatic hydrocarbon resistance abilities and comfort features of PVC hoses. It is important for the hose to remain stable with changing temperature, because portable gas equipments are used them during summer excursions, and also at high mountain climbing as well. The advantage of using PVC hose is the gas resistance.

The PVC (polyviny-chloride) is one of the most widely used polymers in the field of hose systems. However, the PVC resin is only suitable for processing with additives. The additives modify the PVC's morphology and structure, which can be measured by FTIR and DMA methods.

II. MATERIALS

Hydrocarbon resistant hose was produced according to own formulation and mixing. For comparison a commercial product was used. This hose is made for LPG. The similarity between the hoses is the aliphatic hydrocarbon resistance; both of them can be used as gas hose. The structures of these polymers are more complex than those, used for other applications. For the simplification of sample identification, from now on the own hose is to be called Hose1, and the other Hose2. Basically the Hose1 includes PVC powder raw material and additives, which are: plasticizer (two types of plasticizer: monomer and polyester), lubricants, stabilizer, nitrile rubber (NBR) and filler. The lubricants and stabilizer are essential for processing. The NBR provides hydrocarbon resistance for the hose two types of plasticizers were used to avoid the separation of the mixture. The ingredients of Hose2 are unknown, but it may be similar in composition.

III. MEASUREMENTS

3.1 Sample preparation

The commercial hose consists of two layers. The outer layer is common – probably light stabilized PVC; the internal layer is the gas barrier i.e. the hydrocarbon resistant material. In case of the commercial product the layers were mechanically separated.

Own formulation was produced by mixing component with laboratory fluid mixer; roll milled at 170°C thereafter compression molded into sheets of 1 mm thickness.

For the commercial product the compression molded sheets were produced directly from the separated internal layer.

Specimens were die-cut for all measurements from the compression molded sheets.

3.2 Fourier transformed infrared spectroscopy (FTIR)

Fourier transformed infrared spectroscopy analysis and testing identifies chemical compounds in products, polymers, coating and other products. It is suitable for indentifying of additives of PVC and the internal structure and components. The analysis helps to understand materials and products. Indentified are the chemical bonds in the molecule by producing an infrared absorption spectrum. The FTIR analysis can be further used for examining the components of a basic polymer, and the organic pollutants. [1][2]. Measurements were carried out with a Bruker Tensor 27 FTIR instrument in reflection ATR mode.

3.3 Dynamic Mechanical Analysis

The Dynamic Mechanical Analysis (DMA) is a thermal analysis method, where during the analysis the elastic behavior of the material can be tested with a periodic load in respect to the function of temperature. Complex elastic modulus can be determined; the usual representation of the results is the storage modulus (E') in logarithmic scale and the mechanical loss factor (tgδ) which is the ratio of loss modulus (E'') and storage modulus. The method is applicable to examine the mechanical properties of the plastic products. The loss modulus is very sensitive to internal molecular motions therefore it gives information about the internal structure of the material, too. Dynamic Mechanical measurements were carried out with Metravib 1db DMA25 instrument in tensile arrangement at 1Hz frequency in the temperature range of -60°C to 120°C. Heating rate was 2°C/minute. [3][4]

3.4 Gas diffusion method

Aliphatic hydrocarbon resistant hoses are tested for gas diffusion. During the gas diffusion analysis, the gas transferring ability through the structure of the plastic is determined. The structure depends on the additives especially the plasticizer. If more plasticizer is used, the hoses are more flexible and durable. The Hose2 is same on appearance by visual inspection, but harder at touch.

The gas diffusion testing methods differ a little bit to the permeability testing method. The changes in pentane weight permeability can determine. Measured the weight loss every day, it determined the permeability. If the polymer only transfers little quantities of gas, then the hose is resistant to pentane. If it transfers significant amounts, then determining the gas's quantity is relevant. From the mass change, the materials resistance can be derived. The standard values cannot be exceeded the by measured values. If lots of gas can pass through the polymer, then that is not suitable for gas transferring tube. For measurements I used 1mm thickness samples, but in fact the original hose thickness is 19mm.

FIG. 1: MEASUREMENT TECHNIQUE

3.5 Swelling and plasticizer extractability

Both own formulation and the commercial product were tested by immersion in pentane in order to determine the hydrocarbon uptake and the extractability of plasticizer. Disks of 30mm diameter were die-cut from the compression molded sheets and immersed in pentane at room temperature. The laboratory was air-conditioned according to ISO291-23. Room temperature was controlled 23 ± 1 °C. The full immersion time was 30 days.

Specimen weights were measured daily, exception at the weekends. Extraction causes weight loss, swelling causes increase in weight.

IV. RESULT AND DISCUSSION

4.1 Fourier transforms infrared spectroscopy (FTIR)

The internal structure determined by FTIR analysis is shown on Fig 2. The line 1 presents the Hose1 product; the line 2 presents the Hose2 product.

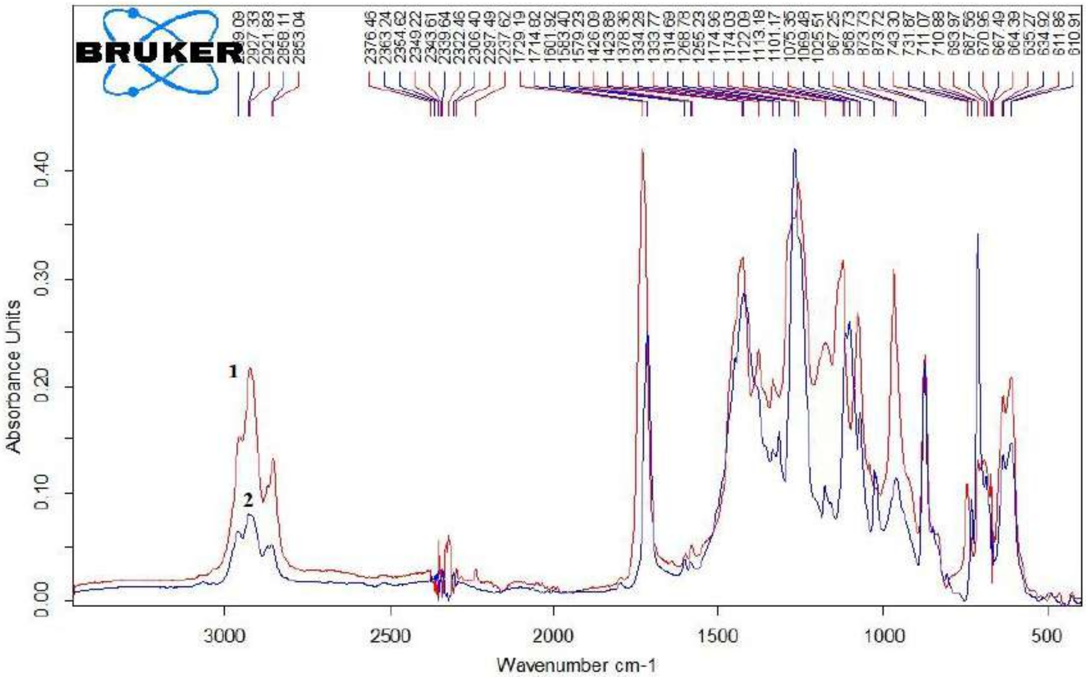

FIG. 2: FTIR ANALYSIS RESULT

All ingredients of the PVC product could be measured. Compared the materials peaks and the product peaks, the products components can be determined.

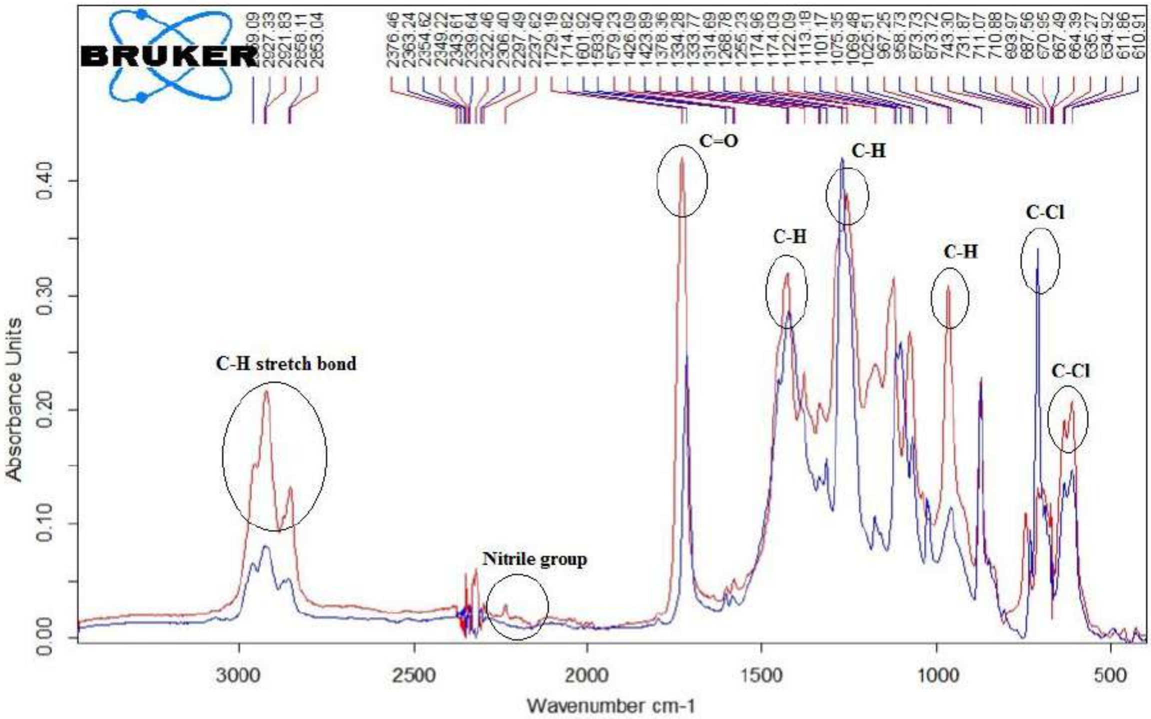

FIG. 3: FTIR ANALYSIS WITH CHEMICAL BONDS

Fig. 3 shows the chemical bonds and molecules. During the analysis the types of developed bonds can be determined with high precision. Based on the types of bonds and the adherent wavenumber, the additives and the components of the product can be determined. Every additive is measured in order to get the corresponding peaks.

TABLE 1
CONTAIN THE WAVENUMBER WITH ADDITIVES FOR HOSE1

Wavenumber cm^{-1}	Additives
711	Filler
743	Plasticizers
874	Filler
967	NBR
1040	Plasticizers
1255	NBR
1378	Plasticizers
1579	Plasticizers
1729	Plasticizers

The results show that plasticizers and copolymer modifies the ability of the polymer. The most bonds were established by the plasticizer and the applied NBR. The plasticizers modified the overall structure. The FTIR analysis gives basic knowledge about the composition of the product; hence the material's inner structure can be determined also by the relations of the inner bonds.

The FTIR analysis of Hose2 proves that similar types of additives were used during the production of the hose. The similarity is more outstanding at lower wavelength. Comparing the two measurement results, the difference between the two samples rests in the quantity of the plasticizer and the NBR component, or the difference of the plasticizer.

4.2 Dynamic Mechanical Analysis

Hose1 and Hose2 samples were measured by DMA. The system gives information about the internal structure and the mechanical loss factor of the samples.

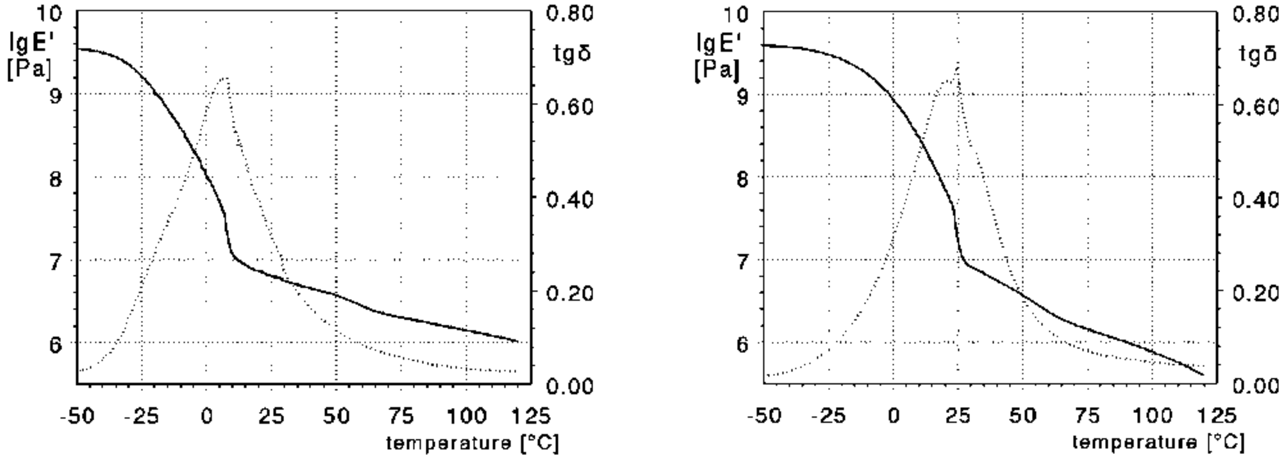

FIG. 4: DMA RESULTS: RIGHT: HOSE1 OWN FORMULATION; LEFT: HOSE2 COMMERCIAL PRODUCT SOLID LINE: STORAGE MODULUS (E'); DOTTED LINE: LOSS FACTOR (tgδ)

Hose1 and Hose2 samples were measured by DMA. The system gives information about the internal structure and the mechanical loss factor of the samples. The temperatures of tgδ maxima were considered as glass transition temperature. tgδ peaks of both materials are not regular proving that a second, partly compatible polymer is present in the composition. Formulation of Hose1 is known, this polymer is the nitrile rubber (NBR).

The two types of mixtures are very similar. The curves characteristics are similar and they run similar. The E' curve shape is a little bit different from the Hose2. The Hose1 sample is apparently more stable at lower temperatures. The glass transition temperature is lower than that Hose2. The Hose2 is rigid at the warmer temperature. The result means that the Hose1 is more resistant and flexible at the lower temperature.

TABLE 2
GLASS TRANSITION TEMPERATURE RESULTS

	Hose1	**Hose2**
T_g [°C]	7	25

4.3 Gas diffusion method

During analysis the value of gas diffusion was matched against the passed time.

Comparing the results it is seen that the gas permeability of Hose1 is slightly higher than of Hose2. Presumably the reasons are the different additives and Hose1 is significantly softer. The softer transferred slightly more gas than the harder. For comparison of the two results linear approximation was made on the measured values. It shows that the Hose2 is more resistant that the Hose1, but this is because it is harder and contains less plasticizer. Both results are within the permitted limits.

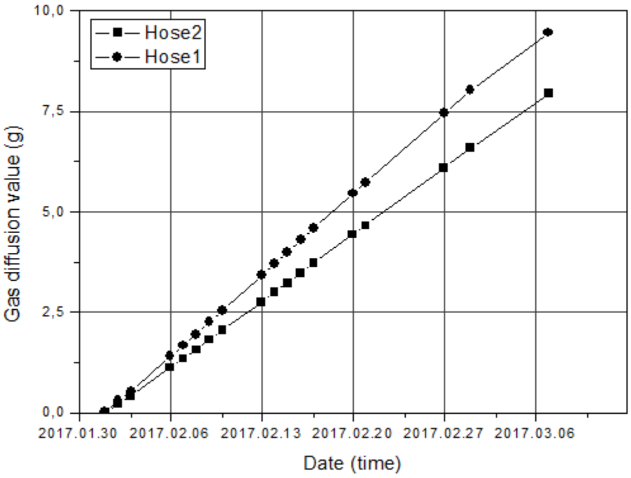

FIG. 5: GAS DIFFUSION RESULTS

4.4 Pentane resistance measuring method

The pentane resistance methods were used for analyzing the pentane weight change. Thanks to the alteration, we can gain more insight in to the pentane resistance of PVC mixtures

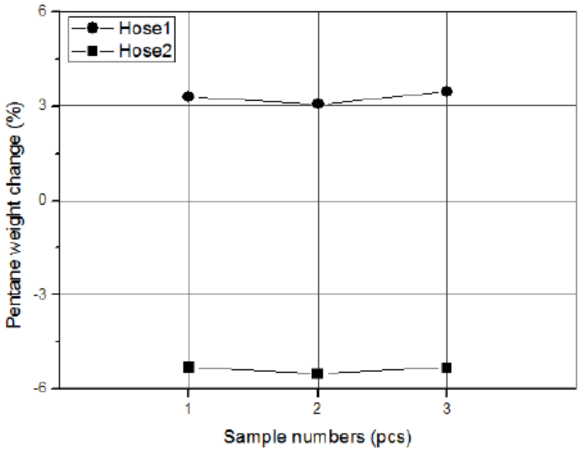

FIG. 6: PENTANE RESISTANCE MEASURING RESULT

According to the analysis Hose2 was less effective, since the applied plasticizer migrated out of the polymer. Due to the migration of the plasticizer, the mechanical properties of the product will change deteriorate? The properties are worsening because the sample will be harder than the original sample. This means, that Hose2 is less adequate at low temperature or with larger amount of aliphatic hydrocarbons. The Hose1 have a plus value that is appropriate, because if the pentane flow disappears, the sample returned to it is original value. During the analysis of Hose1 plasticizer migration did not occur, only the structure of the polymer swelled. From this point of view, the Hose1 is more appropriate.

V. CONCLUSION

Overall, the experiments carried out provided useful information on the composition of the two types of hoses. Comparing the tubes mechanical properties the results shows differences. The additives which were used in Hose1 are more resistant to aliphatic hydrocarbons than the Hose2 ingredients. The most important feature of these types of hoses should be their resistance to aliphatic hydrocarbons.

Both types of hoses are suitable for both industrial and domestic use, but Hose1 was far safer concerning gas release. The slightly better (lower) gas permeability of Hose2 is caused by lower plasticizer content. It caused the inconvenient hardness of the product. It must also be mentioned, that Hose2 does not contain real hydrocarbon resistant plasticizer, and this additive is extractable from the product.

It was proved during the analysis, that even small changes in the composition, can cause high impact on the mechanical properties of the product.

REFERENCES

[1] Kalman Marossy: Testing polymer mixtures by Dynamic Mechanical Analysis, Manuscript of a lecture (2006)
[2] Kalman Marossy: Dynamic Mechanical Analysis, Manuscript of a lecture (2016)
[3] http://www.intertek.com/analysis/ftir/
[4] https://chemistry.oregonstate.edu/courses/ch361-464/ch362/irinstrs.htm

Characterization of Layered GaSe Crystals Intercalated with $RbNO_3$ Ferroelectric Salt and their Application for Electric Capacitors

YuriyZhirko[1], VasiliyGrekhov[2], ZakharKovalyuk[3], Victor Netyaga[4]

[1,2]Institute of Physics, ProspektNauki, 46, 03028, Kiev, Ukraine
[3,4]Chernivtsy Branch of Institute for Material Science Problem, Vilde str., 5, 58001, Chernivtsy, Ukraine

Abstract— *XRD, SEM, EDX investigations as well as wide temperature (T = 5–300 K) photoluminescence measurements of GaSe single crystals intercalated from the melt of $RbNO_3$ ferroelectric salt at various temperatures and exposure times are performed in this work. Intercalation by this method results in GaSe matrix fragmentation by separate polycrystals 1 mm in size which consist of bulk GaSe segments (with sizes up to 50.0 mkm) and veins of $RbNO_3$ ferroelectric salt with thickness reaching 2–3 mkm. Within the GaSe segments are inclusions of nano-sized phases consisting of $RbNO_3$ salt whose diameter does not exceed 120 nm. It has been shown that the creation of GaSe<$RbNO_3$> hybrid structure has an insignificant influence on the optical properties of GaSe matrix, since in the photoluminescence spectra of GaSe<$RbNO_3$> at T = 300 K one can observe emission of free excitons which is typical for GaSe single crystals. The electrical investigations performed indicate that the intercalated GaSe<$RbNO_3$> or GaSe<KNO_3> are capable of accumulating electric energy, and prototypes of supercapacitors based on them possess: specific long-time energy 105 kJ/kg and resource of cycles > 10^6.*

Keywords*— *Layered crystal, GaSe, intercalation, ferroelectric, supercapacitors.

I. INTRODUCTION

Anisotropy of chemical bonds in layered crystals, weak van der Waals bonds between crystalline layers, and strong covalent bonds between adjacent atoms inside the layers define anisotropy of electric and dielectric properties of these crystals, which results in instability of synthesis when forming the crystalline lattice of these compounds. The following intercalation of the interlayer space in these crystals with foreign atoms or molecules, beside obtaining some expected changes in physical-and-chemical properties of hybrid materials based on them, finds its practical applications in power engineering, in particular, as solid-state hydrogen storages [1, 2], accumulators of electric energy [3], and sensors of physical fields [4]; moreover, heterostructures with high photosensitivity based on these materials can be applied in solar cells [5–7].

In this paper we present our recent investigation of some physical and chemical properties of GaSe single crystals intercalated in melts of $RbNO_3$ ferroelectric salt and done some estimates of their application as working materials for solid state supercapacitors in the up-to-date semiconductor element base.

II. EXPERIMENTAL METHODS

Pure GaSe crystals were grown using the Bridgman method from a stoichiometric melt. The obtained semiconductor layered single crystals had the following properties: hexagonal structure of ε-modification (space group D^1_{3h}) with unit cell parameters of $a = 3.7549 \pm 0.0002$ Å, $c = 15.9483 \pm 0.0001$ Å; conduction of *p*-type; carriers concentration of $2.3 \cdot 10^{15}$ cm^{-3}; and resistivity of $2.1 \cdot 10^9 \Omega \cdot cm$.

Then, from large ingots of the obtained single crystals, using mechanical spalling, we separated plates with sizes of 3 mm × 3 mm × 1 mm along the cleavage plane. In what follows, these plates were intercalated in the melt of $RbNO_3$ ferroelectric salt.

Intercalation in the melt was realized in the following manner. Ferroelectric material of rubidium nitrate was melted in a porcelain crucible (chemically inert in the melt) at a temperature within the range of 365–411 ºC. The melting temperature of $RbNO_3$ is 313.3 °C. The temperature of melt was automatically maintained by a temperature regulator with accuracy ± 0.1 ^{0}C. The samples of GaSe single crystals were wholly dipped into the melt, where the process of $RbNO_3$ intercalation into the layered crystal GaSe took place. The principal setup of the facility for intercalation in the melt is shown in Fig. 1. The process of intercalation and “*in-situ*” measurements was performed in a hermetic box in air dried with P_2O_5.

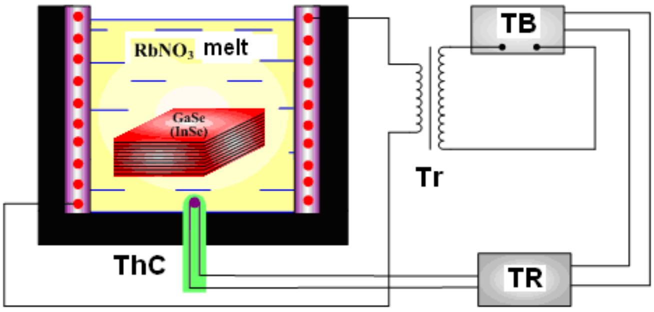

Fig. 1 Scheme of GaSe intercalation in $RbNO_3$ melt. Here: Tr – Transformer, TB – Thyristor Block, TR – Temperature Regulator, ThC – Thermocouple

Fig. 2 shows stereo-microscopic images (Leika) of the cleavage surfaces of GaSe crystals intercalated in the $RbNO_3$ melt at various temperatures and times of exposure. As can be seen, intercalation in the melt results in fragmentation of the crystalline matrix.

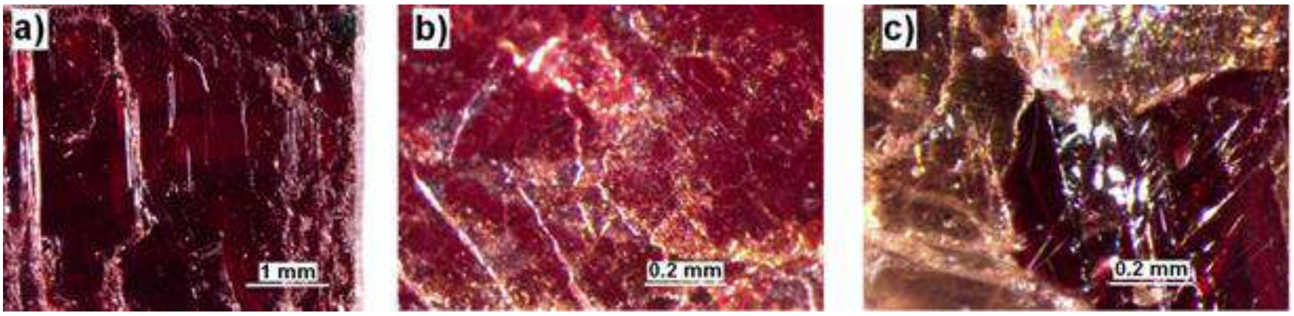

Fig. 2. Stereo-microscopic images of cleavage surfaces of the intercalate GaSe<$RbNO_3$> after exposure of the GaSe crystal in the melt of $RbNO_3$ salt for various time at a temperature of 367 °C: a) sample #1 - 17 min, b) sample #2 - 32 min, c) sample #4 - 68 min.

In addition to fragmentation of the GaSe crystal, in the process of its intercalation in the $RbNO_3$ melt, growth of the mass and thickness of the sample is observed. As seen in Fig. 3, in the first stage, one can observe a noticeable increase in the mass and thickness of the sample. In the second stage, this growth is insignificant, but in the third stage the mass and thickness of the sample grow very fast, accompanied by subsequent destruction of GaSe< $RbNO_3$>intercalate. This part of the experiment is described in more detail in [8].

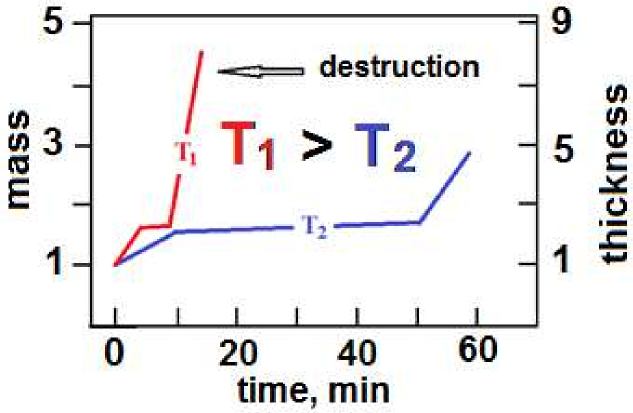

Fig. 3. Dependences of the mass and thickness of GaSe<$RbNO_3$>intercalate on the time and temperature of the $RbNO_3$ melt.

2.1 Electron-microscopic and energy-dispersion investigations of GaSe<$RbNO_3$> intercalates

Characterization of GaSe crystals and GaSe<RbNO3> intercalates was done ne scanning electron microscope (SEM, Vega3 SBU, Tescan) equipped with secondary-electron (SE) and back-scattering electron (BSE) emission detectors as well as EDX spectrometer (Oxford Instruments) with an X-act (10 mm^2) SSD detector and Inca EDS Software.

Fig. 4 shows the technological (external) surface of GaSe single crystal intercalated in the $RbNO_3$ melt. After intercalation, this surface has new formations in the form of dendrites of various shapes and sizes. It is noteworthy that these new formations define the mass and thickness of intercalated samples to some extent. At the same time, the spot in Fig. 4a indicates the part of the crystal that was investigated using the energy-dispersion analysis of the chemical composition of this technological surface.

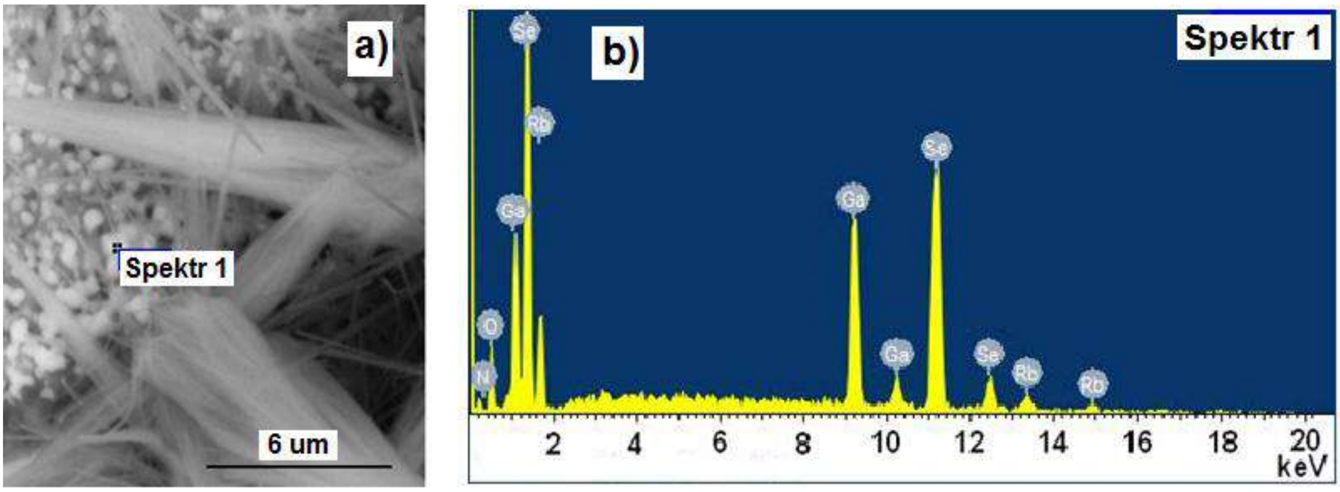

FIG. 4. A) ELECTRON-MICROSCOPIC IMAGE OF TECHNOLOGICAL SURFACE OF GaSe<RbNO3>; b) EDX SPECTRA OF SELECTED POINT ON TECHNOLOGICAL SURFACE OF GaSe<$RbNO_3$> INTERCALATE

Fig. 4b shows the EDX spectrum of the spot illustrated in Fig. 4a. In this spectrum, one can see the peaks corresponding both to the Ga and Se atoms that form the matrix and to the Rb, N, and O atoms related with the ferroelectric salt. The concentration of atoms at the technological surface differs to some extent from the stoichiometric compositions of the GaSe matrix and $RbNO_3$ salt.

Fig. 5 shows the cleavage surface of GaSe<$RbNO_3$> intercalate for various magnifications in the range of 251× to 50,000×. Juxtaposing Figs. 2 and 5, one can see that after intercalation in the $RbNO_3$ melt, the monocrystalline GaSe matrix forms disordered crystalline blocks (up to 1 mm in size), that is, it becomes polycrystalline. Inside large blocks, one can observe further segmentation of the matrix with the creation of $RbNO_3$ salt veins between the segments.

In our opinion, these veins are created during intercalation in the places of dislocations and point defects in GaSe, which results in the appearance of stress-strain regions in the lattice of polycrystals. The above veins of $RbNO_3$ salt possess complex 3D forms, and their thickness reaches 2 to 3 mkm. Also, one can see that inside the segments, whose sizes reach 50 mkm (Figs. 5c to 5d), there are inclusions of the ferroelectric salt solid phase that are non-uniformly distributed inside the segments. The mean diameter of these inclusions does not exceed 120 nm.

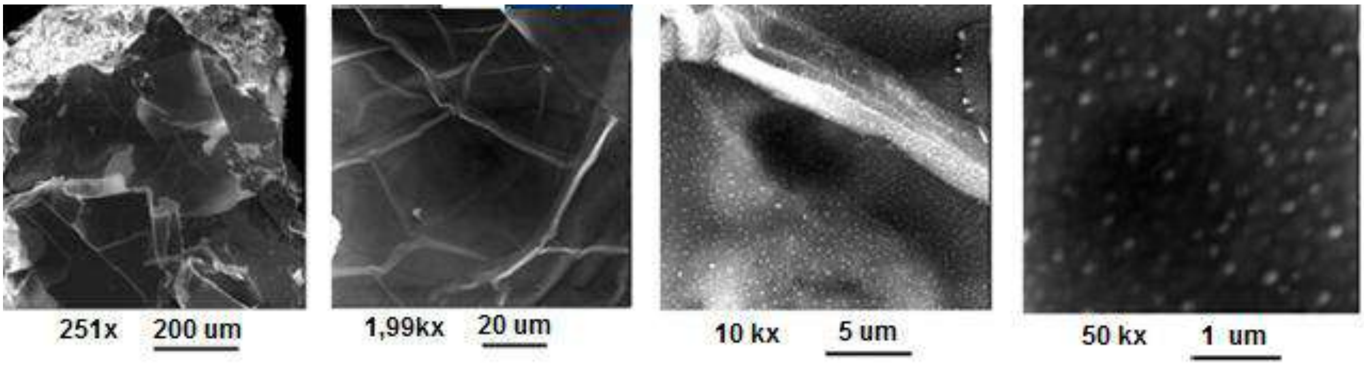

FIG. 5. SEM IMAGES OF THE FRESH CLEAVAGE SURFACE OF THE GaSe<$RbNO_3$> INTERCALATE AT MAGNIFICATIONS OF 251× to 50,000×.

As can be seen from Figs. 5c and 5d, the concentration of $RbNO_3$ inclusions related to the total scanned surface in the SEM image rages from 2 to 10% in segments of the GaSe matrix and up to 100% in the $RbNO_3$ veins.

2.2 X-ray diffraction investigations

Fig. 6 presents the XRD spectrum of GaSe<$RbNO_3$> intercalates obtained using the diffractometer DRON-3. As seen in this spectrum, beside the diffraction peaks corresponding to the GaSe crystal, there are peaks corresponding to the crystals of $RbNO_3$ salt.

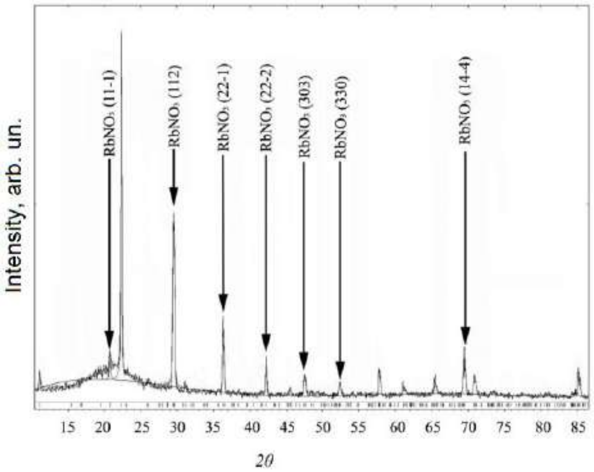

FIG. 6.DIFFRACTOGRAM OF THE COMPOSITE NANOSTRUCTURE GaSe<$RbNO_3$>. THE ARROWS INDICATE DIFFRACTION PEAKS INHERENT TO THE $RbNO_3$ CRYSTALLINE PHASE.

The obtained XRD data confirms that the intercalation process in the GaSe single crystal leads to the transition of the unit cell belonging to GaSe in ε-modification to that observed in δ-modification, whose parameters are as follows: a = 3.7550 Å and c = 31.8903 Å. In accordance with [9], the unit cell in δ-modification consists of four crystalline layers. When intercalating the GaSe matrix from the melt, the parameter a is practically unchanged, while the parameter c is noticeably reduced. This reduction of c parameter is caused by pressure that is related to the embedding of the $RbNO_3$ inclusions into the GaSe matrix. Indeed, according to [10], the hydrostatic pressure in GaSe crystals reduce the width of van der Waals gap and the length of double bond between Ga atoms inside the GaSe crystalline layer and also reduce the parameter c, while the parameter a remains unchanged.

In the case of the $RbNO_3$ ferroelectric salt intercalated to the GaSe crystal, the growth of both parameters in the $RbNO_3$ unit cell (a = 10.4996 Å and c = 7.3810 Å) is involved. It should be noted that standard parameters of the $RbNO_3$ salt unit cell in our investigations were a = 10.4352 Å and c = 7.3710 Å, in full agreement with the literature data [11].

These changes in the parameters of the GaSe and $RbNO_3$ unit cells indicate creation of mechanical stress-strain states at the boundaries between the matrix and intercalant, which causes pressure inside the GaSe< $RbNO_3$> intercalate. In turn, it results in rupture (crushing) of crystalline layers and segmentation of the GaSe matrix.

Using the crystals InSe and GaSe as examples, earlier XRD investigations showed that electrochemical intercalation of these layered crystals with hydrogen [1] results in growth of the parameter c due to increasing of the width of van der Waals gap in the crystal. At the same time, SEM investigations confirmed that intercalation of GaSe and InSe crystals in solutions of hydrogen-containing molecules (H_2O, C_2H_5OH, C_6H_7) leads to swelling of the van der Waals gap [2]. However, in both of these cases of intercalation with hydrogen or hydrogen-containing molecules, segmentation of GaSe and InSe matrixes was not observed even after cooling them down to T = 5 K and then heating them up to room temperature.

Also, it was shown in [1, 2] that hydrogen and hydrogen-containing molecules are intercalated and de-intercalated from these layered crystals without any destruction of the crystal, and the concentration of hydrogen molecules during intercalation reaches 2 to 3 per molecule of Ga_2Se_2.

This different reaction of the matrix from the reaction of the chemical compound intercalated in it can be related to the difference in the physico-chemical properties of the hydrogen-containing molecules and ferroelectric salts in the matrix of GaSe (InSe). In accordance with [1, 2], the hydrogen-containing molecules passivate point defects (donors/acceptors) of the layered GaSe (InSe) matrix. On the contrary, $RbNO_3$ pass its Rb or O atoms to point and spatial defects of GaSe matrix which create different intermediate chemical compounds between them. The thickness of these intermediate compounds can vary between one and several molecules of GaSe and $RbNO_3$.

Juxtaposing between: i) optical images of cleavage surfaces for the GaSe<$RbNO_3$> intercalates, dependences of the mass and thickness of samples on the time of their intercalation in the melt of ferroelectric salt at various temperatures, data obtained from SEM, EDX, and XRD investigations of the GaSe<$RbNO_3$> intercalates; and ii) taking into account the classical theory of materials strength (and considering in this model action of the $RbNO_3$ salt intercalated into GaSe as an external pressure applied to the GaSe monocrystalline matrix) one can make the following assumption:

- Three stages of growth of the thickness and mass of the samples with time and temperature of intercalation of the layered GaSe matrix with the $RbNO_3$ salt are similar to the three stages of application of the external force that stretches or compresses the studied solid.

Namely,

- in the first stage, the process of intercalating the GaSe matrix with the $RbNO_3$ melt corresponds to the Hooke law (nano-formations of the $RbNO_3$ salt are created in GaSe matrix);
- in the second stage, plastic deformation of the GaSe matrix takes place, with a possible transition from one modification to another;
- The third stage corresponds to fragmentation of the GaSe matrix, which is completed by its destruction.

Also, it is worth noting that ferroelectrics possess the so-called "soft modes", which lead to phase transitions in ferroelectrics under the changes in temperature. This should also be taken into account when cooling the GaSe<$RbNO_3$> intercalate down to the room temperature after extraction from the $RbNO_3$ melt.

2.3 Photoluminescence spectra

Measurements of photoluminescence (PL) spectra were made using a 0.6-m optical spectrometer MDR-23 (LOMO) with a grating 1200 grooves/mm. Investigations of PL spectra at T = 5–300 K were made using a helium cryostat A-255 designed at the Institute of Physics NAS of Ukraine. It was equipped with a UTRECS K-43 system allowing control of a sample temperature within the range 4.2 to 330 K with an accuracy of 0.1 K.

The excitation of PL spectra was performed using a current-wave semiconductor laser with a wavelength of 532 mn and stable power at 100 mW equipped with laser (SL-532-10 Thorlabs) and edge (LP-03-532-RS Semrocks) filters. An a FEU-79 photomultiplier tube was served as the radiation detector. The slit spectral width of monochromator did not exceed 0.2 meV at T = 5 K and 0.5 meV at T = 300 K.

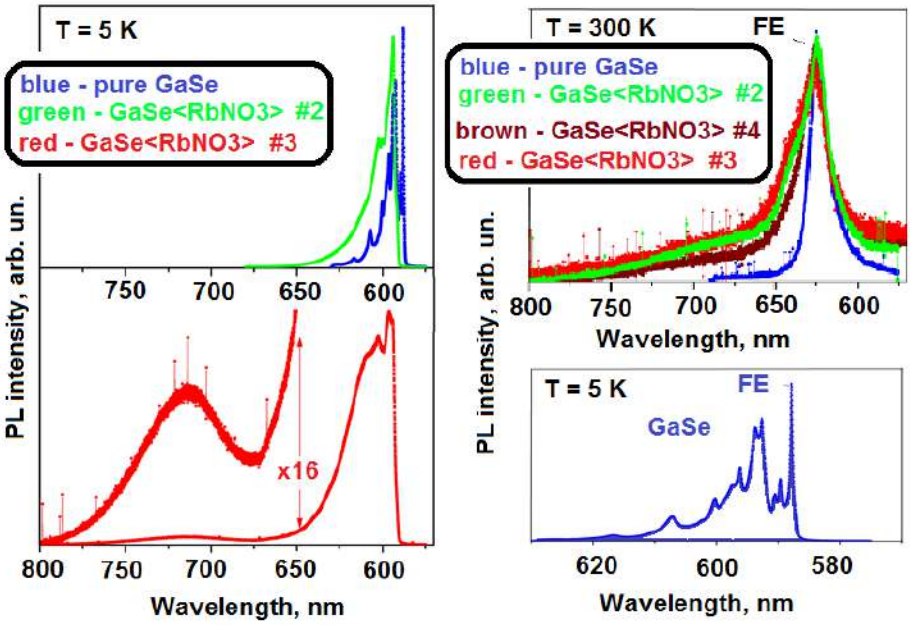

FIG. 7. PHOTOLUMINESCENCE SPECTRA: (A) AND (B) FOR THE GaSe SINGLE CRYSTALS AND SAMPLES #2 AND #3 OF THE GaSe<$RbNO_3$> INTERCALATES AT T = 5 K; (c) FOR THE GaSe CRYSTAL AND THE SAMPLES #2, #3 AND #4 OF THE GaSe<$RbNO_3$> INTERCALATES at T = 300 K; (d) FOR THE GaSe SINGLE CRYSTAL T = 5 K. THE TEMPERATURE OF GaSe<$RbNO_3$> MELT WAS 367 °C

Fig. 7 are the photoluminescence spectra at the temperatures of $T = 5$ and 300 K for GaSe single crystals and the samples of GaSe<$RbNO_3$> intercalates prepared under various exposure times and the melt temperature of 367 °C.

As it can be seen in Fig. 7d, at $T = 5$ K the PL spectrum of GaSe crystal consists of lines corresponding to radiation of the free excitons (λ = 587.8 nm, $E_{exc} = 2.108$ eV) [12] as well as of excitons bound to stacking faults of crystalline layers, dislocation, and point defects. Besides, the PL spectrum in the range $E < 2.050$ eV ($\lambda > 605.0$ nm) contains several bands of a low intensity which, according to [4], are caused by transitions between the direct and indirect conduction bands and shallow acceptors in GaSe<$RbNO_3$>.

As seen in Fig. 7a, the PL spectra of the GaSe<$RbNO_3$> intercalates do not contain emission lines of free excitons or excitons localized at the stacking faults of crystalline layers [13–15] or at extended spatial defects of the dislocation type. But emission lines of excitons localized on point defects (see sample #3) and broad band's associated with radiative recombination of electrons from direct/indirect conduction bands at the deep acceptor levels (155, 190, 310, and 460 meV) with participation of one to three optical fully symmetric (A) or polar (LO, TO) phonons of crystalline lattice are available in these spectra. The similar optical transitions in the forbidden gap depth are also observed in GaSe crystals doped with 3-d elements of the iron group at concentrations up to 1 wt. %, and take place between direct/indirect conduction bands and deep acceptor levels with participation of optical phonons [4].

The results of these investigations clearly indicate imperfection of the GaSe crystal, which is caused by its intercalation in the melt of $RbNO_3$ salt. This imperfection defines lowering the polariton lifetime in the exciton-like state, fast exciton localization, and recombination near defects. Therefore, at $T = 5$ K one cannot observe emission of free excitons in the GaSe<$RbNO_3$> intercalates.

Growth of the temperature up to 300 K in the GaSe single crystal sample leads to uniform scattering of free exciton by phonons of the crystalline lattice [16]. As a consequence, the lifetime of polariton in the exciton-like state becomes lower than the time of exciton localization on the defect. Therefore, in the PL spectrum of GaSe single crystal (Fig. 7c) only the emission line of free excitons remains at T = 300 K.

In the case of GaSe<$RbNO_3$> at $T = 300$ K, like the case of GaSe single crystals, one can observe emission of free excitons, which is accompanied by emission of broad bands caused by radiative recombination of electrons from direct/indirect conduction bands to the deep acceptor levels (155 and 190 meV) with participation of one to three optical full-symmetric or polar phonons of the crystalline lattice.

Up to the experimental accuracy, one can state that the energy of the emission line corresponding to free exciton in the GaSe crystal and in GaSe<$RbNO_3$> intercalates coincides. It is indicative of the fact that under intercalation from the melt, the width of the forbidden gap in GaSe polycrystalline blocks (which is defined by electron orbitals of adjacent atoms Ga and Se in the crystalline layer) does not change even in the presence of $RbNO_3$ salt nano-formations in the matrix. Therefore, one can state that lowering of the parameter c in the GaSe polycrystalline matrix intercalated with $RbNO_3$ salt takes place due to lowering the width of the van der Waals gap.

Taking into account the size of GaSe matrix segments in the GaSe<$RbNO_3$> intercalates, the so-called “blue shift” of free excitons can be neglected.

Thus, one can draw a conclusion that the GaSe<$RbNO_3$> polycrystalline matrix keeps the optical properties inherent in monocrystalline GaSe, despite the fact that, during intercalation from the ferroelectric salt melt, large spatial veins and nanoparticles of $RbNO_3$ are embedded there.

2.4 Development of supercapacitor prototype and studying of its properties

The prototype of a supercapacitor based on the GaSe<$RbNO_3$> or GaSe<KNO_3> intercalates whose electric and dielectric properties were investigated was developed in the following way. We deposited plain conducting ohmic contacts with leads onto the planes of intercalated samples GaSe<$RbNO_3$> or GaSe<KNO_3> (oriented along the normal to the crystallographic axis *C*) which were spalled from both sides of the surfaces. Then, the sample as a whole was sealed with a silicon sealant. The prototype prepared in this way was investigated as an accumulator of electric energy. The basic sketch of the supercapacitor based on the GaSe<$RbNO_3$> intercalate is shown in Fig. 8a; and a photograph of this prototype covered with a metal envelope is presented in Fig. 8b.

We applied the constant electric field with the voltage 200 V to the contacts of the prototype shown in Fig. 8 for 10 min. As a result, after stopping the action of the external electric field, the capacitor plates kept the voltage close to 19.5 V. The specific long-time energy was higher than 105 kJ/kg. The specific energy was 29.1 W·h/kg

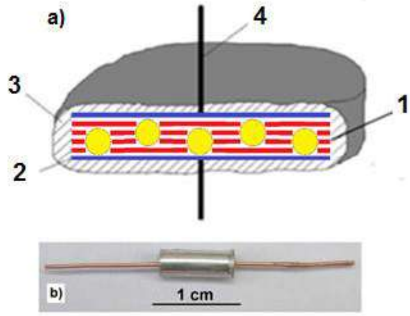

FIG. 8 A) BASIC SKETCH OF THE SUPERCAPACITOR PROTOTYPE. HERE: 1 – GaSe<KNO$_3$> or GaSe<RbNO$_3$> INTERCALATE (YELLOW BALLS – RbNO$_3$ SALT); 2 – CURRENT-CONDUCTING PLANE CONTACT (BLUE); 3 – COMPOUND ENVELOPE; 4 – CURRENT TAP. B) PHOTOGRAPH OF THE SUPERCAPACITOR PROTOTYPE.

The studied capacitor of electric energy capable of operating within the range of 50 to 200 V; its operation temperature lies within the interval of –40 to +50 °C; and its number of charge cycles > 10^6.

Table 1 summarized the data comparing the energy performances of the proposed electricfl energy capacitor based on the GaSe<KNO$_3$> intercalate and other supercapacitors.

TABLE 1
SOME TECHNICAL PERFORMANCES OF THE OFFERED GaSe<KNO$_3$> PROTOTYPE AND OTHER SUPERCAPACITORS

	C, F	$C_{spesific}$, F/g	$C_{specific}$, F/cm3
Maxwell	3000	6	68
Loxus	5000	12,5	110
Wima	5000	1,76	1,8
Nesscap	5000	11,11	100
Prototype GaSe<KNO3>	58	2148	2320

III. CONCLUSIONS

From the performed investigations of processes taking place in GaSe crystals when intercalating them in the melt of ferroelectric salt RbNO$_3$ and studying the physical and chemical properties of the prepared GaSe<RbNO$_3$> intercalates, the following features could be ascertained:

1. Non-monotonous growth of the mass and thickness of the crystal takes place over time. This process consists of three stages: i) the mass and thickness of the sample grow; ii) the mass and thickness of the sample are not practically changed with time; iii) both parameters increase to the limit when matrix destruction is observed.

In accord with the classical theory of the strength of materials, intercalation of the GaSe matrix in the first stage obeys Hooke's law: nanoparticles of RbNO$_3$ salt are formed in this matrix, resulting in growth of the mass and thickness of the sample. In the second stage, plastic deformation of the GaSe matrix takes place with a possible transition to another modification, when GaSe bulk polycrystals are created. In the third stage, we observe a transition to final fragmentation of the GaSe matrix when veins of RbNO$_3$ salt are created between these fragments. Further intercalation is completed by destruction of the GaSe matrix.

2. In the process of intercalation, the GaSe matrix becomes polycrystalline, and these polycrystals (with the sizes up to 1 mm) consist of segments (with sizes of up to 50 mkm), between which ferroelectric salt veins of a complex 3D form are created, whose thickness is close to 2 – 3 mkm. Inside the matrix segments, one can observe non-uniformly distributed inclusions of ferroelectric salt with a mean size of 120 nm. The concentration of these inclusions in the matrix segments reaches 2% to 10% and becomes 100% in the veins between segments.

3. The unit cell of the GaSe single crystal in ε-modification makes the transition into δ-modification, which consist of four crystalline layers with the following parameters: a = 3.7550 Å and c = 31.8903 Å. This lowering of the parameter c takes place due to a reduction in the width of the van der Waals gap caused by pressure related with embedding the veins and nano-sized $RbNO_3$ inclusions in the GaSe matrix.

4. Both parameters of the unit cell of the ferroelectric salt $RbNO_3$are increased to a = 10.4996 Å and c = 7.3810 Å.

5. Despite the creation of a large numbers of defects (veins and nanoparticles of $RbNO_3$) during intercalation by using the "from the melt" method, the GaSe polycrystalline matrix retains the optical properties inherent in the GaSe single crystal. At the same time, the number of point and spatial defects becomes larger, which creates deep acceptor levels responsible for the processes of radiative recombination of electrons from direct/indirect conduction bands with participation of one to several optical phonons.

6. The electrical investigations performed indicate that the intercalated GaSe<$RbNO_3$> or GaSe<KNO_3> can find application as working materials for solid state supercapacitors in the up-to-date semiconductor element base. They are capable of accumulating electric energy, and prototypes of supercapacitors based on them possess: specific long-time energy 105 kJ/kg and resource of cycles > 10^6.

ACKNOWLEDGEMENTS

Performing these investigations became possible owing to the project No. 0108U000252 within the framework of the departmental subject area in the National Academy of Sciences of Ukraine in accord with the Program for Scientific Instrument Engineering.

Also, the authors are very grateful to Dr. Z.R. Kudrynskyi for fruitful discussion of the experimental results obtained in this work.

REFERENCES

[1] Y.Zhirko, V.Trachevsky, and Z.Kovalyuk, "On the possibility of layered crystals application for solid state hydrogen storages – InSe and GaSe crystals", In book: "Hydrogen storage", by Editor Jianjun Liu, (ISBN) 978-953-51-0731-6, InTech, 2012, pp.211– 242.

[2] Y. Zhirko, V. Grekhov, N. Skubenko, Z. Kovalyuk,and T.Feshak, "Characterization and optical properties of layered InSe and GaSe crystals intercalated with hydrogen and oxygen-hydrogen-containing molecules", In book: "Advanced Materials for Renewable Hydrogen Production, Storage and Utilization",by Editor Jianjun Liu, (ISBN) 978-953-51-2219-7, InTech, 2015, pp.11–50.

[3] I.I. Grigorchak, A.V.Zaslonkin, Z.D. Kovalyuk et al., Patent of Ukraine (2002), Bulletin No5, No46137.

[4] Y.I. Zhirko, N.A. Skubenko, V.I. Dubinko, Z.D. Kovalyuk,and O.M. Sydor, "Influence of Impurity Doping and γ-Irradiation on the Optical Properties of Layered GaSe Crystals", Journal of Materials Science and Engineering B, pp.91–102, 2012.

[5] A.A. Lebedev, V.Yu. Rud', and Yu.V. Rud', "Photosensitivity of geterostructures porous silicon-layered $A^{III}B^{VI}$ semiconductors", Fiz.Tekch. Polupr. (in Russian),vol.32,pp.353–355, 1998.

[6] J. Martines-Pastor, A. Segura, and J. L. Valdes,"Electrical and photovoltaic properties of indium-tin-oxide/p-InSe/Au solar cells", J. Appl. Phys., vol. 62,pp.1477–1483, 1987.

[7] S. Shigetomi, and T. Ikari, "Electrical and photovoltaic properties of Cu-doped *p*-GaSe/*n*-InSe hetero-junction", J. Appl. Phys.,vol. 88 pp.1520–1524, 2000.

[8] Z.R. Kudrynskyi, and V.V. Netyaga, "Nanocomposite Material Based on GaSe and InSe Layered Crystals Intercalated by $RbNO_3$ Ferroelectric", Journal of Nano- and Electronic Physics, vol. 5,03028(7pp), 2013.

[9] A.Polian, K. Kunc, and A. Kuhn,"Low-frequency lattice vibrations of δ-GaSe compared to ε- and γ- polytypes", Sol. St. Commun., vol.19, pp.1079–1082, 1976.

[10] D.Olguin,A.Cantarero,C.Ulrich,and K.Suassen,"Effect of pressure on structural properties and energy band gaps of γ-InSe",PhysicaStatusSolidi (b), vol.235, pp.456–463,2003.

[11] V.E. Plustchev, andB.D. Stepin, "Chemistry and technology of lithium, rubidium, and cesium compounds",Moscow: Khymija, 1970.

[12] Yu.P. Gnatenko, P.A. Skubenko, Yu.I. Zhirko, and O.V.Fialkovskaya,"Emission of Free and Bound Excitons in GaSe and InSe Crystals in Direct and Indirect Transition Region", J. Luminescence,vol. 31&32, pp.472–475, 1984.

[13] N. Kuroda, and Y. Nishina,"Stacking-fault splitting of exciton spectrum in GaSe",NuovoCimento, vol.32B, pp. 109–115, 1976.

[14] Le Chi Thanh, and C. Depeursinge, "Fine structure of the exciton spectrum in GaSe", Sol. St. Com., vol.25, pp. 499–503, (1978).

[15] Y. Sasaki, and Y. Nishina, "Mobile and immobile localized excitons induced by the stacking faults in GaSe", Physica, vol. BC105, pp.45–49, 1981.

[16] Yu.I. Zhirko,"Investigation of the light absorption mechanisms near exciton resonance in layered crystals. Part 2. N=1 state exciton absorption in GaSe", PhysicaStatusSolidi (b), vol.219, pp.47–61, 2000.

On the Method of Construction of the Dependence of the Heat Extension Coefficient on Temperature in Heat-resistant Alloys

Dr. Sairanbek Akhmetov[1], Dr. Anarbay Kudaykulov[2]

[1]Department of Mechanics, L.N. Gumilyov Eurasian National University, Astana – 010000, Kazakhstan
[2]Department of Fluid and Gas Mechanics, Al-Farabi Kazakh National University, Almaty – 050040, Kazakhstan

Abstract— *In this paper, we consider methods and methods for studying rods from high-temperature alloys, in particular, the study of the dependence of the coefficient of thermal expansion on temperature. According to the tasks of the paper, methods are developed for taking into account the presence of local surface heat exchanges, temperatures, and internal point heat sources in the study of rods made of high-temperature alloys. The scientific significance of the project is due to the fact that the results of the development can be used for in-depth study of the nonlinear thermal and physical state of the structural rod elements that work in the presence of heterogeneous types of heat sources. Such designs include gas-generating, nuclear, thermal and hydrogen power plants, as well as jet engines and internal combustion engines. In order to ensure continuous reliable operation of these facilities, the authors developed fundamental methods that allow to adequately simulate non-linear thermophysical processes in the rod bearing elements of installations taking into account simultaneous presence of local thermal insulation, heat exchange, temperatures, and internal point heat sources. The laws of the distribution of temperature, elastic, temperature and thermoelastic components of strains and stresses, as well as displacement, are obtained. This became the basis for the creation in the future of a program in the programming language PYTHON, with the help of which it is possible to construct the corresponding fields of temperature distribution, all the components of deformation, stress and displacement in the form of graphs.*

Keywords*— *Coefficient of thermal expansion, High-temperature alloy, steady-state thermophysical process, Thermal conductivity.

I. INTRODUCTION

1.1 State of the problem

Bearing elements of many designs of power objects, such as nuclear, thermal and gas-generating power plants, as well as modern metallurgical plants, mainly work under the influence of complex heterogeneous heat sources. Some load-bearing elements of jet and hydrogen engines, as well as internal combustion engines, work similarly under the influence of local temperatures.

In most cases, the supporting elements have a structural form of a rod of limited length, and are made of heat-resistant materials. This is due to the fact that the strength characteristics of heat-resistant materials are usually higher than those of conventional materials. Simultaneous long-term exposure to rod-bearing elements of dissimilar heat sources leads to the emergence of a stable complex thermophysical state in the system. For example, in the case where the rod-bearing structural member of the structure is clamped at one end and the other end is free, it is prolonged due to the long-term action of dissimilar heat sources. In this case, the amount of elongation depends on the types and quantities of the operating heat sources, the presence of local thermal insulation and heat exchange, as well as the heat transfer coefficient, ambient temperature, rod length, thermal conductivity and thermal expansion of the heat-resistant alloy.

In the case when the rod is pinched at both ends, a steady state will occur only after the temperature distribution, a steady-state displacement distribution field and a compressive force arise, and a steady-state distribution field of the thermoelastic and temperature components of the stress and deformation appears.

To ensure reliable operation of power plants in the above situations, it is necessary to ensure the thermal strength of their load-bearing elements made of heat-resistant materials working for a long time under the influence of dissimilar kinds of heat sources. In this regard, the development of effective methods of accounting for the presence of local surface heat exchanges, temperatures, thermal insulation and internal point heat sources that arise in the structural support element in the case of manifestation of non-linear thermophysical phenomena is an actual problem. Relevance is also due to the fact that in order to obtain results of high accuracy, the process of developing methods must be based on the application of fundamental energy conservation laws for the problems under consideration.

The solution of the above-mentioned topical problems will subsequently put forward new tasks related to the development of an application package in one of the modern programming languages where, the software products and computational algorithms of which should facilitate a series of in-depth studies.

A review of the results of previous studies by various authors showed that the disclosure of questions in the formulation discussed in this paper is insufficient.

For example, one of the studies presents the theory of finite elements for the analysis of the thermoelastic plastic reaction of solids, including the conditions for their contact [1]. In this paper, the constraint function method is used to superimpose the contact condition at the Gauss points of the contact surface. Other procedures widely used in the finite element analysis presented in this paper can be considered as special cases of the constraint function method. The solution technique presented here is promising and requires further research on the accuracy of mathematical modeling.

1.2 Literature review

In the author's paper [2], the main equations of thermoelasticity are given, including the laws of conservation of mass, momentum, and energy. In the results, the kinematic equations are presented, as well as the corresponding relations that close the system of equations. The numerical solution of one of the nonlinear problems of thermophysics is presented in [3]. Here we give a proof of the existence and uniqueness of the solution of the problem under consideration, the corresponding iterative scheme is applied, which makes it possible to apply the results obtained in practice.

Examples of solving the problems associated with the thermal regime of air cooling of stator windings in large turbogenerators, taking into account the possible deterioration and failure of insulation in the hole of both conventional and global YPI stators, which arise in connection with the vibration of the coil are reflected in the studies [4].

Some researchers have carried out theoretical studies on the thermoelasticity of rod elements [5]-[10].

Methods and software systems for simulating stationary thermal stress of load-bearing structural elements working under simultaneous influence of local temperatures, heat fluxes, heat transfer and thermal insulation have been developed [11]. In this work, the total dependence of the coefficient of thermal expansion on temperature is taken into account.

In some results of scientists, a functional formula is used for discretization, which indicates its total thermal energy [12], [13].

On the basis of the research, a computational algorithm and a technique for solving the problem of a given temperature field, deformations and stresses of components along the entire length of the rod were proposed [14], [15]. The work also takes into account the physical and mechanical properties of the test rod. And thermodynamic relationships, nucleation, growth and stress influence are considered and applied to thermoelasticity, pseudoelasticity and memory effects associated with martensitic transformations are presented in [16], [17].

1.3 Problem statement and its solution

Analysis of the state of previously conducted studies and the results obtained in them state the need for further improvement of methods and methods for constructing the dependence of the coefficient of thermal expansion on temperature in high-temperature alloys. Namely, the possibility of calculating the magnitude of the thermal elongation of the rod and the axial force arising in connection with this is not taken into account. Besides, from the results obtained by other methods one can not make an unambiguous conclusion that they really satisfy the fundamental laws of conservation of energy. To date, there has not yet been developed a fundamental mathematical model of steady nonlinear thermophysical processes in a limited length of rods made of heat-resistant alloys under simultaneous influence of local heat exchanges, temperatures, thermal insulation and internal point heat sources. In this regard, there are no corresponding computational algorithms, methods and PYTHON programs that allow simulating the established complex nonlinear processes in rods of limited length made of heat-resistant alloys under simultaneous action of dissimilar kinds of heat sources taking into account the presence of local thermal insulation. As a result, in order to solve this scientific problem, we set the following research tasks:

1) Development of methods for accounting for the presence of local surface heat exchanges in rods of a heat-resistant alloy. Development of PYTHON programs, that allows to study complex thermophysical phenomena in the core;
2) Development of a method for accounting for internal heat sources in rods of a heat-resistant alloy of limited length. Development of appropriate PYTHON programs, that allows to study the steady nonlinear thermophysical state of the investigated rod;

3) Development of methods for the formation of composite functions characterizing the laws of conservation of energy for a limited length of a rod of a heat-resistant alloy those are under simultaneous action of local temperatures, heat exchange, thermal insulation, and internal point heat sources. Development of a software product in the programming language PYTHON, which allows investigating the arising steady nonlinear thermophysical process in the investigated rod.

4) Construction of a physico-mathematical model of the thermophysical state of a limited length of a rod made of a heat-resistant alloy, which is under simultaneous action of local temperatures and thermal insulation. Development of appropriate PYTHON programs, that allows to determine the temperature field arising in the rod, thermoelastic, temperature and elastic components of deformation and stress, and also displacement. Using the software package developed on this basis, determine the value of the thermal elongation of the rod and the compressive axial force.

The above objectives of the research cover the entire research work carried out by us. The coverage of the task in full in this article was necessary to understand the issue. However, in view of the limited size of the paper, in this paper we present only the results of solving only the first problem posed. The results of solving the remaining problems will be covered in other publications of the authors.

This article presents some research results carried out by the authors within the framework of the state budget theme of the research project of the Ministry of Education and Science of the Republic of Kazakhstan, state registration number 0115RK00547, and cipher of International rubric of scientific and technical information 38.65.17.

II. DEVELOPMENT OF THE METHODOLOGY OF SOLVING THE PROBLEM AND ITS DISCUSSION

2.1 Method for constructing the dependence of the coefficient of thermal expansion on temperature in high-temperature alloys

The actual experiments carried out to determine the dependence of the thermal expansion coefficient on the temperature for the sets of high-temperature alloys show that an increase in temperature leads to an increase in the coefficient of thermal expansion (see Fig. 1).

From this it can be seen that the dependence $\alpha = \alpha\big(T(x)\big)$ takes place in the rods of high-temperature alloys (see Fig. 1).

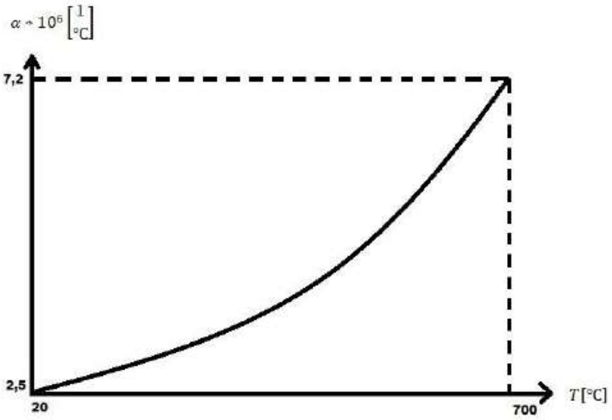

FIGURE 1: DEPENDENCE $\alpha(T)$ FOR A HIGH-TEMPERATURE ALLOY

For example, consider one discrete element from a heat-resistant rod. The length element l [cm] is <<1 . The cross-sectional area of this element will be denoted by S [cm^2]. In this case, it is constant along the length of the element. Through the area of the lateral surface of this element, heat exchange takes place with its surrounding medium. Heat transfer coefficient is denoted by h [W/cm^2°C]. Ambient temperature is T_{amb} [˚C]. The physico-mechanical property of the core material from the heat-resistant alloy is characterized by the dependence of the coefficient of thermal expansion α on the temperature distribution field, $T(x)$ i.e. $\alpha = \alpha\big(T(x)\big)$. Hence, the coefficient of thermal expansion of material α will also depend on the coordinate x.

In addition, the physical and mechanical properties of the rod material are characterized by the coefficient of thermal conductivity of the material of the rod $k_x\left[\frac{W}{cm^2 °C}\right]$ and the elastic modulus $E\left[\frac{kg}{cm^2}\right]$. Taking into account that the length of the considered discrete element is much smaller (0.1 - 1) mm, then the field of temperature distribution and coefficient of thermal expansion along the length of this element is approximated by a complete second-order polynomial. The calculation scheme of the problem under study is shown in Fig. 2.

We introduce the following notation:

$$T(x=0)=T_i; \quad T\left(x=\frac{l}{2}\right)=T_j; \quad T(x=l)=T_k$$

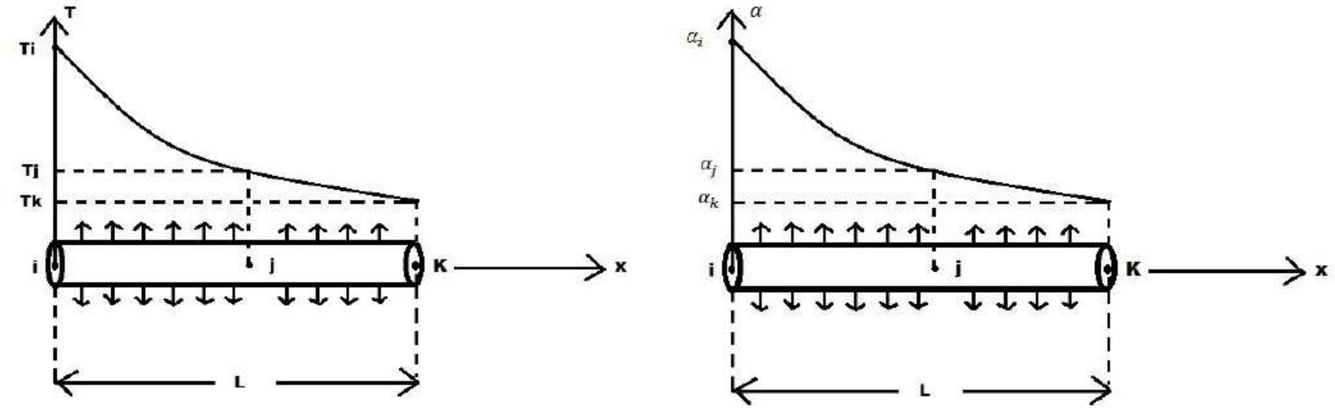

(A) CHANGE IN TEMPERATURE ALONG THE LENGTH OF THE ROD **(B) CHANGE OF THE GENERAL FUNCTION FOR NODAL ELEMENTS**

FIGURE 2: CALCULATION SCHEME OF THE DISCRETE ELEMENT UNDER CONSIDERATION

The temperature field distribution along the length of one discrete element is approximated by a complete polynomial of the second order:

$$T(x)=ax^2+bx+c, 0 \le x \le l; \quad a,b,c=const \tag{1}$$

Here, the values of the constants *a*, *b* and *c* are unknown yet. Such an approximation of the temperature field is based on the fact that the process under consideration is a steady-state thermal conductivity. In this connection, in a small section ($0 \le x \le l <<< L$) of the rod, the law of temperature distribution can be approximated by a curve of the second order. Then from (1) we obtain the following system of linear algebraic equations for determining the values of the constants *a*, *b* and *c*:

$$\begin{gathered} T(x=0)=a\cdot 0+b\cdot 0+c=T_i \\ T\left(x=\frac{l}{2}\right)=a\cdot\left(\frac{l}{2}\right)^2+b\cdot\frac{l}{2}+c=T_j \\ T(x=l)=a\cdot l^2+b\cdot l+c=T_k \end{gathered} \tag{2}$$

Hence from the first equation we have that:

$$c=T_i. \tag{3}$$

Further, from the last two equations we obtain:

$$\begin{gathered} al^2+2bl=4T_j-4T_i \\ al^2+bl=T_k-T_i \end{gathered} \tag{4}$$

By subtracting the second equation from the first, we obtain:

$$bl=4T_j-4T_i-T_k+T_i=4T_j-3T_i-T_k$$

$$b=\frac{4T_j-3T_i-T_k}{l} \tag{5}$$

Substituting (5) into the second equation of system (4), we get:

$$al^2+\frac{4T_j-3T_i-T_k}{l}l=T_k-T_i$$

$$al^2 = T_k - T_i - 4T_j + 3T_i + T_k = 2T_k + 2T_i - 4T_j$$

$$a = \frac{2T_k+2T_i-4T_j}{l^2} \tag{6}$$

Now, substituting the values of a, b and c in equation (1) we obtain:

$$T(x) = \left(\frac{2T_k+2T_i-4T_j}{l^2}\right)x^2 + \frac{4T_j-3T_i-T_k}{l}x + T_i,\ 0 \le x \le l$$

We rewrite the last expression in the following form:

$$T(x) = (\dots)T_i + (\dots)T_j + (\dots)T_k$$

i.e.

$$T(x) = \left(\frac{2x^2}{l^2} - \frac{3x}{l} + 1\right)T_i + \left(\frac{4x}{l} - \frac{4x^2}{l^2}\right)T_j + \left(\frac{2x^2}{l^2} - \frac{x}{l}\right)T_k$$

or

$$T(x) = \left(\frac{2x^2-3lx+l^2}{l^2}\right)T_i + \left(\frac{4lx-4x^2}{l^2}\right)T_j + \left(\frac{2x^2-lx}{l^2}\right)T_k, \qquad 0 \le x \le l \tag{7}$$

We introduce the following notation:

$$\varphi_i(x) = \frac{2x^2-3lx+l^2}{l^2};\ \varphi_j(x) = \frac{4lx-4x^2}{l^2};\ \varphi_k(x) = \frac{2x^2-lx}{l^2},\ \ 0 \le x \le l \tag{8}$$

These functions are called form functions for three nodes of a quadratic discrete element in the local coordinate system0 ≤ x ≤ l . These functions have the following properties:

$$\varphi_i(x) = \begin{cases} when\ x = 0, & \varphi_i(0) = 1; \\ when\ x = \frac{l}{2}, & \varphi_i\left(\frac{l}{2}\right) = 0; \\ when\ x = l, & \varphi_i(0) = 0; \end{cases}$$

$$\varphi_j(x) = \begin{cases} when\ x = 0, & \varphi_j(0) = 0; \\ when\ x = \frac{l}{2}, & \varphi_j\left(\frac{l}{2}\right) = 1; \\ when\ x = l, & \varphi_j(0) = 0; \end{cases}, \tag{9}$$

$$\varphi_k(x) = \begin{cases} when\ x = 0, & \varphi_k(0) = 0; \\ when\ x = \frac{l}{2}, & \varphi_k\left(\frac{l}{2}\right) = 0; \\ when\ x = l, & \varphi_k(0) = 1 \end{cases}$$

Also these functions have the following properties:

$$\varphi_i(x) + \varphi_j(x) + \varphi_k(x) = \frac{2x^2-3lx+l^2+4lx-4x^2+2x^2-lx}{l^2} = 1 \tag{10}$$

These properties of the form function make it possible to provide continuity conditions for the desired function in the transition from one discrete element to another.

From (7) it is also possible to determine the temperature gradient in the local coordinate system

$$\frac{\partial T}{\partial x} = \frac{\partial \varphi_i}{\partial x}T_i + \frac{\partial \varphi_j}{\partial x}T_j + \frac{\partial \varphi_k}{\partial x}T_k = \left(\frac{4x-3l}{l^2}\right)T_i + \left(\frac{4l-8x}{l^2}\right)T_j + \left(\frac{2x-l}{l^2}\right)T_k, 0 \le x \le l \tag{11}$$

Similarly to (7) within the length of one discrete element, the distribution field of the thermal distribution coefficient is also approximated by a curve of the second order:

$$\alpha\big(T(x)\big) = \varphi_i(x)\cdot\alpha_i + \varphi_j(x)\cdot\alpha_j + \varphi_k(x)\cdot\alpha_k\ ,\ 0 \le x \le l \tag{12}$$

Here $\alpha_i(T_i)$, $\alpha_j(T_j)$ и $\alpha_k(T_k)$are determined from the directory. Dependence $\alpha = \alpha(T)$ is determined for each heat resistant material separately.

2.2 The method of accounting for the presence of local surface heat exchanges in rods of high-temperature alloys

Consider one discrete element of the rod through the lateral surface of which there is a heat exchange with its surrounding medium (see Fig. 3).

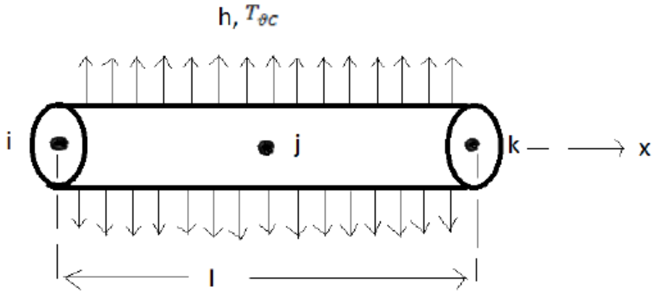

FIGURE 3: CALCULATION SCHEME FOR THE PROBLEM OF LOCAL SURFACE HEAT EXCHANGE

Heat transfer coefficient $h\,[\frac{W}{cm^2\cdot°C}]$, ambient temperature T_{amb} [°C]. For the problem under consideration, we write the expression for the functional that characterizes the law of conservation of energy:

$$J = \int_V \frac{k_{xx}}{2}\left(\frac{\partial T}{\partial x}\right)^2 dV + \int \frac{h}{2}(T - T_{oc})^2 dS, \qquad 0 \le x \le l \tag{13}$$

Where V is the volume of the discrete element: S_{ls} – is the area of the lateral surface of the discrete element under consideration.

The unit of measurement of the first member will be:

$$\frac{W}{cm\cdot°C}\cdot\frac{°C^3}{cm^2\cdot°C}\cdot cm^3 = W\cdot°C$$

The unit of measurement of the second term will also be:

$$\frac{W}{cm^2\cdot°C}\cdot°C^2\cdot cm^2 = W\cdot°C$$

We now integrate the first term in (13):

$$J_1 = \int_V \frac{k_{xx}}{2}\left(\frac{\partial T}{\partial x}\right)^2 dV = F\int_0^l \frac{k_{xx}}{2}\left(\frac{\partial T}{\partial x}\right)^2 dV = \frac{F\cdot k_x}{2}\int_0^l \frac{k_{xx}}{2}\left(\frac{\partial T}{\partial x}\right)^2 dV;$$

Here, F [cm^2] is the cross-sectional area of the rod. It is constant along the entire length of the rod. In addition, the cross-section of the rod can be a circle, an ellipse, and any polygon. Further substituting the formula (1) in the last expression of J_1, we obtain:

$$J_1 = \frac{Fk_x}{2}\int_0^l \left[\left(\frac{4x-3l}{l^2}\right)T_i + \left(\frac{4l-8x}{l^2}\right)T_j + \left(\frac{4x-l}{l^2}\right)T_k\right]^2 dx = \frac{Fk_{xx}}{2l^4}\int_0^l [(16x^2 - 24lx + 9l^2)T_i^2 + 2(40lx - 32x^2 - 12l^2)T_iT_j +$$

$$+2(16x^2 - 16lx + 3l^2)T_iT_k + (16l^2 - 64lx + 64x^2)T_j^2 + 2(24lx - 4l^2 - 32x^2)T_jT_k + (16x^2 - 8lx + l^2)T_k^2\,]dx =$$

$$= \frac{Fk_{xx}}{2l^4}\int_0^l \left[\left(\frac{16x^3}{3} - 12lx^2 + 9l^2x\right)T_i^2 + 2\left(40lx^2 - \frac{64x^3}{3} - 24l^2x\right)T_iT_j + \left(\frac{32x^3}{3} - 16lx^2 + 6l^2x\right)T_iT_k +\right.$$

$$\left. + \left(16l^2 - 32lx + \frac{64x^3}{3}\right)T_j^2 + \left(24lx^2 - 81l^2x - \frac{64x^3}{3}\right)T_jT_k + \left(\frac{16x^3}{3} - 4lx^2 + l^2x\right)T_k^2\right]dx =$$

$$= \frac{Fk_{xx}l^3}{2l^4}\left[\frac{7}{3}T_i^2 - \frac{16}{3}T_iT_j + \frac{2}{3}T_iT_k + \frac{16}{3}T_j^2 - \frac{16}{3}T_jT_k + \frac{7}{3}T_k^2\right] = \frac{Fk_{xx}}{6l}(7T_i^2 - 16T_iT_j + 2T_iT_k + 16T_j^2 - 16T_iT_k + 7T_k^2) \tag{14}$$

Here it should be noted that the sum of the coefficients before the node temperatures will always be zero. For example, in our case (7-16 + 2 + 16-16 + 7) = 0. This is a sign of the fulfillment of the law of conservation of energy.

We now integrate the second term in (13):

$$J_2 = \int_{S_{ls}} \frac{h}{2}(T - T_{amb})^2\, ds = P\int_0^l \frac{h}{2}(T - T_{amb})^2 dx.$$

Here P is the perimeter of the cross-section of the rod. Substituting (7) in the expression J_2, we obtain:

$$J_2 = \frac{Ph}{2}\int_0^l [(\frac{2x^2 - 3lx + l^2}{l^2})\,T_i + \left(\frac{4lx - 4x^2}{l^2}\right)T_j + \left(\frac{2x^2 - lx}{l^2}\right)T_k - T_{amb}\,]^2 dx =$$

$$= \frac{Ph}{2}\int_0^l [\left(\frac{4x^4-12lx^3+13l^2x^2-6l^3+l^4}{l^4}\right)T_i^2 + [\left(\frac{40lx^3-16x^4-32l^2x^2-8l^3x}{l^4}\right)T_iT_j + + \left(\frac{8x^4-40lx^3+10l^2x^2-2l^3x}{l^4}\right)T_iT_k +$$

$$+ \left(\frac{16l^2x^2-32lx^3+16x^4}{l^4}\right)T_j^2 + \left(\frac{24lx^3-8l^2x^2-16x^4}{l^4}\right)T_iT_k + \left(\frac{16x^4-32lx^3+l^2x^2}{l^4}\right)T_k^2 -$$

$$-\left(\frac{4x^2 - 6lx + 2l^2}{l^4}\right)T_{amb}\,T_i - \left(\frac{8lx - 8x^2}{l^4}\right)T_{amb}\,T_j - \left(\frac{4x^2 - 2lx}{l^4}\right)T_{amb}\,T_k + T_{amb}^2\,]dx =$$

$$= \frac{Phl}{30}(2T_j^2 + 2T_iT_j - T_iT_k + 8T_j^2 + 2T_k^2 + 2T_jT_k - 5T_{amb}\,T_i - 20T_{amb}\,T_j - 5T_{amb}\,T_k + 15T_{amb}^2\,) \tag{15}$$

It is also seen here that the sum of the coefficients before the temperatures will be zero. In our case (2 + 2-1 + 8 + 2 + 2-5-20-5 + 15) = 0. This is a sign of the fulfillment of the law of conservation of energy. Then substituting (14) and (15) into (13) we obtain an integrated form of the functions J - which characterizes the law of conservation of energy for the discrete element under investigation, through whose lateral surface heat exchange takes place with its surrounding medium:

$$J = J_1 + J_2 = \frac{Fk_{xx}}{6l}\left(7T_i^2 - 16T_iT_j + 2T_iT_k + 16T_j^2 - 16T_iT_k + 7T_k^2\right) + \frac{Phl}{30}(2T_j^2 + 2T_iT_j - T_iT_k +$$

$$+ 8T_j^2 + 2T_k^2 + 2T_jT_k - 5T_{amb}\,T_i - 20T_{amb}\,T_j - 5T_{amb}\,T_k + 15T_{amb}^2\,) \tag{16}$$

Further minimizing J from the desired T_i, T_j and T_k we obtain a resolving system of linear algebraic equations taking into account the presence of local lateral heat exchange:

$$\frac{\partial J}{\partial T_i} = 0; => \frac{Fk_{xx}}{6l}\left(14T_i - 16T_j + 2T_k\right) + \frac{Phl}{30}\left(4T_i + 2T_j - T_k - 5T_{amb}\,\right) = 0$$

$$\frac{\partial J}{\partial T_j} = 0; => \frac{Fk_{xx}}{6l}\left(-16T_i - 16T_k + 32T_j\right) + \frac{Phl}{30}\left(2T_i + 16T_j + 2T_k - 20T_{amb}\,\right) = 0$$

$$\frac{\partial J}{\partial k} = 0; => \frac{Fk_{xx}}{6l}\left(2T_i - 16T_j + 14T_k\right) + \frac{Phl}{30}\left(-T_i + 2T_j + 4T_k - 5T_{amb}\,\right) = 0$$

Here it was meant that the cross-sectional areas of the two ends of the discrete element of the rod are thermally insulated. Solving the last system, we find the nodal temperatures:

$$T_k = \frac{[2b_1(a_{11}a_{22}-a_{12}a_{21})-b_1(3a_{11}-2a_{21})a_{12}]}{2[(a_{11}+a_{13})(a_{11}a_{22}-a_{12}a_{21})-a_{12}a_{21}(a_{11}-a_{13})]};$$

$$T_j = \frac{(a_{13}a_{21}-a_{11}a_{21})}{(a_{11}a_{22}-a_{12}a_{21})}T_k + \frac{b_1(3a_{11}-2a_{21})}{2(a_{11}a_{22}-a_{12}a_{21})}; \tag{17}$$

$$T_i = -4T_j + 15T_k - 400;$$

$$a_{11} = \left(7 + \frac{4hl^2}{5k_x}\right);\ a_{12} = \left(\frac{2hl^2}{5k_x} - 8\right);\ a_{13} = \left(1 - \frac{hl^2}{5k_x}\right);\ a_{11} = \left(7 + \frac{4hl^2}{5k_x}\right);$$

$$b_1 = \frac{hl^2T_{oc}}{k_x};\ a_{21} = \left(1 + \frac{3hl^2}{20k_x}\right); a_{22} = \left(2 + \frac{6hl^2}{5k_x}\right);$$

$$T(x) = \varphi_i(x)T_i + \varphi_j(x)T_j + \varphi_k(x)T_k = \frac{2x^2-3lx+l^2}{l^2}T_i + \frac{4lx-2x^2}{l^2}T_j + \frac{2x^2-lx}{l^2}T_k \tag{18}$$

If we take $r = 1$ cm for the initial data; $F = \pi r^2 = \pi\ \text{cm}^2; P = 2\pi r = 2\pi$ cm; $k_{xx} = 100\left[\frac{W}{cm\,°\text{C}}\right]; l = 10$ cm; $h = 10\left[\frac{W}{cm^2\,°\text{C}}\right]$, it follows from (17) we find that:

$$T_i = T_k = 37{,}037°\text{C};\ T_j = 29.62963°\text{C}$$

Then the law of temperature distribution along the length of the investigated rod will be as follows:

$$T(x) = \varphi_i(x)T_i + \varphi_j(x)T_j + \varphi_k(x)T_k =$$

$$= \frac{1}{12}\left[(2x^2 - 3xl + l^2)T_i + (4xl - 4x)T_j + (2x^2 - xl)T_k\right] =$$

$$= \frac{1}{100}[(2x^2 - 30x + 100) \cdot 37.037 + (40x - 4x^2) \cdot 29.62963 + (2x^2 - 10x) \cdot 37.037] =$$

$$= \frac{1}{100}[(148.148 - 118.51852)x^2 + (1185.1852 - 1111.11 - 370.37)x + 3703.7] =$$

$$= \frac{1}{100}[29.62948x^2 + 296.2948x + 3703.7] = 0.2962948x^2 - 2.962948x + 37.037; \quad 0 \le x \le l$$

Here, because of the symmetry of the problem under study $T_i = T_k$. Further substituting (17) into (7) we find the law of temperature distribution. If the left end of the test element is rigid, that it lengthens. According to the fundamental laws of thermophysics, the magnitude of the elongation of the rod element is determined by the formula $\Delta l_T = \int_0^l \alpha T(x)dx$. Here it must be taken into account that the values of the coefficient of warm expansion of the material of rod α for different heat-resistant materials will be different. They are determined experimentally for different temperatures and materials. If we take α = const, then we get that:

$$\Delta l_T = \alpha \int_0^l [\varphi_i(x)T_i + \varphi_j(x)T_j + \varphi_k(x)T_k]dx = \alpha \int_0^l \left[\frac{2x^2-3lx+l^2}{l^2}T_i + \frac{4lx-4x^2}{l^2}T_j + \frac{2x^2-lx}{l^2}T_j\right]dx =$$

$$= \frac{\alpha}{l^2}\left[\left(\frac{2x^3}{3} - \frac{3lx^2}{2} + l^2x\right)T_i + \left(2l^2x - \frac{4x^3}{3}\right)T_j + \left(\frac{2x^3}{3} - \frac{lx^2}{2}\right)T_k\right]\Bigg|_0^l = \alpha l\left[\left(\frac{4-9+6}{6}\right)T_i + \left(\frac{6-4}{3}\right)T_j + \left(\frac{4-3}{6}\right)T_k\right] =$$

$$= \alpha l\left[\frac{1}{6}T_i + \frac{4}{6}T_j + \frac{1}{6}T_k\right] = \frac{\alpha l}{6}\left(T_i + 4T_j + T_k\right) \tag{19}$$

If both ends of the rod are rigidly clamped, an axial compressive force occurs in the rod (see Fig. 4):

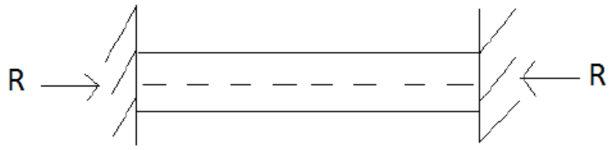

FIGURE 4: EFFECT OF COMPRESSIVE FORCES

The value of this force is determined from the compatibility condition of the deformation:

$$\frac{Rl}{EF} + \Delta l_T = 0 => R = -\frac{\Delta l_T EF}{l} = -\frac{EFl}{6} \tag{20}$$

In this case, a thermoelastic stress component arises in the cross sections of the rod. It is determined in accordance with Hooke's law:

$$\sigma = E\varepsilon => \varepsilon = \frac{\sigma}{E} = -\frac{\alpha}{6}(T_i + 4j + T_k), \; 0 \le x \le l \tag{21}$$

It should be noted that in the rods of heat-resistant materials, in the case of pinching the two ends and conventional heat transfer through the side surface, the temperature and elastic components of the strain and stress also appear. For example, the field of distribution of the temperature component of the deformation is determined in accordance with the fundamental laws of thermal physics:

$$E_T(x) = -\alpha T(x) = -\frac{\alpha}{l^2}\left[(2x^2 - 3lx + l^2)T_i + (4lx - 4x^2)T_j + (2x^2 - lx)T_k\right], \quad 0 \le x \le l \tag{22}$$

Then, in accordance with the generalized Hooke's law, the distribution of the temperature component voltage is determined by the formula:

$$\sigma_T(x) = E\varepsilon_T(x) = -\frac{\alpha}{l^2}\left[(2x^2 - 3lx + l^2)T_i + (4lx - 4x^2)T_j + (2x^2 - lx)T_k\right], \quad 0 \le x \le l \tag{23}$$

In addition to these components, the field of distribution of the elastic deformation component also takes place in the investigated rod. It is determined from the following relation:

$$\varepsilon = E_x(x) + \varepsilon_T(x) \Rightarrow \varepsilon_x(x) = \varepsilon - \varepsilon_T(x) = -\frac{\alpha}{6}(T_i + 4j + T_k) +$$

$$+\frac{\alpha}{l^2}\left[(2x^2 - 3lx + l^2)T_i + (4lx - 4x^2)T_j + (2x^2 - lx)T_k\right],\ 0 \le x \le l \qquad (24)$$

The corresponding field of distribution of the elastic component of the voltage is determined in accordance with the generalized Hooke's law:

$$\sigma_x(x) = \sigma - \sigma_T(x) = E\varepsilon_x(x) = -\frac{\alpha E}{6}(T_i + 4j + T_k) +$$

$$+\frac{\alpha E}{l^2}\left[(2x^2 - 3lx + l^2)T_i + (4lx - 4x^2)T_j + (2x^2 - lx)T_k\right],\ 0 \le x \le l \qquad (25)$$

Finally, we can determine the law of distribution of displacement along the length of the rod. It is determined from the general Cauchy relations:

$$\varepsilon_x(x) = \frac{\partial U}{\partial x}; \Rightarrow U(x) = \int \varepsilon_x(x)dx = -\frac{\alpha}{6}(T_i + 4j + T_k)x +$$

$$+\frac{\alpha}{l^2}\left[\left(\frac{2x^3}{3} - \frac{3lx^2}{2} + l^2x\right)T_i + \left(2lx^2 - \frac{4x^3}{3}\right)T_j + \left(\frac{2x^3}{3} - \frac{lx^2}{2}\right)T_k\right] + C \qquad (26)$$

Here C is the integration constant. Its values are determined from the boundary condition at x = 0. Since this end of the investigated rod is rigidly constrained, then for x = 0, U (x = 0) = 0. From this physical condition we get that C = 0. Then the law of distribution of displacement along the length of the rod will have the following form:

$$U(x) = -\frac{\alpha}{6}(T_i + 4j + T_k)x + \frac{\alpha}{6l^2}\left[(6l^2x)T_i + (12lx^2 - 8x^3)T_j + (4x^3 - 3lx^2)T_k\right],\ 0 \le x \le l \qquad (27)$$

III. CONCLUSION

The developed technique for taking into account the simultaneous presence in the rod of the heat-resistant alloy of local surface heat exchanges allowed:

1) To obtain a resolving system of linear algebraic equations taking into account natural boundary conditions for a limited length of a rod made of a heat resistant alloy under the influence of local surface heat exchange;

2) To obtain, within the framework of the task at hand, the laws for the distribution of temperature, elastic, temperature, and thermoelastic components of deformations and stresses, and also for displacement;

3) Within the framework of the task set, to create a program in PYTHON programming language, with the help of which the corresponding fields of temperature distribution, all the components of deformation, stress and displacement in the form of graphs are constructed.

REFERENCES

[1] J. Deang, Q. Du, and M. Gunzburger, "Modeling and computation of random thermal f1uctuations and material defects in the Ginzburg-Landau model for superconductivity", *J. Computational Physics*, vol. 181, pp. 45-67, 2002

[2] B. A. Biswajit, "Material Point Method Formulation for Plasticity", *J. Computational Physics*, vol. 51, pp. 1-25, 2006.

[3] D. Pantusoa, Klaus-Juergen Bathe, P. A. Bouzinov, "A finite element procedure for the analysis of thermo-mechanical solids in contact", *Computers and Structures 75*, vol. 2. pp. 551-573, 2000.

[4] B. Z. Kenzhegul, A. K. Kudaykulov, and A. N. Myrzasheva, "Numerical study of stem elongation of heat-resistant alloy based oп the availability of all types of sources", *J. Science and new technologies*, vol. 3. pp. 67-75, 2009.

[5] M. D. Greenberg, J. Pryor, and W. ElЬan, "On the Formu1ation of the Zero Creep Method for Small Diameter Wires", *Materials Science and Engineering*, vol. 33. pp. 63-67, 1978.

[6] M. E. Gurtin, "An Introduction to Continuum Mechanics", *New York: Academic Press*, 830 p., 1981.

[7] O. A. Maugin, "The Thermomechanics of Nonlinear Irreversible Behaviors: An Introduction", *Singapore: World Scientific*, 375 p, 1999.

[8] T. Belytschko, У. Guo, W. Liu, and S. Xiao, "A unified stability analysis of meshless particle methods", *Int. J. Numerical Methods in Engineering*, no. 48 (9), pp. 1359-1400, 2000.

[9] T. W. Wright, "The Physics and Mathematics of Adiabatic Shear Bands", *Cambridge: Cambridge University Press, UK*, 240 p., 2002.

[10] R. C. Batra, "Elements of Continuum Mechanics", *American Institute of Aeronautics and Astronautics*, 325 p., 2006.

[11] Zh. M. Tashenova, E. N. Nurlybaev, and A. K. Kudaiykulov, "Method of Solution and Computational Algorithm for Mixed Thermo-Mechanics Problem", *World Applied Sciences J., (Spec. Issue on Techniq. and Technol.,* vol. 22, pp. 49-57, 2013.

[12] K. H. Huebner, "The Finite Element Method for Engineers", *Wi1ey*, pp. 183- 187, 1975.

[13] Lishirong Yangjingning, "Accurate model of post bucking of elastic rod with Mirabel cross sections", *Gansu University of Science*, vol. 1, pp. 98-102, 1999.

[14] Zh. M. Tashenova, E. Nurlybaeva, and A. K. Kudaykulov, "Method Preparation and Solution Algorithm for Resolving Stationary Problem of a Rod under Thermo-Stressed Condition Restrained at both Ends Affected by Heat Exchange and Heat Flows", *World Applied Sciences J., (Spec. Issue on Techniq. and Technol.)*, vol. 22, pp. 49-57, 2013.

[15] Wu Jie, Wei Dong Yang, and Yu. ZhiHao, "An Examination of Blade Load Ca1culations Based оп Rigid-Flexible Coupling Model" *J. Applied Mechanics and Materials*, vol. 18, pp. 741- 745, 2013.

[16] L. Delaey, R. V. Krishnam, and H. Tas, Warlimont, "Thermoelasticity, pseudoelasticity and the memory effects associated with martensitic transformations", *J. of Materials Science*, no. 9, pp. 1359 -1363, 1974.

[17] R. J. Wasilewski, "The effect of applied stress оп the martensitic transformations in TiNi", *J. Met. Trans, v*ol. 2, no. 11, pp. 2973-2981, 1975.

AUTHOR DETAILS

Dr. Sairanbek Akhmetov is a Professor of the L.N. Gumilyov Eurasian National University, who made researches in mechanisms and machinery dynamics; moreover, he is the editor-in-chief and chairman of the editorial board of several Russian and Kazakh scientific journals, an acting member of the National Academy of the Republic of Kazakhstan and of the Russian Academy of Natural Sciences. He published more than 200 scientific papers, prepared 18 PhD in technical direction.

Dr. Anarbay Kudaykulov is a Professor of Al-Farabi Kazakh National University, who is actively involved in reading special courses in mechanics, fluid and gas in the leading universities of Russia and China, whose scientific interests include dynamic and thermal processes in liquid medium and in structural elements of machines and mechanisms. He is the author of more than 300 published papers.

Characteristics of Settlement Consolidation and Influencing Factors Analysis of Dredger Fill of Clay Soil Mixing Sand

Jihui-Ding[1], Qi-Zhao[2], Yafeng-Zhao[3], Mengjia-Xiang[4], Mingjiang-Wu[5]

[1,2,4]College of Civil Engineering Hebei University, Baoding , Hebei, China 071002
[3,5]CCCC Road & Bridge Special Engineering Co Ltd, Wuhan, Hubei, China 430071

Abstract**—** *Sedimentation column that the size of100×500mm is used to study the relationship between the self weight settlement of cohesive soil and the initial sand-mud ratio and initial water content of dredger fill of clay soil mixing sand. Test results show that:(1) the consolidation time of dredger fill of clay soil mixing sand is mainly related to the size of the settlement column, compared with the initial water content, the influence of sand-mud ratio is not significant. The larger the size of the settlement column, the longer time of gravity consolidation will be completed, and the higher initial water content, the shorter time of consolidation. (2) The settlement curve of dredger fill of clay soil mixing sand is in accordance with the relation formula* $S = A_1 e^{-\frac{t}{t_1}} + A_2 e^{-\frac{t}{t_2}} + S_0$*.In the formula,* S_0 *is the steady settlement. The stability time of settlement consolidation can be deduced by this formula. Under the condition of the same water content, the consolidation settlement of dredger fill of clay soil mixing sand increases linearly with the sand-mud ratio, but the amplitude of the increase is not large; (3) the logarithmic curve of consolidation settlement is basically divided into three stages: The straight line segment, the upper concave line segment and the lower concave line segment. At first, the slope of the linear section increases gradually with the increase of the initial water content; The upper concave curve gradually decreases with the increase of water content, and when the initial water content reaches a certain value, the concave curve becomes a straight line; The lower concave curve section gradually changes to the curve type, then the slope of the settlement curve decreases and finally tends to the horizontal.*

Keywords**—** ***clay soil mixing sand; self weight consolidation settlement; initial water content; initial sand-mud ratio.***

I. INTRODUCTION

When the filling material flows out from the blowpipe, the filling material has the characteristics of sorting and partitioning. As the distance from the distance to the fill increases, the deposited soil particles gradually become coarser. Generally, dredger fill is characterized by obvious heterogeneity, high natural water content, poor water permeability, difficult drainage consolidation, high compressibility, low shear strength, thixotropy and rheological properties. The settlement consolidation characteristics of dredger fill are related to the design of yard volume, the selection of foundation treatment method and the effect of foundation treatment. Most of the existing scholars at home and abroad are pure silt soil, the simulation is the initial stage of dredging, the water content is very high, and the study of the self weight consolidation law of sand and clay soil mixing system is not very common. Stokes[1] formula is the most classical particle settling velocity formula at present. In the aspect of settling velocity of mud water interface, IMAI[2-3] considered that there are 3 stages of consolidation of cohesive sediment suspended sediment with high water content, namely, flocculation stage, settlement stage and consolidation stage. Liangtong Zhan[4] used the 50cm high sediment column (high 50cm, inner diameter 9cm)to study muddy water mixtures. Test results show that the higher the content of fine particles (especially clay) in dredger fill, the longer the process of self weight deposition, the ratio of pore to sediment is larger, and the pore ratio of silty soil after consolidation is 1~2, while silty clay is between 2~6. Xianwei Zhang[5] took the dredger fill mud in Tianjin Binhai New Area as the object of study, and studies the rule of mud self weight settlement and consolidation of initial water content 200~2000%.The sedimentation types of dredger fill mud in Tianjin are mainly sedimentary subsidence and consolidation subsidence. The sedimentation process is divided into flocculation stage, hindered settlement stage and self consolidation stage. In the process of settlement, the consolidation settlement gradually changes with the decrease of water content. When the initial moisture content is less than 400%, consolidation settlement occurs, and sedimentation occurs when the initial water content is greater than 400%.

Guizhong Xu [6]used a diameter of 6.5cm 1000ml cylinder to test, the soil moisture content of Baima Lake is 397~1991%, and the water content of soil sample in Wenzhou is 325%~1921%. The soil moisture content of the soil samples in the gateway and the soil samples in is 255%~2120%, and the water content of the soil samples in Zhangjiagang is 64.1~455.5%. The moisture content of soil formation (When the mud enters the consolidation state, the water content is the moisture content of soil formation) is related to the liquid limit of soil sample, the clay soil is about 9 times of the liquid limit, and the silty soil is about 3 times of the liquid limit. Nan Zhang [7] uses a settlement column with a height of 0.8m and an inner diameter of 0.1m. The silt is dredged from the Yixing iron ore yard in Jiangsu, and the initial water content is 1103%. During the settlement of dredger fill mud, the settlement rate of particles will appear mud water interface, floc settlement and floc compression settlement interface and self weight consolidation interface. Ming Zhang[8] is based on the boundary void ratio as the dividing line between the deposition and the consolidation of gravity in the process of silt deposition, and considering the deformation after gravity deposition. Shaolin Le, Wei Bai, Mingjiang Wu researched the dredger fill. Large scale settlement column test for mixed sand and dredger fill is carried out, The test results show that the sediment and sediment distribution and the distribution of particles are closely related to the initial sand content and initial water content. The settlement time curve can be divided into 3 stages: rapid subsidence, slow subsidence, and slow settlement consolidation. The second stage shows obvious nonlinear characteristics. With the decrease of initial water content, the 3 stages of sedimentation time curve and nonlinear characteristics are not obvious.

In this paper, mixed soil of clay soil and sand are taken as the object, and the settlement consolidation law of dredger fill of clay soil mixing sand is studied by the settlement column test.

II. TEST METHOD

The clay mixed sand samples used in the test are configured. Clay soil is taken from the site near Baoding, East Lake. The plastic limit is 22.6%, the liquid limit is 41.7%, the water content is 45.2%, and the density is 1.822g/cm^3.

The gradation of sand using in the test: Particle size d>0.5mm, particle content 2%, 0.25mm~0.5mm accounted for 84.1%, particle size 0.075mm~0.25mm accounted for 12.01%, particle size <0.075mm accounted for 1.9%. According to current regulations[10] belongs to medium sand.

The water contents were 80%, 100% and 200% respectively. Clay sand mixed soil with sand-mud ratios of 0,5%, 10%,15%,20% and 25%, respectively, as in the settlement column. The settlement column size is 100 × 500mm. The consolidated height of liquid between clayey soil and sand fill is between 400~430mm, and the self weight consolidation test is carried out.

III. ANALYSIS OF TEST RESULTS

3.1 Settlement curve

Fig. 1 shows the variation of the settlement with time when the sand content ratio is between 0~25% and when the water content is 80%, 100% and 200% respectively. Fig. 2 is the test result of the reference [9]. When the water content is 100%, 200% and 300%, the sand content ratio varies with time at 10%, 20% and 30% respectively. From Fig.1 and Fig. 2, the main factor affecting the settlement of clay soil and sand mixed dredger fill is the initial water content. With the increase of initial water content, mud sinking faster, sedimentation value increased, the consolidation time decreased. The completion time of consolidation decreases obviously with the increase of initial moisture content. The consolidation stability time is obviously lower than the stability time of the reference [9], the main reason is that the settlement column size of the literature [9] is 2 times of the test, the diameter is 200mm, the height is 1300mm.

The results show that when the initial water content is 200%,100%, 80% and the sand content ratio is between 0~25%, the settlement values are 18.66~26.11%, 26.67~33.60% and 50.9~55.35% respectively. The results in the reference [9], when the moisture content is 100%, the sand-mud ratio is 20% and 30%, stable subsidence values were 29.09% and 30.50% respectively; when the initial water content is 200%, the sand-mud ratio is 10%, 20% and 30%, stable subsidence values were 43.65%, 57.12% and 53.47%. There is little difference between the results and this test.

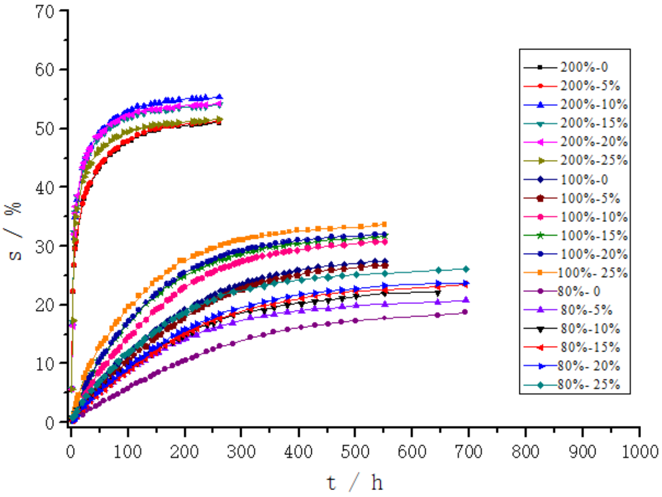

FIG. 1 s-t CURVE OF DIFFERENT WATER CONTENT AND DIFFERENT SAND-MUD RATIO

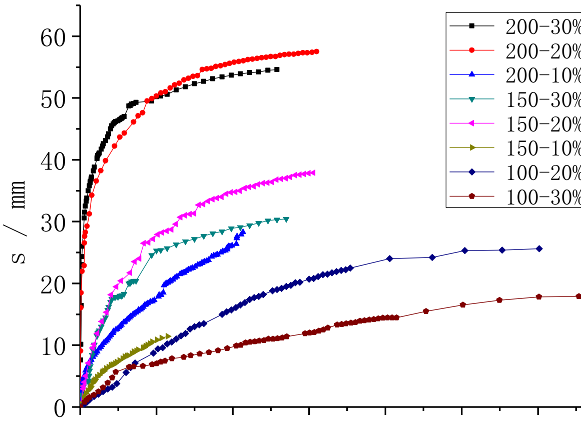

FIG. 2s-t CURVE OF DIFFERENT WATER CONTENT AND DIFFERENT SAND-MUD RATIO(REFERENCE [9])

The s-t curve of dredger fill of clay soil mixing sand is fitted according to the following functions:

$$S = A_1 e^{-\frac{t}{t_1}} + A_2 e^{-\frac{t}{t_2}} + S_0 \tag{1}$$

In the formula, S is the settlement, and A_1, A_2, S_0, t_1, t_2 is the fitting parameter.

The relation in the upper form is $S_{t\to\infty} = S_0$, so S_0 is the stable value when the settlement consolidation is completed.

Table 1~ Table 3 provides the corresponding fitting parameters for different water content and different sand-mud ratio. From table 1~table 3, the fitted function of the time dependent relationship between the sedimentation and the time is nonlinear exponential polynomial, and the correlation coefficients are greater than 0.995. Therefore, the correlation is good

TABLE 1
FITTING PARAMETERS WITH WATER CONTENT OF 80%

Sand-mud ratio	A_1	t_1	A_2	t_2	S_0	Correlation Coefficient
0	-10.5887	280.0482	-10.5887	280.0464	20.87022	0.99795
5	-10.6600	187.1941	-10.6600	187.1939	21.42909	0.99894
10	-11.5269	203.2542	-11.5269	203.2550	23.45973	0.99854
15	-12.5249	214.3406	-12.5249	214.3402	24.77805	0.99891
20	-12.5452	198.5618	-12.5452	198.5620	24.88548	0.99900
25	-13.1941	169.3581	-13.1941	169.3583	26.67707	0.99915

TABLE 2
FITTING PARAMETERS WITH WATER CONTENT OF 100%

Sand-mud ratio	A_1	t_1	A_2	t_2	S_0	Correlation Coefficient
0	-14.99742	193.0823	-14.9974	193.0825	30.09272	0.99947
5	-15.3231	215.4505	-15.3231	215.4523	30.44765	0.99867
10	-16.9343	162.7865	-16.9343	162.787	33.89887	0.99933
15	-31.4496	140.3179	-2.00026	10.17136	32.77557	0.99971
20	-16.5151	133.7142	-16.5151	133.7142	33.23667	0.99957
25	-30.7086	129.2871	-3.20926	12.05774	33.28825	0.99959

TABLE 3
FITTING PARAMETERS WITH WATER CONTENT OF 200%

Sand-mud ratio	A_1	t_1	A_2	t_2	S_0	Correlation Coefficient
0	-40.13903	2.12109	-21.8216	45.16486	49.88555	0.99737
5	-39.98749	2.11719	-21.7335	45.13955	49.6558	0.99738
10	-15.89544	49.98365	-44.1232	3.62553	52.21738	0.99519
15	-47.19616	3.43505	-14.8783	48.20942	53.07849	0.99867
20	-15.08462	46.23893	-46.5062	3.49794	53.16765	0.99933
25	-45.05877	3.22394	-15.5957	45.59238	52.47949	0.99971

In the s-t curve, when the settlement curve tends to horizontal, the excess pore water pressure in the slurry is dissipated, and the mud self weight consolidation is completed, indicating the end of the natural settlement. The time required for the end of a natural settlement is called settling time and is expressed by T_c. T_c is an important reference index for design of yard capacity in blowing and filling project. T_c is closely related to initial water content. The settlement consolidation time is defined as settlement consolidation time of 95%, which is used as settling stability time. With the formula (1) , it is easy to determine the time at which the settlement consolidation is completed 95% (as shown in Fig.3).When the initial water content is 200%, the settling time is less affected by sand content than between 82~98h; When the initial water content is 100% and 80%, the consolidation time is related to the sand content. Except for individual points, settling stability time decreases with the increase of sand content, and when the water content is 100% and 80%, respectively, 650~375h, 845~506h.Compared with the reference [9], 200% when the initial water content, sand-mud ratio were 10%, 20% and 30%, stable settlement time were 365h, 610h and 2920h is much higher than the test value, the main reason is 2 times the size of the settlement column close to the test size, drainage distance is 2 times as the test, so the consolidation settlement completion time is far greater than the consolidation time.

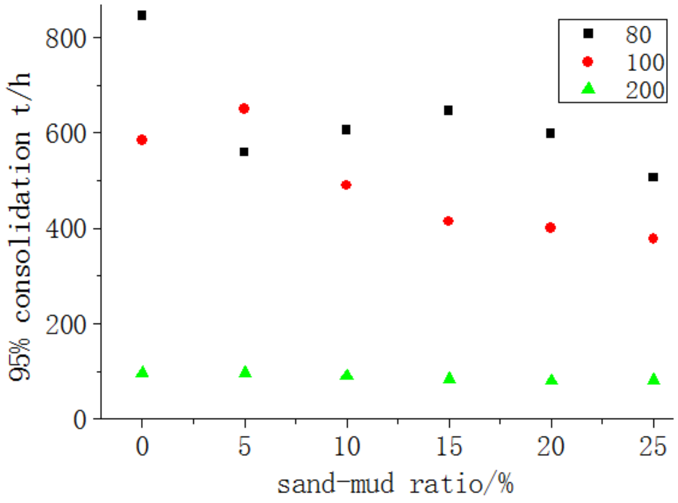

FIG.3 RELATIONSHIP BETWEEN CONSOLIDATION TIME, *w* AND SAND-MUD RATIO WHEN CONSOLIDATION IS COMPLETED 95%

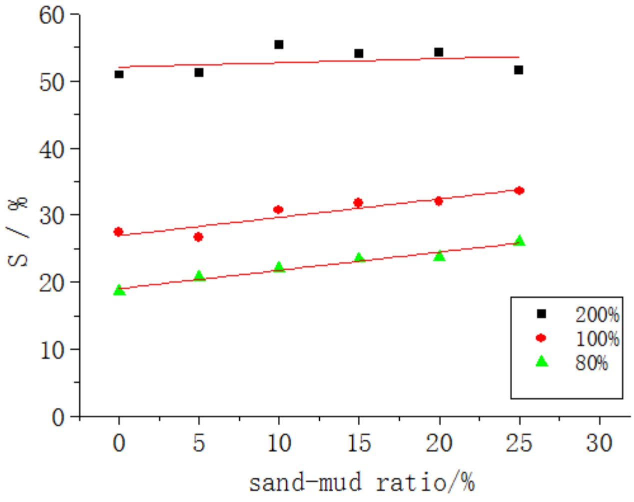

FIG.4 RELATIONSHIP BETWEEN SETTLEMENT STABILITY VALUE AND SAND-MUD RATIO UNDER DIFFERENT WATER CONTENT

Fig. 4 is the change of settlement stability value with sand-mud ratio under different water content. As shown in Fig. 4, the settlement stability value increases linearly with the increase of sand content ratio. Linear equation is for:

$$S_c = 52.104 + 0.06218\alpha \qquad (w_0 = 200\%) \tag{2}$$

$$S_c = 26.95 + 0.27358\alpha \qquad (w_0 = 100\%) \tag{3}$$

$$S_c = 19.07 + 0.27162\alpha \qquad (w_0 = 80\%) \tag{4}$$

In the formula, S_c is the stable settlement value, and α is sand-mud ratio between 0~25%.

3.2 Settlement rate curve

Fig.5~Fig.7 is the curve of settlement rate versus time. As shown in Fig. 3~ Fig. 5, at the initial stage of settlement, the settlement rate is greatly affected by the initial water content. When the water content is 200%, the initial settlement rate is about 35mm, and the settlement rate is less than 0.007 when the settlement is 95%;When the water content is 100% and 80%, the maximum velocity is about 2 and 1.5 respectively. When the settlement is 95%, the rates are less than 0.002 and 0.004 respectively.

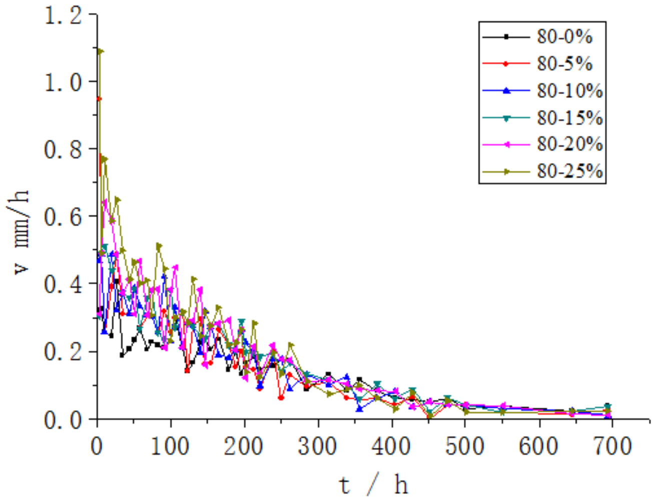

FIG. 5: v-t CURVE OF DIFFERENT SAND-MUD RATIO *w*= 80%

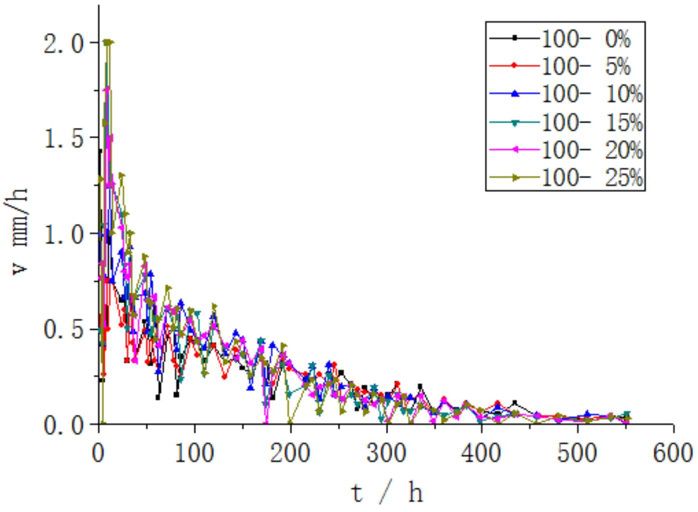

FIG. 6 v-t CURVE OF DIFFERENT SAND-MUD RATIO *w*=100%

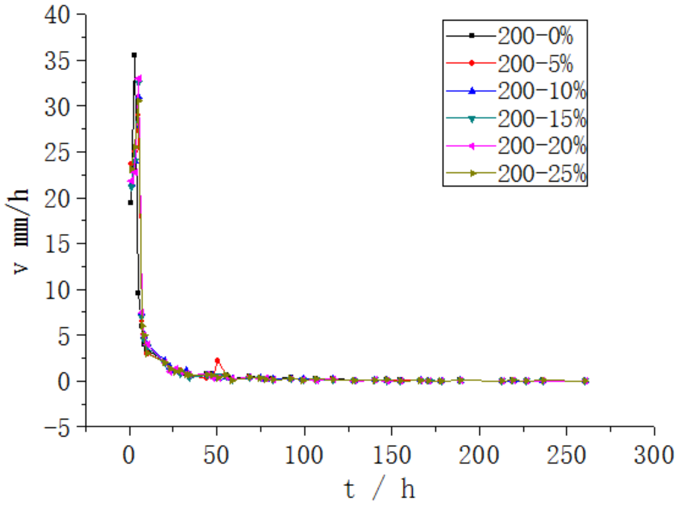

FIG. 7 v-t CURVE OF DIFFERENT SAND-MUD RATIO *w*=200%

3.3 Log curve of settling time

Fig.8 is the change curve of settlement with time logarithm. Fig.9 is the change curve of settlement with time logarithm in reference [9]. As can be seen from Fig.8 and Fig.9, the curve is basically divided into three stages: the straight line segment, the upper concave line segment and the lower concave line segment. At the begin, the curve begins is linear, and with the increase of the initial water content, the slope of the straight line segment increases gradually; The upper concave curve gradually decreases with the increase of water content; The concave curve section gradually changes to the curve type, then the slope of the settlement curve decreases and finally tends to the horizontal. In this experiment, when the water content is 200%,the upper concave line is close to the straight line, while in the reference [9], when the water content is 200% and the sand-mud ratio is 20% and 30%, the upper concave line is close to the straight line, and when the sand-mud ratio is 10%, the upper concave curve is a curve.

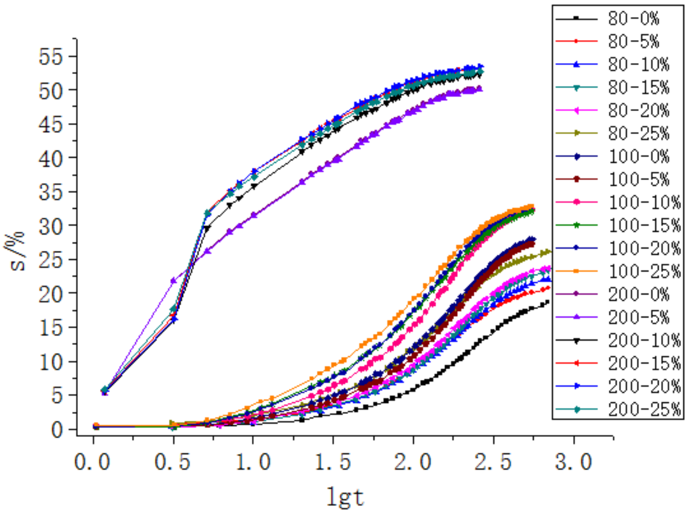

FIG. 8 s-logtcurve WITH DIFFERENT *w* AND DIFFERENT SAND-MUD RATIO

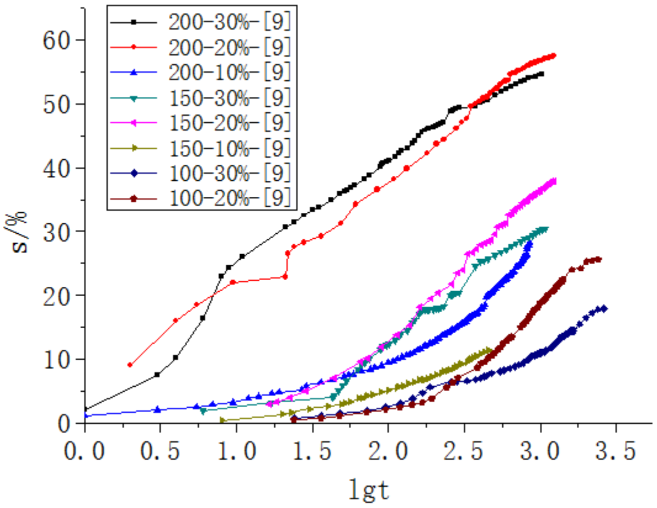

FIG. 9 s-logtcurve WITH DIFFERENT *w* AND DIFFERENT SAND-MUD RATIO(REFERENCE [9])

3.4 Test index of settlement consolidation is completed

Fig.10~Fig.12 show the variation of density and dry density, void ratio and water content with sand content after completion of settlement consolidation. When the water content were 80%, 100% , 200% and the sand-mud ratio is between 0~25%, the density increased along with increasing sand-mud ratio. After completion of the test, 80% water content, soil density changes in the range of 1.722~1.8, the dry density changes in the range of 1.105~1.149; 100% water content, soil density changes in the range of 1.697~1.743, the dry density changes in the range of 1.058~1.114; 200% water content, soil density changes in the range of 1.859~1.768, the dry density changes in the range of 1.174~1.201.After self consolidation, the void ratio of soil samples is between 1.2~1.6 and the moisture content is between 45~60%, and the water content is higher than that of the initial clay soil (45.2%).

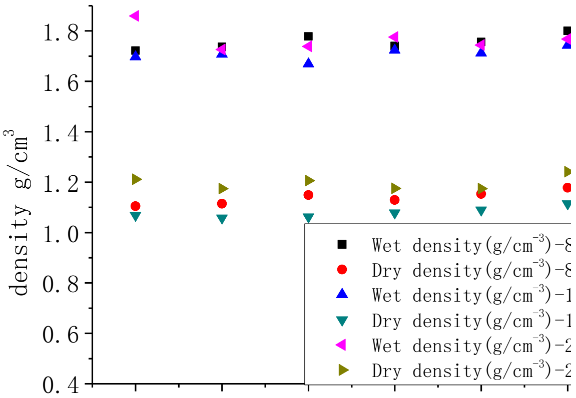

FIG. 10 RELATION BETWEEN DENSITY AND SAND-MUD RATIO AFTER CONSOLIDATION OF SELF WEIGHT SETTLEMENT

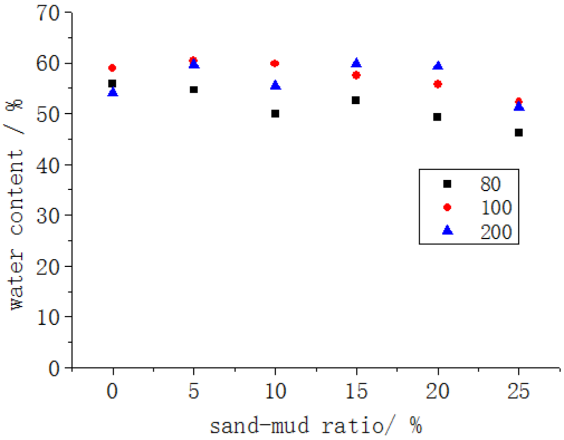

FIG. 11 RELATION BETWEEN W AND SAND-MUD RATIO AFTER CONSOLIDATION OF SELF WEIGHT SETTLEMENT

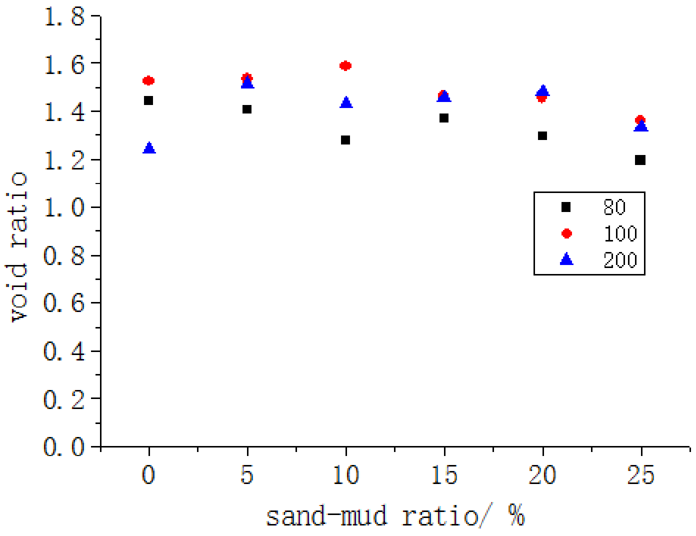

FIG. 12 RELATIONSHIP BETWEEN VOID RATIO AND SAND-MUD RATIO

IV. CONCLUSION

1) The primary factor affecting the settlement of dredger fill of clay soil mixing sand is the initial water content. With the increase of initial water content, the settlement speed of slurry interface is faster, the settlement value increases, and the time of completion of consolidation decreases. The completion time of consolidation decreases obviously with the increase of initial water content. Settlement column size is also one of the major factors of settling stability time, as the settlement column size and drainage distance increase, the consolidation time increases.

2) The settlement curve of mixed sand and clay filled soil conforms to the relation of $S = A_1 e^{-\frac{t}{t_1}} + A_2 e^{-\frac{t}{t_2}} + S_0$. In the formula, S_0 is the stable settlement. According to the formula, the consolidation stability time and the consolidation settlement amount can be determined according to the percentage of completion settlement consolidation. Under the condition of certain water content, the settlement is basically linear with the sand content ratio.

3) The logarithmic time curve of consolidation settlement is basically divided into three stages: straight line section, the upper concave section and the lower concave line segment are formed. At the begin, the curve begins is linear, and with the increase of the initial water content, the slope of the straight line segment increases gradually; With the increase of water content, the upward trend of the concave curve decreases gradually, and when the initial water content reaches a certain value, the upper concave curve becomes a straight line; The lower concave curve section gradually changes to the curve type, then the slope of the settlement curve decreases and finally tends to the horizontal. In this test, when the water content is 200%, the upper concave line is close to the straight line, while in the reference [9], when the water content is 200% and the sand-mud ratio is 20% and 30%, the concave line is close to the straight line.

REFERENCES

[1] Stokes G G. On the effect of the internet friction of fluids on the motion of pendulums[J]. Trans. Combridge Philo. Soc., 1851.9(2)：89-106.

[2] IMAI G. Experimental studies on sedimentation mechanism and sediment formation of clay materials[J].Soils and Foundations,1981,21(1):7-20.

[3] IMAI G. Settling behavior of clay suspension[J]. Soils and Foundations, 1980,20(2):61-77.

[4] Liangtong Zhan, Jun Tong, Jie Xu.Laboratory study on self-weight sedimentation and consolidation behaviors of hydraulic-dredged mud[J].SHUILIXUEBAO, 2008,39(2):201-206.

[5] Guizhong Xu, Feng Ji, Jiaxing Weng.Sedimentation Behavior of Dredged Slurry at High Water Contents[J].Journal of Civil Engineering and Management,2012,29(3):22-28.

[6] Nan Zhang, Wei Zhu, Liang Wang. Study of sedimentation and consolidation of soil particles in dredged slurry[J].Rock and Soil Mechanics,2013,34(6):1682-1688.

[7] Ming Zhang, Guonan Liu, Youming Zhao.Study on Self Weight Consolidation Behaviors of Dredged Fill[J].CHINA RAILWAY SCIENCE,2013,34(5):15-21.

[8] Xianwei Zhang, Aiwu Zhang, Lingwei Kong.Self-weight sedimentation and consolidation characteristics ofhydraulic-dredged slurry in Tianjin Binhai District[J].Chinese Journal of Geotechnical Engineering,2016,38(5):769-777.

[9] Shaolin Le, Wei Bai, Mingjiang Wu.Effect of Sand-mud Ratio on Heterogeneous Dredger Fill Soil and Particle Distribution under Deposited Deadweight[J].Rock and Soil Mechanics,2017:38(S1):233-240.

[10] Ministry of Construction of the PRC, GB 50021-2001. Code for investigation of geotechnical engineering[S].Beijing: China Architecture and Building Press, 2009.

Parametric Analysis of Hyperbolic Cooling Tower under Seismic Loads, Wind Loads and Dead Load through Staad. Pro

Akash Goyal[1], A N Shankar[2], S K Sethy[3]

[1]M.tech Student: Structural Engineering with Specialization in Offshore Structures, University of Petroleum and Energy Studies, Dehradun India.

[2,3]Asst. Professor Civil Engineering Department U.P.E.S, Dehradun

Abstract**—** *Hyperbolic cooling towers are large, thin shell reinforced concrete structures which contribute to environmental protection and to power generation efficiency and reliability. The safety of hyperbolic cooling towers is important to the continuous operation of a power plant. It is observed from the analysis that maximum displacement, support reactions, support moments, stresses and bending moments in plates due to seismic loading, wind loading and dead load i.e. its self weight on a hyperbolic cooling tower is continuous function of geometry (top diameter, throat diameter and height). Earthquake zone plays the important role in analysis. So from this work it can be observed that 300 mm thickness, throat diameter 60m and height 250m is much efficient among all but if height is mandatory to extent than height should not be more than 159m (height taken from actual work) and 170 m height is critical.*

Keywords**—** ***Cooling tower, node displacement, support reactions, plate stresses.***

I. INTRODUCTION

Cooling tower is a tall cylindrical concrete tower used for cooling water or condensing steam from an industrial process. It is a heat rejection device which extracts waste heat to the atmosphere through the cooling of a water stream to a lower temperature. It is generally of 2 shapes, hyperboloid or hyperbolic and rectangular. Hyperboloid cooling towers will be around 130-200m tall and 100 mm in diameter while the rectangular cooling towers will be around 40m tall and 80m long. Cooling tower is generally made of concrete and rebar. The type of foundation required for each cooling tower, e.g. individual foundations, ring foundation or piling, is determined according to the ground conditions. Applications of cooling tower include Oil refineries, petrochemical and other chemical plants, thermal power stations and HVAC systems for cooling buildings. The safety of hyperbolic cooling towers is important to the continuous operation of a power plant. Depending upon the site, earthquake may govern the design of the tower.

II. CLASSIFICATION OF COOLING TOWERS

Cooling towers can generally be classified by it’s

Use:

- Build
- Heat Transfer methods
- Air flow generation methods

Classification by Use:

Heating, Ventilation and Air Condition (HVAC) Cooling towers.

A. Shape of a Cooling Tower

Cooling towers are generally of 2 shapes, hyperboloid or hyperbolic and rectangular. Rectangular cooling towers are generally small in size which are associated with small buildings such as residential buildings, small industries etc. Height of a rectangular cooling tower will be around 40-80m. In this study, 4 cooling towers of height 150m, 200m, 250m and 300 m with three different plate thicknesses of 200mm, 250mm and 300mm were modelled using STAAD Pro software. The radius of throat and base diameters were also varied according to different models. These models were analysed for wind load as well as seismic loads. Equivalent static analysis and Response Spectrum analysis were carried out for seismic loads. Nodal displacement, support reactions, mode shapes, base shear and plate stress of the models were compared and the optimum height of the plate and thickness of the plate were obtained. The critical plate was designed manually.

III. MODELLING

Modelling a building involves the modelling and assemblage of its various load carrying elements. The model must ideally represent the mass distribution, strength, stiffness and deformability. The first part of this chapter gives a summary of various parameters such as material properties, basic geometry required to define the model. Accurate modelling of the nonlinear properties of various structural elements is very important in nonlinear analysis. In this study, STAAD Pro v8i is used for the modelling and analysis of the structure.

3.1 Details of Modelling

The modelling of the structure is done in STAAD Pro. Four models of heights 150m, 200m, 250m and 300m were modelled and each model was assigned with three different thicknesses 200mm, 250mm and 300mm for the concrete plates used in the model. The models were analysed for both wind load as well as seismic load. The top edge of the cooling tower is free to translate and rotate in all directions, while the base is completely fixed.

3.2 Structural Details of the Models

The structural details of four different models created are given in Table1

TABLE 1
STRUCTURAL DETAILS OF THE MODELS

S. No	Parameters (m)	Model 1	Model 2	Model 3	Model 4
1.	Height	150	200	250	300
2.	Base diameter	118	115	110	105
3.	Top diameter	60	65	70	90
4.	Throat diameter	40	50	60	80

IV. MATERIAL PROPERTIES

This section provides the properties of the material used for the modelling of the cooling tower. Reinforced concrete with a unit weight of 25 kN/m3, Poisson's ratio of 0.2, damping ratio of 5% and elastic modulus of 39 GPa were considered for the finite-element modelling of the cooling tower.

4.1 Loading

Dead load, wind load and seismic load were applied on the structure. Dead load shall be calculated on the basis of the unit weights taken in accordance with IS: 875 (part 1)-1987. Wind loads shall be taken as specified in IS: 875 (part 3)1987. Seismic load shall be taken in accordance with IS: 1893 (part 1)-2002 .The instances where concentrated loads occur, special consideration should be given in analysis and design. Dynamic loads of interest include wind loads and seismic actions that are time dependent and asymmetric. The use of equivalent static loads simplifies the analysis, however, it does not account for interaction between the frequencies of the applied load and the characteristic natural frequencies of the structure and limited knowledge on the dynamic behavior of structure. Parameters that are considered for wind loading according to IS875-Part 3 details are given in Table 2.

TABLE 2
WIND LOAD PARAMETERS

S. No.	Parameters	Value
1	Basic wind speed (V_b)	39 m/sec
2	Probability factor/Risk coefficient (K_1)	1.06
3	Terrain roughness and height factor (K_2)	2
4	Topography factor (K_3)	1
5	Exposure of Building	100%, 1

4.2 Earthquake Loads

Parameters for Earth quake loads according to IS 18932002 (Part 2) are given in Table 3.

TABLE 3
SEISMIC LOAD PARAMETERS

S. No.	Parameters	Value
1	Zone	4
2	Zone Factor	0.24
3	Response reduction factor (RF)	5
4	Importance factor (I)	1.5
5	Soil Type(SS), Medium soil	2
6	Damping ratio	5%, .05

V. RESULT

12 different models were analyzed for wind load and seismic loads. Seismic analyses included equivalent static analysis and response spectrum analysis. Maximum nodal displacement, support reactions and stress for each case was determined and compared to study the impact of the different load conditions for varying height and thickness of plate in a simulated model. Table 4 shows the maximum node displacements for wind load for the cooling tower model of height and table 5 shows the Support Reactions of all the models 150 m and varying plate thicknesses of 200mm, 250mm and 300 mm.

TABLE 4
MAXIMUM NODE DISPLACEMENTS FOR WIND LOAD

S. No	Thickness of plate (mm)	Maximum Displacement (mm)
1.	200	67.314
2.	250	51.903
3.	300	42.049

TABLE 5
SUPPORT REACTIONS OF ALL THE MODELS

Height (m)	Thickness (mm)	Wind (KN)	ESA (KN)	RSA (KN)
150	200	3257.11	3328.09	9106.94
150	250	2943.79	2961.63	4666.53
150	300	2642.87	2092.01	3975.45
200	200	2786.046	2557.472	3005.85
200	250	2564.103	2208.38	3903.43
200	300	2350.066	1850.23	4686.75
250	200	2458.526	1700.575	2246.26
250	250	2304.855	1461.078	2997.58
250	300	2153.708	1216.747	3510.014
300	200	3228.64	2020.508	2840.05
300	250	3022.091	1729.904	3547.5
300	300	2820.721	1434.257	4145.81

VI. CONCLUSION

From the analysis results, it can be concluded that

- The nodal displacement of the structure increases by 30% as the height of the Cooling tower is increased while the nodal displacement can be reduced by around 20-25 % by increasing the thickness of the plate used for modelling the cooling tower.
- Mass participation of more than 75% is obtained for all the dominant modes.
- The variation in plate stress was found to be minimum (5%) with the increase in height of the model and thickness of the plate.
- The CQC shear of the increased by around 35% as the height of the tower and thickness of the plate is increased.

From the above results taking cost effectiveness into consideration, the optimum height for a cooling tower can be considered as 250m, optimum plate thickness as 300mm and optimum throat diameter as 60m.

REFERENCES

[1]. IS 1893 (Part 2&3): 2002," Criteria for Earthquake Resistant Design of Structures", Bureau of Indian Standards, New Delhi.

[2]. IS 11504-1985, Criteria for structural design of RCC natural draft cooling towers, BIS new Delhi.

[3]. Seismic analysis and design of hyperbolic cooling tower by A.K.GUPTA, Sergeant and Lundy, Chicago Illinois 60603 USA. Pg 1-10.

[4]. IS: 875(Part3): Wind Loads on Buildings and Structures

[5]. Parametric Earthquake Analysis of Natural Draught Hyperbolic Cooling Tower by Akhil Nema, K. K. Pathak NITTTR Bhopal.

[6]. Static and dynamic analysis of structures" A physical approach with emphasis on earthquake engineering, Pg 111-225.

Sub-pixel Distance Measurement Algorithm Based on Improved SURF

Zixiang Fu

College of Science, Tianjin Polytechnic University, Tianjin, 300387, China

Abstract— *A sub-pixel-level measurement algorithm based on improved SURF is proposed. Firstly, the sobel operator is used to extract the edge of the image quickly in order to highlight the potential feature point, and reduce the detected range of the SURF algorithm. Then use the SURF algorithm to obtain the sub-pixel level coordinates of the matching feature points in the two images. After the match, the affine transformation remove the wrong match point. Finally, the moving distance is calculated by using the sub-pixel-level coordinates of the matching points. The experimental results show that the error of the moving distance is less than 3 %, according to the feature points of the two images. And if the original image resolution is 2560 * 1440, the required running time is only 0.3 to 0.4 seconds.*

Keywords*— *Distance Measurement, SURF, Sub-pixel, Sobel.

I. INTRODUCTION

At present, there are many image-based measurement distance algorithms have been proposed. These image-based ranging methods can be roughly divided into two categories. In the first categories, the image obtained by a single camera is processed to measure distance. For example, Suraphol proposed to measure the length of an object [3] by using the acceleration signals and object differences. Han et al. used the highest feature point of the marker crown and the triangular similarity theory to measure the length [4]. Zhao et al. proposed to obtain the centroid of the odd and even field by using the interval scan to measure speed [5]. The second category is through two cameras to obtain images, using the difference between the two images to calculate the distance. For example, Yasir et al. used visual differences and camera focal lengths from two parallel cameras to measure distance [6]. Hou A-Lin built stereoscopic vision with two cameras and then calibrates with the projection matrix to measure the safe distance traveled by the vehicle [7]. Hai-Sung Baek proposed to use two cameras to build stereoscopic vision. Through the difference between the two images calculated in a larger field of view, a more accurate measurement of object distance is got [8].

The first categories are not only the image processing, in most cases also need to utilize laser, ultrasonic and other auxiliary equipment to obtain relevant information. The second categories require multiple devices to coordinately use, with more complex hardware devices. Thus, a new distance measurement based on single image is proposed in this paper, which is a more economical and convenient measurement manner.

The SURF algorithm is generally used for matching, comparing and tracking of target objects in various scenarios. Its advantage is that it can quickly locate the coordinates of the feature points, and the coordinates can be subpixel [11-14]. In this paper, the Sobel edge extraction is utilized to reduce the scope of feature extractions, and affine transformation is utilized to avoid false matching result of the SURF algorithm. Afterwards, the SURF algorithm will be used to extract the feature points before and after the target object is moved. Then the result of feature extractions is calibrated by affine transformation. Combined with the angle information, calculate the average of the components from multiple groups measured length values in the direction of motion, and utilize this average value to estimate the distance. The innovation of this paper is to apply the SURF matching algorithm to distance measurement. It not only can quickly and stably obtain the result of the measurement, but also the coordinates of the measured feature point which can reach the sub-pixel precision.

II. METHODOLOGY

Step1: First at all, the two images of the natural scene along a certain direction of movement are shot. It is required that is overlap or have the same part, because the next algorithm will be based on the characteristics of the two images to the estimated moved distance. When shooting images, it could not take into account the effects of light, allowing a small angle of rotation, and allowing a slight change in height, but as far as possible to keep the image shot in the same depth of field. The original image resolution of is 2560 * 1440. Taking into account the actual shooting of the image may be too large, so the appropriate reduction is needed to improve efficiency. The following results are obtained at a compression ratio of 0.2(the problem of compression ratio will be discussed in detail below). The default direction of movement is horizontal, and the measured distance is also in this direction. In the actual measurement, the height of the camera determines the camera to capture the scope of view. Fig. 1 shows the results of the algorithm in camera scope of view. And the algorithm can still be stable to obtain the test results, even in different backgrounds and different light.

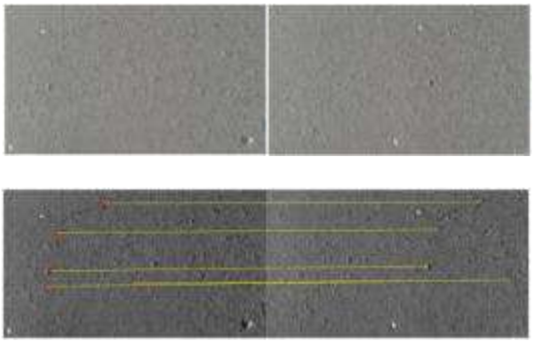

FIG. 1 THE TOP ROW IS THE ORIGINAL IMAGE, THE BOTTOM ROW IS THE MATCHING RESULTS, THE BACKGROUNDS IN ORIGINAL IMAGES ARE: CEMENT ROAD.

Step 2: In order to reduce the computational complexity of the SURF algorithm, it needs to firstly utilize the sobel operator to extract the edge of the image, which will be also more conducive to extract feature points for the SURF algorithm. This paper chooses Fig1 to extract the edges. The results are shown in Fig. 2.

FIG.2. EXTRACT THE EDGES FROM THE ORIGINAL IMAGE

Step 3: After the images have been extracted the edge, the SURF algorithm is used to match the image to find the feature points quickly. After matching, multiple sets of matching feature points will be obtained. Fig. 3 shows the obtained results according to Fig. 2. For Fig. 2, the picture is a combination of two images, the red pixels stand for before moving, green pixels stand for after moving, the red circle stand for feature points of the image before moving (matched point1), the green cross stand for feature points of the image after moving (matched point2). Finally, connect the matching feature points in two images with a yellow line.

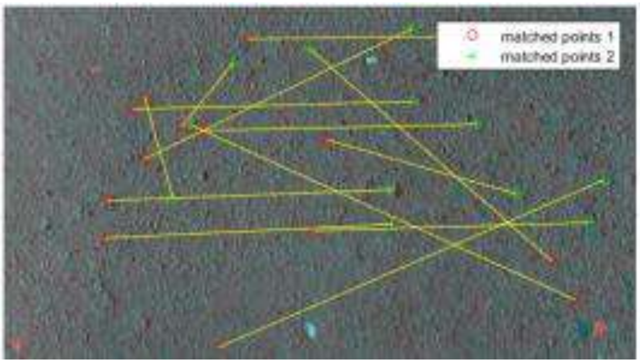

FIG. 3. MATCH THE IMAGES

Step 4: After the images matched, the affine transformation is utilized to calculate the transformation associated with the matching point. This conversion allows us to filter the matched results in two images. The result is shown as Fig. 4.

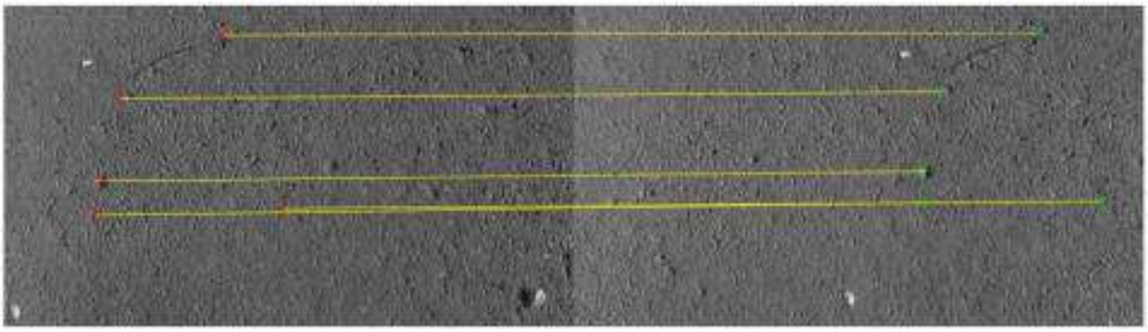

FIG. 4. FILTER MATCHED RESULTS

Step 5: After the SURF algorithm, the coordinates of these feature points have reached the sub-pixel level. Next, the corresponding vectors will be calculated by using these coordinates. Each pair of matching successfully points has two coordinates, so it can get a vector, which contains two information's, namely the length and the angle. It is considered that the direction of the vector formed by matching the feature points cannot be exactly the same as the horizontal direction. Therefore, it is necessary to calculate the angle θ between the residual vector and the direction of motion (namely, the horizontal direction) to make the results as accurate as possible. In order to eliminate the impact of MSAC algorithm, this paper needs to calculate the average of the length value $\overline{d}$ and the average of the angle value $\overline{\theta}$. Here, the length of vector is *d*. The number of vectors is *n a*nd there are:

$$\overline{d} = \frac{\sum_{i=0}^{n} d_i}{n} \tag{1}$$

$$\overline{\theta} = \frac{\sum_{i=0}^{n} \theta_i}{n} \tag{2}$$

Step 6: The length value $\overline{d}$ is multiplied by the cosine of $\overline{\theta}$ to obtain the length component $\overline{w}$ of the vector in the direction of motion. The result is:

$$\overline{w} = \overline{d}\, cos\, \overline{\theta} \tag{3}$$

Here, as the image is reduced, it is necessary to divide by the corresponding reduction ratio *k*. This result *w* is the displacement in the pixel sense *w* is:

$$w = \frac{\overline{w}}{k} \tag{4}$$

Step 7: The image pixel length *h1* and the actual length *h2*are known, the actual moving distance *s* is obtained from the average value *w*. If the shooting time of two images is known, the speed can be further measured. So the moving distance*s* is:

$$\frac{w}{s} = \frac{h_1}{h_2} \tag{5}$$

III. EXPERIMENTAL RESULTS

In order to accurately measure the accuracy of the algorithm, move the camera in parallel at a fixed height. For the distance of 20 cm, 9 sets of data are measured. Fig. 5 shows the line graph of the standard distance and the measured distance for each movement. As it can be seen from Fig. 5, the relative error measured is less than 3 %. In the actual movement of the process, due to man-made reasons, the camera's viewing angle and height may be a slight change, which will naturally have an impact on the measurement results. Therefore, the actual error is less than 3 %.

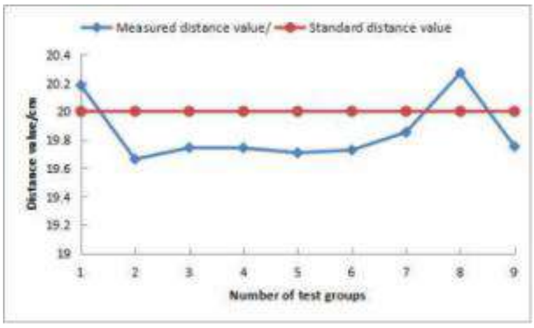

FIG. 5. THE RESULT IS MEASURED WHEN CAMERA MOVING 20 cm EACH TIME.

IV. CONCLUSION

This paper presents a subpixel distance measurement algorithm. It has rotational invariance, scale invariance, and satisfies the velocity measurement in strong light and low light. The experimental results show that according to the feature points of the image, the error between the measured distance and the actual moving distance is less than 3 % and the time is only 0.3 to 0.4 seconds. The measurement results are retained to 0.0001. The algorithm is applied to the measurement of distance, and can also be used to measure the speed. The algorithm can be used for the speed measurement of the moving objects in a quiescent state. It can also be made on the vehicle equipment, to measure its speed.

REFERENCES

[1] L. Suraphol, W. Akarapas, and P. Karn, "Measurement of Size and Distance of Objects Using Mobile Devices", in: Proceedings - 2013 International Conference on Signal-Image Technology and Internet-Based Systems, SITIS 2013, 2013, pp.156-161.

[2] D. Y. Han, C. D. Wang, "Tree Height Measurement based on image processing Embeded in Smart Mobile phone", in: 2011 International Conference on Multimedia Technology, 2011, pp. 3293 – 3296.

[3] P. Zhao, "Precise speed measurement using an interlaced scan image", Optics & Laser Technology,vol.43, 2011, pp. 204-207.

[4] Y. M. Mustafah, R. Noor, H.h Hasbi, A. W. Azma, "Stereo Vision Images Processing for Real-time Object Distance and Size Measurements", in: 2012 International Conference on Computer and Communication Engineering (ICCCE) , 2012, pp.659 - 663.

[5] A. Hou, X. Cui, Y. Geng, W.J. Yuan, and J. Hou, "Measurement of Safe Driving Distance Based on Stereo Vision", in: 2011 Sixth International Conference on Image and Graphics, 2011 , pp. 902 - 907.

[6] H.S. Baek, J.M. Choi, and B.S. Lee, "Improvement of Distance Measurement Algorithm on Stereo Vision System (SVS)", in: Proceedings of the 5th International Conference on Ubiquitous Information Technologies and Applications, 2010, pp. 1-3.

[7] Y. Luo, Y.Z. Chen, "Robust matching algorithm based on SURF", in: 2015 12th International Computer Conference on Wavelet Active Media Technology and Information Processing (ICCWAMTIP) , 2015,pp.7- 10.

[8] W. Saelao, S.t Wangsiripitak,and C. Pluempitiwiriyawej, "Feature-based motion detection and tracking on approximate 3D ground plane", in: 2016 Visual Communications and Image Processing (VCIP) , vol.201,2016, pp. 1 - 46.

[9] L. Xia, Y.G. Gao, and X.D. Han, "Novel theory for propagation of tilted Gaussian beam through aligned optical system", Optics Communications, vol. 387, 2017, pp. 281-289.

[10] P. Chen, F. Chen, Y.X Han, and Z.S Zhang, "Sub-pixel dimensional measurement with Logistic edge model", Optik , vol. 125,2014,pp. 2076-2080.

Trace Analysis of Carbazole in Commercial Diesel by using Adsorption on Activated Biochar from Rice Husk Pyrolysis

Gabriela P. S. Maciel[1], Eliane Lazzari[2], Thiago Bjerk[3], Samir M. Ahmad[4],
Ana P. Carvalho[5], José M. F. Nogueira[6], Elina B. Caramão[7]

[1]Departamento Interdisciplinar, Universidade Federal do Rio Grande do Sul – Campus Litoral Norte, Tramandaí, RS, Brazil.
[2,7]Instituto de Química, Universidade Federal do Rio Grande do Sul, Porto Alegre, RS, Brazil
[4,5,6]Centro de Química e Bioquímica, Faculdade de Ciências, Universidade de Lisboa, Campo Grande Ed. C8, 1749-016 Lisboa, Portugal
[7]Instituto Nacional de Ciência e Tecnologia - Energia e Meio Ambiente, Salvador,BA, Brazil
[3,7]Departamento de Biotecnologia Industrial, Universidade Tiradentes, Aracaju, SE, Brazil

Abstract— *The valorization of rice husk biochar obtained by pyrolysis was studied by production high quality activated carbon. Activated carbon (AC) chemically treated by K_2CO_3, was used as sorbent phase in bar adsorptive microextraction followed by comprehensive two-dimensional gas chromatography coupled to a quadrupole mass spectrometer analysis (BAμE/GC×GC-qMS) for trace analysis of carbazole in commercial diesel. The prepared AC was characterized by N_2 adsorption, SEM-EDS and pH_{PZC}. Assays of nitrogen adsorption isotherm demonstrated that the AC presented microporosity and the Density Functional Theory Calculation was applied to obtain information concerning the micropore size distribution. The BET surface area and total pore volume were 1850 $m^2g^{-1}$and 0.83 cm^3g^{-1}, respectively. AC from rice huskpyrolysis (RH) showed an acceptable adsorption capacity for Carbazole in diesel matrices allowed us to obtain average recoveries of 91.0 % and convenient analytical parameters. From the data obtained, the proposed methodology proved to be a suitable sorption-based static microextraction alternative for monitoring trace levels of carbazole in commercial diesel.*

Keywords— ***Rice husk pyrolysis, Activated carbon, Chemical activation, Bar adsorptive microextraction, BAμE/GC×GC-qMS, Nitrogen compounds, Diesel.***

I. INTRODUCTION

In the last year, there was a growing interest in using low-cost and abundantly available waste materials as precursors of carbon materials. Actually, any carbonaceous material with high carbon content can be used as raw material for the preparation of activated carbons (ACs) [1]. This is the case of t agricultural solid wastes [2] , such as, cotton stalk [3,4], tobacco stem [5], rice husk [6], cork [7], bamboo [8], waste tea [9, 10], coconut shell [11], oil palm fiber [12], durian shell [13], wood [14], sisal [15] and many others.

In South Brazil, rice processing is an important agro-industrial sector, giving rise to large amounts of rice husk (about 2.5 million metric tons per year) produced as agricultural waste. Fast pyrolysis is an interesting option for the reducing the environmental impact and to valorize rice husk, as shown in a previous study [16]. The production of AC from rice husk is achieved through chemical or physical activation [17].

Chemical activation is a widely used method to obtain AC with a very large surface area and great micropore volume and is usually performed using NaOH/KOH [18-21], H_3PO_4 [22] or $ZnCl_2$[20, 23]. K_2CO_3 is an alternative to KOH with the advantage that carbonate mediated activation is less extensive, as well as being a more environmental friendly activating agent when compared to the most commonly reported chemical activating agents above mentioned. In fact, K_2CO_3 is nontoxic (can be used as food additives), is easy removed by water washing, has weak corrosion thus allowing good operating conditions. The uses of K2CO3 as activating agent have been reported by several authors [3, 7, 15, 24-29] resulting in the preparation of ACs with high surface area [13] and developed microporosity.

ACs exhibit excellent adsorption performance in the process of nitrogen and sulfur removal from many different matrices and are the most used adsorbents [30, 31]. Adsorptive denitrogenation and desulphurization is considered promising methodology when compared with the conventional hydrodenitrogenation and hydrodesulphurization process, because it can be run at ambient conditions without using hydrogen and catalysts [32]. The importance of denitrogenation process results from the fact that although nitrogen compounds are present at low concentrations, they play an important role in the quality of oil products. Non-basic nitrogen compounds (*e.g.* carbazole) account for about 70 % of the load of nitrogen compounds in the atmospheric gas oil, being a major nitrogen component of diesel fuel [33].

Since nitrogen compounds are more difficult to be eliminated in hydroprocessing, several methods for their isolation are described in the literature [34, 35]. However, many procedures use separation with open column liquid chromatography, which implies the use of large volumes of solvent, costly adsorbent materials as stationary phases, and long separation times.

In the last decades, new microextraction techniques have emerged, namely solid-phase microextraction and stir bar sorptive extraction, since they use negligible amount of solvent, low sample volume and simplified approach [36]. However, these techniques use a small number of polymeric materials (*e.g.*, polydimethylsiloxane) as sorbents and the coating with ACs is still little explored. As an alternative, a new technique was introduced, bar adsorptive microextraction (BAμE) [37], which offers the operator the possibility to choose the most convenient sorbent phase (polymers or ACs), according to the chemical characteristics of the target analytes [36].

In recent years, researchers have explored environmental friendly and low cost materials as precursors to prepare ACs that presented high apparent specific surface areas and good performance when tested as adsorbents for nitrogen compounds [32, 38].Examples of these materials are biochars from the pyrolysis or combustion of biomasses. The possibility of producing carbon materials with high specific surface areas and micropore volume allied with a considerable surface reactivity make these materials adequate for a great number of applications. According to the authors' knowledge, AC prepared from rice husk pyrolys is using K_2CO_3 activating agent has not still investigated in the analysis of the nitrogen compounds of diesel samples until now.

In this study, rice husk biochar (obtained from the pyrolysis of rice husk) was subjected to a chemical treatment with K_2CO_3 and the chemical characterization of the prepared AC was performed. The purpose of this research is to evaluate the microextraction feasibility of traces of nitrogen compounds from diesel using BAμE coated with novel AC sorbents following by comprehensive two-dimensional gas chromatography coupled to a quadruple mass spectrometer (GC×GC-qMS) analysis. The proposed methodology was applied, for the first time, in the analysis of carbazoles in commercial diesel samples and the analytical performance was evaluated in terms of accuracy, precision, linearity and detection limits.

II. MATERIAL AND METHODS

2.1 Materials and chemical reagents

All reagents used in this work were of analytical grade. HPLC-grade methanol (MeOH, 99.9%) and acetonitrile (ACN, 99.9%) were purchased from Panreac (Spain).Dichloromethane (DCM, 99%) was provided by Vetec (Brazil). Reference standards carbazole and acenaphthene D-10 (internal standard), as well as nonane, tetradecane and hexadecane, were used to prepare the standard solutions and for sample dilution, which were provided by Sigma–Aldrich (Seelze, Germany), with purity higher than 97%. K_2CO_3(99.6 %) used as activating agent was supplied by Prolabo, VWR Chemicals. Rice husk was gathered from a farm in Rio Grande do Sul, south of Brazil. All the biomass material was crushed by a high-speed rotary cutting mill, sieved to limit the particle size (40-60 mesh). Commercial diesel fuel was obtained from a local gas station in Lisbon, Portugal.

2.2 Biomass pyrolysis and preparation of AC

The pyrolysis procedure of rice husk (RH)was performed in a stainless steel vertical oven containing a quartz reactor; more details can be obtained from other study [39]. After some optimization experiments,3 g of rice husk were heated under nitrogen atmosphere, N_2 flow of 1 L min^{-1}, at 650 ºC using a heating rate of 100 ºC min^{-1}. The reactor was maintained at 650 ºC for 5 min at the end of the process.

To prepare the active carbon, in the following designated as AC-RH, biochar was mixed with K_2CO_3in 1:3 weight ratio of char: K_2CO_3. The mixture was activated in a horizontal furnace (Thermolyne mod. 21100), under N_2 flow (5 mLs^{-1}). The temperature was raised (10 ºC min^{-1}) up to the activation temperature (800 ºC) that what kept for 2 h. After cooling, under N_2 flow, the sample was washed with distilled water up to pH 7 and dried at 100 ºC.

2.3 Characterization of AC

Textural characterization was performed using N_2 adsorption-desorption isotherms at -196 ºC, using a Tristar Kr 3020 Micromeritics equipment. The samples were previously degassed at 120 °C under vacuum, for 12 h. The specific surface area was determined by BET (Brunauer, Emmett and Teller) multipoint technique. The pore size distribution in the micropore range was obtained using the Horvàth–Kawazoe (HK) method [40]. Meanwhile, the whole pore size distribution was computed by the DFT (Density Functional Theory) method [41].

In order to observe the morphological textures onto the char and AC, these samples were examined by using a high-resolution scanning electron microscopy equipped with an energy-dispersive spectrometer (SEM-EDS). The SEM-EDS analysis was carried out with Zeiss (EVO MA10 model) which was operated at 15 kV accelerating potential. Prior to the SEM-EDS observation, samples were previously coated with gold.

Further characterization was performed by means of the point of zero charge (pH_{PZC}), of the sample by reverse mass titration, following the method procedure described in Mestre et al [42].

2.4 Preparation of BAµE devices

For the bar configuration, the BAµE devices were prepared by coating polyethylene hollow cylindrical tubes (7.5 mm in length and 3.0mm in diameter) with adhesive films, which was coated with the powdered AC (approximately 2mg). Before use, the bars were previously cleaned through ultrasonic treatment using heptane as solvent. The detailed description of devices manufacturing can be checked at other works [37, 43].In real sample assay, the standard addition methodology (SAM) was applied, followed by the same procedure employed for the validation experiments. The mixture of nonane, tetradecane and hexadecane was denominated synthetic diesel. 10 mL of commercial diesel sample diluted 5 times with synthetic diesel spiked with carbazole standard, using three levels of concentration (0.100, 0.025, 0.0125 mg L^{-1}), and a µ-extraction bar device previously coated with AC were introduced into glass flasks. The glass flasks were placed in a multipoint agitation plate (Variomag) with agitation speed of 750 rpm at room temperature for 1h. The assays were performed in triplicate. For back-extraction, the µ-extraction bar device was removed from the samples with clean tweezers and placed into a 1.5mL vial with a glass insert containing 200 µL of MeOH/ACN (1:1 v/v), ensuring their total immersion prior to ultrasonic treatment at room temperature using a desorption time of 30 min. After back-extraction, the AC-RH bar was removed with clean tweezers and the stripping solvent was evaporated until dryness under a gentle stream of purified nitrogen (99.9%), followed by reconstitution with 200 µL of dichloromethane. The vial was then sealed and placed in the auto sampler for GC×GC/qMS analysis. Blank assays were also performed using the procedure above described without spiking.

2.5 Instrumentation settings

The GC×GC-qMS system consisted of a chromatograph Shimadzu QP2010 Ultra (Shimadzu, Japan) equipped with a cryogenic modulatorZX1-GC×GC(ZOEX Corporation, Houston, USA). This modulator utilizes liquid nitrogen (Linde Gases, Brazil) for the cold jet and gaseous nitrogen for the hot jet. A non-polar column DB-5 (5% of phenyl groups in a methyl silicon stationary phase, with 60 m × 0.25 mm i.d. × 0.25 µm film thicknesses, Ohio Valley Specialty Company, USA) was used in the first dimension. A more polar column DB-17 (50% of phenyl groups in a methyl silicon stationary phase, with 2.15m× 0.18mm× 0.18 µm, J&W Scientific, Agilent Technologies, USA), was used in the second dimension. Different temperature programs, modulation periods and column flow rates were tested. A conventional split/splitless injector was used at 280 ºC, with an injection volume of 1.0 µL in splitless mode. The GC program began at an initial temperature of 70 ºC and was held at this temperature for 2 min, then the oven was heated to 200 ºC at 3 ºC min^{-1} and then to 280 ºC at 5 º$Cmin^{-1}$ and held for 3 min. The carrier gas was helium under a constant flow rate of 0.86 mL min^{-1}. The interface and ion source were maintained at 280 ºC, and the total flow rate was 21.1 $mLmin^{-1}$. The fast quadrupole MS conditions were: energy of 0.83 kV and mass scan range from 45 to 300 Da, corresponding to a frequency of 73.3 Hz. A modulation period of 4 s and the hot jet time was set to 300 ms. Data processing by GC×GC-qMS was performed using the GC Image 2.2b1 software (ZOEX Corporation), and the NIST-05 library was used to identify carbazole with a similarity of at least 90%, which was confirmed by the retention time of the standard.

2.6 Recovery assays and method validation

For identification purposes, pure standards samples were injected for comparing the retention parameters and peak purity with the MS spectral reference database. For recovery calculations, peak volumes on the tridimensional diagram obtained from each assay were compared with the peak volumes of standard control used for spiking. For quantification purposes on real matrices, calibration plots using the SAM approach were performed. The present methodology was validated according to international guidelines for linearity, limits of detection (LOD) and quantification (LOQ), as well as intra- and inter-day precision.

III. RESULTS AND DISCUSSION

3.1 N_2 adsorption isotherm and pore size distribution of AC

The BET surface area ($0<p/p^0< 1$) increased from 223 m^2g^{-1} to 1850 m^2 g^{-1} after the activation. According to the literature, for example the study of Adinata et al. [24] the specific surface areas of K_2CO_3ACs increases with the carbonization temperature up to 800 ºC and slightly decrease when higher temperatures are applied. Therefore, it was deduced that K_2CO_3 was effective as activation reagent below 800 ºC.As reported in the literature alkali metal atoms are removed from the intercalated system at higher temperature; therefore the surface area and pore diameter may increase [1].

The N_2 adsorption and desorption isotherms obtained for the biochar and AC-RH samples were shown in Figure1, in accordance with the International Union of Pure and Applied Chemistry (IUPAC) [44] classification the isotherms resembles a combination of type I and type IV isotherms, displaying a marked characteristic microporous associated with a mesoporous structure, as demonstrated by its initial adsorption and the plateau region at higher relative pressure. After a sharp increase up to 0.1 of relative pressure, the isotherm showed a slow increment in the further adsorption at higher pressure.

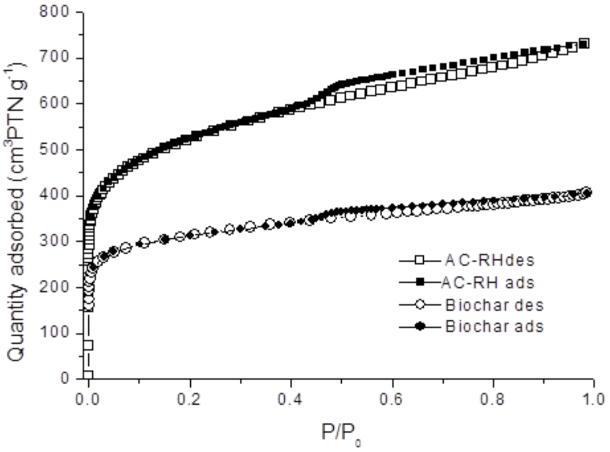

FIGURE 1. NITROGEN ADSORPTION-DESORPTION ISOTHERM SAT -196 ºC ON THE MENTIONED SAMPLES. CLOSED SYMBOLS REPRESENT DESORPTION POINTS.

The corresponding pore size distribution for the AC according to the HK method was shown in Figure 2a, in which micropores less than 1.0 nm were presented. Figure 2a exhibited a narrow micropore distribution at the range of 0.50-0.75 nm and showed that the vast majority of micropores were ultra micropores (pore widths <0.7 nm), which represents an important contribution for the overall porosity of this carbon material. The whole pore size distribution was calculated by Density Functional Theory (DFT) method as illustrated in Figure2b. The pore size distribution curve suggested a predominant micropore owing to the sharp increase of pore size distribution curve to pore diameter less than 2.0 nm, in good agreement with the HK method results.

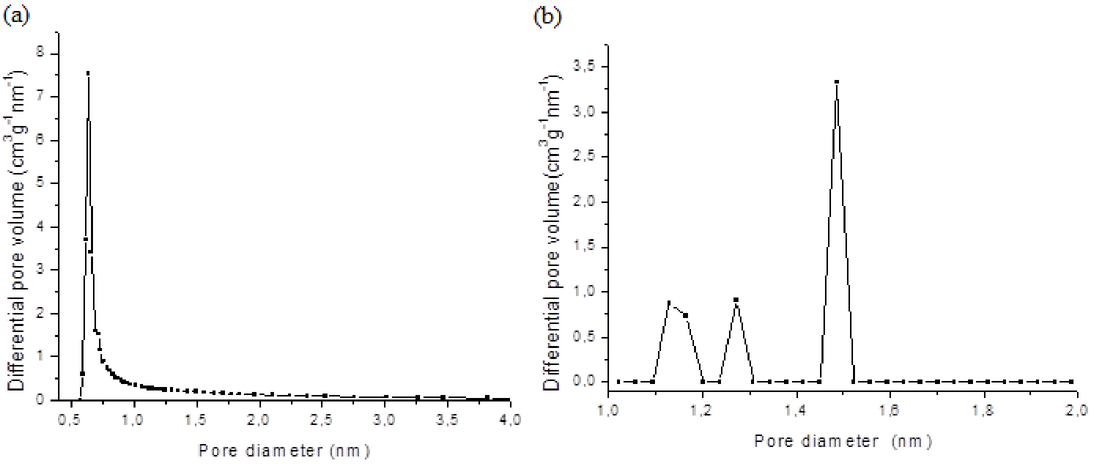

FIGURE 2. MICROPORE SIZE DISTRIBUTION OF AC-RH BY HK METHOD (a) AND PORE SIZE DISTRIBUTION OF AC-RH BY DFT METHOD (b).

3.2 Visual inspection of SEM images

Scanning electron microscopy (SEM-EDS) technique was employed to observe the surface physical morphology of samples. Figure 3 depicts the SEM images of the char and AC, respectively. A significant difference of the surface topography between biochar and AC-RC was observed. The image of the biochar showed a smooth surface with slit like cracks and voids, relatively organized on the surface (Figure 3a). The image of the biochar sample in another region (Figure 3b) demonstrates porous less regular, whereas remarkably regular and homogenous surface morphology are observed for the AC sample (Figure 3c). Nevertheless, it could be seen from the micrographs that the external surface of the chemically AC-RH was full of cavities. A gradual improvement is observed on the surface morphology with the chemical activation. The surface of the AC is smoother and more porous structured than that of the biochar, and illustrated significant changes in the total surface area as reported in the previous sections. As seen in the images (Figure 3d), crater like macropores formed during the reactions between the biochar and K_2CO_3.Examination of the image (Figure 3d) clearly reflects that the holes on the particles are in macropore size and have various geometry but majority of them in more distorted circular shape. Those pores resulted from the reactions between carbon matrix and the chemical reagent during activation. In addition, after K_2CO_3 activation, the AC is washed, these salts formed in the activation can be leached out by water to form micropores within the carbon matrix, vide Figure 3e and f [45, 46].

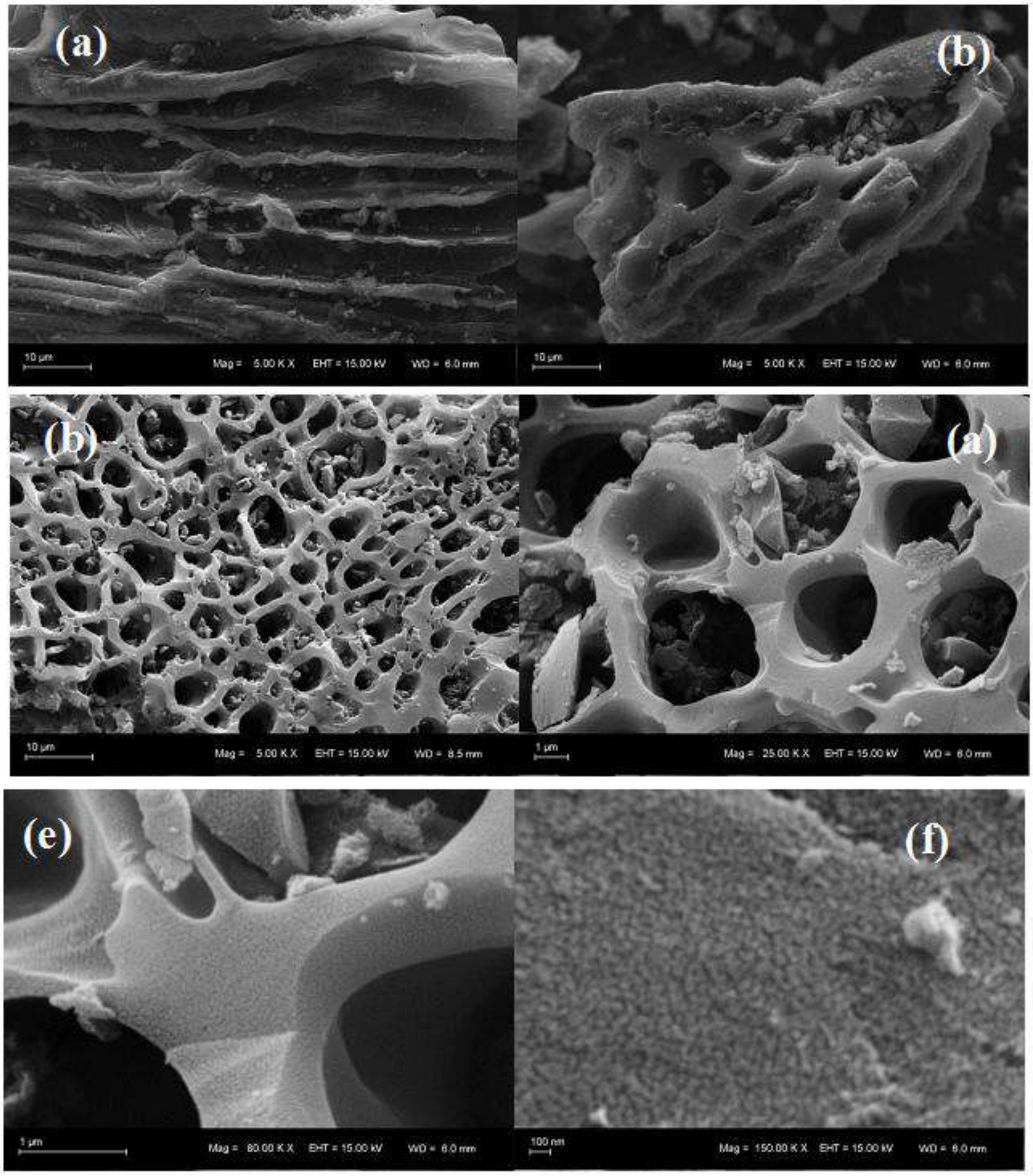

FIGURE 3. SEM MICROGRAPHS OF (a, b) THE BIOCHAR AND (c, d,e, f) AC-RH.

The SEM-EDS studies shed more light on leaching results. These analyses also indicated that silicates would be the dominating compounds in the biochar. This was expected for the biomasses, given the high content of this element in RH[47]. The rice husk silica was found in large shell-like inclusions in the biochar consisted in a carbon structure coated of practically pure silica particles. Skrifvars et al. [48] defined as "skeleton" that pure silica layer. As shown in Figure 4a there was a shell-like (Point 1) and the silica content obtained by EDS around Point 1 was 12.4wt%, which was righter than that around Point 2 (2.0wt%).However, in AC the silica was found fairly evenly distributed around the carbon inclusions. It can be clearly seen with the EDS map presented in Figure 5. In addition to C, O and Si, a minimal amount of others elements were found in both samples. The detailed elemental spectra data at biochar (Point 1 and 2) and A Care shown in Table 1.

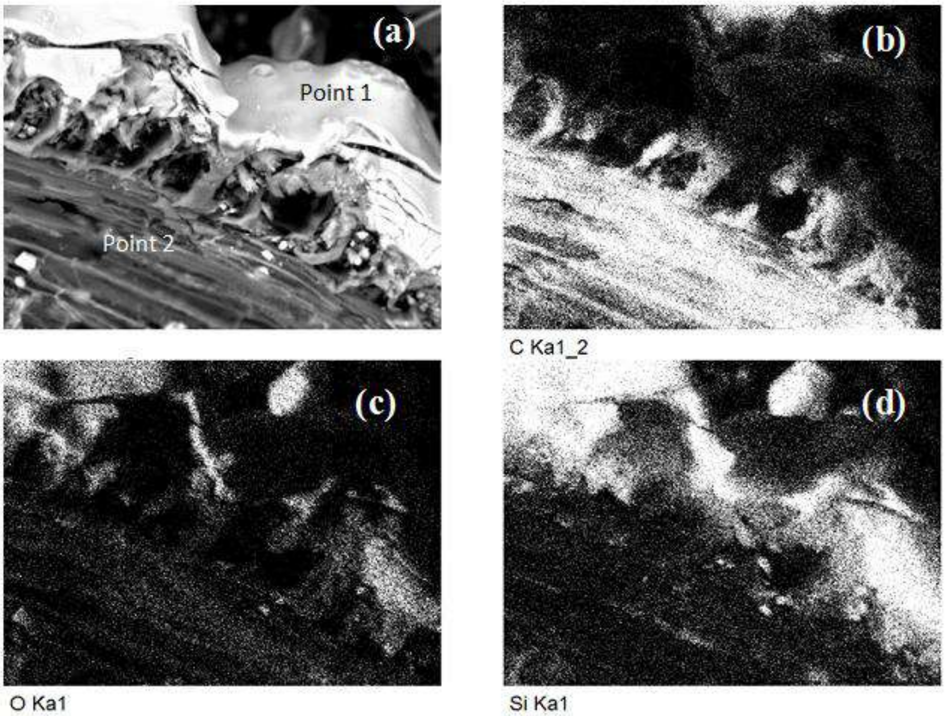

FIGURE 4. SEM-EDS IMAGES OF THE BIOCHAR (a) AND MAPPING OF (b) CARBON, (c) OXYGEN AND (d) SILICON.

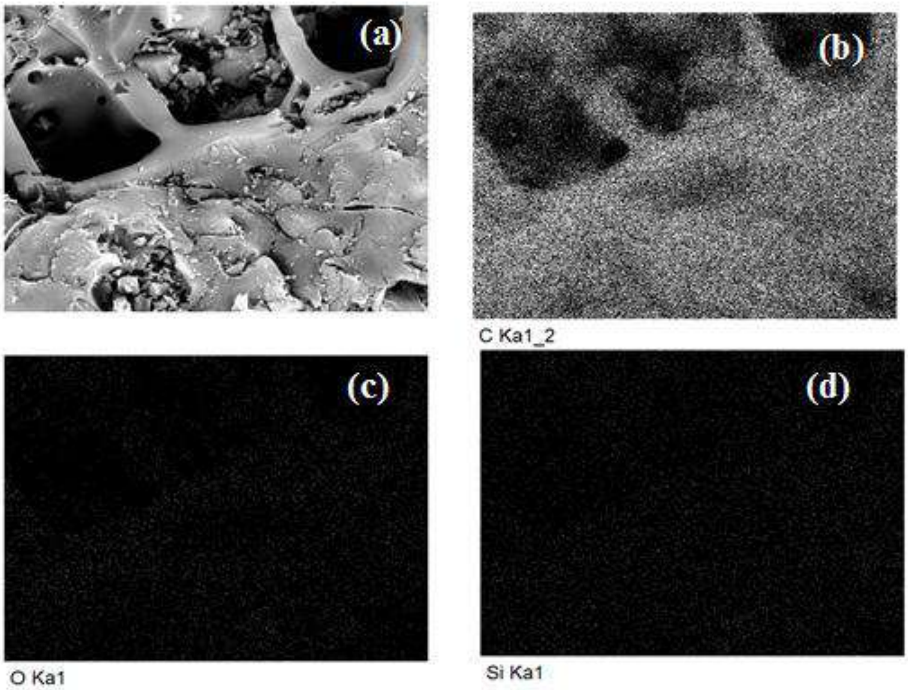

FIGURE 5. SEM-EDS IMAGES OF THE AC-RH (a) AND MAPPING OF CARBON (b).

TABLE 1
CHEMICAL COMPOSITION OF THE ACTIVATED CARBON AND CHAR (POINT 1 AND 2), AS DETERMINED BY EDS ANALYSIS

Sample	Average mass percentage %						
	C	O	Si	Mg	P	Ca	K
AC	91.96	7.52	0.40	-	-	-	0.05
Char (Point 1)	67.54	18.70	12.37	0.02	0.05	0.29	1.03
Char (Point 2)	86.25	11.08	2.00	0.03	0.04	0.03	0.42

3.3 Point of zero charge analysis of AC and char

The surface acidity and basicity is an important criterion describing the surface chemistry of the carbon adsorbents. The pH_{PZC}, defined as the pH at which the adsorbent surface has net electrical neutrality, in other words, the point that the net charge of adsorbent is zero. Regarding the surface chemistry, the pH_{PZC} value revealed that the as-received biochar has basic nature (pH_{PZC}9.0).The chemical activation process led to a sample with an acidic surface since the pH at the point of zero charge decreased more than 3 pH units. The pH_{PZC} of AC-RH was found to be as 5.6.

IV. CONSIDERATIONS ON TRACE ANALYSIS OF NITROGEN COMPOUNDS IN DIESEL

There is a general consensus on the difficulty of removing nitrogen compounds in diesel samples. The very low concentrations of nitrogen compounds in commercial diesel and the presence of huge hydrocarbon matrix and sulfur/oxygen-containing compounds interferes with the analysis. To overcome the problems of having a low concentration of nitrogen compounds in diesel, it was vital perform a previous enrichment step. Several approaches have been proposed for the speciation of nitrogen in diesel, and a lot of methods for their isolation are reported in the literature [34, 35, 49-52].However, these methods generally comprise a combination of several analytical steps and use different laborious techniques, such as liquid-liquid extraction [51, 52], solid-phase extraction[49, 50], ion-exchange chromatography [34, 35], and others [53]to concentrate and isolate the nitrogen compounds in diesel. The liquid-liquid extraction methods are complex and may cause the significant loss particular types of nitrogen compounds, such as the more neutral species, due to their lower extraction selectivity. Most of these proposed techniques involve separation by open column chromatography [34, 35, 49]and though useful, use large volumes of solvents and many expensive materials and demand long separation times. Furthermore, these separation processes show low selectivity for nitrogen species, poor control over sorbent activity, and incomplete separation of the specific compound classes. Nevertheless, it turned out that these procedures are time consuming and neither selective nor quantitative because some of the nitrogen compounds are only partially extracted or are lost during the extraction procedure due to matrix effects, thusly influencing the quality of the analytical response.

Currently, preparative and sample preparation techniques have been oriented to simplification, miniaturization, easy manipulation of the analytical devices, large reduction of toxic organic solvents, as well as small sample volume requirements in line with the principles of green analytical chemistry. For trace analysis in particular, the sorption-based methods have proved the best option enabling direct microextraction, mainly volatile and semi-volatile compounds, in almost all type of aqueous matrices.

Bar adsorptive microextraction (BAμE) was recently introduced[37] and offers to the operator the possibility to choose the most convenient sorbent phase (polymers or ACs), according to the chemical characteristics of the target analytes [36]. This analytical approach is an alternative by simplification, miniaturization and high-throughput to enhance selectivity and sensitivity, in particular for trace analysis. Furthermore, this new technique uses negligible amount of solvents and low sample volumes [36].This enrichment technique simultaneously combines microextraction and concentration of the analytes, operating under the floating sampling technology, in a one single step. On the other hand, reduces handling, the overall time required for sample preparation and is suitable to be combined with the high sensitivity of modern analytical instrumentation. Because all these reasons, BAμE could be a good alternative to monitor traces of nitrogen compounds in commercial diesel.

4.1 Application as novel sorbent phases for BAμE

Production and improper disposal of agro-industrial waste from manufacturing processes are detrimental to sustainable development of natural resources and energy. Due to the amount of waste and harmful action on the environment, the fate of the waste originated in agro-industrial activities is a major concern of public managers, who seek a sustainable solution. The use of this waste is a desire not yet reached by Brazil, so it is necessary to search for alternatives to minimize this problem. Pyrolysis is an economical alternative to the use of agro-industrial waste to obtain products with higher added value. The production of biochar (pyrolysis carbonaceous residue) can be used as adsorbents source by minimizing the amount of waste released in the environment and consequently improving the environmental quality. In the process of pyrolysis of rice husk is generated a lot biochar for which it is necessary to use modern technology to reduce the volume, characterization, processing and utilization in order to add value and optimize the production process. The use of rice husk biochar as an alternative adsorbent is a possibility of proper disposal and environmentally friendly for this material. From the analytical point of view, the use of this material means a breakthrough in terms of methods of preparing samples absolutely environmental friendly.

Agro-industrial wastes have been used as precursors to prepare ACs and are getting more important due to their low costs, high apparent specific surface areas and good performance when tested as adsorbents for organic compounds. Recently, there is an increased emphasis on the topic of green chemistry, which is defined as the design of chemical products and processes that reduce or eliminate the use and generation of hazardous substances. The potentialities of rice husk ACs in the removal of nitrogen pollutants from diesel, an extremely complex matrix containing numerous organic constituents, in the case of the present study, was observed by microextraction technique involving the use of devices containing the produced alternative adsorbent and operated using the floating sampling technology [8] facilitating the identification, concentration and isolation of target compounds. The use of viable alternative systems which take into consideration the principles of Green Analytical Chemistry, using small amounts of organic solvents few steps and capacity extracting multiple samples simultaneously, is desirable to methods of preparing samples used in analytical chemistry.

The efficiency of BAμE can be substantially affected by the complexity of the matrices involved, since potential interferences with the actual matrix constituents may influence the yield of recovery. One way to minimize potential effects matrix is by using the standard addition method. This approach provides the level of accuracy required for trace analysis in a variety of systems. Another way to minimize the effects of matrix and co-elutions problems is the use of advanced analytical techniques such as GC×GC, showing a significant increase in chromatographic resolution, which is crucial for the identification and quantification of analytes in complex mixtures.

To the best of our knowledge, a systematic study involving the production, characterization and application of selective bio-adsorbent for analytical microextraction nitrogen compounds of interest in diesel using products derived from rice husk pyrolysis has not been reported before. In addition, the AC-RH may be used as a low-cost adsorbent, which is a kind of sorbent phase that offers many economic and environmental advantages compared to traditional sorbents. Furthermore, this approach is the first ever report of BAμE applied in organic matrix and showed great ability to selectivity and sensitivity gain compared with conventional microextraction technique which was carried out in aqueous solution until the time.

4.2 Detection and quantification of Carbazole in Diesel by BAμE/GC×GC-qMS

Nitrogen compounds in diesel fuel have typically been studied using GC with several specific detectors, including nitrogen and phosphorus (NPD) [35], nitrogen chemiluminescence (NCD) [53] and mass spectrometer (MS) [34] detectors. However, the complexity of diesel matrices and the limited peak capacity of GC columns appear, many times, as a drawback for the identification of nitrogen compounds during analytical separation, due to co-elution with interferences [35]. Consequently, unresolved peaks and low sensitivity are observed and a separation is required prior to the detection step for detailed molecular analysis of nitrogen compounds in diesel samples. Thus, the extraction and concentration of nitrogen compounds is either performed by liquid/liquid extraction (LLE) [51] or liquid/solid extraction (LSE) [53]. However, these procedures are time consuming and neither selective nor quantitative. Miniaturized analytical systems are effective alternatives for microextraction with little solvent consumption, reproductive, robust and reduced time.

One way to improve peak capacity of conventional separation techniques is to add another separation dimension. Therefore, comprehensive two-dimensional gas chromatography (GC×GC) is a promising alternative to the limited resolution of conventional separation techniques. In GC×GC, the entire sample is submitted to two online GC separations involving different properties of analytes. Two columns connected in series through a cryogenic modulator that traps, focuses and reinjects the effluent from the first column into the second one. The orthogonality of the separation is achieved by using columns of different selectivity, from data combining boiling point (related to the carbon atom number) and the polarity (related to the chemical structure) when using a classical combination of non-polar polar columns. Indeed, owing to a higher resolution power and an enhanced sensitivity [35], comprehensive two-dimensional gas chromatography offers unsurpassed possibilities for the characterization of nitrogen compounds in diesel. Several studies have employed GC×GC for the analysis of nitrogen compounds using specific detectors[35, 50-52]. However, the use of one selective detector needs a preliminary and not exhaustive activity of assignment of the peaks on the basis on retention times of specific standard solutions or with the help of complementary analyses in the presence of mass spectrometer detector for analysis of the real sample. Regarding to the mass detectors, same studies have shown the consolidation of the fast quadrupole MS system for operation in the rapid scanning mode, allowing high data acquisition rates with values of up to 50Hz [45, 54-56]. In order to solve the above problems, we developed a new method of the extraction and analysis using BAµE and GC×GC coupled to a quadrupole mass spectrometer (BAµE/GC×GC-qMS) representing the state of the art organic chemical analysis of complex matrices.

In this contribution was produced, characterized and applied as adsorbent AC from the rice husk pyrolysis for analytical microextraction of carbazole in commercial diesel and the results were analyzed by GC×GC-qMS to check the applicability of this new method to extraction and to confirm its potential to quantitatively analyze diesel samples. Standard addition method was employed to reduce possible matrix interferences from the diesel sample. The diesel was fortified with carbazole standardto produce the corresponding spiking levels (0.0125, 0.025 and 0.1 mg L^{-1}) of carbazole. Blank assays were also evaluated without spiking to ensure minimum or absence of matrix effects. The quantification (mgL^{-1}) of carbazole was performed by measuring of the peak volume for fortified component in the 2D diagram and plotting the measured analytical signal against concentrations of the standard added. The unknown concentration of analyte in the sample was then determined by extrapolating the standard addition curve to the zero response value. Due to the low concentration of nitrogen compounds in diesel fuel sample, the quantification of carbazole is very difficult without the use of the standard addition method. Figure 6 shows the color diagram by GC×GC-qMS for the commercial diesel fortified, as can be seen in this figure the use of GC×GC allowed the separation of the carbazole from all the other compounds along the y axis**.** The problem of matrix effect was not observed for the real sample before standards addition, where the peak is more clearly identified. The average of data points per peak was 18, which is an appropriate value for quantitative analyses, literature reference values were 15 to 20 data points [57].Results obtained showed good linearity, with r^2 higher than 0.9984and values of LOD and the LOQ were 0.45 µg L^{-1} and 1.37 µg L^{-1} respectively. Relative standard deviation (RSD) was less than 3.5% in the accuracy of analysis. For reproducibility, the RSD did not reach 6%. Results obtained for the carbazole showed average recoveries of 91.0 %, which confirmed the great availability of the sites created from the chemical activation.

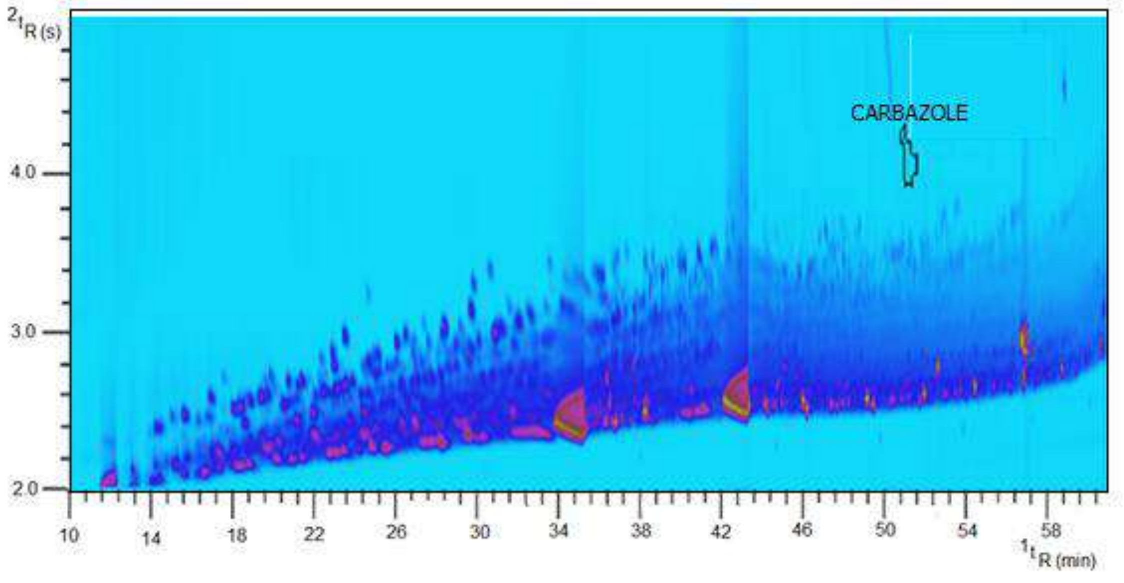

FIGURE 6. EXAMPLE OF A TWO-DIMENSIONAL CHROMATOGRAM FROM A COMMERCIAL DIESEL SPIKED WITH CARBAZOLE (STANDARD ADDITION, 0.1 mg L^{-1}), OBTAINED BY BAµE/GC×GC-qMS, UNDER STANDARD EXPERIMENTAL CONDITIONS.

Therefore, the recovery results indicate that it is possible to add value to biochar from the rice husk pyrolysis to produce AC by chemical activation with K_2CO_3 preparing materials with appropriated characteristics to be used in carbazole removal in diesel oil. Whereas, neutral nitrogen species such as carbazoles, which are of low reactivity, tend to stay through the whole stage of deep hydrodesulfurization [58]. In general, the removal of nitrogen compounds from middle distillates by solid adsorbents (silica gel, alumina, AC, ion exchanged polymers) improves the reaction rate of the sulfur compounds through HDS process as stated by several authors [59-61].

V. CONCLUSIONS

Rice husk biochar may be converted into a cost-effective adsorbent to remove compounds with the use of chemical activation, being a good alternative to be used in adsorption-based technologies. Considering there is an urgent need to explore new applications of the rice husk, an important agro-industrial waste in South Brazil, and solve the environmental problems, both in relation to use of agricultural waste such as emissions of nitrogen from fuel, this study showed good answers to these challenges.

In the present study, a microextraction technique and a sensitive method using BAµE-LD/GC×GC-qMS were applied for the first time for trace analysis of carbazole in diesel oil sample. The potential for the carbazole removal in diesel oil of low-cost ACs, obtained from rice husk pyrolysis and prepared by chemical activation was also investigated. Overall results indicate that it is possible to add value to thesebiochars. Besides the appearance of the micropores, which is generally promoted by the chemical activation, the present values of surface areas are much larger than those obtained after silica removal during the washings. Therefore, it is noteworthy that the results of this study point to the potential of producing high quality AC with surface area 1850 m^2 g^{-1}, with satisfactory adsorbent proprieties, using rice husk as starting material and K_2CO_3 as activating agent.

The sorbent tested demonstrated a good stability, robustness and microextraction efficiency. Furthermore, the enhanced peak capacity of comprehensive two-dimensional GC and the great identification capacity of mass spectrometry allow in the same analysis the accurate identification and quantification of carbazole. Therefore, this is a valid analytical technique with good selectivity and high sensitivity for the detection of compounds with very strong interference from the matrix.For the first time, a cost-effective and environmentally friendly method for extraction and detection of nitrogen compound in commercial diesel is reported.

ACKNOWLEDGEMENTS

The authors wish to thank CAPES and CNPq(Brazil; nº401352/2014-5), as well as Fundação para a Ciência e a Tecnologia (Portugal; UID/MULTI/00612/2013, SFRH/BD/107892/2015) for financial support.

REFERENCES

[1] S. Nanda, A.K. Dalai, F. Berruti, J.A. Kozinski, "Biochar as an Exceptional Bioresource for Energy, Agronomy, Carbon Sequestration, Activated Carbon and Specialty Materials," Waste Biomass Valor, vol. 7, pp. 201-235, 2016.

[2] W. Kwapinski, C.M.P. Byrne, E. Kryachko, P. Wolfram, C. Adley, J. J. Leahy, E.H. Novotny, M.H.B. Haye, "Biochar from Biomass and Waste," Waste Biomass Valor, vol. 1, pp. 177–189, 2010.

[3] H. Deng, G.X. Li, H.B.Yang, J.P. Tang, J.Y. Tang, "Preparation of activated carbons from cotton stalk by microwave assisted KOH and K_2CO_3 activation," Chem. Eng. J., vol. 163, pp. 373–381, 2010.

[4] H. Deng, G.L. Zhang, X.L. Xu, G.H. Tao, J.L. Dai, "Optimization of preparation of activated carbon from cotton stalk by microwave assisted phosphoric acid chemical activation," J. Hazard. Mater., vol. 182, pp. 217–224, 2010.

[5] W. Li, L.B. Zhang, J.H. Peng, N. Li, X.Y. Zhu, "Preparation of high surface area activated carbons from tobacco stems with K_2CO_3 activation using microwave radiation," Ind. Crop. Prod., vol. 27, pp. 341–347, 2008.

[6] S.S. Lv, X.G. Chen, Y. Ye, S.H. Yin, J.P. Cheng, M.S. Xia, "Rice hull/$MnFe_2O_4$ composite: preparation, characterization and its rapid microwave-assisted COD removal for organic wastewater," J. Hazard. Mater., vol. 171, pp. 634–639, 2009.

[7] A.S. Mestre, J. Pires, J.M.F. Nogueira, J.B. Parra, A.P. Carvalho, C.O. Ania, "Waste-derived activated carbons for removal of ibuprofen from solution: Role of surface chemistry and pore structure," Bioresour. Technol., vol. 100, pp. 1720–1726, 2009.

[8] Q.S. Liu, T. Zheng, P. Wang, L. Guo, "Preparation and characterization of activated carbon from bamboo by microwave-induced phosphoric acid activation," Ind. Crop. Prod., vol. 31, pp. 233–238, 2010.

[9] M. Auta, B.H. Hameed, "Preparation of waste tea activated carbon using potassium acetate as an activating agent for adsorption of Acid Blue 25 dye," Chem. Eng. J., vol. 171, pp. 502–509, 2011.

[10] E. Yagmur, M. Ozmak, Z. Aktas, "A novel method for production of activated carbon from waste tea by chemical activation with microwave energy," Fuel, vol. 87, pp. 3278–3285, 2008.

[11] K.B. Yang, J.H. Peng, C. Srinivasakannan, L.B. Zhang, H.Y. Xia, X.H. Duan, "Preparation of high surface area activated carbon from coconut shells using microwave heating," Bioresour. Technol., vol. 101, pp. 6163–6169, 2010.

[12] K.Y. Foo, B.H. Hameed, "Microwave-assisted preparation of oil palm fiber activated carbon for methylene blue adsorption," Chem. Eng. J., vol. 166, pp. 792–795, 2011.

[13] T.C. Chandra, M.M. Mirna, Y. Sudaryanto, S. Ismadji, "Adsorption of basic dye onto activated carbon prepared from durian shell: studies of adsorption equilibrium and kinetics," Chem. Eng. J., vol. 127, pp. 121–129, 2007.

[14] T.H. Wang, S.X. Tan, C.H. Liang, "Preparation and characterization of activated carbon from wood via microwave-induced ZnCl2 activation," Carbon, vol. 47, pp. 1860–1883, 2009.

[15] A.S. Mestre, C. Freire, J. Pires, A.P. Carvalho, M.L. Pinto, "High performance microspherical activated carbons for methane storage and landfill gas or biogas upgrade," J. Mater. Chem. A, vol. 2, pp. 15337–15344, 2014.

[16] A. Alvarez, G. Lopez, M. Amutio, J. Bilbao, M. Olazar, "Bio-oil production from rice husk fast pyrolysis in a conical spouted bed reactor," Fuel, vol. 128, pp. 162–169, 2014.

[17] C.H. Yun, Y.H. Park, G.H. Oh, C.R. Park, "Contribution of inorganic components in precursors to porosity evolution in biomass-based porous carbons," Carbon, vol. 41, pp. 2009–2012, 2003.

[18] D. An, Y. Guo, B. Zou, Y. Zhu, Z. Wang, "A study on the consecutive preparation of silica powders and active carbon from rice husk ash," Biomass Bioenergy, vol. 35, pp. 1227–1234, 2011.

[19] Y. Guo, S. Yang, K. Yu, J. Zhao, Z. Wang, H. Xu, "The preparation and mechanism studies of rice husk based porous carbon," Mater. Chem. Phys., vol. 74, pp. 320–323, 2002.

[20] S.A. Uzunova, I.M. Uzunov, S.V. Vassilev, A.K. Alexandrova, S.G. Staykov, D.B. Angelova, "Preparation of low-ash-content porous carbonaceous material from rice husks," Bulgarian Chem. Commun., vol. 42, pp. 130–137, 2010.

[21] Z. Yu, X. Meng, N. Liu, L. Shi, "A novel disposal approach of deactivated resin catalyst for methyl tert-butyl ether synthesis: Preparation of low-cost activated carbons with remarkable performance on dibenzothiophene adsorption," Fuel, vol. 207, pp. 47–55, 2017.

[22] T. Budinova, E. Ekinci, F. Yardim, A. Grimm, E. Björnbom, V. Minkova, M. Goranova, "Characterization and application of activated carbon produced by H_3PO_4 and water vapor activation," Fuel Process. Technol., vol. 87, pp. 899–905, 2006.

[23] X. Li, Y. Zuo, Y. Zhang, Y. Fu, Q. Guo, "In situ preparation of K_2CO_3 supported Kraft lignin activated carbon as solid base catalyst for biodiesel production," Fuel, vol. 113, pp. 435–442, 2013.

[24] D. Adinata, W.M.A. Wan Daud, M.K. Aroua, "Preparation and characterization of activated carbon from palm shell by chemical activation with K_2CO_3," Bioresour. Technol., vol. 98, pp. 145–149, 2007.

[25] M. Galhetas, A.S. Mestre, M.L. Pinto, I. Gulyurtlu, H. Lopes, A.P. Carvalho, "Chars from gasification of coal and pine activated with K_2CO_3: Acetaminophen and caffeine adsorption from aqueous solutions," J. Colloid Interface Sci., vol. 433, pp. 94–103, 2014.

[26] K.Y. Foo, B.H. Hameed, "Utilization of rice husks as a feedstock for preparation of activated carbon by microwave induced KOH and K_2CO_3 activation," Bioresour. Technol., vol. 102, pp. 9814–9817, 2011.

[27] K.Y. Foo, B.H. Hameed, "Microwave-assisted preparation and adsorption performance of activated carbon from biodiesel industry solid reside: influence of operational parameters," Bioresour. Technol., vol. 103, pp. 398–404, 2012.

[28] K.Y. Foo, B.H. Hameed, "Preparation, characterization and evaluation of adsorptive properties of orange peel based activated carbon via microwave induced K_2CO_3 activation," Bioresour. Technol., vol. 104, pp. 679–686, 2012.

[29] I.I. Gurten, M. Ozmak, E. Yagmur, Z. Aktas, "Preparation and characterisation of activated carbon from waste tea using K_2CO_3," Biomass Bioenergy, vol. 37, pp. 78–81, 2012.

[30] A. Zhou, X. Ma, C. Song, "Liquid-phase adsorption of multi-ring thiophenic sulfur compounds on carbon materials with different surface properties," J. Phys. Chem. B, vol. 110, pp. 4699–4707, 2006.

[31] M. Almarri, X. Ma, C. Song, "Selective adsorption for removal of nitrogen compounds from liquid hydrocarbon streams over carbon- and alumina-based adsorbents," Ind. Eng. Chem. Res., vol. 48, pp. 951–960, 2009.

[32] M. Almarri, X. Ma, C. Song, "Role of surface oxygen-containing functional groups in liquid-phase adsorption of nitrogen compounds on carbon-based adsorbents," Energy Fuels, vol. 23, pp. 3940-3947, 2009.

[33] G.C. Laredo, J.A. De los Reyes, J.L. Cano, J.J. Castillo, "Inhibition effects of nitrogen compounds on the hydrodesulfurization of dibenzothiophene," Applied Catalysis A: General, vol. 207, pp. 103–112, 2001.

[34] E.C. Oliveira, M.C.C. Campos, A.S.A. Lopes, M.G.R. Vale, E.B. Caramão, "Ion-exchange resins in the isolation of nitrogen compounds from petroleum residues," J. Chromatogr. A, vol. 1027, pp. 171–177, 2004.

[35] C. von Mühlen, E.C. Oliveira, P.D. Morrison, C.A. Zini, E.B. Caramão, P.J. Marriott, "Qualitative and quantitative study of nitrogen-containing compounds in heavy gas oil using comprehensive two-dimensional gas chromatography with nitrogen phosphorus detection," J. Sep. Sci., vol. 30, pp. 3223–3232, 2007.

[36] J.M.F. Nogueira, "Stir-bar sorptive extraction – 15 years making sample preparation more environment friendly," Trend Anal Chem., vol. 71, pp. 214–223, 2015.

[37] N.R. Neng, A.R.M. Silva, J.M.F. Nogueira, "Adsorptive micro-extraction techniques—Novel analytical tools for trace levels of polar solutes in aqueous media," J Chromatogr. A, vol. 1217, pp. 7303-7310, 2010.

[38] S.M. Anisuzzaman, D. Krishnaiah, S. Abang, G.M. Labadin, "Adsorptive denitrogenation of fuel by oil palm shells as low cost absorbents," J. Applied Sciences, vol. 14, pp. 3156–3161, 2014.

[39] M.S.A. Moraes, F. Georges, S.R. Almeida, F.C. Damasceno, G.P.S. Maciel, C.A. Zini, R.A. Jacques, E.B. Caramão, "Analysis of products from pyrolysis of Brazilian sugar cane straw," Fuel Process. Technol., vol. 101, pp. 35−43, 2012.

[40] G. Horvàth, K. Kawazoe, "Method for the calculation of effective pore size distribution in molecular sieve carbon," J Chem Engineer Japan, vol. 16, pp. 470−475, 1983.

[41] J. Landers, G.Y. Gor, A.V. Neimark, "Density functional theory methods for characterization of porous materials," Colloids Surf. A, vol. 437, pp. 3−32, 2013.

[42] A.S. Mestre, J. Pires, J.M.F. Nogueira, A.P. Carvalho, "Activated carbons for the adsorption of ibuprofen," Carbon, vol. 45, pp. 1979–1988, 2007.

[43] N.R. Neng, A.S. Mestre, A.P. Carvalho, J.M.F. Nogueira, "Powdered activated carbons as effective phases for bar adsorptive micro-extraction (BAμE) to monitor levels of triazinic herbicides in environmental water matrices," Talanta, vol. 83, pp.1643–1649, 2011.

[44] M. Thommes, K. Kaneko, A.V. Neimark, P.J. Olivier, F. Rodriguez-Reinoso, J. Rouquerol, K.S.W. Sing, "Physisorption of gases, with special reference to the evaluation of surface area and pore size distribution (IUPAC Technical Report)," Pure Appl. Chem., vol. 87, pp. 1051–1069, 2015.

[45] M. Adahchour, M. Brandt, H. Baier, R.J.J. Vreuls, A.M. Batenburg, U.A.T. Brinkman, "Cromprehensive two-dimensional gas chromatography coupled to a rapid-scanning quadrupole mass spectrometer: principles and applications," J. Chromatogr. A, vol. 1067, pp 245–254, 2005.

[46] F.C Wu, R.L Tseng , C.C Hu, "Comparisons of pore properties and adsorption performance of KOH-activated and steam-activated carbons," Micropor. Mesopor. Mater, vol. 80, pp. 99–106, 2005.

[47] D. Dias,N. Lapa, M. Bernardo, D. Godinho, I. Fonseca, M. Miranda, F. Pinto, F. Lemos, "Properties of chars from the gasification and pyrolysis of rice waste streams towards their valorisation as adsorbent material," Waste Management, vol. 65, pp. 186–194, 2017.

[48] B-J. Skrifvars, P. Yrjas, J. Kinni, P. Siefen, M. Hupa, "The fouling behavior of rice husk ash in fluidized-bed combustion. 1. Fuel characteristics," Energy Fuel, vol. 19, pp. 1503–1511, 2005.

[49] L.L. Okumura, N.R. Stradiotto, "Simultaneous determination of neutral nitrogen compounds in gasoline and diesel by differential pulse voltammetry," Talanta, vol. 72, pp. 1106–1113, 2007.

[50] K.Lissitsyna, S. Huertas, L.C. Quintero, L.M. Polo, "Novel simple method for quantitation of nitrogen compounds in middle distillates using solid phase extraction and comprehensive two-dimensional gas chromatography," Fuel, vol. 104, pp.752–757, 2013.

[51] F. Adam, F. Bertoncini, N. Brodusch, E. Durand, D. Thièbaut, D. Espinat, M.C. Hennion, "New benchmark for basic and neutral nitrogen compounds speciation in middle distillates using comprehensive two-dimensional gas chromatography," J. Chromatogr. A, vol. 1148, pp. 55–64, 2007.

[52] F. Adam, F. Bertoncini, C. Dartiguelongue, K. Marchand, D. Thièbaut, M.C. Hennion, "Comprehensive two-dimensional gas chromatography for basic and neutral nitrogen speciation in middle distillates," Fuel, vol. 88, pp. 938–946, 2009.

[53] Y. Yongtan, "Determination of nitrogen compounds in catalytic diesel oil using gas chromatography," Chin J Chromatogr A, vol. 26, pp. 478–483, 2008.

[54] G. Purcaro, P.Q. Tranchida, C. Ragonese, L. Conte, P. Dugo, G. Dugo, L. Mondello, "Evaluation of a Rapid-Scanning Quadrupole Mass Spectrometer in an Apolar × Ionic-Liquid Comprehensive Two-Dimensional Gas Chromatography System," Anal. Chem., vol. 82, pp. 8583–8590, 2010.

[55] C. Cordero, C. Bicchi, D. Joulain, P. Rubiolo, "Identification, quantification and method validation for the analysis of suspected allergens in fragances by comprehensive two-dimensional gas chromatography coupled with quadrupole mass spectrometry and with flame ionization detection," J. Chromatogr. A, vol. 1150, pp. 37–49, 2007.

[56] P.Q. Tranchida, F.A Franchina, M. Zoccali, S. Panto, D. Sciarrone, P. Dugo, L. Mondello, "Untargeted and targeted comprehensive two-dimensional GC analysis using a novel unified high speed triple quadrupole mass," J. Chromatogr. A, vol. 1278, pp. 153–159, 2013.

[57] N. Dyson, "Peak distortion, data sampling errors and the integrator in the measurement of very narrow chromatographic peaks," J Chromatogr. A, vol. 842, pp. 321–340, 1999.

[58] A. Szymanska, M. Lewandowski, C. Sayag, G.D. Mariadassou, "Kinetic study of the hydrodenitrogenation of carbazole over bulk molybdenum carbide," J. Catal., vol. 218, pp. 24–31, 2003.

[59] H. Yang, J. Chen, C. Fairbridge, Y. Briker, Y. Jie Zhu, Z. Ring, "Inhibition of nitrogen compounds on the hydrodesulfurization of substituted dibenzothiophenes in light cycle oil," Fuel Process Technol, vol. 85, pp. 1415–1429, 2004.

[60] Y. Sano, K. Choi, Y. Korai, I. Mochida, "Adsorptive removal of sulfur and nitrogen species from a straight run gas oil over activated carbons for its deep HDS," Applied Catalysis B: Environmental, vol. 49, pp. 219–225, 2004.

[61] M. Sau, K. Basak, U. Manna, M. Santra, R.P. Verma, "Effects of organic nitrogen compounds on hydrotreating and hydrocracking reactions," Catalysis Today, vol. 109, pp. 112–119, 2005.

Research on the Unsteady Discharge Flow of Dry Chemical Powder Tank

HeeGeun Song[1], Junhyo Kim[2], Jungpil Noh[3], Sunchul Huh[4], Byeongkeun Choi[5], Hanshik Chung[6], *Hyomin Jeong[7]

[1]Department of Energy and Mechanical Engineering, Gyeongsang National University, Cheondaegukchi-Gil 38, Tongyeong, Gyeongnam, 650-160, South Korea

[2]Department of Marine Engineering, Mokpo National maritime University, 61 dorim-ri, 1666 Yeongsan-ro, Cheonggye-myeon, Muan-gun, Jeonnam, South Korea

[3,4,5,6,7]Department of Energy and Mechanical Engineering, Gyeongsang National University·Institute of Marine Industry, Cheondaegukchi-Gil 38, Tongyeong, Gyeongnam, 650-160, South Korea

***Abstract*— *In this study, we investigated the activation of powders by the supply of N_2 gas in the dry chemical powder tanks. In this study, we investigated the effect of N_2 gas on the activation of dry chemical powder ($KHCO_3$) in Dry chemical Powder Tank, We studied how dry chemical powder ($KHCO_3$) is activated according to the number of nozzles in the tank. 170 kg, and 3000 kg models, the number of nozzles was 4, 8. We gave the points to confirm the activation of the powder. This study describes the optimal conditions for activation depending on the type of dry chemical powder tank and the number of nozzles.*

Keywords*— *Powder activation, Discharge Flow, Dry Chemical Powder Tank, nitrogen gas.

I. INTRODUCTION

According to the "Marine Accident Statistics" at the Maritime Tribunal, the number of ship fires and explosions in the Republic of Korea is 465 cases (2011 ~ 2015) for 5 years, accounting for about 6% of all marine casualties. Among them, the oil tanker fire and explosion accident accounted for 8% of the total of 256 cases [1]. Generally, half of ship fire accidents are reported to occur in the engine room. In case of an accident, it is difficult to receive support for fire suppression from the land, and therefore, many lives and property are lost [2].

The Powder fire extinguishing system is a fire extinguishing system that suppresses fire which is less effective by water extinguishing method such as sprinkling water or scattered water and combustible gas or oil with the risk of fire spreading. The powder fire extinguishing system is a device that injects N_2 gas filled in N_2 cylinder into powder tank, push powder fire extinguishing agent into N_2 gas pressure in powder tank and spray fire extinguishing agent in fire area. The principle of extinguishing the powder absorbs heat from the fire by the rapid endothermic reaction of the powder which is released in the place where the fire occurs. As the volume of the non-combustible powder expands, the powder covers the fire and blocks the supply of oxygen, thereby suppressing the fire.

The powder fire extinguishing system is suitable for the extinguishing of large-scale flammable gas fires and is suitable for the fire extinguishing of liquefied natural gas carrier (LNGC), liquefied petroleum gas carrier (LPGC), liquefied natural gas - floating production storage facility (FLNG)), Drillships, and gas and marine plant facilities. Powder in Dry Powder Tank mixed well with N_2 gas in case of fire suppression needs to be maintained after optimal activation.

In this study, we have investigated the activation of powders in accordance with the supply of N_2 gas in the dry powder tank and studied how the powder is activated according to the number of nozzles in the dry powder tank.

II. EQUATIONS AND MATHEMATICS

The volume fraction equation, turbulent kinetic energy and flow equation applied to the calculation are as follows[3-5].

The volume fraction equation is as follows.

$$\frac{\alpha_q^{n+1}\rho_q^{n+1}-\alpha_q^{n}\rho_q^{n}}{\Delta t}V+\sum_f\left(\rho_q^{n+1}U_f^{n+1}\alpha_{q,f}^{n+1}\right)=\left[s_{\alpha_q}+\sum_{p=1}^{n}\left(\dot{m}_{pq}-\dot{m}_{qp}\right)\right]V \tag{1}$$

The turbulent kinetic energy k is as follows.

$$\frac{\partial(\rho k)}{\partial t}+\frac{\partial(\rho k u_i)}{\partial x_i}=\frac{\partial}{\partial x_j}\left[\frac{\mu_t}{\sigma_k}\frac{\partial k}{\partial x_j}\right]+2\mu_t E_{ij}E_{ij}-\rho\epsilon \tag{2}$$

III. CALCULATION CONDITION

3.1 Preparation condition

The fluid analysis and the activation analysis of the powder were carried out for 170 kg and 3000 kg dry powder tanks. The number of nozzles was set to 4 and 8 for each model. The inlet consists of two pipes, and the outlet consists of one pipe (Figure 1). Two thin pipes come in with nitrogen gas and nozzles at their ends. And the activated powder is discharged into a thick pipe.

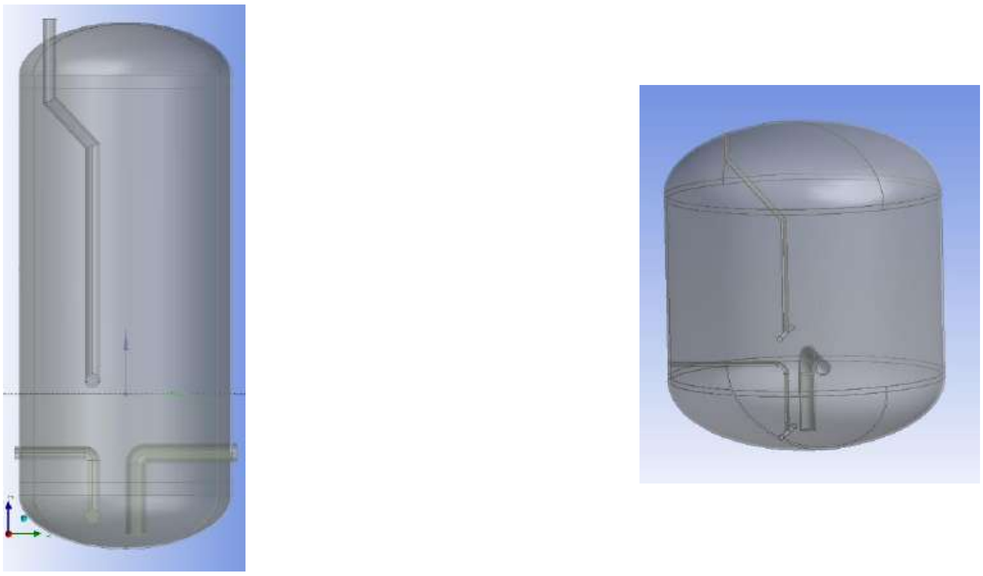

FIG 1. THE IMAGE OF DRY POWDER TANKS (170, 3000kg)

3.2 Calculation condition

Before calculation, boundary condition was set as shown in Table 1. At first, type of fluid inlet was set as Pressure inlet and the value of the fluid pressure was set at 15.7 bar.abs. The properties of the powder are shown in Table 2

TABLE 1
CASES OF THE POWDER TANK

	Powder Tank	Nozzle	Outlet
Case 1	170kg	4	None
Case 2	170kg	8	None
Case 3	3000kg	4	None
Case 4	3000kg	8	None

TABLE 2
PROPERTIES OF THE POWDER

Items	Requirements
Main Components	Potassium Bicarbonate
Type	Pure substance
Group	Particle Solid
Density	0.95 g/cm^3
Particle distribution	<40μm : 55% 40 – 63μm : 20 ± 8% 63 - 125μm : 20 ± 8% >125μm : 5 ± 5%

IV. RESULT AND DISCUSSION

4.1 Result

We set the points as shown in Figure 2 to confirm the activation of the powder. We set 10 points for 170 kg and 8 points for 3000 kg. In this study, we proceed to analyze for 20 seconds to see that the powder is activated. And it was interpreted as a condition without outlet [6].

FIG 2. SET THE POINTS OF DRY POWDER TANK

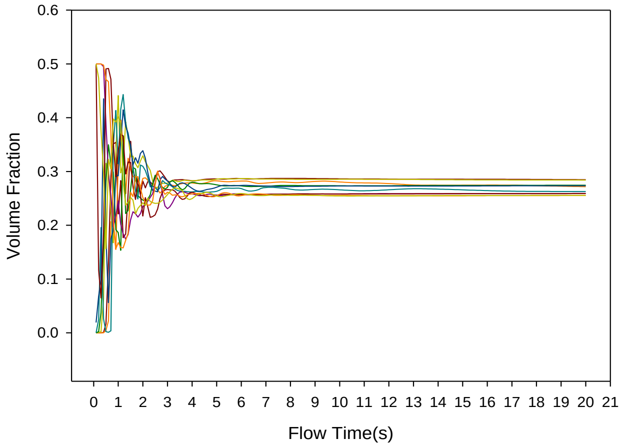

FIG 3. POWDER VOLUME FRACTION OF CASE 1

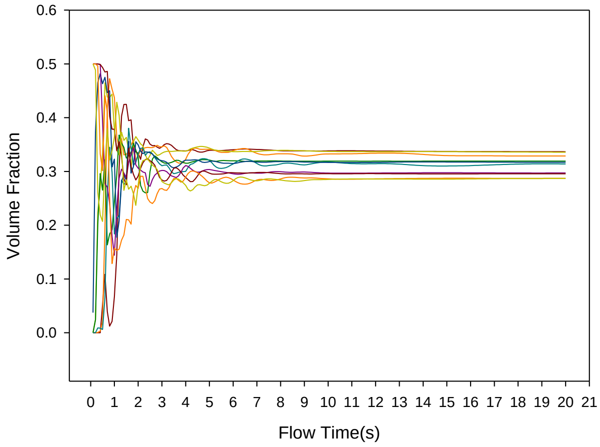

FIG 4. POWDER VOLUME FRACTION OF CASE 2

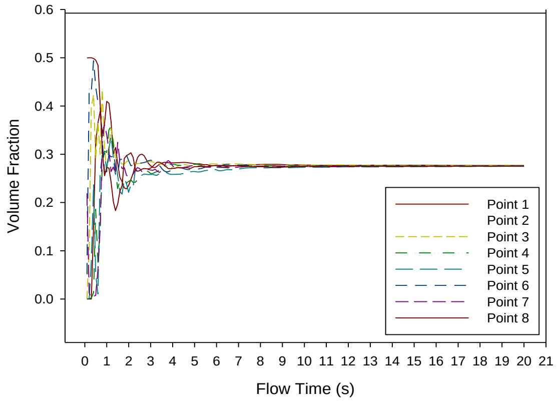

FIG 5. POWDER VOLUME FRACTION OF CASE 3

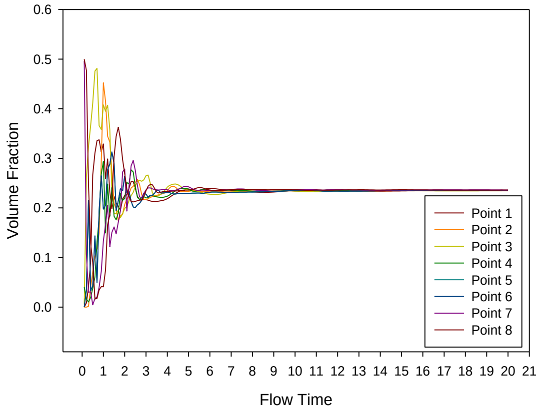

FIG 6. POWDER VOLUME FRACTION OF CASE 4

Figure 3-6 shows the powder activation in case 1-4.

4.2 Discussion

When nitrogen gas was pressurized in a 170 kg-Dry powder tank for 20 seconds, some mixing appeared but it was not completely mixed. In the 170kg-Dry powder tank, when the number of nozzles is 4, the dispersion of powder is better.

It was confirmed that when the nitrogen gas was pressurized in the 3000 kg-Dry powder tank for 20 seconds, the dispersion of powder was uniform. In the 3000 kg-Dry powder tank, when the number of nozzles is 8, the dispersion of powder is better.

As a result, it was confirmed that the powder was well dispersed in case of 3000 kg, but in case of 170kg, both cases showed insufficient activation. Therefore, we reanalyzed the powder to activate the 170 kg model. The value of the fluid pressure was set at 16.7, 17.7, 18.7 bar.abs (Table 3).

TABLE 3
CASES OF THE POWDER TANK

	Powder Tank	Nozzle	Pressure (bar.abs)
Case 5	170kg	4	16.7
Case 6	170kg	4	17.7
Case 7	170kg	4	18.7
Case 8	170kg	8	16.7
Case 9	170kg	8	17.7
Case 10	170kg	8	18.7

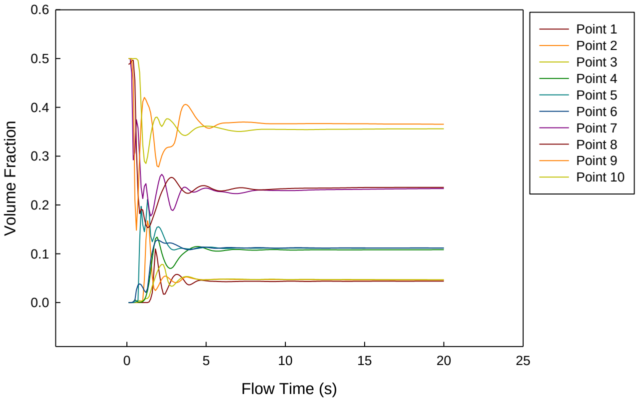

FIG 7. POWDER VOLUME FRACTION OF CASE 5

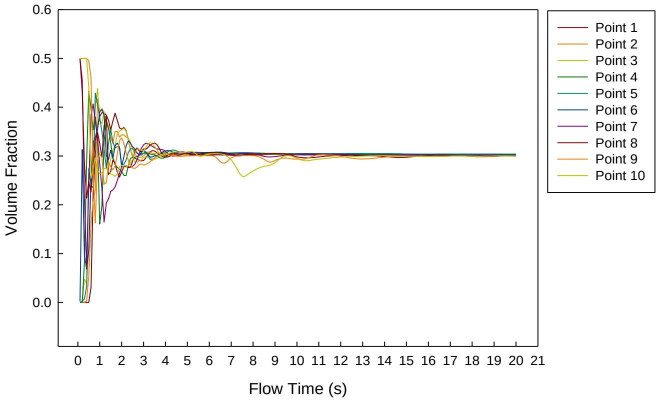

FIG 8. POWDER VOLUME FRACTION OF CASE 6

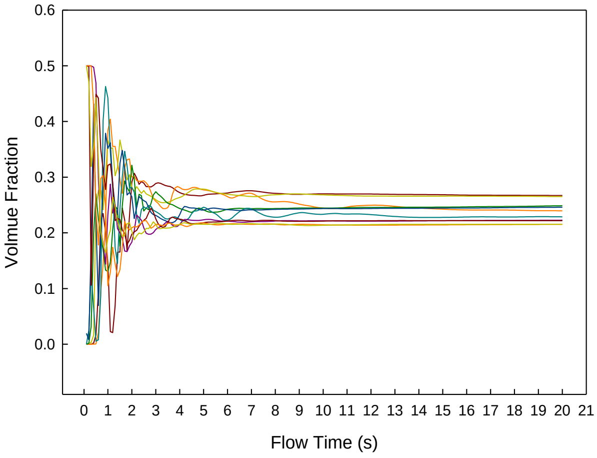

FIG 9. POWDER VOLUME FRACTION OF CASE 7

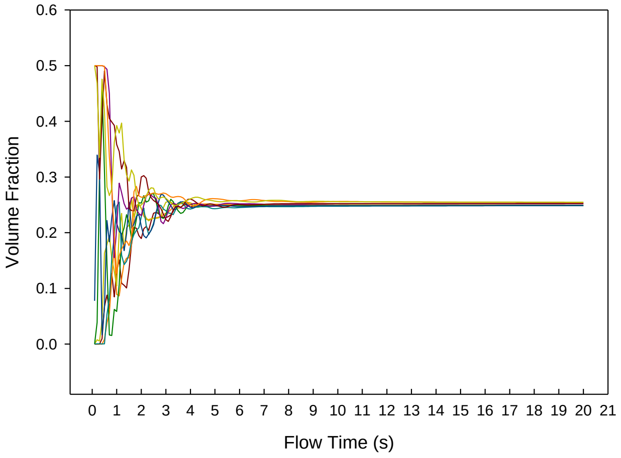

FIG 10. POWDER VOLUME FRACTION OF CASE 8

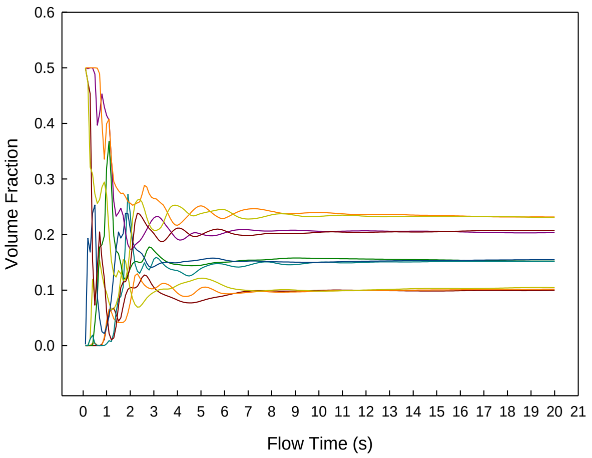

FIG 11. POWDER VOLUME FRACTION OF CASE 9

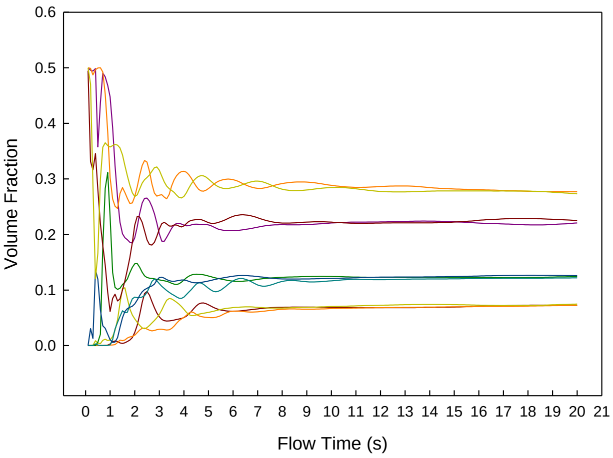

FIG 12. POWDER VOLUME FRACTION OF CASE 10

As a result of analysis, it was confirmed that powder was activated at 17.7 bar.abs when the number of nozzles was 4 when more pressure was applied. When the number of nozzles was 8, the powder was activated well at 16.7 bar.abs. In the case of 170kg-Dry powder tank, the number of nozzles was 8 and the highest powder activation was observed at 16.7 bar.abs.

V. CONCLUSION

In this study, we investigated the activation of powders in dry powder tanks. The effect of the number of nozzles and pressure on the powder is summarized as follows. It was confirmed that when the nitrogen gas was pressurized in the 3000kg-Dry powder tank for 20 seconds, the dispersion of powder was uniform. In the 3000kg-Dry powder tank, when the number of nozzles is 8, the dispersion of powder is better. In the case of 170kg model, it was confirmed that there is a pressure to activate the powder according to the number of nozzles. When the number of nozzles was 4 and 8, it was activated well at 17.7 bar and 16.7 bar. It was defined that the state of activation depends on the shape of powder tank of 170kg and 3000kg. Therefore, the more the shape of the tank is closer to the ellipse, the better the activation is.

ACKNOWLEDGEMENTS

This research was supported by creative convergence R&D of local main industry promotion business.

REFERENCES

[1] Dong-Suk Kim, “Development of fire extinguishing system suitable for unmanned engine room f a small ship”, T. of Korean Institute of Fire Sci. & Eng., Vol. 20, No. 3, 2006.

[2] Ha-Sung Kong and Jong-Jin Kim, “A study on improving extinguishing capacity of mobile water mist equipment”, Korea Safety Management&Science, Vol. 11, No. 1, pp 15-26, 2009.

[3] K. W. Chu, B. Wang and A. B. Yu, “DISCRETE PARTICLE SIMULATION OF THE GAS-SOLID FLOW IN A CIRCULATING FLUIDIZED BED,” Engineering Conferences International, 2007.

[4] Chan-Young Cho, “Numerical Study on rotational flow and slurry dispersion in stirred tanks,” unpublished.

[5] “Fluent User Guide,” unpublished.

[6] Myeong-Rok Ryu and Kweon-Ha Park, “Hydrogen explosion effects at a containment building following a severe accident”, Journal of the Korean Society of Marine Engineering, Vol. 40, No. 3 pp. 164~172, 2016.

Numerical Analysis of Heat Transfer in Unsteady Nanofluids in a Small Pipe with Pulse Pressure

Cheol Park[1], Junhyo Kim[2], Jungpil Noh[3], Sunchul Huh[4], Byeongkeun Choi[5],
hanshik Chung[6], *HyoMin Jeong[7]

[1]Department of Energy and Mechanical Engineering, Gyeongsang National University. Institute of Marine Industry,
Cheondaegukchi-Gil 38, Tongyeong, Gyeongnam, 650-160, South Korea
[2]Department of Marine Engineering, Mokpo National MaritimeUniversity,61 dorim-ri,
1666 Yeongsan-ro. cheonggye-myeon, Muan-gun, jeonnam, South Korea
[3,4,5,6,7]Department of Energy and Mechanical Engineering, Gyeongsang National University · Institute of Marine Industry,
Cheondaegukchi-Gil 38, Tongyeong, Gyeongnam, 650-160, South Korea

Abstract**—** *In the present paper, developing turbulence forced convection flows were numerically investigated by using water-*Al_2O_3 *nano-fluid through a circular compact pipe which has 4.5mm diameter. Each model has a steady state and uniform heat flux (UHF) at the wall. The whole numerical experiments were processed under the RPM 100 to 500 and the nano-fluid models were made by the Alumina volume fraction. Single-phase fluid models were defined through nano-fluid physical and thermal properties calculations, Two-phase models (mixture granular model) were processed in 100nm diameter. The results show that comparison of nusselt number and heat transfer rate are improved as the* Al_2O_3 *volume fraction increased. All of the numerical flow simulations are processed by the FLUENT. The results show an increase from volume fraction concentration and an increase in heat transfer coefficient with increasing RPM.*

Keywords**— nanofluid, mixture, alumina, nusselt number, heat transfer coefficient, Pulsation pressure.**

I. INTRODUCTION

Heat transfer fluids play an important role in many industries, including power plants; production processes, transportation and electronics, and the heat transfer characteristics of thermal fluids play an important role in the development of energy efficient heat transfer devices. Past improvements have been based on structural changes and the addition of heat transfer areas, vibrations on the surface of the heat, injection or inhalation of fluids and the application of electrons or magnetic fields. These enhancement techniques rarely meet the increase in heat transfer coefficient and, in this connection; there is a strong demand for the development of advanced heat transfer fluids with higher heat transfer properties. Therefore, a number of recent studies on nanofluids for experimental convective heat transfer through circular tubes have been conducted by senior scholars. However, nanofluid research is still in the hot debate and investigation. In addition, research on the pulse pressure has been actively carried out all over the world, and many research results have been published especially in the field of noise vibration. Non-steady pulsating flow phenomena will be generated by internal smoke and reciprocating compressors. The pulsating pressure in the internal combustion engine will be the silencer part. The function of this silencer is to reduce the pulsation pressure inside the silencer as well as to reduce the back pressure.

Maxwell [1,2] has demonstrated that increasing the volume fraction of solid particles can increase the thermal conductivity of the mixture. The particle diameter currently available for particle manufacturing technology development is smaller than 100 nm, called nano-size. This effort allows the particle mixing fluid to increase the thermal conductivity of the heat transfer fluid by increasing the critical thermal conductivity. In addition, solid nanoparticle colloids are very stable and do not exhibit significant sedimentation under static conditions after weeks or months. In addition, solid colloids float easily when you reduce particle size. Therefore, nanofluidic technology is expected to be suitable for heat transfer fluids.

Mohamad and viskanta [3] studied the abnormal natural convection for a low prandtl number of fluids in the cavity, and patterson and Imberger [4] conducted a study on the abnormal natural circulation in a square cavity. Hellims and Churchill [5] numerically studied the natural convection in an unsteady state in a closed vessel. Therefore, this study focuses on the nanofluid only for pulsating pressure in a small tube with a pulse pressure. The purpose of this study is to verify the numerical analysis technique in terms of the fluidity of the nanofluids in a small tube with a pulsating pressure through numerical analysis. The purpose is to secure the data.

II. MATHEMATICAL MODELING

2.1 Geometry and boundary condition

Fig. 1a shows the actual model of geometry and Fig. 1b is the part of the Two-dimensional Mesh. One of the main purpose of this simulation is trying to understand the near wall behavior of nano-particles, velocity distribution perpendicular to the pipe surface and drag coefficient at the near of pipe wall, so the relatively concentrated mesh in the near wall area is needed. As a result, the mesh has a non-uniform quadratic mesh. The bottom horizontal line is an axis which makes Three-dimensional pipe model at the asymmetric environment. The upper horizontal line is a wall with Uniform heat flux. The tube consisted with a diameter (D) of 4.5 mm and a length (L) of 1.17 m. Nanofluids is composed of Al_2O_3 particles and water have the physical properties such as Table.1[6]. The total flow rate for each fluid model is input at a constant temperature of 293K and the axial velocity is defined as pressure change over time at 100,300,500RPM and the wall surface has a Heat flux of 5000 (w / m2).

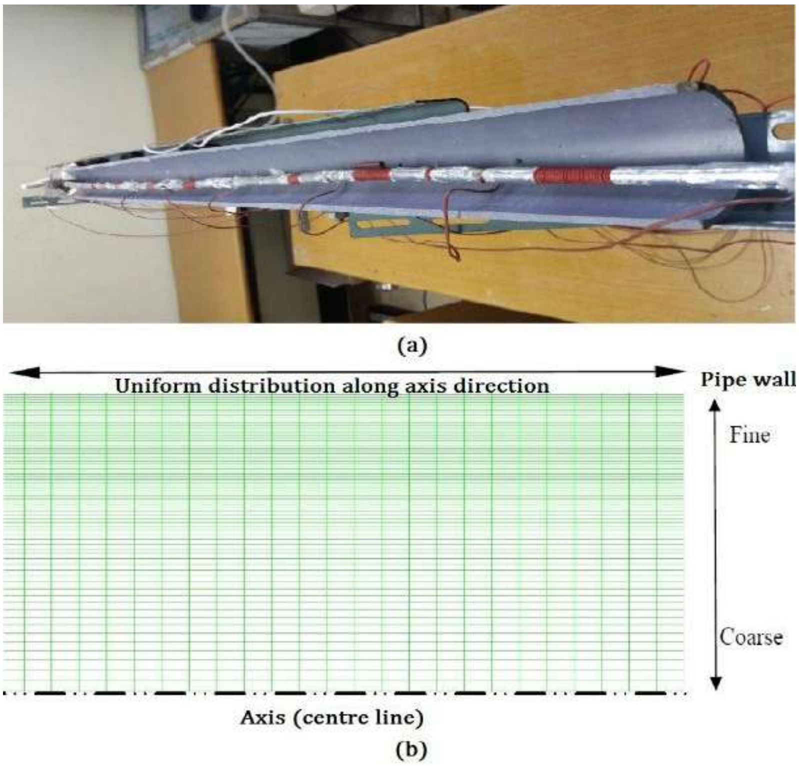

FIGURE 1. PART OF THE MESH OF COMPUTATIONAL CELL. 80 X 8000 WITH 0.96 RATIO

TABLE 1
Al_2O_3 NANOPARTICLE AT TEMPERATURE OF 293K

Chemical formula	Density(kg/m^3)	Heat conductivity(W/mK)	Specific heat(J/kgK)	Spherical diameter(nm)
Al_2O_3	3880	36	773	100

2.2 Governing equation

The single-phase model is investigated for the comparison of mixture model as prescribed. Following equations are representing the mathematical formulation of the single-phase model and of the continuous phase of the mixture model. The exact k-ε equations contain many unknown and un-measurable term [6-8]

Energy equation:

$$div\left(\mathrm{\rho}\vec{\mathrm{V}}\mathrm{CpT}\right) = div(kgradT) + S_e \tag{1}$$

turbulent kinetic energy k

$$\frac{\partial(\rho k)}{\partial t} + \frac{\partial(\rho k u_i)}{\partial x_i} = \frac{\partial}{\partial x_j}\left[\frac{\mu_t}{\sigma_k}\frac{\partial k}{\partial x_j}\right] + 2\mu_t E_{ij} E_{ij} - \rho\epsilon \tag{2}$$

dissipation ε

$$\frac{\partial(\rho\epsilon)}{\partial t} + \frac{\partial(\rho\epsilon u_i)}{\partial x_i} = \frac{\partial}{\partial x_j}\left[\frac{\mu_t}{\sigma_\epsilon}\frac{\partial\epsilon}{\partial x_j}\right] + C_{1\epsilon} 2\mu_t E_{ij} E_{ij} - C_{2\varepsilon}\rho\frac{\epsilon^2}{k} \tag{3}$$

And k- ε equation of represents velocity component in corresponding direction (u_i), represents component of rate of deformation(E_{ij}) , represents eddy viscosity(μ_t) (Rate of change of k or ε +Transport of k or ε by convection = Transport of k or ε by diffusion + Rate of production of k or ε – Rate of destruction of k or ε)

Conservation of mass:

$$\frac{\delta\rho_m}{\delta t} + \nabla\cdot(\rho_m u_m) = 0 \tag{4}$$

Where u_m is the mass-averaged velocity?

$$u_m = \frac{\sum_{k=1}^{n}\alpha_k\rho_k u_k}{\rho_m} \tag{5}$$

and ρ_m is the mixture density with α_k volume fraction of phase k:

$$\rho_m = \sum_{k=1}^{n}\alpha_k\rho_k \tag{6}$$

Momentum equation for single-phase:

$$div\left(\mathrm{\rho}\vec{\mathrm{V}}\vec{\mathrm{V}}\right) = -grad\ P + \nabla\cdot\left(\mu\nabla\vec{\mathrm{V}}\right) + S_m \tag{7}$$

Momentum equation for multi-phase:

$$\nabla\cdot\sum_{k=1}^{n}\alpha_k\rho_k u_k u_k = \nabla\cdot(\rho_m u_m u_m) + \nabla\cdot\sum_{k=1}^{n}\alpha_k\rho_k u_{Mk} u_{Mk} \tag{8}$$

The compression and viscous lose by heat are assumed to be excluded in the energy equation. The source/sink terms S_m and S_e represent the unitize effects of energy and momentum exchange with base fluid. These are zero value in the single-phase model. Momentum equation of multi-phase are affected by volume fraction (α), velocity of phase (u_k), diffusion velocity (u_{Mk}).

The determinations of particle motion are particle mass (m_p), cross-sectional area of the particle(A_p), drag coefficient(C_D), slip velocity(u_{cp}).

The drag force in this study is following Clift et al equation (7) for single rigid spherical particle in a fluid:

$$\mathrm{F}_D = -\frac{1}{2}A_p\rho_c C_D\left|u_{Cp}\right|u_{Cp} - \frac{1}{2}V_p\rho_c\frac{du_{Cp}}{dt} - 6\gamma_p^2\sqrt{\pi\rho_c\mu_c}\int_0^t\frac{\frac{du_{Cp}}{ds}}{\sqrt{t-s}}ds \tag{9}$$

2.3 Numerical approach

The computational fluid dynamic code FLUENT 16.1 is employed to solve the present problem. The governing Eqs. (1)-(3) are solved by control volume approach. The algebraic “discretize equations,” resulting from spatial inter-fraction process, are sequentially solved throughout the physical domain considered. ANSYS Fluent 16.1 solves the systems resulting from discretization schemes using a numerical method. For the convective and diffusive terms, a second order upwind method was used. Pressure and velocity were coupled using Semi Implicit Method for Pressure Linked Equations (SIMPLE) in single-phase. To calculate the pulse pressure, Figure 2. The PISO algorithm was used to calculate the anomalous state as a complete negative solution. The continuity equation and the momentum equation are used to calculate the pressure inside the small tube.

The turbulence model is based on the standard model k -ε model which has already proved its engineering validity. The convergence judgment of the residuals was regarded as convergence when the residual value reached 10 or less.

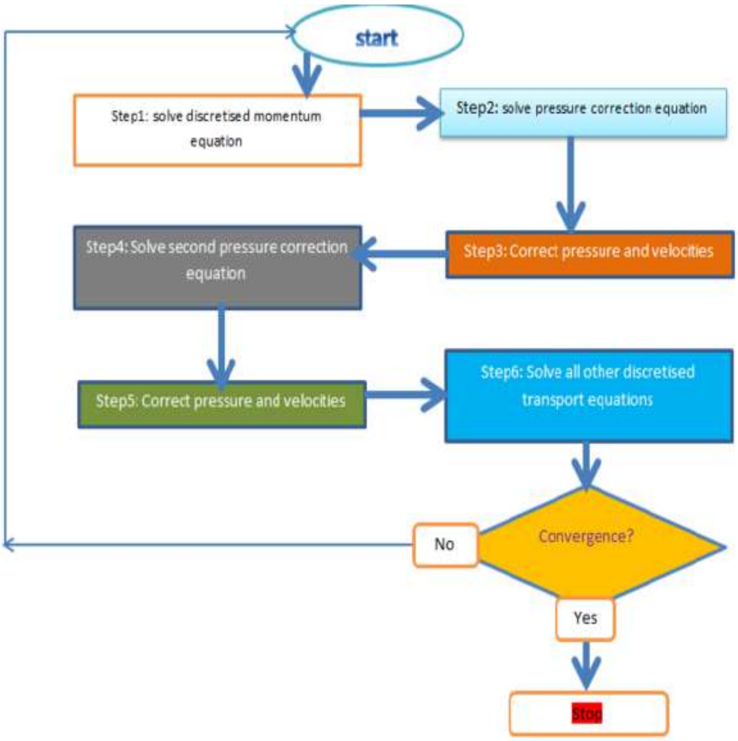

FIGURE 2. FLOW CHART OF PISO ALGORITHM

As already seen for the SIMPLE algorithm, the steps 4 and 5 can be repeated for a prescribed number of times to correct for non-orthogonality.

III. RESULTS

The In this work a number of numerical simulations have been performed to study forced convective heat transfer of Al_2O_3-water in a circular tube under turbulence flow and results were conducted to employing the single phase and mixture model for φ=1% to 4%, 100to500RPM as q=5000 W/m^2 with a constant state. In all cases the size of the spherical particles is 100 nm.

Thermal entrance length depends on Prandtl number.[9] So when concentration increases Pr number also increases and consequently, thermal entrance length becomes greater.

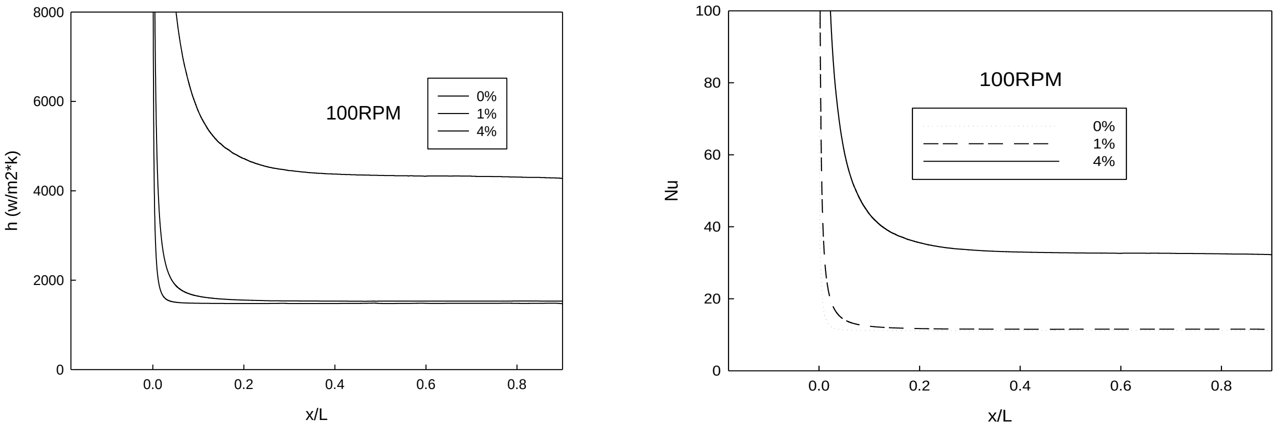

(a) **(b)**

FIGURE 3.(A) 100RPM, HEAT TRANSFER COEFFICIENT FOR Al_2O_3-WATER, (B)100RPM, NUSSELT NUMBER

As shown in Fig. 3 (a), the difference between 0% and 1% seems to be insignificant in the range of 0.1x / Lmm, but the heat transfer rate of 4% Al_2O_3 is 2 times larger than 0,1% Respectively. Likewise, in figure (b)

The transmission rate of 0 and 1% Al_2O_3 is less than 10, but 4% nanofluids can be seen to have more than twice the Nusselt number.

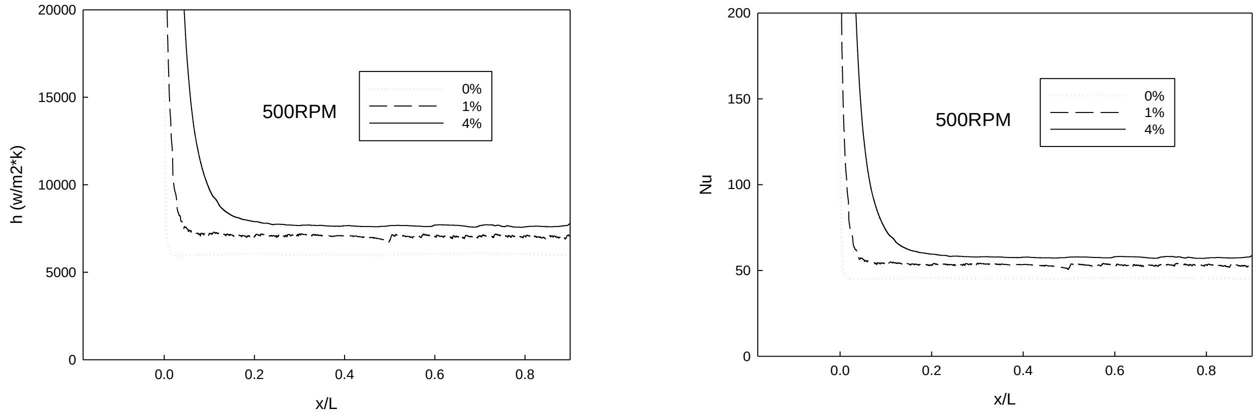

(a) (b)

FIGURE 4.(a) 500RPM, HEAT TRANSFER COEFFICIENT FOR Al_2O_3-WATER, (b) 500RPM, NUSSELT NUMBER

In Fig. 4 (a), unlike 100RPM, the phenomena appearing more than twice as much as 0%, 1% and 4% are not shown in the figure. This phenomenon can be grasped by increasing the internal pressure at 500 RPM. Also, in Fig. (B), the Nusselt number seems to be closer to 1% Al_2O_3 than 4%.

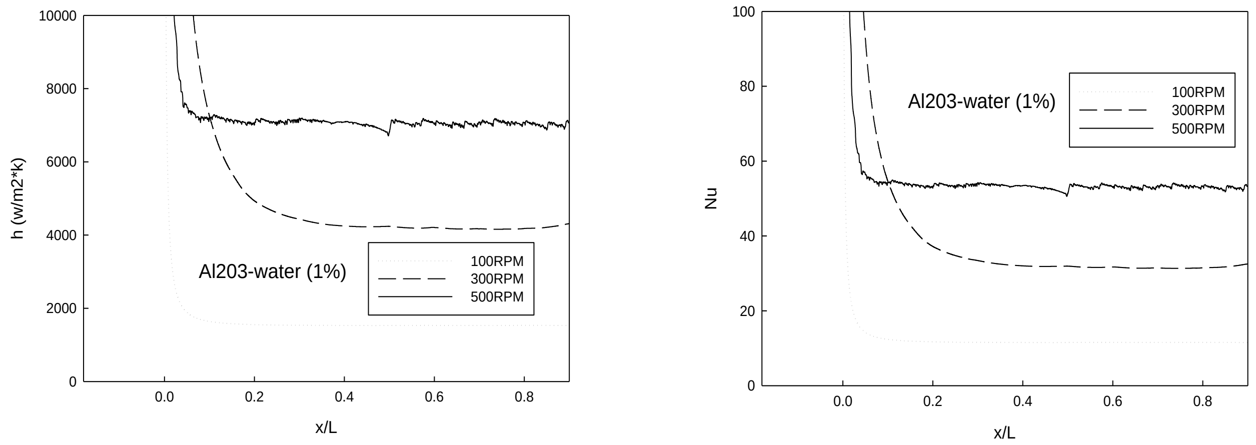

(a) (b)

FIGURE 5.(a) Al_2O_3-WATER, HEAT TRANSFER COEFFICIENT FOR 100 TO 500RPM, (B) Al_2O_3-WATER, NUSSELT NUMBER FOR 100 TO 500RPM

Figures 3 and 4 shows the difference in heat transfer coefficient and number of nuns in the nanofluid for each RPM. 5 (a) and (b), however, the heat transfer coefficient and the number of nuclei for RPM changes of the same 1% Al_2O_3 can be confirmed. The heat transfer rate and the number of nusselts are significantly lower than those of 300 and 500 RPM . However, at 300 RPM, it can be confirmed that the heat transfer coefficient and the number are higher than 500 RPM in the early stage.

IV. CONCLUSION

Numerical analysis of the heat transfer of the nanofluid in the unsteady state in the small tube into which the pulsating pressure is introduced showed that the effect of the content of Al_2O_3, which is a nanofluid, was further increased in the low 100 RPM. In addition, it was confirmed that the nanofluids of 0% and 1% compared to 0% and 1% of Al 2 O 3 have a data difference of more than 2 times. In 500 RPM, the difference in content is not significant compared to 100 RPM, but nanofluids with high Al 2 O 3 The heat transfer coefficient and the number of nuns were better. And the increase in the heat transfer coefficient of the nanofluid to the RPM change shows better results as the RPM increases. Therefore, nanofluid with high Al_2O_3 content and high RPM can improve the thermoelectric coefficient and increase the number of nuts. But the CFD should be progressed with constant and transient numerical investigation parallel. Basically, It would be pace with the experiment especially different model scale study. Also, uniform heat flux sample, wall shear stress, body force researches does not include this paper. This compact size model is not usual model on the nano-fluid CFD study so these factors need to be proved.

ACKNOWLEDGEMENTS

This research was supported by Basic Science Research Program through the National Research Foundation of Korea (NRF) funded by the Ministry of Science, ICT and future Planning (No. 2017R1A2B4007620).

REFERENCES

[1] J. C. Maxwell, A Treatise on Electrictiy and Magnetism, Oxford University Press, Cambridge, 1881J. Clerk Maxwell, A Treatise on Electricity and Magnetism, 3rd ed., vol. 2. Oxford: Clarendon, 1892, pp.68–73

[2] Q. Li, Y. Xuan, Heat transfer enhancement of nanofluids, International Journal 21, pp.58-64, 2000.

[3] A.A Mohamad, and R.Viskanta: Int. J. Numerical Method in Fluid, 12, 61-81(1991)

[4] Sunghoon kim,HyeMin Son,JaeCheon Lee, The effect of eccentricity between gear and housing in involute gear pump, Journal of the Korean Society of Marine Engineering 37(6) 2013.9,631-637

[5] Yangwoo Mo,YoungTae Yoo,GeeDae Na,JiHwan Kim, A Characteristics of Impedance Propagation by the Unsteady Flow in a Hydraulic Pipeline, Journal of the Korean Society of Manufacturing Technology Engineers 13(6), 2004.12, 48-55

[6] M. Nazififard, M. Nematollahi, K. Jafarpur, K. Y. Suh, Numerical Simulation of Water-Based Alumina Nanofluid in Subchannel Geometry, Science and Technology of Nuclear Installations, Vol 2012, 2012

[7] ANSYS Fluent Theroy Guide, pp. 501, November 2013

[8] V. Bianco, F. Chiacchio, O. Manca, S. Nardini, Numerical investigation of nanofluids forced convection in circular tubes, Applied Thermal Engineering 29, pp 3632-3642, 2009

[9] V. Bianco, F. Chiacchio, O. Manca, and S. Nardini, Numerical investigation on nanofluids turbulent convection heat transfer inside a circular tube, International Journal of Thermal Sciences, vol. 50, no. 3, pp 341-349, 2011

[10] Chungseub Yi ,kyujin shim,wanda ali akbar,hanshik chung,hyomin Jeong, study on the Pressure Variation in a Chamber Caused by Pulsation Pressure, Transaction of Korean Society of Automotive Engineers 15(4),2007.7, 132-138(7pages)

Analysis of laminar nanofluid forced convection heat transport through the CFD

Kitae Yu[1], Junhyo Kim[2], Jungpil Noh[3], Sunchul Huh[4], Byeongkeun Choi[5], Hanshik Chung[6],*Hyomin Jeong[7]

[1]Department of Energy and Mechanical Engineering, Gyeongsang National University
[2]Department of Marine Engineering, Mokpo National Maritime University, 61 dorim-ri, 1666 Yeongsan-ro, Cheonggye-myeon, Muan-gun, jeonnam, South Korea
[3,4,5,6,7]Department of Energy and Mechanical Engineering, Gyeongsang National University · Institute of Marine Industry, Cheondaegukchi-Gil 38, Tongyeong, Gyeongnam, 650-160, South Korea

Abstract**—***In the present paper, developing laminar forced convection flows were numerically investigated by using water-Al_2O_3 nano-fluid through a circular compact pipe which has 4.5mm diameter. Each model has a steady state and uniform heat flux (UHF) at the wall. The whole numerical experiments were processed under the Re = 1050 and the nano-fluid models were made by the Alumina volume fraction. Single-phase fluid models were defined through nano-fluid physical and thermal properties calculations, Two-phase model (mixture granular model) were processed in 100nm diameter. The results show that Nusselt number and heat transfer rate are improved as the Al_2O_3 volume fraction increased. All of the numerical flow simulations are processed by the FLUENT. The results show the increment of thermal transfer from the volume fraction concentration.*

Keywords—Nanofluid, Alumina, Laminar flow, Mixture, Nusselt number, Heat transfer coefficient, Homogeneous flow.

I. INTRODUCTION

To enhance the heat exchangers energy transfer efficiency, Engineers have interested not only the development exchanger or enhanced its structure, but also improvement of heat transfer fluid itself. Maxwell [1] proved the possibility of increasing thermal conductivity of a mixture by higher volume fraction of solid particle. Nowadays available particle diameter is smaller than 100nm which is called 'Nano-sized'. This effort makes particle mixture fluid would enhance the heat transfer performance of heat transfer fluids. [2] Moreover, solid nanoparticle colloids are highly stable and exhibit no significant settling under static conditions. Also, decreasing particle size makes suspending solid colloid easily. So that nano-fluid technology is expected to suitable of heat transfer fluid. [3] However, nano-fluid development is interrupted by the lack of agreement with different research group, theoretical understanding of the heat transfer mechanisms, different suspension conditions. [4]In this paper, Nano-fluid model assume that the Homogeneous flow mixture model [5] which is the dispersed and continuous phase with very strong coupling and the nano-particles is moving at the same inlet velocity. Therefore the dispersed granular mixture models are made by 'Mixture model' which is one of the Euler-Euler approaches. This numerical investigation purpose is an observation of heat transfer coefficient increment in a compact pipe and comparison between single-phase and multi-phase model. Geometry model size is as same as experimental pipe which will use in a university laboratory. Nano-particle volume fractions are less than 5 percent, and divided by 1 percent from 0 to 4 percent. The wall has constant surface heat flux as known as Uniform Heat Flux (UHF). The numerical simulation geometry is asymmetric two-dimensional model. Through the limit of 2D model and assumption, implicit effect such as gravity and buoyancy force are excluded. The nano-particle material is an Aluminium Oxide with a spherical size of 100 nm diameter and simulations are processed in a steady state. The purpose of this study is comparing heat transfer ability between single and mixture model which have same heat transfer value except the particle presence.

II. MATHEMATICAL MODELING

2.1 Geometry and boundary condition

Fig. 1a shows the actual model of geometry and Fig. 1b is the part of the Two-dimensional Mesh. One of the main purpose of this simulation is trying to understand the near wall behavior of nano-particles, velocity distribution perpendicular to the pipe surface and drag coefficient near at the pipe wall, so the relatively concentrated mesh in the near wall area is needed. As a result, the mesh has a non-uniform quadratic mesh. The bottom horizontal line is an axis which makes Three-dimensional pipe model at the asymmetric environment. The upper horizontal line is a wall with UHF. The tube consisted with a diameter (D) of 4.5 mm and a length (L) of 1.17 m. The nano-fluid is composed of water and Al_2O_3 particles. Whole velocity inlet for each fluid models enter with uniform temperature and axial velocity profiles are defined by Re = 1050. The fluid is flow out to the outflow outlet.

2.2 Governing equation

The single-phase model is investigated for the comparison of mixture model as prescribed. Following equations are representing the mathematical formulation of the single-phase model and of the continuous phase of the mixture model. [5-7]

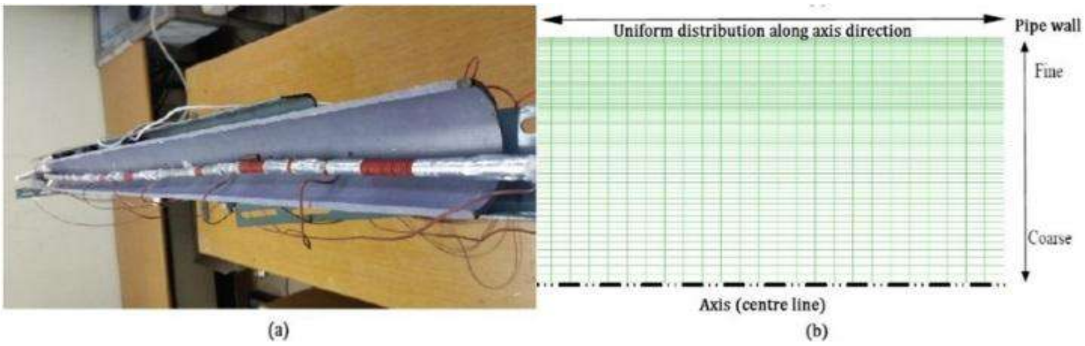

FIGURE 1. (A) ACTUAL MODEL OF GEOMETRY (B) PART OF THE MESH OF COMPUTATIONAL CELL. 80 X 8000 WITH 0.96 RATIO

Energy equation

$$div(\rho\vec{V}CpT) = div(kgradT) + S_e \tag{1}$$

Conservation of mass

$$\frac{\delta\rho_m}{\delta t} + \nabla\cdot(\rho_m u_m) = 0 \tag{2}$$

Mass-averaged velocity u_m is

$$u_m = \frac{\sum_{k=1}^{n}\alpha_k\rho_k u_k}{\rho_m} \tag{3}$$

and ρ_m is the mixture density with α_k volume fraction of phase *k*

$$\rho_m = \sum_{k=1}^{n}\alpha_k\rho_k \tag{4}$$

Momentum equation for single-phase

$$div(\rho\vec{V}\vec{V}) = -grad\,P + \nabla\cdot(\mu\nabla\vec{V}) + S_m \tag{5}$$

Momentum equation for multi-phase

$$\nabla\cdot\sum_{k=1}^{n}\alpha_k\rho_k u_k u_k = \nabla\cdot(\rho_m u_m u_m) + \nabla\cdot\sum_{k=1}^{n}\alpha_k\rho_k u_{Mk}u_{Mk} \tag{6}$$

The compression and viscous lose by heat are assumed to be excluded in the energy equation. The source/sink terms S_m and S_e represent the unitive effects of energy and momentum exchange with base fluid. These are zero value in the single-phase model. Momentum equation of multi-phase are affected by volume fraction (α), velocity of phase (u_k), diffusion velocity (u_{Mk}).The determinations of particle motion are particle density (ρ_c), cross-sectional area of the particle (A_p), drag coefficient(C_D), slip velocity(u_{cp}).The drag force in this study is following Clift et al equation (7) for single rigid spherical particle in a fluid.

$$F_D = -\frac{1}{2}A_p\rho_c C_D\left|u_{Cp}\right|u_{Cp} - \frac{1}{2}V_p\rho_c\frac{du_{Cp}}{dt} - 6\gamma_p^2\sqrt{\pi\rho_c\mu_c}\int_0^t\frac{\frac{du_{Cp}}{ds}}{\sqrt{t-s}}ds \tag{7}$$

The drag coefficient which is already showed in equation (7) depends on small Particle Reynolds numbers with particle Reynolds number

$$C_{D,St} = \frac{24}{Re_p} \tag{8}$$

The slip velocity is following equation (9) with τ_p the particle relaxation time, $\vec{a}$ is the secondary-phase particle's acceleration

$$u_{pq} = \frac{\tau_p(\rho_p-\rho_m)}{f_{drag}}\vec{a} \tag{9}$$

The default drag function is taken Schiller and Naumann. Reynolds numbers in this paper are over 1000 so the equation is defined as follow

$$f_{drag} = 0.0183\mathrm{Re} \tag{10}$$

2.3 Physical properties of the nanofluid for single-phase model and Boundary conditions

At inlet boundary condition, axial velocity V_0 is defined from $\mathrm{Re} = 1050$ according to the fluid properties and a constant temperature (293K) as described. On the tube wall, the usual non-slip conditions and uniform wall heat flux $q = 5000\ \mathrm{W}/m^2$are implemented.The determination of nano-fluid physical, thermal properties are at the center of current nano-fluids research as previously mentioned.[7] For the single phase model properties of the nano-fluids have been calculated by using classical formulas developed for conventional solid-liquid mixtures.[8] The following equations are considered to evaluate Al_2O_3-water nano-fluids thermo-physical properties and were used for CFD simulation.[6]

$$\rho_{nf} = (1-\varphi)\rho_{bf} + \varphi\rho_p \tag{11}$$

$$c_{p,nf} = \frac{(1-\varphi)(\rho c_p)_{bf} + \varphi(\rho c_p)_p}{\rho_{nf}} \tag{12}$$

$$\mu_{nf} = (123\varphi^2 + 7.3\varphi + 1)\mu_{bf} \tag{13}$$

The φ is the volume fraction of the Al_2O_3. The dynamic viscosity that temperature depended properties are excluded and has a constant value. The equation (13) is applicable for spherical particle in volume fractions less than 5% [9] and determination of nano-fluid effective thermal conductivity as follow. [10]

$$k_{nf} = \left[\frac{k_s + 2k_w + 2(k_s - k_w)(1+\beta)^3\varphi}{k_s + 2k_w - (k_s - k_w)(1+\beta)^3\varphi}\right] k_w \tag{14}$$

In Equation (14), β is the ratio of nano-layer thickness to the original particle radius, and $\beta = 0.1$ is used for calculation in this equation. The result of physical and thermal properties of nano-fluid models are presented in Table 1 and Al_2O_3 particle physical and thermal properties as follow in Table 2

2.4 Numerical approach

The computational fluid dynamic code FLUENT 16.1 is employed to solve the present problem. The governing Eqs. (1)-(3) are solved by control volume approach. For the convective and diffusive terms, a second order upwind method was used. Pressure and velocity were coupled using Semi Implicit Method for Pressure Linked Equations (SIMPLE) in single-phase. Unlike single-phase, multi-phase was approached by Coupled algorithm which offers an alternative to the density-based and pressure-based segregated algorithm with SIMPLE-type pressure-velocity coupling. The difference between SIMPLE and Coupled is a Convergence time [6] and Couple algorithm has converged faster than SIMPLE in multi-phase. The laminar flow has fully developed region that distribution of flow velocity maintains constant. In this study, fully developed region appears after 0.307m according to equation (15). [12].

TABLE 1
PROPERTIES OF NANO-FLUID AT 293K AND RE = 1050

Φ(%)	Density(kg/m^3)	Viscosity(kg/ms)	Inlet velocity(m/s)	Heat conductivity(W/mK)	Specific heat(J/kgK)
0	998.2	9.98e-4	0.233	0.5970	4182.0
1	1027.018	1.023e-3	0.2324	0.6200	4053.21
2	1055.836	1.048e-3	0.2316	0.6436	3931.451
3	1084.654	1.073e-3	0.2308	0.6678	3816.162
4	1113.472	1.098e-3	0.2300	0.6926	3706.840

TABLE 2
Al_2O_3 NANOPARTICLE AT TEMPERATURE OF 293K

Density(kg/m^3)	Heat conductivity(W/mK)	Specific heat(J/kgK)	Spherical diameter(nm)
3880	36	773	100

$$\mathrm{L}_{laminar} = 0.065 \cdot Re \cdot D \tag{15}$$

The velocity distributions are showed in Figure 2. It is only 0.6737 percent less than outlet at an axial velocity at the 0.307m in Fig. 2a and all mixture models are following the Fully developed region in Fig. 2b. This means nano-fluid motion is fully developed at exit section model, when properties are not dependent on temperature, velocity profile and hydrodynamic entrance length are nearly identical at 0.307m for Φ = 0%, 1%, 2%, 3% and 4%.[7]A Nusselt number is converged to 4.36 in the UHF.[13] Comparing Nusselt number to Churchill-Ozoe equation (16) [14] and Siegel Sparrow-Hallman calculation equation (17) [15] and common Nusselt number equation (18) which used in present study in Figure 3. x^* is a dimensionless axial position for thermally developing flows. Pr is the Prandtl number.

$$\mathrm{Nu} = 5.364\left[1 + (70.0x^*)^{-10/9}\right]^{3/10} - 1 \tag{16}$$

$$Nu = \frac{2}{\left[\left(\frac{t_w - t_0}{q r_0/k}\right) - \left(\frac{4x/r_0}{RePr}\right)\right]} \tag{17}$$

$$Nu = \frac{h(x)D}{k_{inlet}} \tag{18}$$

The heat transfer coefficient h(x) is defined as

$$\mathrm{h}(x) = \frac{q}{T_w(x) - T_b(x)} \tag{19}$$

The $T(x)_w$ is the solid surface temperature at the wall temperature, and $T(x)_b$ is the mean bulk temperature. Average Nusselt number is defined as

$$\mathrm{Nu}_{av} = \frac{h_{av} \cdot D}{k_{inlet}} \tag{20}$$

Current study model on $\varphi = 0\%$ is going to 4.69 Nusselt number which has a 7 percentage point gap between normal convergence value. Therefore velocity distribution and Nusselt number show the model has fitted in the theory.

III. RESULTS

In this work a number of numerical simulations have been performed to study forced convective heat transfer of Al_2O_3-water in a circular tube under laminar flow and results were conducted to employing the single phase and mixture model for $\varphi = 1\%$ to 4%, Re = 1050 as q = $5000\ W/m^2$ with a constant state. In all cases the size of the spherical particles is 100 nm.

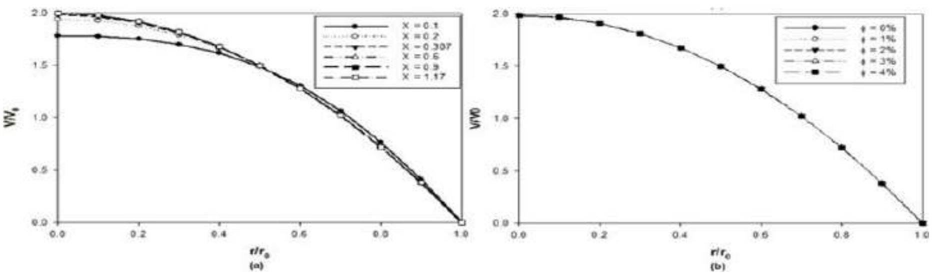

FIGURE 2. (a) PROFILES OF AXIAL VELOCITY AT SEVERAL LOCATIONS FOR Re = 1050, q = 5000 W/m^2, Φ= 4%. (b) PROFILES OF AXIAL VELOCITY AT x = 0.307m for Re = 1050, q = 5000W/m^2 AND SEVERAL VOLUME FRACTIONS.

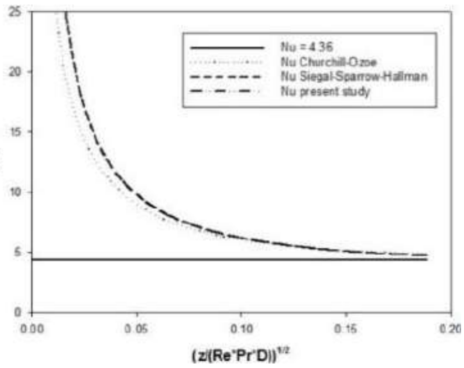

FIGURE 3. GRID VALIDATION BY MEANS OF CHURCHILL AND OZOE, SIEGAL-SPARROW-HALLMAN

Dimensionless temperature shows the particle concentration increase happens the thermal development acceleration of the fluid at several axial locations along the radius is reported in Fig. 4 for $\boldsymbol{\varphi = 0\%}$ and $\mathbf{4\%}$. For the both the base fluid and the nano-fluid, the motion is not thermally developed. As it is also noticed by a higher slope of relative local heat transfer coefficient h_r for $\boldsymbol{\varphi = 4\%}$ shown in Fig. 5a.Relative local heat transfer coefficient is increasing with axis location and volume fraction rise when fluid properties are constant in Fig. 5a. Because of narrow hydrodynamic radius of model, correlation between wall and bulk temperature is higher than larger model. Consequently, difference between the wall and bulk temperature is decrease and with the heat flux on the wall being constant, there is an increase in the heat transfer coefficient, as shown in Fig. 5b.

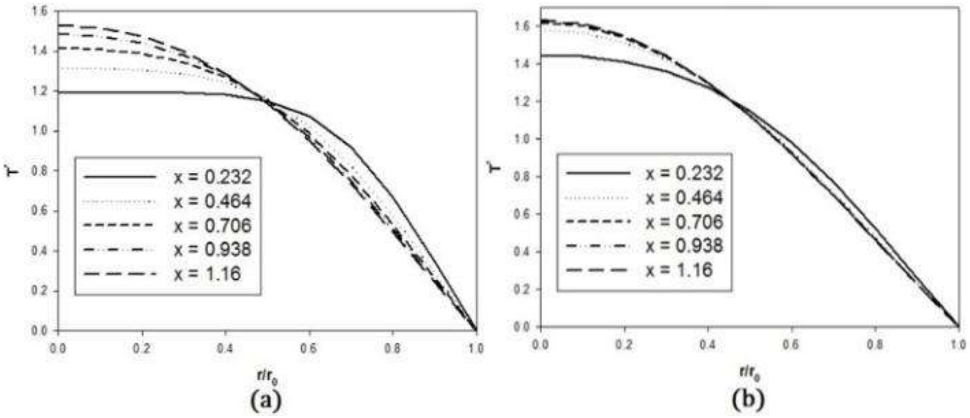

(a) (b)

FIGURE 4. DIMENSIONLESS TEMPERATURE FOR Re = 1050 and q = 5000 W/m2 AT SEVERAL LOCATIONS FOR : (a)Φ=0% and (b)Φ= 4%

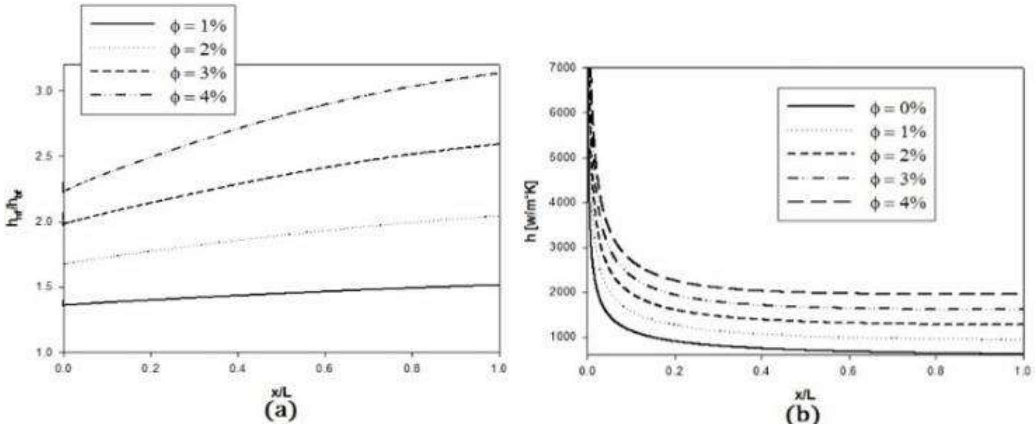

(a) (b)

FIGURE 5. (A) INCREASE IN NANO-FLUID HEAT TRANSFER COEFFICIENT ALONG TUBE AXIS FOR Re = 1050 and q = 5000 W/m^2 FOR CONSTANT PROPERTIES AND INCREMENT OF VOLUME FRACTION. (B) HEAT TRANSFER COEFFICIENT OF EACH VOLUME FRACTION FOR CONSTANT PROPERTIES.

In Fig. 6, radial temperature profiles at profiles at $x/L = 1.0$ for Re = 1050 and q = 5000 W/m^2 are investigated for the effect of particle presence. The temperature is strongly dependent on φ concentration. When the multi-phase concentration increases, the difference between temperature at surface and axis decrease by higher forced convection heat transfer. This effect is the cause of wall temperature decrease. It is also implemented in single-phase however, due to the particle absence, heat transfer between wall and inner side is not remarkable. Furthermore the only average temperature 1.3K increase than 293K on single-phase models. Both of phase show there is a clear existence of a uniform temperature fluid zone that becomes more visible for higher value of Φ at the $r/r_0 = 0.6$.

IV. CONCLUSION

Average heat transfer coefficient and Nusselt number are shown in Table 3 with relative increase of the total heat transfer rates and Nusselt number as a concentration of the nano-particle volume fraction φ. Significant increases of the total heat transfer rates can be found with the use of fully dispersed nanoparticles multi-phase. These results have indicated the nano-fluids beneficial effects of thermal properties improvement. The results showed that the nanoparticles inclusion produced considerable heat transfer with respect to base fluid. Heat transfer enhancement was increasing with concentration of particle volume. But the CFD should be progressed with constant and transient numerical investigation parallel and these numerical researches would be pace with the experiment especially.

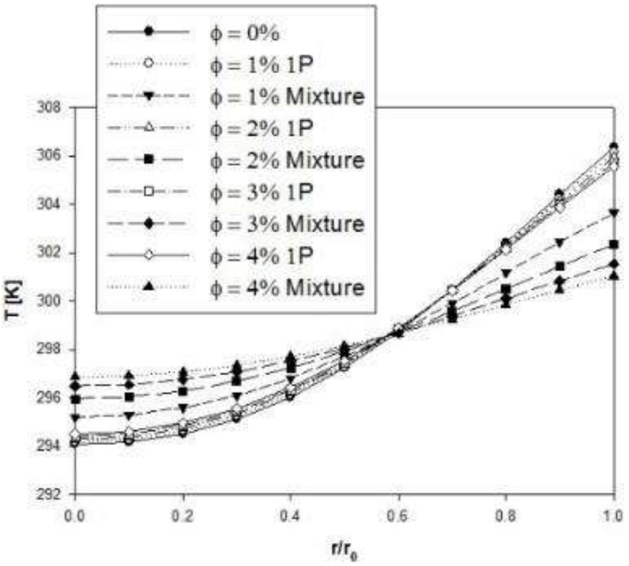

FIGURE 6. COMPARISON OF TEMPERATURE ALONG TUBE RADIUS AT x/L = 0.99 FOR SEVERAL CONCENTRATION AND FOR Re = 1050 and q = 5000 W/m^2 IN CONSTANT PROPERTIES

TABLE 3
HEAT TRANSFER COEFFICIENTS FOR Re = 1050, q = 5000 W/m^2 AND THE INVESTIGATED MODELS

Φ(%)	h_{av} (W/mK)	h_{nf}/h_{bf}	Nu_{av}	Nu_{nf}/Nu_{bf}
0	861.815	1	6.5	1
1	1233.288	1.431	8.95	1.377
2	1592.853	1.848	11.1	1.707
3	1954.472	2.268	13.2	2.027
4	2301.521	2.671	14.9	2.302

ACKNOWLEDGMENTS

This research was supported by Basic Science Research Program through the National Research Foundation of Korea(NRF) funded by the Ministry of Education(No. 2015R1D1A1A01058030).

REFERENCES

[1] J. C. Maxwell, A Treatise on Electricity and Magnetism, Oxford University Press, Cambridge, 1881
[2] Taylor, R. A, Small particles, big impacts: A review of the diverse applications of nanofluid, Journal of Applied Physics 113, pp. 1, 2013
[3] S. M. S. Murshed, K. C. Leong, C. Yang, Thermophysical and electrokinetic properties of nanofluids – a critical review, Applied Thermal Engineering 28, pp. 2109-2125, 2008
[4] X. Q. Wang, A. S. Mujumdar, Heat transfer characteristics of nanofluids: a review, International Journal of Thermal Sciences 46, pp. 1-19, 2007
[5] Mi. Manninen, V. Taivassalo, S. Kalliio, On the mixtrue model for multiphase flow, Valtiion Teknillinen Tutkmuskeskus, 1996
[6] ANSYS Fluent Theroy Guide, pp. 501, November 2013
[7] V. Bianco, F. Chiacchio, O. Manca, S. Nardini, Numerical investigation of nanofluids forced convection in circular tubes, Applied Thermal Engineerinig 29, pp. 3632-3642, 2009
[8] S. K. Das, S. U. S. Choi, W. Yu, and T. Pradeep, Nanofluids Science and Technology, John Wiley & Sons, Hoboken, Nj, USA, 208
[9] D. A. Drew, S. L. Passman, Theory of Multicomponent Fluids, Springer, Berlin, 1999
[10] S. J. Kline and F. A. McClintock, Mechanical Eng. 75, 3, 1953

[11] M. Nazififard, M. Nematollahi, K.Jafarpur, K. Y. Suh, Numerical Simulation of Water-Based Alumina Nanofluid in Subchannel Geometry, Science and Technology of Nuclear Installations, Vol 2012, 2012

[12] Kominu Natsuo, Fluid Engineeriing, Syuwa system, pp. 176, 2006

[13] Mohammad Z. Hasan, Effects of non-uniform surface heat flux and uniform volumetric heating on blanket design for fusion reactors, Fusion Science and Technology, Los Angeles, May 1988

[14] S. W. Churchill, H. Ozoe, Correlations for forced convection with uniform heating in flow over a plate and in develooping and fully developed flow in a tube, Journal of heatTrnasfer 95, pp. 78-84, 1973

[15] R. Siegel, E. M. Sparrow, T. M. Hallman, Steady laminar heat transfer in a circular tube with prescibed wall heat flux, Cleveland, Ohio, UA, Aplied Scientific Research, Section A, Volume 7, Issue 5, pp. 386-692, September, 1958

Experimental-laboratory study of the flow around mussel shocks

George Pechlivanidis[1], Alexandros Antoniou[2], Yiannis Savvidis[3*]

Department of Civil Engineering T.E., Alexander Technological Institute of Thessaloniki, Greece
*Corresponding Author Email: savvidis@aqua.teithe.gr

Abstract**—** *The productivity in an organized mussel culture area is closely related to the hydrodynamics in the area where the mussel units are located. The interaction between the hydrodynamics and mussel farming in Chalastra (NW Thessalonikigulf) has been investigated during last decades. In the framework of the study of optimizing the quality of mussels production in mussel farming areas, a laboratory channel was designed, where the flow around and possibly through the mussel shocks would be studied in physical scale. The experiments were designed in physical/natural scale and the relevant variables were determined. Moreover, the specific positions for the measurements, the depth of the flow and the velocity currents were also determined. The following three mean velocity values of entrance water velocity U were used in the experiment; 5 cm/sec, 7 cm/sec and 9cm/sec. A basic research parameter used in the experiment was the distance between the mussel shocks. Four cases were taken into account: 300mm, 500mm, 700mm and 900mm. The final goal was the determination of the velocity field in the areas around the shocks. The velocity field was studied with the modern Particle Image Velocimetry technique. According to the above presented experiments, for distances between the shocks greater than 500 mm the velocity field is almost restored. Furthermore the case of larger distance between the shocks (i.e. 90cm) present the largest percentage of the velocity class 5-10cm/sec(occurring for entrance current velocities 7 and 9 cm/s)which seem to be the best range for mussel's growth.*

Keywords**— *current velocity, laboratory experiments, mussel shocks, PIV method.***

I. INTRODUCTION

It is well known that the productivity in a mussel farm is closely related to the hydrodynamics in the area. That significant factor, i.e. the hydrodynamics in a mussel farm has been extensively investigated during last decades in the coastal area of Chalastra (W-NW gulf of Thessaloniki, North Greece). Thus, such relevant studies for the specific area started to take place, in a more insistent and organized way, at the beginning of the 21st century. More specifically, [1] realized field measurements in the area which showed that currents are quite weak in the area of the mussel farms. Galinou-Mitsoudi et al. [2] later worked on a mathematical simulation showing that field measurements, mentioned before, were very well approximated by the results of a coarse hydrodynamic model. [3], [4] and [5] conducted field and numerical experiments while [6]and [7]studied mussel cultures and hydrodynamics with the help of mathematical simulations and the development of general management tools.These afore mentioned research works finally led to the findings listed below: (a) the largest proportions of current speeds (>40%) were recorded between 0 and 5 cm/s, which corresponded to very weak currents, suitable only for low density farming, (b) the longest treatment configuration (from the four configurations corresponding to distance between shocks 30 or 50 or 70 or 90 cm)i.e. shock distance 90 cm, led to the larger values of current speeds (90cm treatment had the largest percentage for the class 5-10cm/sec which is the most suitable current speed for the mussel farming activity according to [8] (c) there was a great variability of the current direction at the long line level and (d) it was observed that sometimes the current, moving towards the mussel unit deviates its route and is not entering inside the farm, which may lead to less food availability inside the farm.[9] in the framework of his doctoral research conducted both field and laboratory experiments however the latter experiments were based on the use of cylinders. The flow over two in-line cylinders in laminar and turbulent flows was also studied with the help of numerical simulations by [10].Furthermore, [11] studied the turbulent-flow characteristics and the mechanism of vortex shedding behind one and two square obstacles centered inside a 2-D channel. The study was based on the use of large eddy simulation and finite-element technique.

Taking into account the aforementioned research works, the need of a more detailed investigation on the hydrodynamics related to the mussel shocks, in a small scale, laboratory level was arisen. More specifically, it was considered that this research could take place in a laboratory channel with natural shocks from the sea field so that the experiments would lead to the best possible integrity of the results. In the framework of the study of optimizing the quality of mussels production in mussel farming areas, a laboratory structure (channel) was designed, where the flow around and possibly through the mussel shocks would be studied in physical (natural) scale. Therefore, an extension of the already existed channel in the hydraulic laboratory of Civil Eng. Dept. of ATEITh (Alexander Technological Educational Institute of Thessaloniki) was realized. More specifically, the old channel length increased from 4 to 10 m, while the dimensions of a cross section (width and height) of the channel were 50 cm x 50 cm, with the ability of variable inclination of the channel's floor (Fig 1).

FIGURE 1. THE NEW CHANNEL OF THE HYDRAULICS LABORATORY OF CIVIL ENG. DEPT. OF ATEITh

The mussel shocks were always taken directly from the mussel farmer and placed in the central axis of the channel leaving space up to the vertical wall of the channel around 16 cm from both sides (since the diameter of each shock was nearly 18 cm). Thus, the laboratory experiments were realized using the physical scale of a shock and using current velocities in the entrance of the channel that were usually recorded in the field.

II. MATERIAL AND METHOD

2.1 The experimental procedure

The experiments were designed in physical scale and the relevant variables were determined. Moreover, the specific positions for the measurements, the depth of the flow and the velocity currents were also determined. From the aforementioned data, the appropriate mechanical and electrological mechanisms were resulted for the successful realization of the experiments. Then, the onomatology of the different experiments followed, in such way that the exact determination of each specific experiment could be resulted from the file's name. The water flowing in the channel was always collected in a tank. The level of the free surface of the water in the channel was determined by a sluice gate in the downstream part of the channel's water reservoir with accuracy of 0.5 mm. The water would overflow from the sluice gate and finally go to a circular tank outside the room of the laboratory experiments. From there, with the help of a pump and a water pipe the water would go back to the entrance of the channel. Thus, continuous flow of recycled water was achieved with fixed hydraulic conditions. So, in this way the hydraulic parameters had the eligible fixed and invariable values while the phenomenon could be repeated at any time. The flow rate was controlled by the help of an orifice plate in the discharge pipe of the pump of the water recirculation. Downstream and upstream of the orifice plate pressure transducers were located. The difference of the indicated values in volt of the two pressure transducers was due to the flow rate and consequently from the water velocity in the channel. The pressure transducers were calibrated in order to give certain flow values corresponding to certain volt values. The following three mean velocity values were used in the experiment: 5 cm/sec, 7 cm/sec and 9cm/sec corresponding to 0.5 Volt, 3 Volt and 3.5 Volt respectively. The depth of the flow was 20 cm and was specified with the help of a sluice gate in the downstream part of the channels' water reservoir. The sketch below depicts a ground plan of the experimental configuration. More specifically, the layout for the computation of the velocity field in front of the second mussel shock, placed at a distance L (300, 500, 700 or 900 mm) from the first shock, is shown (Fig. 2).

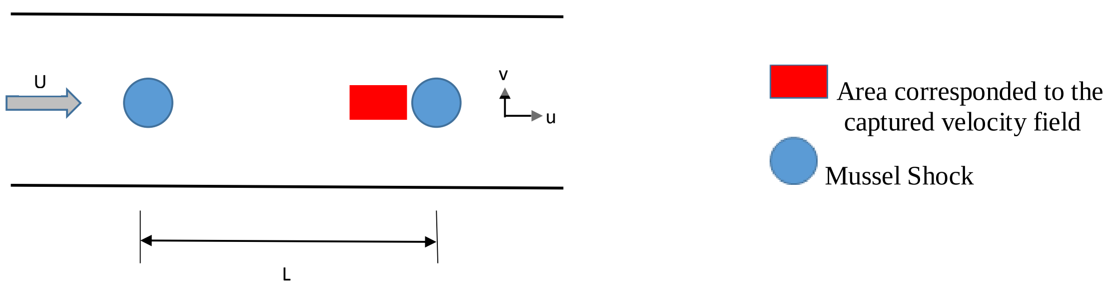

FIGURE 2. SKETCH SHOWING THE MUSSEL SHOCKS (BLUE CIRCLES) AND THE AREA FOR THE DESCRIPTION OF THE VELOCITY FIELD IN FRONT OF THE SECOND MUSSEL SHOCK (RED RECTANGULAR BOX) I.E. UPSTREAM OF THE SECOND SHOCK PLACED AT A DISTANCE L FROM THE FIRST MUSSEL SHOCK

For a certain fixed entrance water velocity U, the velocity field in the orthogonal areas of the above figure (marked in red) was determined. The blue circles in the figure correspond to the mussel shocks depicted as 1a and 2a. The shock 2a can be found either on the axis of channel's symmetry or to the lateral vertical wall of the channel. A basic research parameter used in the experiment was the distance between the shocks 1a and 2a. Four cases were taken into account: 300mm, 500mm, 700mm and 900mm. The final goal was the determination of the velocity field in the areas around the shocks.

2.2 Measurement Technique

The velocity field was studied with the modern technique of PIV (Particle Image Velocimetry) as described in [12]. This technique was recently used successfully by [13] who studied experimentally the effects of surrounding outer porous cylinder on vortex structure downstream of a circular inner cylinder in deep water flow. Furthermore, PIV experiments were conducted by [14] and also included in the recent research by [15]. The specific experimental procedure, adjusted in our laboratory, is described as follows: The system has two lasers which give light pulses in a controlled time (synchronizer) while the time step between two successive pulses for the velocities that we study was determined to 1.5 msec. Two photographs (twin photographs) were taken with camera CCD for each couple of pulses from the two lasers. In 1sec about 3 couples of photographs would be taken. During the realization of the experiment 200 couples of photographs were taken. From each couple a velocity field resulted. The technique of velocity calculation was based on the program INSIGHT 3G of the company TSI. The area of the photograph was divided into small orthogonal/rectangular parts –control areas (interrogation spot) with dimensions 32pxX32px. The distance of the camera from the section of measurements was selected so that in each mm should be 6.5 px and the photographs should have dimensions 20cmx18 cm. From the photographs resulting from the light of the two lasers which ranged in time 1.5 m sec and lightened the exit particles, the particle motion and transport was calculated with the help of FFT method (Fast Fourier Transform) and the Convolution Theorem. In this way the velocities u and v were computed and then the resultant velocity at each control area. The total number of the spots that the velocity value was computed was about 7300.From the measurements the instant values of flow velocity at different places were computed in time and space as well as the mean temporal and spatial velocity value. Moreover, the curves of the velocity profiles along x and y axis resulted as well as the resultant velocities. In this way the water flow around and through the shocks was described.

III. RESULTS

3.1 Distance of 300 mm

In the case of distance between the shocks 300 mm the phenomenon of influence of the first mussel shock to the second shock was very intense, i.e. the generation of the Von Karman vortexes behind the first shock was influenced by the second shock: thus, conclusions for the flow could not be clear (since the flow field behind and the first shock was formed in combination with the flow field of the one in front of the second shock).

3.2 Distance of 500 mm

The velocity field in front of the second shock, corresponding to mean flow velocity of the water at the entrance of the channel 5 cm/sec, is depicted in the following Fig.3a. The velocity field in front of the second shock, corresponding to mean flow velocity of the water at the entrance of the channel 7 cm/sec, is depicted in Fig.3b. The velocity field in front of the second shock, corresponding to mean flow velocity of the water at the entrance of the channel 9 cm/sec, is depicted in the following Fig.3c.

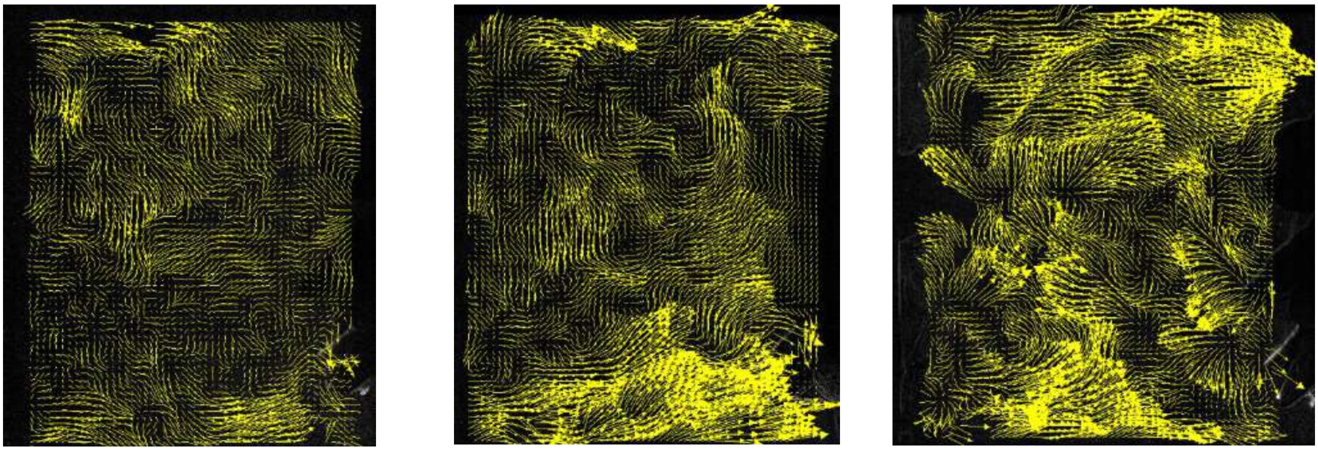

(a) **(b)** **(c)**

FIGURE 3: QUALITATIVE REPRESENTATION OF THE VELOCITY FIELD IN FRONT OF THE SHOCK, CORRESPONDING TO MEAN FLOW VELOCITY AT THE CHANNEL'S ENTRANCE 5 cm/s (3a), 7 cm/s (3b) and 9 cm/s (3c). THE SECOND SHOCK IS PLACED AT A DISTANCE OF 500 mm FROM THE FIRST SHOCK

Intense formation of eddies in front of each mussel shock. From the velocity fields it is clear that the vorticities seem to be intense due to spottiness of the external surface of the mussel shocks. It is this fact that causes reverse water flow.

The velocity profiles near the obstacle (mussel shock), corresponding to the three different cases of the entrance flow velocity (5, 7 and 9 cm/sec) are given all together in Fig 4.

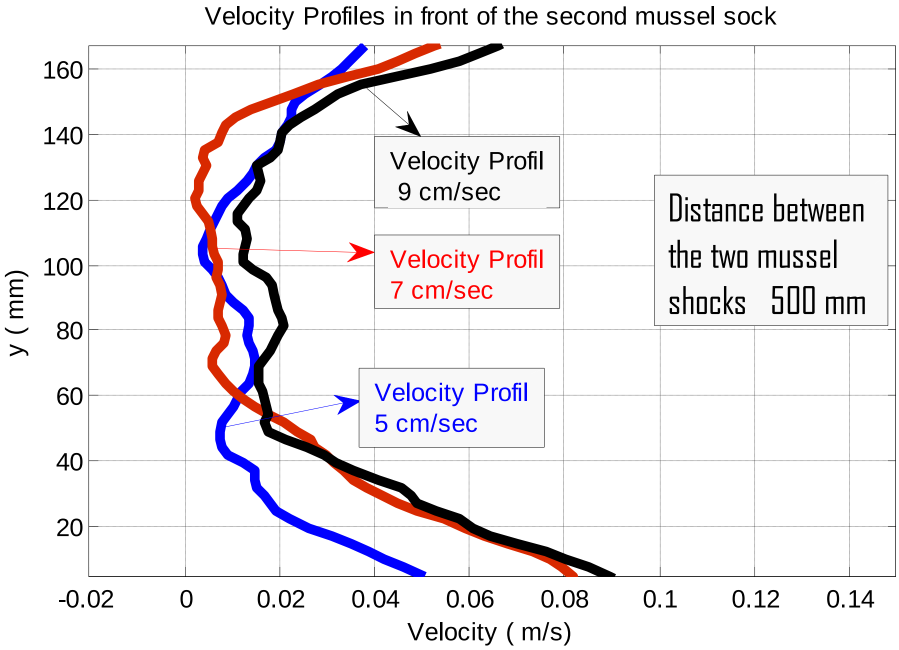

FIGURE 4: VELOCITY PROFILES IN FRONT OF THE SECOND MUSSEL SHOCK, CORRESPONDING TO ENTRANCE FLOW VELOCITIES 5, 7 and 9 cm/sec. THE SECOND SHOCK WAS PLACED AT A DISTANCE OF 500 mm FROM THE FIRST SHOCK.

The three above profiles show that as the entrance flow velocity increases the mean value of the velocity in the axis of symmetry as well as the reflected mass of water decrease. The velocity values greater than zero (u>0) show that the water flow close to the shock is nearly getting zero while the larger amount of the water mass moves laterally of the shocks, i.e. in the vicinity of the channel's walls. The velocity values less than zero (u< 0) are due to the fact that the mussels of the shock create cavities and therefore return of the water mass is observed. It is noted that figure 6showsthemeaninspace (in a distance of 20 mm) as well as mean in time (in a time window of 15 sec) velocity values.

3.3 Distance of 700 mm

The velocity fields in front of the second shock, corresponding to mean flow velocities of the water at the entrance of the channel 5, 7 and 9 cm/sec, is depicted in figure 5a, 5b and 5crespectively.

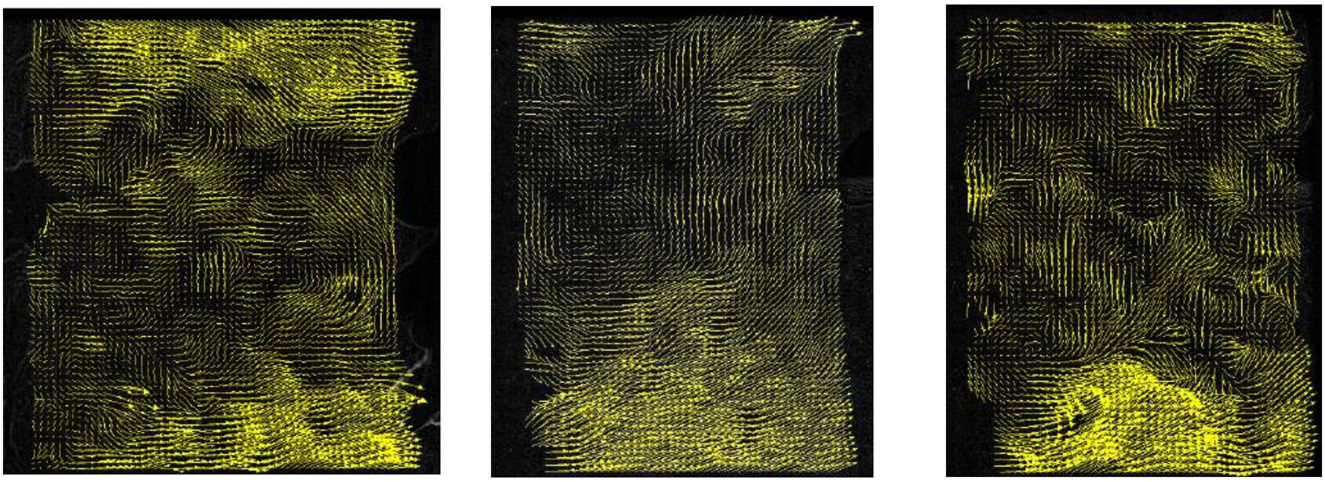

(a) **(b)** **(c)**

FIGURE 5: QUALITATIVE REPRESENTATION OF THE VELOCITY FIELD IN FRONT OF THE SHOCK, CORRESPONDING TO MEAN FLOW VELOCITY AT THE CHANNEL'S ENTRANCE 5 cm/s (5a), 7 cm/s (5b) and 9 cm/s (5c). THE SECOND SHOCK IS PLACED AT A DISTANCE OF 700 mm FROM THE FIRST SHOCK

The velocity profiles near the mussel shock (which obviously behaves as an obstacle), corresponding to the three different cases of the entrance flow velocity (5, 7 and 9 cm/sec) are given all together in the same plot of Fig.6.

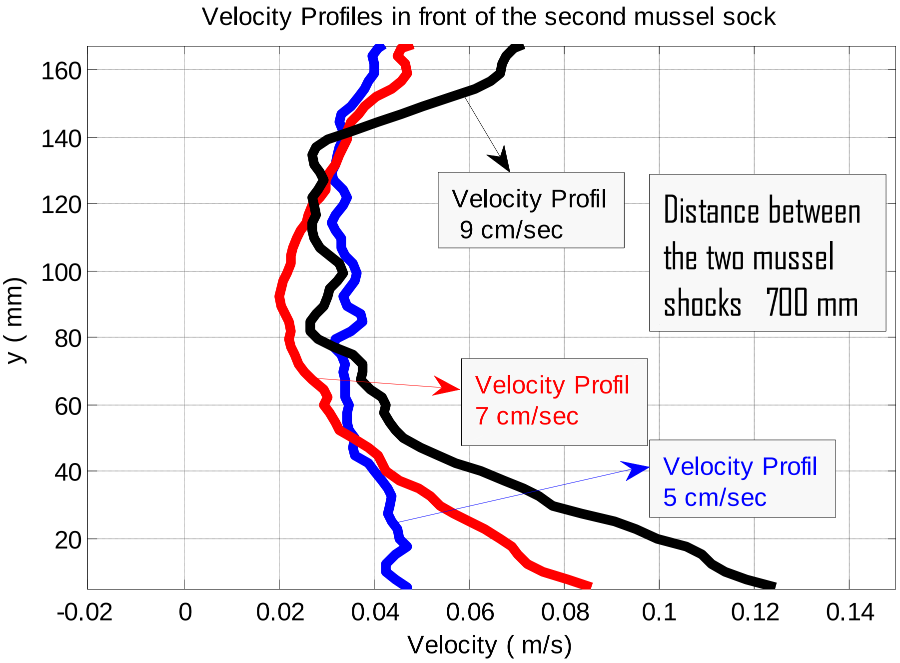

FIGURE 6: VELOCITY PROFILES IN FRONT OF THE SECOND MUSSEL SHOCK, CORRESPONDING TO ENTRANCE FLOW VELOCITIES 5, 7 and 9 cm/sec. THE SECOND SHOCK IS PLACED AT A DISTANCE OF 700 mm FROM THE FIRST SHOCK

3.4 Distance of 900 mm

The velocity fields in front of the second shock, corresponding to mean flow velocities of the water at the entrance of the channel 5, 7 and 9 cm/sec, is depicted in Fig.7a, 7b and 7c respectively.

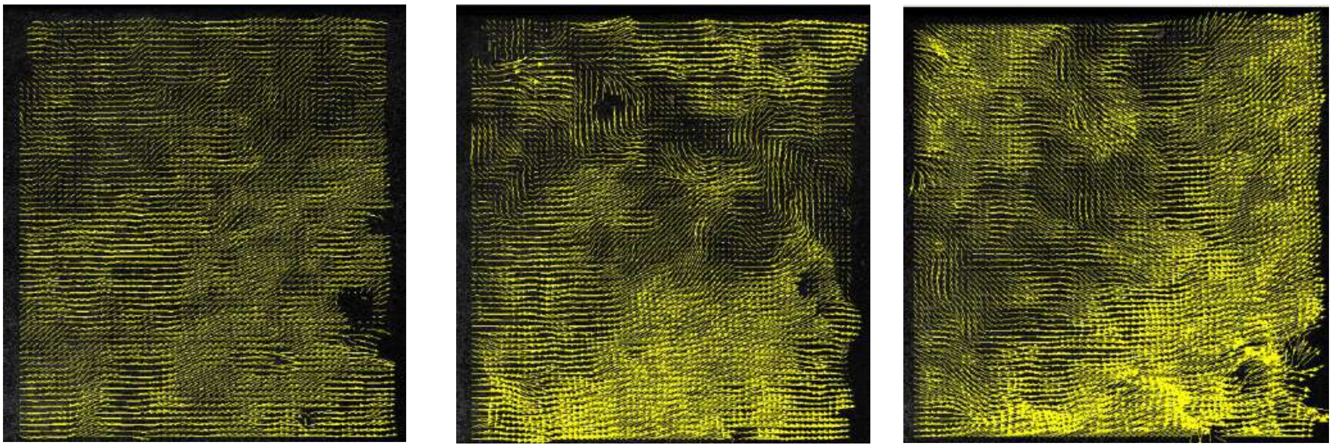

(a) **(b)** **(c)**

FIGURE 7: QUALITATIVE REPRESENTATION OF THE VELOCITY FIELD IN FRONT OF THE SHOCK, CORRESPONDING TO MEAN FLOW VELOCITY AT THE CHANNEL'S ENTRANCE 5 cm/s (7a), 7 cm/s (7b) and 9 cm/s (7c). THE SECOND SHOCK IS PLACED AT A DISTANCE OF 900 mm FROM THE FIRST SHOCK

The velocity profiles near the mussel shock, corresponding to the three different cases of the entrance flow velocity (5, 7 and 9 cm/sec) are given all together in Fig 8.

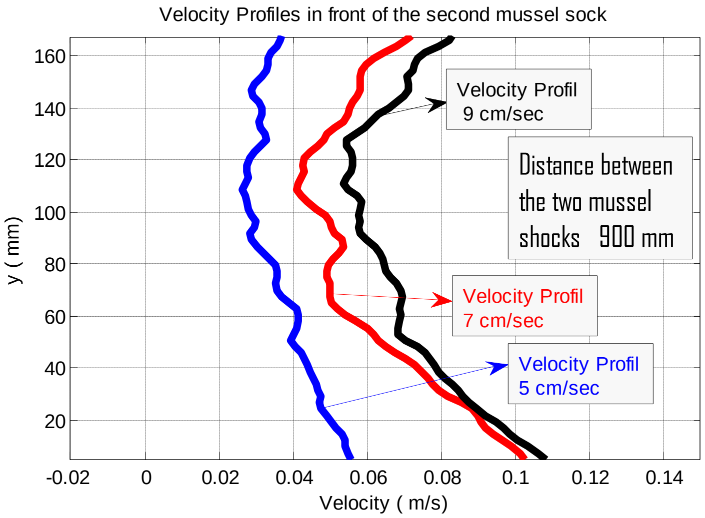

FIGURE 8: VELOCITY PROFILES IN FRONT OF THE SECOND MUSSEL SHOCK, CORRESPONDING TO ENTRANCE FLOW VELOCITIES 5, 7 AND 9 cm/sec. THE SECOND SHOCK IS PLACED AT A DISTANCE OF 900 mm FROM THE FIRST SHOCK.

It is interesting here to note that figure 8 shows that the case of larger distance between the shocks (i.e. 90cm)presents the largest percentage of the velocity class 5-10cm/sec that seems to occur for initial entrance current velocities 7 and 9 cm/s, which is in agreement with field observations reported by Savvidis et al. 2015 and already commented in the introduction. Also, it is observed that for distance between the shocks 900 mm, the differences of velocity profiles is quite more distinct for the different entrance current velocities 5, 7 and 9 cm/sec.

The velocity profiles U along the flow direction (axis x) (with the normal axis corresponding to V velocities) show that the velocities are characterized by intense changes due to the irregularities of the mussels' surface. More specifically, values >0 and <0 observed in the field lead to the conclusion that negligible or minimal flow is developing through the body of the mussels. Consequently the mussel shock behaves as a nearly solid (rigid) body.

3.5 Further issues to be checked

The low velocities close to the shocks raised the question if there is flow through the body of the mussel shocks and for that reason another one experiment was realized for the control of the flow though the shock. The photo below (Fig 9) shows the confirmation that there is minimal flow inside and through the body of the mussel shocks.

FIGURE 9: ADDITIONAL EXPERIMENTS FOR THE FLOW UPSTREAM AND DOWNSTREAM OF THE MUSSEL SHOCK

Two shocks were located normally to the flow direction so that the water flow could be investigated. For mean velocity 10cm/sec rise of the surface water level upstream about 12.5 cm while the surface water level downstream was 2.5cm/sec. The observed flow was due to the spaces in-between the two shocks. The head loss (drop of the pressure) of the 10 cm from the upstream position to the downstream position does not seem to allow flow through the body of the mussel shocks, or at least allows negligible flow. Moreover, if we take into account the fact that the hydraulic head of 5 cm corresponds to velocity 1m/sec, while the water velocity in our experiment is 0.1 m/sec, then we can conclude that there minimal flow through the body of the mussel shocks, while the main flow seems to occur through the spaces between the two shocks (the upper and the lower ones). This conclusion is enhanced from the observation of the flow during the realization of the experiment.

IV. CONCLUSIONS

The following conclusions have been raised from the experimental procedure and the analysis of the data collected.

a) For the distance between the mussel shocks 500 and 700 mm the velocity profiles (fig.6και10) seem to have the same values in the central area of the shock for the different entrance (initial) current velocities with small divergences concerning the velocity profiles for initial current velocity 9 cm/sec

b) For distance between the shocks 900 mm, the distinction (difference) of velocity profiles is more clear (intense) for the different entrance (initial) current velocities. Moreover the case of larger distance between the shocks (i.e. 90cm) seems to present the largest percentage of the velocity class 5-10cm/sec that seems to occur for initial entrance current velocities 7 and 9 cm/s, which is in line with previous research findings in the field.

c) For shock distances between the shocks greater than 500 mm the velocity field is almost restored. This is obvious from the pattern of the velocity fields and the velocity profiles.

d) The comparison of the diagrams with the velocity profiles show that the increase of distance between the shocks leads to increase of the velocity values. For values of the initial current velocity 5 cm/sec the velocity profiles for distances 700 and 900 mm nearly coincide

e) From the velocity fields it is clear that the vorticities seem to be intense due to spottiness of the external surface of the mussel shocks. It is this fact that causes reverse water flow.

f) In large values of the mean water velocities, large returning velocities are observed while the resultant velocities (mean values in time and space) are decreasing significantly close to the mussel shocks. Those mean values close to the shocks are of the order of 1 cm/sec or below this value.

g) Intense formation of eddies in front of each mussel shock is observed.

ACKNOWLEDGMENTS

Acknowledgement: SUCCESS project has received funding from the European Union’s H2020 program under grant agreement No 635188.

REFERENCES

[1] National Center of Marine Research (NCMR) (2001), “Management Study of the Zones of Mussel Production in Thessaloniki and Thermaikos Bays”. Final Report for Fisheries Directorate of Thessaloniki Prefecture, Supervisor E. Papathanasiou, pp. 147

[2] Sofia Galinou -Mitsoudi, Yiannis Savvidis and Xenofon Dimitriadis, (2006). ‘Interaction between mussel cultures and hydrodynamics; a preliminary study in Thessaloniki & Thermaikos Gulfs’ Journal of Biological Research, Vol. 6, pp. 139-145

[3] Savvidis, Y., Antoniou, A., Dimitriadis, X., Moriki, A., Galinou – Mitsoudi, S. Alvanou L., Petridis, D. and Koutitas, C., (2007). “Hydrodynamics in a mussel culture area in Thermaikos gulf” in Proceedings of the 8th International Conference on the Mediterranean Coastal Environment, MEDCOAST 07. Alexandria, Egypt, 1263-1274.

[4] Moriki A, Galinou-Mitsoudi S, Petridis D, Kosti D, Savvidis Y, Dimitriadis X, Koutitas C, Alvanou L (2008),“Environmental impacts of intensive mussel culture in the coastal waters of the gulf of Thessaloniki (N. Greece)”. Fresenius Environmental Bulletin, 17, 1945-1955

[5] Savvidis Yiannis, Alexandros Antoniou, Vasilis-Orestis Stoilas and Sofia Galinou-Mitsoudi (2015) “Hydrodynamics in longline mussel culture layouts” 12h International Conference on the Mediterranean Coastal Environment MEDCOAST 2015, Varna, Bulgaria, 6-10 October 2015

[6] Konstantinou Z, Savvidis Y., Kombiadou K. and Krestenitis Y. (2011), “Mussel farm layout scenarios as management alternatives”,In: Ozhan, E. (Ed),Proceedings of the Tenth International Conference on the Mediterranean Coastal Environment - MEDCOAST 2011, 25-29October, Rhodes, Greece, 735-746.

[7] Konstantinou, Z. (2013), “Integrated Coastal Management through the Utilization of Conceptual and Numerical Tools” Ph.D Thesis, Department of Civil Engineering, Aristotle University of Thessaloniki, Greece (in Greek).

[8] Inglis GJ, Hayden BJ, Ross AH (2000), “An overview of factors affecting the carrying capacity of coastal embayments for mussel culture”,NIWA client report, National Institute for Water and Atmospheric Research Ltd, New Zealand, p. 38.

[9] David Russell Plew (2005) The Hydrodynamic Effects of Long-line Mussel Farms. PhD thesis Department of Civil Engineering, University of Canterbury, Christchurch, New Zealand

[10] DEHKORDI Behzad Ghadiri, MOGHADDAM Hesam Sarvghad, JAFARI Hamed Houri (2011) NUMERICAL SIMULATION OF FLOW OVER TWO CIRCULAR CYLINDERS IN TANDEM ARRANGEMENT. Journal of Hydrodynamics 2011,23(1):114-126, DOI: 10.1016/S1001-6058(10)60095-9

[11] A. F. Abdel Gawad, N. A. Mohamed, S. A. Mohamed, M. S. Matbuly (2013) Investigation of the channel flow with internal obstacles using large eddy simulation and finite-element technique, Applied and Computational Mathematics, 2013; 2(1) : 1-13

[12] Adrian Ronald J., (1991) PARTICLE-IMAGING TECHNIQUES FOR EXPERIMENTAL FLUID MECHANICS, Annu. Rev. Fluid Mech. 1991, 23 : 261 304

[13] B. Gozmen, E. Fırat, H. Akilli and B. Sahin (2017) Flow control behind a circular cylinder via a porous cylinder in deep water EPJ Web of Conferences

DOI: 10.1051/ C_Owned by the authors, published by EDP Sciences, 2013, epjconf201 / 01035 (2013) 4534501035

[14] Keramaris E, Pechlivanidis G (2013) PIV measurements over a permeable and an impermeable bed, J. of Porous Media 16(1):21-28.

[15] Savvidis Y., E. Keramaris, Pechlivanidis G and C. Koutitas (2017) Optimum Design of the Entrance of a Fishpond Laterally to the Main Stream of an Open Channel, Environmental Science and Pollution Research, DOI: 10.1007/s11356-017-8696-z

A Face Recognition Library using Convolutional Neural Networks

Leonardo Blanger[1], Alison R. Panisson[2]

[1]Department of Engineering and Computer Science, URI University, Erechim - Brazil
[2]School of Informatics, Pontifical University of Rio Grande do Sul, Porto Alegre - Brazil

Abstract**—** *In this work, we propose a face recognition library, with the objective of lowering the implementation complexity of face recognition features on applications in general. The library is based on Convolutional Neural Networks; a special kind of Neural Network specialized for image data. We present the main motivations for the use of face recognition, as well as the main interface for using the library features. We describe the overall architecture structure of the library and evaluated it on a large scale scenario. The proposed library achieved an accuracy of 98.14% when using a required confidence of 90%, and an accuracy of 99.86% otherwise.*

Keywords—Artificial Intelligence, CNNs, Face Recognition, Image Recognition, Machine Learning, Neural Networks.

I. INTRODUCTION

Nowadays, face detection and face recognition technologies are commonly present among online services provided by big Internet companies, such as Facebook and Google. Currently, some of the best image recognition techniques we have are based on variations of (Deep) Artificial Neural Networks (ANNs). For instance, the authors in [11] used such techniques to achieve record performance on the LSVRC[1]competition. However, the implementation of such systems is still complex, in the sense of knowledge required. This imposes a great difficulty for independent developers without the necessary AI expertise to apply face recognition in their own projects.

Among the practical situations where face recognition can be applied are:

- Surveillance systems, on places such as industries, offices, banks, etc., where it is necessary to have a control over the allowed staff;
- Employee control, in the form of biometric presence monitoring systems. Controlling the employee frequency provides useful metrics for human resources departments;
- Efficient login on applications, instead of a password, or in addition to it, in order to verify user authenticity on the recovering of forgotten passwords;
- Personalized user experience on systems such as smart houses, cars, or personal assistants;
- Social network applications on which users can share pictures;
- As an additional feature for mobile applications.

In order to provide an easy way for developers to apply face recognition on independent projects, we propose a software library for this task. The library created by us allows users to register new faces, monitoring the expected accuracy of the predictions, and predict probabilities over the registered faces when presented to images.

The proposed library works internally using a Convolutional Neural Network (CNN), a special kind of ANN with architecture specialized for taking advantage of some properties in image data. Beyond this, the library architecture makes heavy use of regularization techniques and artificial generation of data, in order to improve generalization capacity.

The main contributions of this work are: (i) we propose CNN architecture for image recognition; (ii) we developed a general purpose face recognition library for *Python* using the proposed architecture; and (iii) we evaluated the library architecture on a large scale scenario using a public dataset of face images.

II. ARTIFICIAL NEURAL NETWORKS

Artificial Neural Networks (ANNs), or simply Neural Networks (NNs), are a kind of predictive model. It is considered a machine learning technique inspired by the way the biological brain works [15].

---

[1] `www.image-net.org/challenge/LSVR`

Standard NNs are usually interpreted as a set of layers of units, each unit being a function of the previous layer. There is always an input layer, which assumes the values of the input of the prediction, an output layer, which will present the prediction output, and a set of hidden layers, as in Fig.1. The term Deep Learning is usually associated with NNs with multiple hidden layers [15].

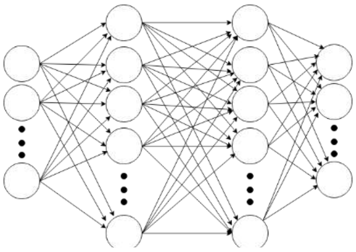

FIGURE 1 - AN ARTIFICIAL NEURAL NETWORK WITH TWO HIDDEN LAYERS

Each unit calculates a *logit* value, that is, a weighted sum of the outputs of the previous layer added to a bias value. The unit's output is then the application of an activation function on this logit value. The set of weights and the bias are the parameters that influence the mapping from the previous layer to the unit's output value. The goal of using ANNs is to adjust all the network parameters to make it predict some data correctly. For instance, predicting the person on a picture based on the pixels intensities. For this, the network uses a set of examples, called the training set. A good training set is a good approximation of the real distribution of data [6].

A cost function is a function, $C(\theta)$, where θ is the set of all the network parameters. This function evaluates how bad a specific configuration of the parameters is at predicting the training data. The training algorithm consists on iteratively adjust the parameters in order to decrease the cost. From calculus, we know that the gradient vector of a function points to the direction of steepest increment of this function. At the same time, the opposite direction points to the direction of steepest decrement. Based on this, at each iteration *t*, the network parameters are adjusted on the following way:

$$\theta_i^{t+1} = \theta_i^t - \epsilon \frac{\partial C}{\partial \theta_i} \tag{1}$$

Where ε is the **learning rate**, a (usually small) positive scalar that controls how much the parameters change at each iteration. This value is usually set to a large value at the beginning of training, to make the network quickly explore the parameter space and find a low cost region, and then we decrease it throughout the training, to make the network sensibly find the local minimum of this region.

This strategy of iteratively decreasing the cost using the partial derivatives is called **Gradient Descent**. We do not usually use all the training examples at each iteration. Instead, we select a different batch to estimate the cost at each iteration. This approach can take more iteration to find a good cost, due to statistical instabilities, but in advantage, it makes the individual iterations much faster. This strategy of estimating the cost using a random batch is called **Stochastic Gradient Descent** [15].

In order to make the network more capable of generalizing the prediction to new data (data not present on the training set), it is common to apply generalization techniques during training. These techniques aim to make the network learn more robust solutions, capable of identifying more frequent and realistic patterns from the training data, which are more likely to be present on the real data.

A commonly used regularization technique is *L2 Penalty* [15], which consists on adding another function to the cost, which grows proportionally to the square of the network parameters, scaled by some penalty. By decreasing the cost, the training algorithm will keep the parameters small in magnitude. This forces the network to find more simple solutions, capable of identifying more frequent patterns on the data.

Another common technique is *dropout* [11][7], which consists on, at each iteration, ignoring the output of some random units of a layer, using some predefined probability. This makes the units more individualistic during learning, which forces the network to find more robust solutions. When presented to unseen data, all the units are used, and the network is expected to perform better.

The easier way to make the network generalize better is by using more data for training, in order to have a sample that better approximates the true distribution of real data, minimizing the effect of individual irregularities. This can be done by either collecting more data or by artificially generating more samples from the already collected data (by distortions, reflections or addition of noise)[17].

2.1 Classification Tasks

When performing classification tasks, it is useful to have a probability distribution over the possible categories as the model's output. For this, the last layer of an ANN is commonly a *softmax* layer. On such layer, the output of the unit, y_i, is defined as:

$$y_i = \frac{e^{z_i}}{\sum_{j=1}^{n} e^{z_j}} \tag{2}$$

with z_i being the logit value of unit *i*.

III. CONVOLUTIONAL NEURAL NETWORKS

CNNs [12] are a kind of Deep Neural Network that uses Convolutional Layers as the first hidden layers of the network. These layers have an architecture designed to make better use of the knowledge obtained from the spatial structure present on image data.

Convolutional layers are based on the concept of local receptive fields[15]. On a convolutional layer, each unit is a mapping from a region (field) of neighboring outputs from the previous layer. In Figure 2, we have a receptive field of size 4×4, from a previous layer of 10×10. The connections to the first unit are shown in gray, on the left. For each of the next units, the receptive field is shifted right or down at a stride length. If this stride length is 1 on the horizontal direction, then the connections of the second unit are as in Figure 2 (right).

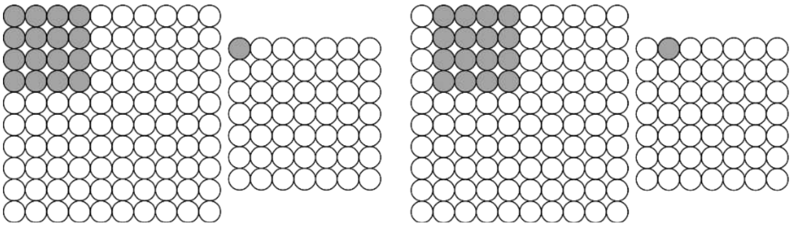

FIGURE 2 - CONNECTIONS OF THE FIRST (LEFT) AND SECOND (RIGHT) UNITS OF A CONVOLUTIONAL LAYER

Also, the set of parameters on all the units on the layer is shared, so that all the units perform the same mapping from different parts of the previous layer. The reason for sharing the mappings is to try to detect the same patterns that are present on different parts of the image. In order to detect multiple patterns, it is used not only one, but several mappings, each of which with a different set of parameters. Each mapping on a convolutional layer is called a *feature detector* [15].

In order to try to identify the presence of the same features on groups of nearby output units, the *polling* technique is frequently applied to the output of convolutional layers [15]. A common kind of pooling is the *max-pooling*, which consists on outputting the maximum value present on a group of units from the convolutional layer. The reason behind this is to try to detect the presence of features, losing some information about its exact position on the image. For instance, knowing that an image has a nose and an eye strongly indicates the presence of a face, not mattering where on the image these features are. The use of pooling on image classification can allow a certain degree of translation invariance [15], and thus, overcome the effects of small variations of pose, angle and distance. Another advantage is that they do not add any extra parameter to be trained.

The main motivation for the use of CNNs on image recognition is the fact that these kinds of models are capable of extracting spatial features from the data. Image data have a nice and useful hierarchical decomposition: groups of nearby pixels can form edges, groups of nearby edges can form polygons, and so on, until complex visual structures are formed. Because of this property, CNNs usually use a chain of convolutional and pooling layers, with the output of one being the input to the next. [14][4][11][10].

IV. FACE RECOGNITION LIBRARY

In this section, we describe the developed face recognition library, focusing on the methods that are used to register new faces, make the recognizer fit the model to the provided data, and use the recognizer to predict the probability of the registered faces when presented to new images. The main class of the library is the Recognizer class, which is instantiated as follows:

```
recognizer = Recognizer(width, height, channels,
                        image_dir, dataset_dir, models_dir,
                        qt_images, valid_proportion)
```

where the parameters `width` and `height` are the dimensions of the images to be fed into the network, `channels` is the depth of the pixels: 1 for grayscale, 3 for RGB, etc., `image_dir` is the path to save the training images, `dataset_dir` is the path to save the preprocessed training data, `models_dir` is the path to save the network's checkpoints, `qt_images` is the minimum number of images of each person to use, and `valid_proportion` is the proportion of these images to be used for validation, i.e., to estimate the prediction accuracy.

The register of a new person on the system is done as follows:

```
recognizer.add_person(pictures, name)
```

where `pictures` is a list containing the paths to the person's pictures that the user is providing for the library. If an image is not of size *width* × *height*, it is automatically reshaped. If there are less than `qt_images`, the library artificially generates more images from these ones, using different degrees of translations and rotations, in a similar way as is done in [17].

The generation of new images is performed as follows. The translations are made by shifting the pixels some number of units to the left, right, top, and bottom of the image, ignoring the parts that end outside the frame, and filling the empty pixels with black. The rotations are made both clockwise and counter-clockwise, also ignoring the outside parts and filling the empty pixels with black. Initially, the images are shifted one unit on each of the four directions, and one degree in each orientation, and then two, and so on, creating six new images for iteration, until the number of original images plus the generated ones reaches the required number of images for training.

The received images have their pixel values rescaled to avoid big input numbers. As grayscale pixels and single components of RGB pixels both assumes single integers from 0 to 255, the recognizer scales the pixel values to (`pixel_value` − 127.5)/255. After this rescaling, the pixel values of all images are compressed on a file inside `dataset_dir`, using a friendlier format for the training algorithm, and with a proper separation between training and validation sets.

To request the library to adjust the model to the currently registered people, we call:

```
recognizer.train_model(num_steps, valid_interval, start_over)
```

where `num_steps` is the number of iterations to train, `valid_interval` is the number of iterations on which the network accuracy is estimated on the validation set, and `start_over` is a boolean variable indicating that the model should either initialize its parameters and start training from the beginning, or use the last checkpoint saved on `models_dir`.

For using the library to predict the person on a picture, we need to call:

```
predictions = recognizer.predict(picture)
```

where this method receives `picture`, the path of the image to be analyzed, and returns a vector with dimension equals to the number of people registered, representing a probability distribution over these people. The higher the probability of a person, the more the network believes the image is from this person.

Other hyper-parameters (batch size, dropout probability, weight penalty, number of units per layer) can be easily modified through this Recognizer object. Although, for any change to reflect on the predictions, it is necessary to retrain the model. The same applies for the addition of new people.

V. NETWORK ARCHITECTURE

The network architecture was developed using *TensorFlow*[2][1], [2], an open source software library for numerical computation that was originally developed by researchers and engineers working on the Google Brain Team, for machine learning purposes.

---

[2] More information available on `www.tensorflow.org`

The network is a chain of convolutional and pooling layers, followed by fully connected layers. The number of layers of each type, as well as the number of units in each layer can be easily set through the `Recognizer` object. The input layer is a 3D tensor of size *width*×*height*×*channels*, which just assumes the pixel intensities of the images. In the default configuration, the first six hidden layers are an intercalation of three convolutional layers and three pooling layers, and the next hidden layer is a fully connected layer which starts with 512 units by default. The output layer is an *n-way* softmax, where *n* is the number of registered people. The softmax function is used to make the output of the last layer a probability distribution over the possible categories [6]. With the exception of the units on the output layer, all the other units apply the *Rectified Linear Function* as an activation function, which is simply equal to *max(0, z)*, with *z* being the unit's logit value.

Each of the convolutions has 16 feature detectors, each of them with a receptive field of size 10 × 10 over the output of the previous pooling layer (or the image pixels for the first convolution). Each of the pooling layers applies a max-pooling function to the convolution's output with a field of size 2 × 2 and a stride length of 2, both horizontally and vertically. With this pooling stride, every pooling layer halves the dimensions of the previous output.

Prior to the training, the network parameters have to be initialized. The unit weights are set to random values, drawn from a normal distribution with mean zero, and standard deviation equals to 0.1. The unit biases are set to zero on the convolution's units and 1 on the last two fully connected layers.

The training phase is performed using an initial learning rate of 0.01, which is decreased by 10% at each 500 training iterations. At each iteration, the cost gradient is estimated based on a batch of 32 samples from the training set, and the cost function used is the average cross entropy error [6]:

$$C = -\frac{1}{|B|}\sum_{x\in B}\sum_{i=1}^{n} t_i^x \ln y_i(x) \tag{3}$$

where *B* is the batch of samples of the current iteration, *x* is a training sample, *n* is the number of people registered, t^x is the one-hot label vector of the samplex, that is, a vector with 1 on the position corresponding to the correct person and zeros on all other positions, and *y(x)* is the output vector of the network for the simplex, that is, the output of the softmax layer. The overall network architecture can be seen on Figure 3.

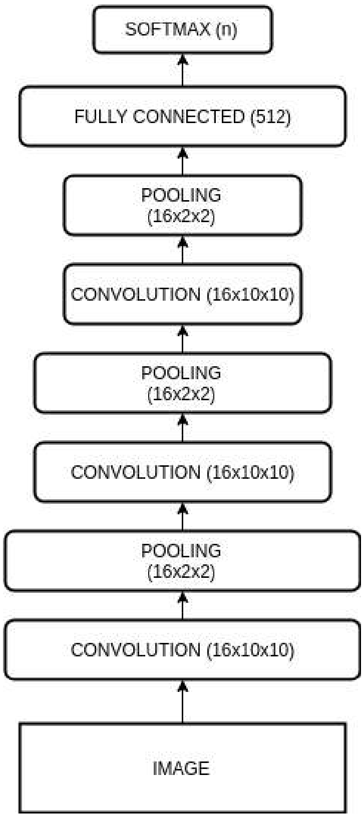

FIGURE 3– OVERALL VIEW OF THE DEFAULT NETWORK ARCHITECTURE

In order to improve the generalization capacity, it is applied an *L2 Penalty* [15] to all the network weights, with a penalty of 0.001, and it is applied dropout [11][7] on the fully connected hidden layers, with the units having a probability of being used of 0.3. The accuracy is estimated on the validation data periodically according to the parameter valid interval, and informed to the user.

For using the model to recognize new faces, the final configuration of the parameters is chosen to be the configuration on which the network had the best validation accuracy, not mattering how many iterations were performed after.

VI. EVALUATION

6.1 Dataset

The data used for the library test is the *Extended Yale Faces Dataset B*(**B+**)[3][5]. This dataset consists of 16380 pictures of 28 different people, with 585 pictures of each person, using different variations of pose and illumination. All the images were grayscale of size 640 × 480 pixels. Some samples of this dataset are shown in Figure 4.

---

[3] Dataset publicly available at `http://vision.ucsd.edu/content/extended-yale-face-database-b-b`

FIGURE 4 - SOME SAMPLES OF THE B+ DATASET

From this datasets, we selected 50 random images from each person to compose the test set. These 1400 images were only used for the final test of the library and were not used for any training or estimation purposes.

The recognizer was instantiated to use grayscale images of size 100 × 100, and expect a minimum of 700 images for each person. The remaining 535 images of each person were registered on the recognizer, which rescaled them to the appropriate size, and artificially generated more images to compose the 700 required images. The recognizer was instantiated with a validation proportion of 0.1, thus, 630 random images of each person were used for training and the remaining 70 images were used as the validation set to estimate the generalization capacity.

6.2 Training Phase

We then run the Gradient Descent algorithm for 3000 iterations, using the default library configuration: initial learning rate of 0.01, L2 penalty of 0.001, the probability of being used when using dropout of 0.3, and the default configuration for the overall network structure. The validation set was analyzed at each 100 iterations.

We recorded the training cost at each iteration, which is plotted on Figure 5. The graph is plotted logarithmically because the main variations occur on the beginning of training. It is possible to see that the network quickly found a low cost region on the parameter space, and then specialized to approximate the local minimum of this region.

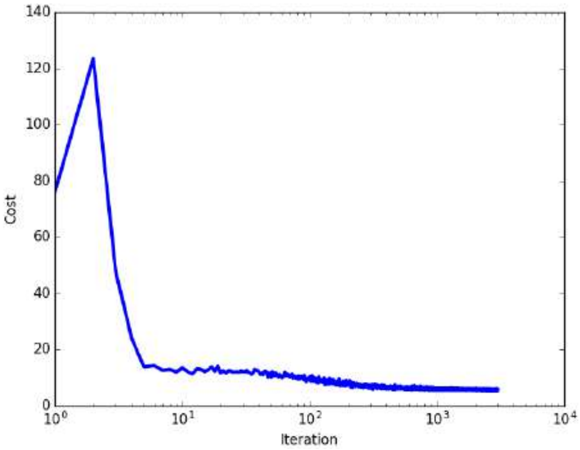

FIGURE 5 - COST RELATED TO THE RANDOM BATCHES OF 32 IMAGES DURING TRAINING ITERATIONS.

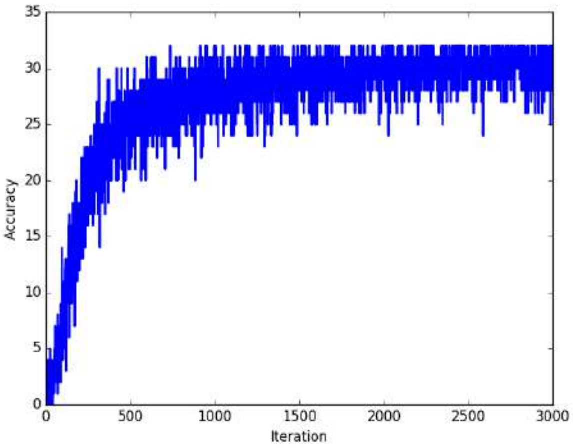

FIGURE 6–NUMBER OF CORRECTLY PREDICTED IMAGES RELATED TO THE RANDOM BATCHES OF 32 IMAGES DURING TRAINING ITERATIONS

On Figure 6, we can see the number of correctly predicted images. This shows that the network learned to recognize the images correctly as the cost lowered, meaning that the cost function truly captures the prediction accuracy. We considered a prediction to be correct if the network attributed the highest probability to the correct person.

On the cost (Figure 7) and accuracy (Figure 8) on the validation set, we can see that the network has extracted real patterns from the faces, being able to generalize the prediction to unseen data.

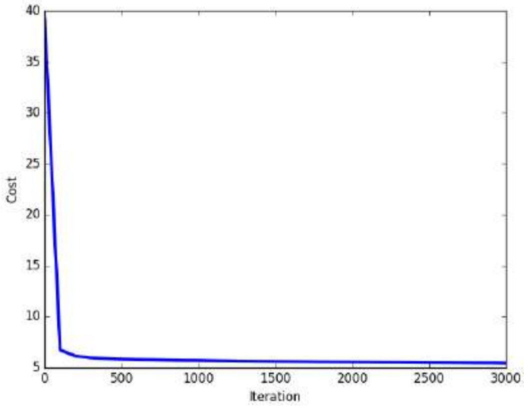

FIGURE 7 - COST FROM THE VALIDATION SET DURING TRAINING ITERATIONS

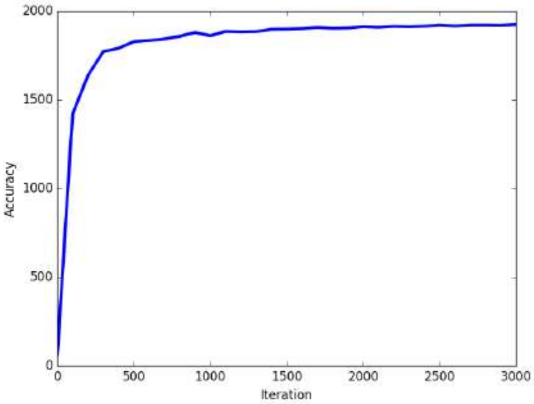

FIGURE 8 - NUMBER OF CORRECTLY PREDICTED IMAGES FROM THE VALIDATION SET DURING TRAINING ITERATIONS

The best validation accuracy occurred on the last validation, at the iteration number 3000 of the training. Then the parameter's configuration on this iteration was chosen to be the official model for future predictions.

As the final evaluation, we presented the trained library with the 1400 images reserved as the test set. If we considered a prediction to be correct if the network assigned the higher probability to the correct person, then the network correctly predicted 1398 of the 1400 images, an accuracy of 99.86%. If we considered a prediction to be correct if the network assigned a probability greater than 0.9 to the correct person, than the network correctly predicted 1374 of the images, an accuracy of 98.14%. However, if we consider this second metric, as the network has never assigned more than 0.9 to a wrong person, than the network did not classify any image erroneously. In these situations, the recognizer considers this face as unknown, which is an important feature on security applications.

VII. RELATED WORK

The authors in [11] used a CNN with dropout trained on a GPU for the *ImageNet* dataset from the LSVRC-2010 contest. The images were of high-resolution and belonging to 1000 different object classes. Their network achieved a top-1 and top-5 error rates of 37.5% and 17.0% respectively, a considerably improvement from the previous state-of-the-art models.

In [17], the authors presented a set of good practices for the development of CNNs for document recognition. It is explained the importance of the dataset size. It is also proposed a flexible architecture for document retrieval that is evaluated on the MNIST dataset [13]. As one of the contributions of our work, we have abstracted the process of artificial generation of data in order to transparently handle the possibility of few data samples.

In [4], it is proposed a model based on a committee of 7 deep CNNs trained on GPUs applied to handwritten digits and letters recognition. They reported an error rate of 0.27% for MNIST dataset [13]. In our work, we extended the application of CNNs to the faces domain, allowing the use images with much higher resolution than the 28 × 28 MNIST images.

In [8], the authors provided an evaluation of CNNs on large-scale video classification using a dataset of 1 million YouTube videos and 487 classes. They analyzed a number of approaches of extending the connectivity of CNNs to the time domain, in order to take advantage of the spatial-temporal information of video data.

In [14], the authors proposed CNN architecture for handling the task of face detection on images. In real world scenarios, this task is considered hard because of the many variations on distance, angle, pose, light, background color and objects, presence of more than one face, etc. The proposed architecture quickly discards large portions of background at low resolution and then carefully analyzes high resolution smaller portions. Our work is complementary with [14], in the sense that face detection is a commonly prior stage of face recognition.

In [9], it is done a research on different face recognition techniques for biometric systems. They showed the advantages of different NN approaches compared to other methods, as well as the current limitations. The contribution of our work is in the sense of providing a library abstracting the complexity of such techniques, as well as demonstrating, through a large scale experiment, the potential of CNNs on achieving high accuracy and not making mistakes on the prediction.

The authors in [16] used CNNs to build a mapping from face images to vector points, and then use the distance between these points as a direct measure of similarity between faces. They achieved a representation efficiency of 128 bytes per face.

In [3], it is proposed an open-source face recognition implementation called *Open Face* based on the work of[16]. They provided a web page with comparisons of accuracies of models[4] and concluded that face recognition is still an unsolved problem, with many issues yet to be handled, and accuracies from research papers have just begun to surpass human accuracies. One important contribution of our work over existing ones is the automatic generation of data, with the objective of compensates small number of pictures available, and thus, improving generalization capacity through better representative datasets.

VIII. CONCLUSION

In this work, we proposed a face recognition library in *Python*, with the objective of lowering the implementation complexity of face recognition features in applications in general. We provided the description of the main library features, as well as a description of the general architectural model of the internal CNN.

Despite the current existence of a similar software library [3], face recognition is still not a fully solved problem, with human level accuracies being surpassed only on the last few years. In this perspective, the main contributions of our work are: (i) we proposed CNN architecture for image recognition; (ii) we developed a general purpose face recognition library for python using the proposed architecture; (iii) we evaluated the library architecture on a large scale scenario using a public dataset of face images;

The proposed library achieved high accuracy on a large scale task of simple recognition. Also, when using a required confidence of 90%, the network did not classified any image erroneously, which is an important requirement for security systems. In summary, the results showed an excellent generalization capacity.

In future works, we intend to apply the library on real mobile apps and evaluate its performance. We also intend to further improve the library, investigating the relation between number of categories (people), amount of available data, and network capacity, with the objective of implementing a partially automatic generation of the model's architecture based on specific problems.

REFERENCES

[1] M. Abadi, A. Agarwal, P. Barham, et al., "Tensorflow: Large-scale machine learning on heterogeneous distributed systems," 2016, *arXiv preprint arXiv:1604467.*

[2] M. Abadi, P. Barham, J. Chen, et al., "Tensorflow: A system for large-scale machine learning," In Proceedings of the 12th USENIX Symposium on Operating Systems Design and Implementation (OSDI), Savannah, Georgia, USA, 2016.

[3] B. Amos, B. Ludwiczuk, M. Satyanarayanan, "Openface: A general-purpose face recognition library with mobile applications," Techical report, CMU-CS-16-118, CMU School of Computer Science, 2016

[4] D. C. Ciresan, U. Meier, L. M. Gambardella, J. Schmidhuber, "Convolutional neural networks committees for handwritten character classification," In 2011 International Conference on Document Analysis and Recognition (ICDAR), IEEE, pages 1135-1139.

[5] A. Georghiades, P. Belhumeur, D. Kriegman, "From few to many: Illumination cone models for face recognition under variable lighting and pose," IEEE Trans. Pattern Anal. Mach. Intelligence, 2001, 23(6):643-660.

[6] I. Goodfellow, Y. Bengio, A. Courville, "Deep Learning," MIT Press, 2016, www.deeplearningbook.com

[7] G. E. Hinton, N. Srivastava, A. Krizhevsky, I. Sustskever, R. R. Salakhutdinov, "Improving neural networks by preventing co-adaptation of feature detectors," 2012,*arXiv preprint arXiv:1207.0580.*

[8] A. Karpathy, G. Toderici, S. Shetty, T. Leung, R. Sukthankar, L. Fei-Fei, "Large-scale video classification with convolutional neural networks," In Proceedings of the IEEE conference on Computer Vision and Pattern Recognition, 2014, pages 1725-1732.

[9] M. M. Kasar, D. Bhattacharyya, T.-h Kim, "Face recognition using neural network: A review," In International Journal of Security and its Applications, 2016, 10(3):81-100.

[10] A. Krizhevsky, G. Hinton, "Learning multiple layers of feature detectors from tiny images," 2009.

[11] A. Krizhevsky, I. Sutskever, G. E. Hinton, "Image net classification with deep convolutional neural networks," in Advances in neural information processing systems, 2012, pp. 1097-1105.

[12] Y. LeCun, L. Bottou, Y. Bengio, P. Haffner, "Gradient-based learning applied to document recognition," Proceedings of the IEEE, 1998, 86(11):2278-2324

[13] Y. LeCun, C. Cortes, C. J. Burges, "The mnist database of handwritten digits," 1998.

---

[4] `http://cmusatyalab.github.io/openface/models-and-accuracies/`

[14] H. Li, Z. Lin, X. Shen, J. Brandt, G. Hua, “A convolutional neural network cascade for face detection,” In Proceedings of the IEEE Conference on Computer Vision and Pattern Recognition, 2015, pages 5325-5334.

[15] M. A. Nielsen, “Neural Networks and Deep Learning,” 2015, Determination Press.

[16] F. Schroff, D. Kalenichenko, J. Philbin, “Facenet: A unified embedding for face recognition and clustering,” In Proceedings of the IEEE Conference on Computer Vision and Pattern Recognition, 2015, pages 815-823.

[17] P. Y. Simard, D. Steinkraus, J. C. Platt, et al., “Best practices for convolutional neural networks applied to visual document analysis,” In ICDSR, volume 3, 2003, pages 958-962. Citeseer.

Optical Rheology of a Polydimethylsiloxane Fluid in Jeffrey-Hamel Type Flow

Ramesh Subramanian[1], Jules Picot[2]

[1]Bharti School of Engineering, Laurentian University, 935 Ramsey Lake Road, Sudbury, Ontario P$_3$E $_2$C$_6$ CANADA
[2]Department of Chemical Engineering, University of New Brunswick, P. O. Box 4400, Fredericton, New Brunswick E$_3$B $_5$A$_3$ CANADA

Abstract**—** *The rheo-optical behavior of a viscoelastic polydimethylsiloxane (PDMS) fluid was examined at room temperature for various pressure drops (flow rates) across a Jeffrey Hamel type converging wedge flow cell. The strain-rates were computed from local velocity measurements using laser Doppler anemometry (LDA), and the planar extensional flow behavior of the polymer melt was studied via birefringence measurements along the centerline of the flow cell. The linear relation between the stress and polarizability tensors were confirmed over a range of strain rates that extended well into the non-Newtonian region. The first normal stress difference (FNSD) was calculated from the local velocity measurements using a two-term Goddard-Miller model with a single Maxwell-type relaxation time constant of 0.0174 s computed from Rouse model and a zero-shear viscosity of 300 Pa.s. A linear stress-optical coefficient of* 1.41×10^{-10} *Pa*$^{-1}$ *was obtained for PDMS in planar extensional flow at room temperature from the flow birefringence measurements and the first normal stress difference (FNSD) computed using the Goddard-Miller model. This compares well with values for PDMS in the range of* $0.909 - 1.84 \times 10^{-10}$ *Pa*$^{-1}$ *at room temperature as reported by various researchers.*

Keywords**—** ***Polydimethylsiloxane, Flow Birefringence, Jeffrey-Hamel Flow, Stress-Optical Coefficient, Goddard-Miller Model.***

I. INTRODUCTION

Polymer macromolecules exhibit isotropic behavior when they are completely randomly distributed. However, flow deformation causes orientation of the macromolecules leading to anisotropy in the transport properties like birefringence [1-3].

Anisotropy to transmission of light by an optical medium produces birefringence, or differences in refractive indices in orthogonal directions. According to Flory [4], the degree of anisotropy in refractive index (birefringence) for a chain network is represented as

$$\Delta N = (2\pi/9)\,(\nu/V)\,[(\bar{n}^2 + 2)^2/\bar{n}\,]\,(\bar{\alpha}_{xx} - \bar{\alpha}_{yy}) \tag{1}$$

Where ν/V represents the number of segments per unit volume (a segment is the portion of a macromolecular chain between two adjacent entanglement points), $\bar{n}$ is the refractive index of the isotropic non-ordered material, and $(\bar{\alpha}_{xx} - \bar{\alpha}_{yy})$ is the difference in the averaged polarizabilities of the chain along the x and y axes.

In the case of flexible polymer solutions and melts, the net optical anisotropy caused by flow can be obtained by measuring differences in refractive indices in the direction of the principal stresses. When the direction of propagation of the electric field vector of a polarized light beam coincides with the direction of one of the principal stresses of an optically anisotropic macromolecular fluid flowing through a transparent channel, the difference in birefringence in the other two directions is related to the difference in the corresponding principal stresses via the stress-optical law. According to this law, in a wide range of conditions involving not too large stresses, there is a linear relation between the components of the refractive index (polarizability) and stress tensors given by

$$\Delta N = C\,\Delta\sigma \tag{2}$$

where C is a material constant known as the stress-optical coefficient, ΔN is the difference in main refractive indices, and $\Delta\sigma$ is the corresponding difference in the two principal stresses. The sign and magnitude of the stress-optical coefficient depends on the chemical structure of the polymer, which is governed by the polarizability of the bonds between the atoms of the polymer molecule and the direction of the bonds with respect to the polymer backbone. Since the deviatoric components of the stress and polarizability tensors are linearly related, the orientation of the principal axes will coincide with that of the optical axes. According to the theory of rubber photoelasticity [4] for a network of freely jointed Gaussian chain, the stress-optical coefficient is given by

$$C = (2\pi/45kT)\ [(\bar{n}^2 + 2)^2/\bar{n}]\ (\alpha_1 - \alpha_2) \tag{3}$$

where $\bar{n}$ is the mean refractive index of the material, k is the Boltzmann constant, T is the absolute temperature, α_1 is the polarizability of the chain link parallel to the link, and $\alpha_2$is the polarizability of the chain link transverse to the link.

Extensive experimental work has been done on stress-optical laws ranging from solids concentrated polymer solutions [5-7]. Since the proportionality of stress and refractive index does not imply proportionality of the stress and strain rate, the stress-optical law holds good for polymer melts well into the non-Newtonian region of flow [8]. The only requirement is that both stress and the refractive index tensors are governed by the orientation function. This will be true as long as the flow does not create a change in the magnitude of the macromolecular chain end-to-end vector. Janeschitz-Kriegl [9] has shown experimentally that, for many polymers, the linearity of the stress-optical law is valid up to a shear stress of 10^4 Pa and tensile stress of 10^6 Pa.

Majority of the rheo-optical studies of polymeric systems done so far involved the mechanical measurements of stress and optical measurements of birefringence to evaluate the linear stress-optical coefficient [10-13]. In this paper we illustrate the use of optical techniques (laser Doppler anemometry) measure birefringence, compute stress and then evaluate the linear stress-optical coefficient of a polydimethylsiloxane (PDMS) melt at room temperature in planar extension along the centerline of a converging wedge flow cell.

1.1 Velocity Vector, Rate-of-Strain and Stress Tensors

Assuming the flow in the converging wedge cell is two-dimensional, the components of the velocity vector in circular coordinates (Figure 1) are

$$V_r = f(r, \theta) \qquad \text{and} \qquad V_\theta = V_z = 0 \tag{4}$$

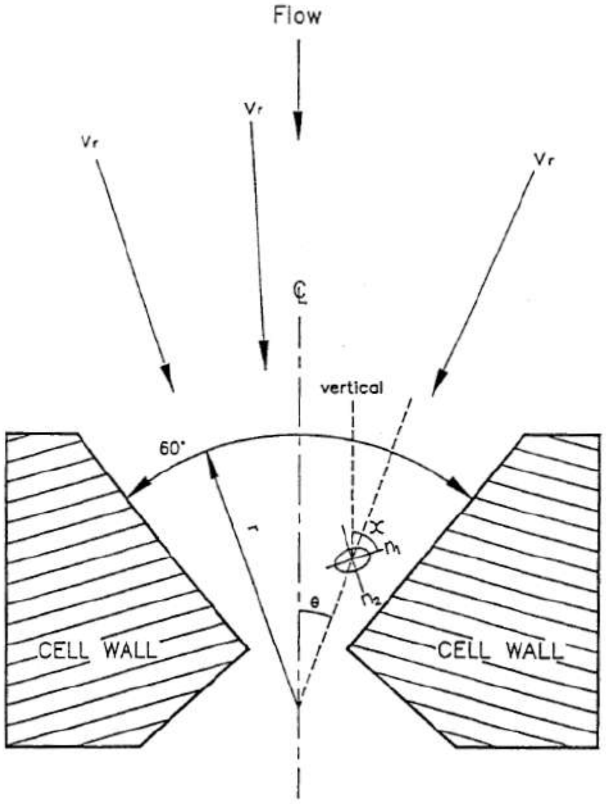

FIGURE 1. GEOMETRY OF THE TWO-DIMENSIONAL JEFFREY-HAMEL TYPE CONVERGING WEDGE FLOW CELL

Along the centerline where the flow is purely extensional, the component of velocity vector is

$$V_r = f(r) \tag{5}$$

The rate of strain tensor ($\underline{\underline{\dot{\gamma}}}$) along the centerline have the following components:

$$\underline{\underline{\dot{\gamma}}} = \begin{bmatrix} 2\partial V_r / \partial r & 0 & 0 \\ 0 & 2V_r / r & 0 \\ 0 & 0 & 0 \end{bmatrix} \tag{6}$$

Since there is no flow of the fluid in the direction of propagation of light (z-direction), the stress tensor ($\underline{\underline{\tau}}$) along the centerline have the following components:

$$\underline{\underline{\tau}} = \begin{bmatrix} \tau_{rr} & 0 & 0 \\ 0 & \tau_{\theta\theta} & 0 \\ 0 & 0 & 0 \end{bmatrix} \tag{7}$$

1.2 Equation of Continuity

The equation of continuity in cylindrical coordinate system for steady-state flow of an incompressible fluid in a converging two-dimensional flow channel (where $\partial V_\theta / r\partial\theta$ is negligible) is given by

$$\partial(rV_r)/\partial r = 0 \qquad \text{or} \qquad rV_r = \text{constant} \tag{8}$$

1.3 Linear Stress-Optical Law Equations

For two-dimensional converging wedge flows, Adams et al. [10] gave the following forms of the linear stress-optical law:

$$\tau_{r\theta} = [\Delta N (\sin 2\chi \cos 2\theta - \cos 2\chi \sin 2\theta)/2C] = [\Delta N \sin (2\chi - 2\theta)]/2C \tag{9}$$

$$\tau_{rr} - \tau_{\theta\theta} = [\Delta N (\cos 2\chi \cos 2\theta + \sin 2\chi \sin 2\theta)/C]$$

$$= [\Delta N \cos (2\chi - 2\theta)]/C \tag{10}$$

Where χ is the angle between the principal molecular orientation axis and the cell centerline, and θ is the angular coordinate of the intersection of the two split monochromatic light beams at the point of measurement (Figure 1).

Here ΔN is the birefringence of the material and given by the equation

$$\Delta N = R \lambda / d \tag{11}$$

where d is the thickness of the birefringent material, λ is the wavelength of the monochromatic light used, and R is the relative retardation of the two plane-polarized components of the monochromatic light emerging from the birefringent material.

Along the centerline of the converging wedge cell where the flow is purely extensional, both χ and θ are zero. Therefore, the linear stress optical relation in the reduces to

$$\tau_{rr} - \tau_{\theta\theta} = \Delta N / C \tag{12}$$

1.4 Goddard-Miller Model

The Goddard-Miller model [14] is a quasilinear corotational constitutive equation obtained by using only the first term in the Goddard memory-integral expansion [15]. This model, which can also be obtained as a result of applying the Boltzmann Superposition principle to a viscoelastic model in a cororating frame of reference, has been used successfully to describe the rheologolical behavior of PDMS [16-17]. In an integral form, the Goddard-Miller model is written as

$$\underline{\underline{\tau}} = -\int_{-\infty}^{t} G(t - t') \underline{\underline{\dot{\Gamma}}}' dt' \tag{13}$$

where G(t – t')is the relaxation modulus and $\underline{\underline{\dot{\Gamma}}}'$ is the corotating rate-of-deformation tensor.

The corotating rate-of-deformation tensor ($\underline{\underline{\dot{\Gamma}}}'$) is represented by the Taylor series expansion about t' as

$$\underline{\underline{\dot{\Gamma}}}' = \underline{\underline{\gamma}}(t) - [(t - t')\, D\underline{\underline{\gamma}}(t)/Dt] + ½\, [(t - t')^2\, D^2\underline{\underline{\gamma}}(t)/Dt^2] - \tag{14}$$

where D/Dt is the corotational time derivative or Jaumann derivative.

The Jaumann derivative tells how the components of a tensor change with time as seen by an observer moving with the fluid and rotating with it. For a second-order tensor, the Jaumann derivative is defined as

$$D(\,)/Dt = \partial(\,)/\partial t + V.\nabla(\,) + [\,\underline{\underline{\omega}}.(\,) - (\,).\underline{\underline{\omega}}\,] \tag{15}$$

where $\underline{\underline{\omega}}$ is the vorticity tensor which corrects for the rotary motion of the fluid.

The rate-of-deformation tensor ($\underline{\underline{\dot{\gamma}}}$) and vorticity tensor ($\underline{\underline{\omega}}$) are given by

$$\underline{\underline{\dot{\gamma}}} = \nabla V + (\nabla V)^t \tag{16}$$

$$\underline{\underline{\omega}} = \nabla V - (\nabla V)^t \tag{17}$$

Along the centerline of the converging wedge cell, the flow is purely planar extensional and hence, the vorticity tensor ($\underline{\underline{\omega}}$) is zero.

For this study, a single Maxwell-type relaxation modulus is used and given by the equation

$$G(t - t') = (\eta_o/\lambda_o)\, e^{-(t - t')/\lambda_o} \tag{18}$$

where η_0 is a characteristic viscosity like zero-shear viscosity and λ_0 is a characteristic time constant.

Substituting the rate-of-strain tensor and using only the first two terms of the Taylor series expansion for the corotating rate-of-deformation tensor ($\underline{\underline{\dot{\Gamma}}}'$) yields the following terms for the stress tensor of the Goddard-Miller model for purely extensional flow along the centerline of the two-dimensional converging wedge cell:

$$\tau_{rr} = -\,2\,\eta_o\,\{(\partial V_r/\partial r) - \lambda_o\,[V_r\,(\partial^2 V_r/\partial r^2)]\} \tag{19}$$

$$\tau_{\theta\theta} = -\,2\,\eta_o\,\{(V_r/r) - \lambda_o\,[(V_r/r)\,(\partial V_r/\partial r - V_r/r)]\} \tag{20}$$

Therefore, the first normal stress difference ($\tau_{rr} - \tau_{\theta\theta}$) according to the truncated Goddard-Miller model is given by

$$\tau_{rr} - \tau_{\theta\theta} = -\,2\,\eta_o\,\{[(\partial V_r/\partial r) - (V_r/r)] - \lambda_o\,V_r\,[(\partial^2 V_r/\partial r^2) - (1/r)(\partial V_r/\partial r) + V_r/r^2]\} \tag{21}$$

II. EXPERIMENTAL

2.1 Flow Cell Geometry

The schematic of the 60° converging wedge flow cell used for this study is shown in Figure 1. The width of the flow cell is 5.00 cm and it is capable of withstanding a pressure of 1000 kPa. Two such cells were used for the study, one for velocity measurements and another for flow birefringence measurements with modified windows in order to minimize the contribution to the measured birefringence.

2.2 Polydimethylsiloxane (PDMS) Fluid Properties

Linear PDMS fluids and melts are ideally suited for flow birefringence studies because of their thermal, physical and chemical stability. They have relatively low surface tension (19-21 x 10^{-3} Nm^{-1}), thus minimizing the problem of formulation and entrainment of bubbles that poses a tremendous practical difficulty in optical measurements. PDMS exits in the liquid or molten state at room temperature, thus eliminating the need to maintain high temperatures that often hinders optical measurements. PDMS fluids are highly transparent and the polymer chain monomer unit has relatively small refractive index anisotropy. The experimental polymer used for this study was a linear amorphous Dow Corning Type 200 polydimethylsiloxane fluid. The polymer was analyzed using a conventional gel permeation chromatograph (GPC) at 30^{o}C with toluene as the solvent, and the following properties were obtained:

Number-Average Molecular Weight (M_n) = 6.79 X 10^4

Weight-Average Molecular Weight (M_w) = 2.327 X 10^5

z-Average Molecular Weight (M_Z) = 3.459 X 10^5

Polydispersity Ratios: M_w/M_n = 3.43

M_z/M_n = 4.95

The steady-state rheometric characterization of PDMS in simple shear was performed using a Weissenberg Rheogoniometer, and the results shown in Figure 2. The zero-shear viscosity was found to be 300 Pa.s.

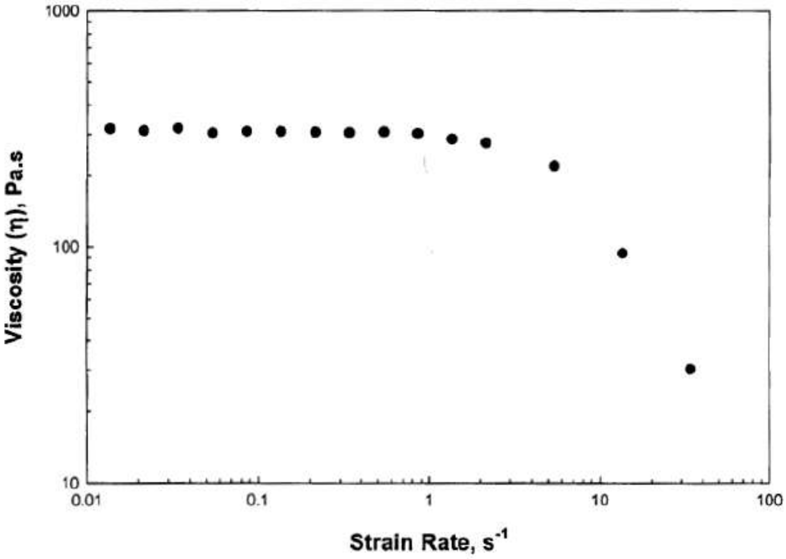

FIGURE 2. STEADY-STATE SIMPLE SHEAR VISCOSITY OF PDMS AS A FUNCTION OF SHEAR RATE USING A WEISSENBERG RHEOGONIOMETER.

2.3 Laser Doppler Anemometry (LDA)

The local velocities along the centerline of the unmodified converging wedge flow cell were measured using a monochromatic laser Doppler anemometry (LDA) in differential Doppler or fringe mode with forward scattering. A monochromatic helium-neon laser beam (wavelength = 0.6328μ, diameter = 600μ) is split into two separate beams and then converges in a small reference volume in the flowing polymer located at the mid-point between the two windows of converging cell. As a result, a diffraction pattern is set up and the motion of the polymer macromolecules moving through this reference volume scatters light. This scattered light produces a Doppler frequency proportional to the velocity of the polymer.

2.4 Orientation Angle and Flow Birefringence

The local flow birefringence of the modified converging wedge flow cell was measured by adding a quartz compensator to the set off cross-polarizers (a half-wave plate and an analyzer). The cross-polarizers were used to measure the orientation angle, which is the angle between the principal molecular orientation axis and the cell centerline. The linearly vertical polarized beam from the monochromatic He-Ne laser traverses the along the width of the flow cell and the transmitted beam is then analyzed to obtain the net molecular orientation. For planar extensional flow along the centerline of the cell, the orientation angle should be zero because the principal molecular orientation axis and the cell centerline coincide. The quartz compensator, placed between the converging flow cell and the analyzer, produces an exact canceling retardation by compensating the phase difference of the polarized monochromatic light introduced by the polymer flowing through the cell.

III. RESULTS AND DISCUSSION

3.1 Linearity of the Stress-Optical Law

When a macromolecular polymer fluid is stretched, there is a decrease in entropy associated with the orientation of the network chains. Stresses and orientation are also caused by the phenomena of macromolecular chain stretching. So it does not come as a surprise that, as a first approximation, a simple proportionality exits between the stress (entropic) and birefringence (orientation). In the limits of small macroscopic deformation, the root mean square (RMS) of the end-to-end distance of a Gaussian chain is rather small compared to the length of the stretched chain. As the strain/stress increases, both orientation and birefringence of the macromolecular chain increases till it approaches a saturation point. In fact, entropy change accompanying a complete alignment of chain segments must be - ∞. From this qualitative discussion one can hypothesize that the ratio of measured birefringence to the corresponding stress difference should deviate in a downward direction from the value of the constant stress-optical coefficient (C). This has been found in polymer melts subjected to very high tensile stresses [18]. However, in an overwhelming majority of experiments [8,11] that are relevant to practical situations in polymer processing, stresses appear to be too small for deviation from the linear stress-optical law.

For the stress-optical law to be linear there are two limits to its validity; (a) an upper limit for the stress and (b) a time scale of the deformation process must be large enough to allow for establishment of internal thermodynamic equilibrium.

The assumption has always been made that the time scales for the establishment of internal equilibrium are due to rapid vibrational modes between backbone molecules. These are very short compared to the macroscopically observable time scales of the bulk motion. As a consequence, the latter time scale must be solely due to the relatively low rates of change of the locations of the entanglements. For this study, we assumed that the internal thermodynamic equilibrium was established very quickly.

The upper bound in the stress can be determined from measurements in pure extensional flow because, generally, stresses in extension are many times higher than stresses in shear. For this study, the flow birefringence measurements were made between any two radial positions along the centerline and related to the first normal stress difference (FNSD) by the following equation:

$$(\tau_{rr} - \tau_{\theta\theta})_{r=r1} - (\tau_{rr} - \tau_{\theta\theta})_{r=r2} = [(\Delta N)_{r=r1} - (\Delta N)_{r=r2}]/C \qquad (22)$$

Therefore, a plot of the difference in normal stresses versus the difference in flow birefringence between the two radial positions along the centerline should yield a straight line in the linear stress-optical region. Figure 3 shows such a plot between r = 1.1 cm and r = 2.1 cm, and it indicates a linear nature of the stress-optical law for PDMS up to a pressure drop of 689 kPa (100 psi) across the converging flow cell. Although this is a necessary condition to confirm the linearity of the stress-optical law, it is not a sufficient condition. The slight zero-offset evident in Figure 3 is probably caused by an optical window effect, and it is extremely difficult to eliminate for PDMS because of the very low intrinsic anisotropy of the fluid.

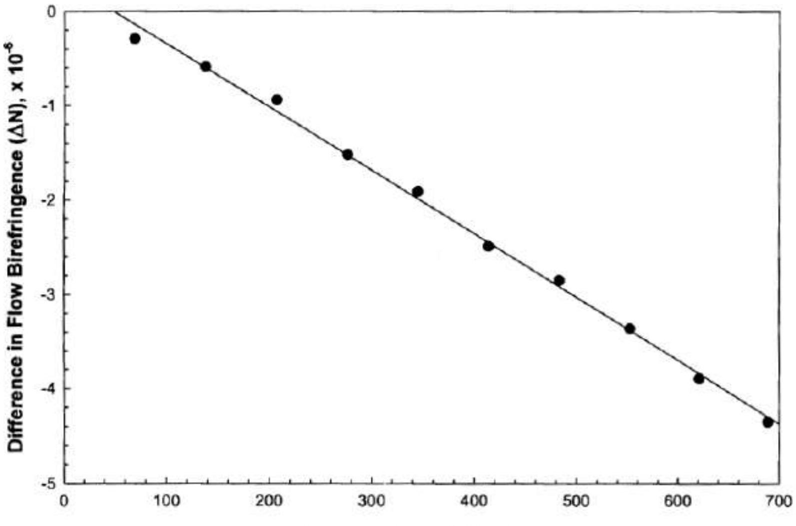

FIGURE 3. DIFFERENCE IN CENTERLINE BIREFRINGENCE (BETWEEN r = 1.1 cm AND r = 2.1 cm) AS A FUNCTION OF PRESSURE DROP ACROSS THE FLOW CELL.

In order to confirm the sufficient condition for the linearity of stress-optical law for PDMS up to a pressure drop of 689 kPa, the equation of momentum along the centerline of the converging flow cell has to be examined. The r-directed momentum balance equation along the centerline is given by

$$\rho\, rV_r\, \partial V_r/\partial r = (\tau_{rr} - \tau_{\theta\theta}) - r\,[\partial(p + \tau_{rr})/\partial r] \tag{23}$$

Using the mean value theorem, we can write the above equation for any radial position (r) as

$$R\, r\, V_r \Delta V_r/\Delta r = \overline{\left(\tau_{rr} - \tau_{\theta\theta}\right)} - (r\,[\Delta\pi/\Delta\rho]) \tag{24}$$

where $\pi = \pi + \tau_{\rho\rho}$.

For the stress-optical law to be linear, the average value of normal stress difference from the entrance to the exit of the flow cell $\overline{\left(\tau_{rr} - \tau_{\theta\theta}\right)}$ must retain a constant proportionality with the overall pressure drop across the flow cell. Therefore,

$$\frac{\int_{r_{in}}^{r_{out}} \Delta N dr}{\left[r_{out} - r_{in}\right]} = \overline{\Delta N} = \overline{\left(\tau_{rr} - \tau_{\theta\theta}\right)} \tag{25}$$

Thus using the measured birefringence (ΔN) versus r data along the centerline from entrance to exit at different pressure drops, the average birefringence (ΔN) can be evaluated. This was done by extrapolating the centerline flow birefringence (ΔN) data measured between r = 1.1 to 2.1 cm to the entrance and the exit using equation 25 as shown in Figure 4. A straight line plot of ΔN vs ΔP was obtained along the centerline, clearly indicating that the linear stress-optical law is valid up to a pressure drop of 689 kPa across the flow cell.

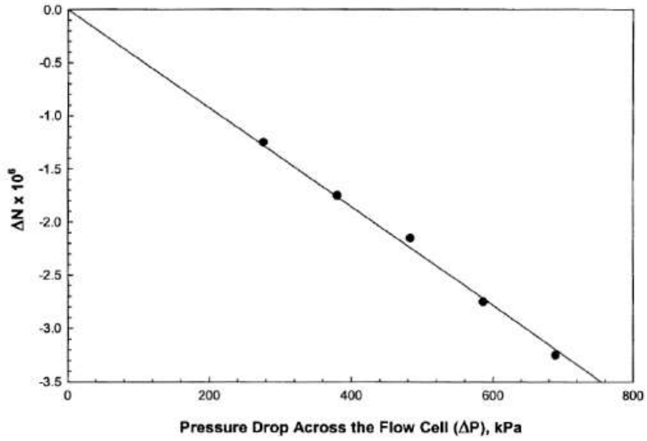

FIGURE 4. AVERAGE CENTERLINE BIREFRINGENCE AS A FUNCTION OF PRESSURE DROPS ACROSS THE FLOW CELL.

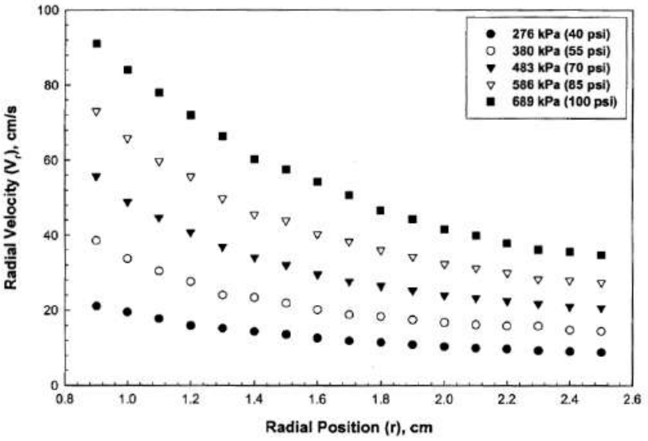

FIGURE 5. CENTERLINE RADIAL VELOCITY AS A FUNCTION OF RADIAL POSITION FOR VARIOUS PRESSURE DROPS ACROSS THE FLOW CELL.

3.2 Velocity and Extensional Rates

The local velocities (V_r) as a function of radial position (r = 0.9 to 2.5 cm) along the centerline of the unmodified converging flow cell for different pressure drops were obtained using LDA and shown in Figure 5. The planar extensional rates ($\partial V_r/\partial r$) were obtained by differentiating the local velocity data. It can be seen that as the radial position increases, both local velocity and the extensional rate decrease.

3.3 Equation of Continuity

As mentioned earlier, the equation of continuity for steady-state flow of PDMS in the converging two-dimensional flow channel (where $\partial V_\theta/r\partial\theta$ is negligible) is given by rV_r = constant. Figure 6 shows a plot of the equation of continuity (rV_r) as a function of the centerline radial position (r) for different pressure drops across the flow cell. It can be seen that the value of rV_r is nearly constant and it is proportional to the pressure drop, thereby indicating the two-dimensional nature of the flow through the converging wedge cell.

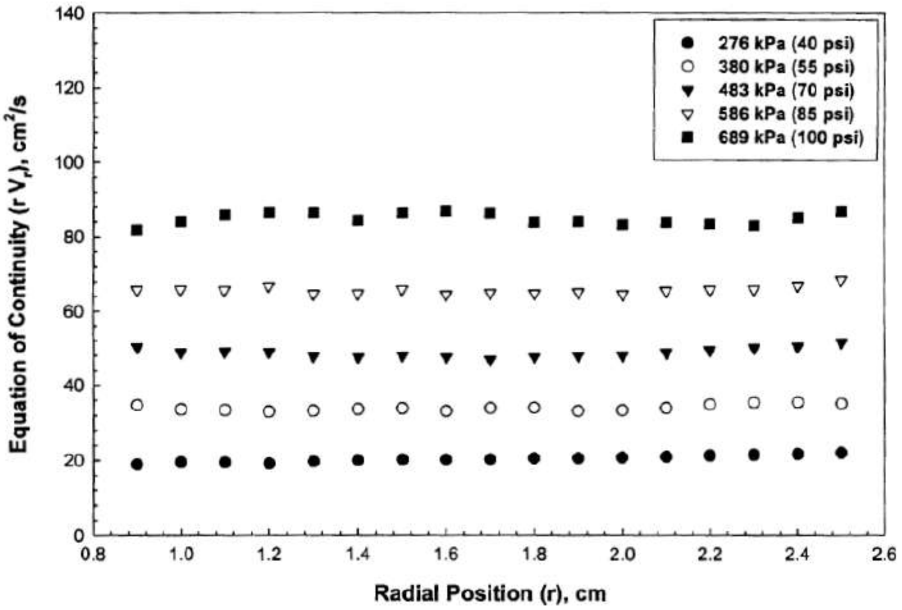

FIGURE 6. EQUATION OF CONTINUITY AS A FUNCTION OF THE CENTERLINE RADIAL POSITION FOR VARIOUS PRESSURE DROPS ACROSS THE FLOW CELL.

3.4 First Normal Stress Difference (FNSD)

The first normal stress difference ($\tau_{rr} - \tau_{\theta\theta}$) can be computed from the truncated Goddard-Miller model using equation 21given by

$$\tau_{rr} - \tau_{\theta\theta} = -2\,\eta_o \{[(\partial V_r/\partial r) - (V_r/r)] - \lambda_o V_r [(\partial^2 V_r/\partial r^2) - (1/r)(\partial V_r/\partial r) + V_r/r^2]\} \tag{27}$$

Thus, we require the local velocity (V_r), extension rate ($\partial V_r/\partial r$) and its derivative ($\partial^2 V_r/\partial r^2$), zero-shear viscosity (η_0) and characteristic time constant (λ_0) in order to evaluate the first normal stress difference ($\tau_{rr} - \tau_{\theta\theta}$) at different radial position along the centerline of the converging flow cell for various pressure drops.

The single Maxwell-type time constant (λ_0) was obtained from the Rouse model [19] for polymer melts. According to the Rouse model for a polymer melt with large number of molecules in the spring-bead molecular structure, the relaxation time (λ_0) is given by

$$\lambda_0 = (6/\pi^2)\,[(\eta_0\, M)/(\rho\, R\, T)] \tag{28}$$

where M is the molecular weight, ρ is the density, R is the Universal gas constant, and T is the temperature. For the PDMS used in this study at room temperature (T = 25 °C), the relation time using equation 27 gives

$$\lambda_0 = (6/\pi^2)\,[(\eta_0 M)/(\rho P T)] = (6/\pi^2)\,[(300 \times 232.7)/(987 \times 82.057 \times 10^{-6} \times 1.01325 \times 10^5 \times 298)] = 0.0174 \text{ s}$$

The first normal stress difference in planar extensional flow along the cell centerline for this study was computed using λ_0= 0.0174s and η_0 = 300 Pa.s, and listed in Table 1.

TABLE 1
FIRST NORMAL STRESS DIFFERENCE ($\tau_{rr} - \tau_{\theta\theta}$) COMPUTED USING THE TWO-TERM GODDARD-MILLER MODEL ALONG THE CENTERLINE OF THE JEFFREY-HAMEL TYPE CONVERGING WEDGE FLOW CELL

Pressure	r = 2.1 cm	r = 1.9 cm	r = 1.7 cm	r = 1.5 cm	r = 1.3 cm	r = 1.1 cm
Drop (ΔP) in kPa	($\tau_{rr} - \tau_{\theta\theta}$) in kPa	($\tau_{rr} - \tau_{\theta\theta}$) in kPa	($\tau_{rr} - \tau_{\theta\theta}$) in kPa	($\tau_{rr} - \tau_{\theta\theta}$) in kPa	($\tau_{rr} - \tau_{\theta\theta}$) in kPa	($\tau_{rr} - \tau_{\theta\theta}$) in kPa
276	- 6.35	- 6.53	- 8.66	- 10.63	- 13.29	- 14.94
380		- 10.05	- 11.76		- 17.25	- 21.09
483	- 12.36	- 13.06	- 14.76	- 20.29	- 21.64	- 28.10
586		- 27.96	- 32. 11		- 38.02	- 42.13
689	- 18.42	- 26.17	- 31.10	- 35.28	- 45.56	- 53.50

3.5 Linear Stress-Optical Coefficient

The room-temperature linear stress-optical coefficient (C) for PDMS in planar extensional flow at various pressure drops (flow rates) can be obtained from equation 12 using the measured birefringence along the cell centerline and the first normal stress difference (FNSD) calculated from the two-term Goddard-Miller model (equation 27) with a single Maxwell-type relaxation time constant of 0.0174 s and a zero-shear viscosity of 300 Pa.s. Thus, a plot of ΔN vs $(\tau_{rr} - \tau_{\theta\theta})$ should give a straight line passing through the origin with the slope equal to the linear stress-optical coefficient (C). Figure 7 shows such a plot for pressure drops of 276, 380, 483, 586, and 689 kPa across the converging wedge flow cell. A linear stress-optical coefficient of 1.41×10^{-10} Pa^{-1} was obtained for PDMS at room temperature. This compares well with values of 1.35×10^{-10} Pa^{-1} by Wales [11], 0.909×10^{-10} Pa^{-1} by Liberman et al. [12], $1.56\text{-}1.84 \times 10^{-10}$ Pa^{-1} by Galante and Frattini [13]for a low and a high molecular weight PDMS, and 1.44×10^{-10} Pa^{-1} by Subramanian et al. [20].The positive sign of the stress-optical coefficient confirms that the polarizability of the backbone of PDMS chain is indeed highest in the chain direction.

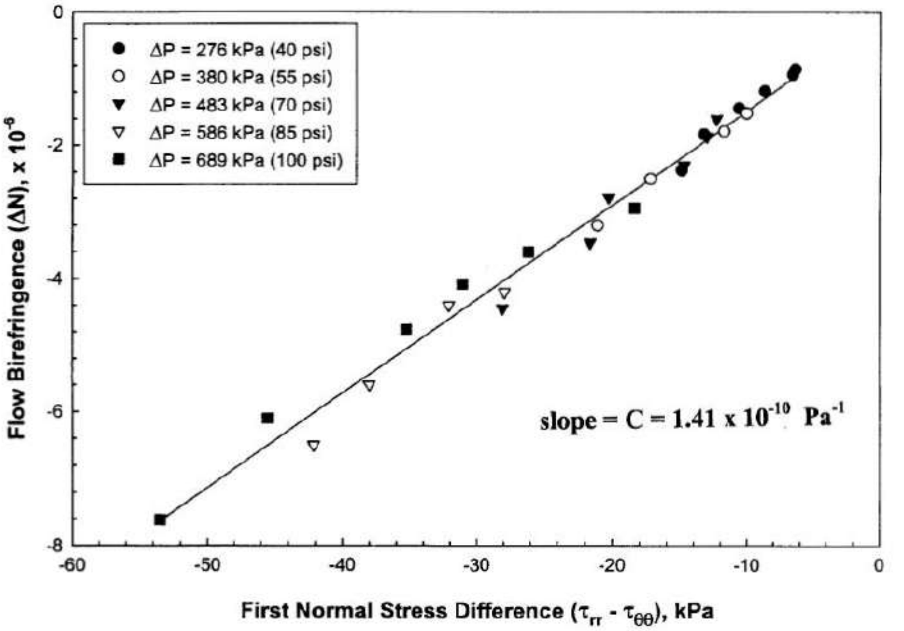

FIGURE 7. MEASURED FLOW BIREFRINGENCE VS. COMPUTED FIRST NORMAL STRESS DIFFERENCE (USING THE TWO-TERM GODDARD-MILLER MODEL) IN PLANAR EXTENSIONAL FLOW ALONG THE CELL CENTERLINE FOR VARIOUS PRESSURE DROPS ACROSS THE FLOW CELL.

IV. CONCLUSION

We have shown that the linear stress-optical coefficients of an amorphous polymer melt or fluid can be estimated from flow-induced birefringence and laser Doppler anemometry measurements. Unlike many previous studies that measured stresses mechanically, the stresses can be evaluated by choosing an appropriate constitutive equation that best describes the rheological behavior of the polymer. The strain-rates can be computed from local velocity measurements using laser Doppler anemometry. The linear relation between the stress and polarizability tensors, which generally valid over a range of strain rates that extended well into the non-Newtonian region, can then be used to obtain the stress-optical coefficient.

REFERENCES

[1] A. A. Cocci, Jr. and J. J. C. Picot, "Rate of Strain Effect on the Thermal Conductivity of a Polymer Liquid", Polym. Eng. Sci., vol. 13 (5), pp. 337-341, 1973.

[2] J. J. C. Picot and D. Debeauvais, "Molecular Orientation Effects on Thermal Conductivity of Polydimethylsiloxane Under Shearing Strain", Polym. Eng. Sci., vol. 15 (5), pp. 373-380, 1975.

[3] F. H. Gortemaker, "A flow birefringence study of stresses in sheared polymer melts",Ph. D. Thesis, Technische Hogeschool, Delft, The Netherlands, 1976.

[4] P. J. Flory, Statistical Mechanics of Chain Molecules, Wiley Interscience, New York, 1969.

[5] W. Phillippoff, "Flow Birefringence and Stress", J. Appl. Phys., vol. 27(9), pp. 984-989, 1956.

[6] W. Phillippoff, "On Shear Stresses, Flow Curves, Flow Birefringence and Normal Stresses of Polyisobutadiene Solutions. Part I: Fundamental Principles", Tran. Soc. Rheol.,vol. 1, pp. 95-107, 1957.

[7] W. Phillippoff, “Elastic Stresses and Birefringence in Flow”, Tran. Soc. Rheol., vol. 5, pp. 163-191, 1961.

[8] H. Janeschitz-Kriegl, Polymer Melt Rheology and Flow Birefringence, Springer-Verlag, New York, 1983.

[9] H. Janeschitz-Kriegl, “Flow Birefringence of Elasto-Viscous Polymer Systems”, Adv. Polym. Sci., vol. 6, pp. 170-318, 1969.

[10] E. B. Adams, J. C. Whitehead, and D. C. Bogue, “Stresses in a Viscoelastic Fluid in Converging and Diverging Flow”, A. I. Ch. E. J., vol. 11 (6), pp. 1026-1032, 1965.

[11] J. L. S. Wales, The Application of Flow Birefringence to Rheological Studies of Polymer Melts, Delft University Press, The Netherland, 1976.

[12] M. H. Liberman, Y. Abe, and P. J. Flory, “Stress-Optical Behavior of Polymethylene and Poly(dimethylsiloxane)”, Macromolecules, vol. 5 (5), pp. 550-558, 1972.

[13] S. R. Galante and P. L. Frattini, “Spatially Resolved Birefringence Studies of Planar Entry Flows”, J. Non-Newtonian Fluid Mech., vol. 47, pp. 289-337, 1993.

[14] J. D. Goddard and C. Miller, “An Inverse for the Jaumann Derivative and Some Applications to the Rheology of Viscoelastic Fluids”, Rheol. Acta., vol. 5, pp. 177-184, 1966.

[15] J. D. Goddard, “A Modified Function Expansion for Viscoelastic Fluids”, Tran. Soc. Rheol., vol. 11, pp. 381-400, 1967.

[16] R. Subramanian, “ Flow Birefringence in Polymer Melt Rheology”, Ph.D. Thesis, University of New Brunswick, Canada, 1994

[17] D. R. Wilson, “Prediction of Molecular Orientation in a Polymer Melt”, M.Sc. Thesis, University of New Brunswick, Canada, 1990

[18] T. Matsumoto and D. C. Bogue, “Stress Birefringence in Amorphous Polymer Under Nonisothermal Conditions”, J. Poly. Sci. Polym. Phys., vol. 15, pp. 1663-1674, 1977.

[19] P. E. Rouse, “A Theory of the Linear Viscoelastic Properties of Dilute Solutions of Coiling Polymers”, J. Chem. Phys., vol. 21, pp. 1272-1280, 1953.

[20] R. Subramanian, D. R. Wilson, and J. J. C Picot, “Flow Birefringence in Polymer Rheology”, Polym. Eng. Sci., vol. 32 (8), pp. 573-578, April 1992.

Innovative anaerobic submerged media in small waste treatment plants in Hungary

Imre Gyulavári[1], Gyula Lakatos[2]

[1]GYULAVÁRI CONSULTING Ltd. Hungary
[2]University of Debrecen, Department of Ecology, Debrecen, Hungary

***Abstract*— *During the past 10 years 32 anaerobic FLEXIPAK®-MINI waste water treatment plants were installed in Hungary, all in unique, energy saving communal areas without public sewer systems. Innovative research and development, as well as planning were carried out by GYULAVÁRI CONSULTING Ltd. (Gyulavári & Kormos, 1993).*

Using the TURBOPAK® contact units developed by our company, the anaerobic treatment process has provided phase separation (removal of suspended solids) and biological partial treatment at the same time, ensured partly by the sloping, 60° angle installation of the units, generating a gravitational upward flow. The multi cell contact unit provides a 150 m^2/m^3 specific anaerobic biofilm surface for the microorganisms.

Based on our experience with combined dual processes, the TURBOPAK® contact unit provides an innovative, efficient and cost effective solution for intensification, compared to formerly known anaerobic, energy free solutions. The new innovative equipment was registered under the FLEXIPAK®-MINI brand name and the manufacturer of TURBOPAK® (System Gyulavári) is PANDAN Ltd. (Hungary).

Keywords*— *FLEXIPAK®-Mini, submerged, anaerobic system, TURBOPAK® submerged, biological, fix-media (System Gyulavári).

I. INTRODUCTION

The lack of a central sewer system near or outside city limits and in certain rural areas, such as farms, it is a global need and task to solve the treatment of waste water and develop sewer systems (Boumai, 1975). It is an additional requirement for these solutions to be small scale, as far as possible without the need for outside energy, simple operation and the possibility of the treated water to be ready for reuse, such as for surface or general irrigation. Another requirement is for the treatment process to be constantly efficient, low noise and without generating large quantities of sludge, etc. (Jewel et al., 1975; Otis & Boyle, 1976).

Besides these advantages, another requirement is to have a large enough area nearby for placing, settling the treated water. For a good settling process "porous" soil layers are needed, preferably with adequate, maximum ground water levels (Jones & Tayler, 1965; Pradhan et al., 2011¸ Veres et al., 2015). The above listed advantageous conditions are not available in every country, but in most cases can be created as realistic or necessary solutions.

One of the solutions for general needs, for plants serving 5-20 people for example, is an anaerobic settling system widely used in the USA as a pretreatment solution installed before septic tanks, where waste is treated for approximately three days, and which does not require added energy and satisfies all requirements (Bouma, 1975).

An additional benefit of this solution is that it can be used intermittently and for periodically changing loads. According to related literature, approximately 19.5 million such systems were used within the USA in 1970 which meant that 30 % of the population applied this supplementary method in combination with other solutions. This is a realistic overview of the present situation within the USA (Otis & Boyle 1976).

We can see similar solutions in Europe as well, such as in Germany, where many different types of pretreatment installations were built (called, Dreikammerausfaulgrube"), with one, two or three in-line, anaerobic settlement and pretreatment units operating in cascading formats.

In 2004 the need arose to further develop these installations or to add a post phase to increase the intensity and efficiency of the treatment, such as in Bayerland. These supplementary solutions are still being added. In France's spread out, small villages and farms a total of approximately 5 million of these anaerobic pretreatment units are used. These units are manufactured by the French Sotralenz company. The company has other manufacturing facilities in Spain and Poland.

In Hungary approximately 10 % of the population has no choice but to use a local, unique solution, since they cannot connect to the public sewer system or treatment plant, due to local problems. One possibility for such situations is to install unique aerobic, so called small waste water treatment units, but the cost of their installation is relatively high and they need a lot of electricity to run. Another problem is the sewer fee, which tends to be quite high.

The specialized engineering firm of GYULAVÁRI CONSULTING Ltd. (Budapest) has been engaged in research and development (R&D), planning and consulting services and solutions for over 30 years now and has been able to add several successful solutions to its resume in the area of communal and industrial waste water treatment during the past few years. (Gyulavári, 1983). Another development alternative for such specific and smaller scale situations is the FLEXIPAK®-MINI plant, where specific needs are satisfied by intensification and further development when it is feasible (Gyulavári & Kormos, 1993). One of the objectives of this development project is the increased removal of suspended solids (SS), which is significant due to oozing and heavy load on the sub-terrain, so clogging can be decreased, whereby overall cleaning efficiency and the lifetime of the system is increased. These ensure heightened protection for our environment, and to the recipient soil layer.

32 FLEXIPAK®-MINI plants have designed and built during the last 10 years in Hungary. These are all prefabricated plastic or polypropylene cylinders or circular cross-section objects. Pre-manufacturing is carried out at the factory of TÜRK Műanyag Limited Partnership (Pilisvörösvár). Planning and licensing were provided by GYULAVÁRI CONSULTING Ltd. (Budapest). In this paper we wish to give a survey of our research, development, planning and operational activities.

II. MATERIALS AND METHODS

The structure of the FLEXIPAK®-MINI installment introduced in this paper is seen in figure 1.

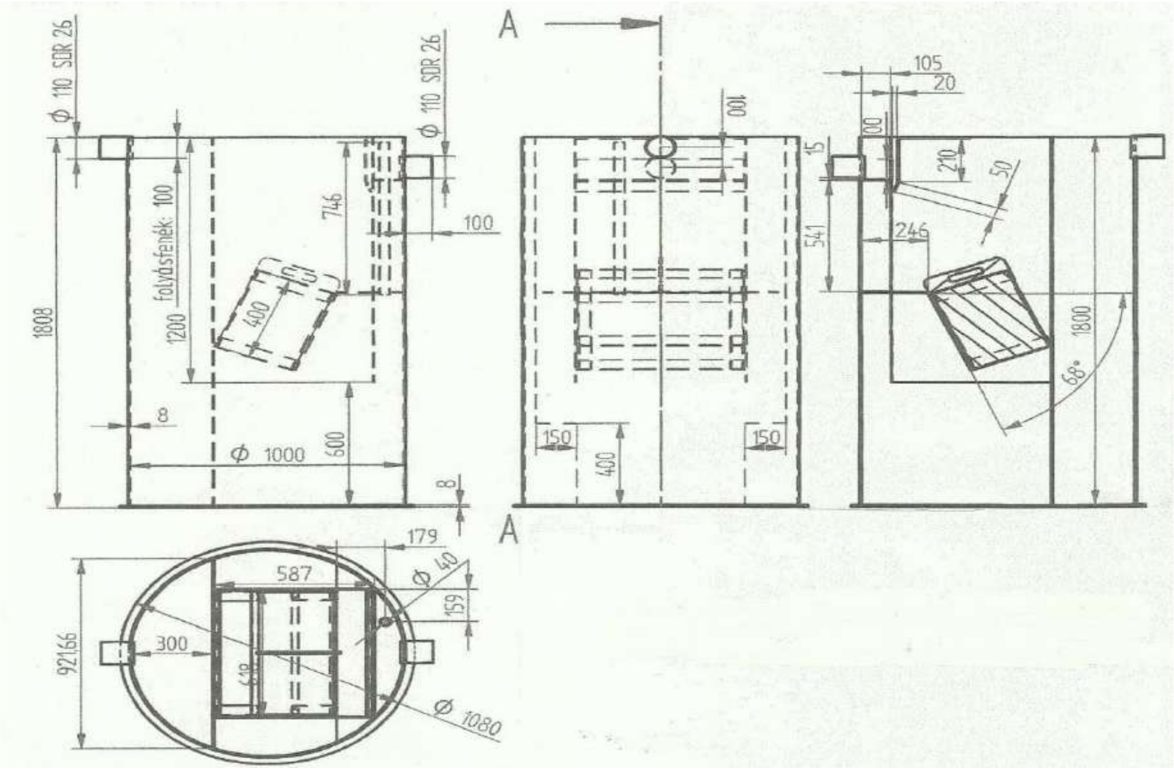

FIG. 1. THE STRUCTURE OF THE FLEXIPAK®-MINI

TABLE 1
CIRCULAR BASED PLASTIC (POLYPROPYLENE) CYLINDER, 1.0 m IN DIAMETER

Installment Ø	1 m	1,3 m	1,85 m	2,0 m
Height in meters	2,3 m	2,5 m	2,6 m	
Volume in m^3	$1m^3$	$2\ m^3$	$2\text{-}5\ m^3$	

Concentrated inflow happens at one location, typically at 80 centimeters below ground level, to prevent freezing. There is a spillover trough at the outflow where after the loss of the hydraulic effect water flow is aided by gravity alone and usually spills over at 100-150 mm. Outflow may be provided both under and above ground level.

Based on technological needs it is possible to install a pump before or after the structure. For the technological development of the FLEXIPAK®-MINI setup was applied by adapting the special multifunctional plastic TURBOPAK® unit. This plant ensures a high level of phase separation in a diversity of fields and applications, as well as an additional combined effect ensuring biological decomposition by contact with the anaerobic biofilm.

The TURBOPAK® plastic unit is a special multi-cell cross-section, multi-channel, honeycomb structured body, with its vertical channels providing a variation in its cross-section every 40 centimeters.

The patented structure is under a USA patent as well: 5,227.054 (Gyulavári & Kormos, 1993). The TURBOPAK® plastic media is manufactured in sizes capable of forming biofilm in a total of 150, 200 and 300 m^2/m^3. The PVC or PP units with UV protection are manufactured using vacuum molding. The units may be placed in two positions: one vertical and one sloping at 50-60 degree angles. The flow of the liquid can be upward.

In case of the FLEXIPAK®-MINI a 60º angle was chosen for implementation with a 150 m^2/m^3 specific biofilm value (Gyulavári, 2015). For the FLEXIPAK®-MINI plant discussed here the technological process is as follows: Raw waste water is let in either gravitationally or through a pressurized pipe preferably using a T fitting. Separation based on specific weight begins within a primary space divided by partition walls. Lighter elements accumulate on the surface while heavier elements sink to the sludge collection and digestion space near or directly at the bottom. An anaerobic partial biological disintegration and settling is ensured within the whole setup with cold digestion near the bottom going on at the same time. Generally these processes take place in a Psychrophile environment, under 20ºC, due to the temperature of the waste water.

Following mechanical detachment and convergence the waste water being treated flows upward and enters the sloping channels of the TURBOPAK® contact media module. Upward flow is achieved gravitationally with added laminar flow with additional refining or polishing phase separation occurring. During this phase sludge slides are downward into the sludge digestion space where it is thickened. The portions of the liquid with a lower specific weight float upward toward the operational surface of the system and form a floating film.

In our current case these processes are intermittent, because the different periods of the processes depend on the varying loads and flow of incoming waste water. The partial biological biodegradation is ensured on the full surface of the TURBOPAK® unit and the anaerobic biofilm at all times. Finally, the pretreated waste water leaves the equipment in phases under the protection of the wall, through the spillover, aided by gravitation alone.

The TURBOPAK® contact unit integrated into the FLEXIPAK®-MINI plant provides a significant additional affect compared to previously known anaerobic equipment. (Gyulavári, 2015). The above introduced technology can be applied in other designs or structures as well:

For example steel structures with stainless steel rails, prefabricated reinforced concrete, made on site or insulated earth basins could also be used as alternatives.

The 32 units installed in Hungary were all made out of polypropylene plastic (SIMONA) using the technology introduced herein.

III. RESULTS

The FLEXIPAK®-MINI plant introduced in the foregoing were all designed and installed during the last 10 years. It can be established that all our clients were satisfied with the results. The initial investment costs of the system were the lowest possible in comparison with other small waste water plants. We are only receiving positive feedback on the operation of the plants, with satisfactory results in each case. Pretreatment parameters reached our projected numbers.

Three of our clients ordered an aerobic polishing amendment to be installed after the FLEXIPAK®-MINI plant, so that the treated water could be used for irrigation on a part of forest and a grassy area, depending on current conditions and seasons. They are using the water for irrigating plants not used for human consumption.

Besides the obvious benefits also known from other, widely used similar anaerobe plants, FLEXIPAK®-MINI has the following added advantages:

- Combining it with TURBOPAK® contact units emphasizes cleaning results and increases the removal efficiency of suspended solids to about 98-99 %. The removal efficiency of solute, organic matter is automatically increased at the same time.
- The percentile value of COD_{Cr} and BOD_5 parameters increased to 70-85 % from the previous 30-40 %.
- The removal efficiency of solute fats and oils further increased to as high as 99 %.
- The accumulation of sludge produced by anaerobic processes decreased while the percentile value of sludge thickening increased.
- As a result there is less sludge therefore removal becomes necessary only after every 1.5-2 years. Additionally fewer odour is emitted.
- Due to increased efficiency the relative area used for settling can be decreased, so the spatial needs of the setup decreases.

In light of all the positive additional effects and benefits we can establish that the new FLEXIPAK®-MINI plant can be installed as a polishing phase of existing traditional, anaerobic systems working over their capacities. In case of the FLEXIPAK®-MINI plants installed for private homes only a limited number of detailed tests and sample analyses were made for the purpose of establishing cost efficiency.

Based on these positive experiences with current operations it is advisable to reuse the partially treated water, for flushing toilets or irrigation for example, with additional UV disinfecting if necessary.

IV. CONCLUSION

By implementing several modern developments FLEXIPAK®-MINI provides various benefits over similar traditional anaerobic equipment.

- By implementing the recommended developments total times spent in the system can be reduced to 2-2,5 days.
- Sludge needs to be hauled away only every 1.5 to 2 years.
- The elimination of unpleasant odors is more efficient, so the setup can be installed as close as 6-8 meters to residential buildings.
- The plant can be installed either over or under ground.
- The shape of the installation can be either circular or rectangular.
- The setup can be built from different materials, such as steel, reinforced concrete or plastic, but it must be corrosion resisting.
- They are generally prefabricated and assembled and installed on site.
- In case of a circular installation diameters can vary between a minimum of 1.0 meter, and up to 1.3, 1.85 and even 2 meters.
- Based on the anaerobic Dual-Biological Process (DBP) energy free operation is available for each installation alternative.
- We use the TURBOPAK® fix submerged biological contact units for each installation, where a total of 150 m2/m3 specific anaerobic biofilm surface is provided.
- The guaranteed lifetime of the poly-propilene (PP) plastic cylinder shaped FLEXIPAK®-MINI tank reactor is 25-30 years.
- The plant ensured increased treatment efficiency, especially for decreasing suspended solids (SS) content, which constitutes an important benefit and ensures longer lifetimes in cases where water is bled into porous soil layers.
- Maintenance needs are minimal; it does not contain any turning parts. It is failsafe.
- In case of technical or power outages the system stays in operation.
- In case of existing anaerobic systems, such as overloaded septic tanks, it can be used as an additional polishing phase.
- Based on results in communal areas the system can be deemed successful for treating waste water with organic pollutants.
- Further development, reviews and research is recommended.

REFERENCES

[1] Bouma I. 1975. Unsaturated flow during soil treatment of septic tank effluent. J. Environ. Eng. Div. American Soc. Civil Eng., 967-983.

[2] Gyulavári I. 1983. Wastewater treatment with contact media. SZTNH Hungarian Patent Office, Patent Number 200739 B.

[3] Gyulavári I. 2015. Alternative examples of contact media bioreactors. Book, Publishing by Könyvműhely, Miskolc, Hungary.

[4] Gyulavári I., Kormos V. 1993. Filling body biological units and cooling towers. United States Patent, Patent Number: 5,227.054

[5] Jewell W.I., Howley J.B., Perrin, D.R. 1975. Design guidelines for septic tank sludge treatment and disposal. Prog. Water Technol. 7:2.

[6] Jones J.H., Tayler G.S. 1965. Septic tank effluent percolation sands through under laboratory conditions, Soil Sci. 99: 301-309.

[7] Otis R., Boyle B.C. 1976. Performance of single household treatment units. Environ Erg. Div. American Soc. Civil Eng. EE1, 175-189.

[8] Pradhan S., Hoover M.T., Gumpretz C.M., Cobb C., Strock, J. 2011. Impacts of biological additives; Part 2 Septic tank effluent quality and overall additive efficacy. Journal of Environmental Health, 74(5): 22-28.

[9] Veres Z., Bencze N., Lakatos G. 2015. Prospects of domestic wastewater treatment for small settlements in North-eastern Hungary. Pol. J. Environ. Stud. 3: 1451-1456.

Big Data, Decision Tree Induction, and Image Analysis for the Discovery of Decision Rules for Colon Examination

Petra Perner

Institute of Computer Vision and Applied Computer Sciences, IBaI, Leipzig, Germany

Abstract*— The aim of our research was to develop a method that allows us automatically to discover the decision rules for diagnosing medical images in normal tissue images and images showing a polyp. We used a data set of images that came from an endoscope video system used for colon examination. The data set contains 283 normal tissue images and 61 polyp images. The 283 normal images consist of dark regions and reflection. One must decide if the image shows a polyp or not. This is a two-class problem. The unequal number of the data in the two classes makes our problem to an unbalanced data set problem. The polyps in the images were identified and selected by a "well-trained" medical expert. Based on these medical images, we study the behavior of two different statistical texture descriptors, the co-occurrence matrix-texture descriptor and our novel Random set texture descriptor. We review the theory of both texture descriptors and then we apply them to our medical data set. We used a decision-tree induction method to learn the classification rules based on our tool "Decision Master". In both cases, for the full unequally distributed data set and for the balanced data set, we achieved the best error rate based the Random-set texture descriptor. The performance of the co-occurrence matrix-texture descriptor was worse. For statistical based texture descriptors large enough texture are necessary that cannot always guaranteed for medical objects. Since the co-occurrence matrix is based on higher order statistic that might be the reason for the worse performance. The results show that decision tree induction and image analysis based on our novel texture descriptor is an excellent method to mine medical images for the decision rules even when the data set is unbalanced, but not only that makes our Random-set based texture descriptor favorable. It also gives a flexible way to describe the appearance of the medical objects in symbolic terms, the computation time is less, and it can be set up as software module that can be flexible used in different systems.*

Keywords— Image Analysis, Endoscope Images, Colon Examination, Polyp Images, Decision Tree Induction, Random Set Texture Descriptor, Co-occurrence Texture Descriptor, Unbalanced Data Set Problem.

I. INTRODUCTION

The aim of our research was to develop a method that allows us automatically to discover the decision rules for diagnosing images in normal tissue images and images containing a polyp. We used a data set of medical images that came from an endoscope video system used for colon examination. Texture seems to be a powerful tool to describe the appearances of medical objects into normal tissue and polyp´s. Therefore, very flexible and powerful texture descriptors are of importance that allows to recognize the texture and to understand what makes up the texture. Texture seems to become an important role to describe the appearance of different medical and biological objects in images. Patterns on cells in cell images, on fungi images or polyp images can be described by texture.

Different texture descriptors have been developed over the past (Rao 1990). The most used texture descriptor is the well-known texture descriptor based on the co-occurrence matrix (Haralick et. al 1973). Although it works well on different applications we prefer to use our texture descriptor based on Random sets (Perner et. al 2002) since this descriptor gives us more freedom in describing different textures. In this paper, we compare the two texture descriptors based on a medical data set. Related work on texture description is given Section 2. The theory of the texture descriptors based on the co-occurrence matrix is reviewed in Section 3 and the texture descriptor based on Random sets is reviewed in Section 4. The material and the application of the texture descriptors and the decision-tree induction-method is explained in Section 5. The used data set of polyp images is derived from colon examination. We calculated the texture features based on the two methods for each image of the data set and learn a decision tree classifier. Cross-validation is used to calculate the error rate. Then we compare the properties of the two best decision trees, the runtime for the feature calculation, the selected features, and the semantic meaning of the texture descriptors. The results are presented in Section 6 and they are discussed in Section 7. Conclusions are given in Section 8.

II. RELATED WORK

Texture description methods are mainly classified into structural, statistical, model-based, and transform-based approaches

(Bharatiet. al 2004, Castellano et. al 2004, Zhang & Tan 2002). Structural methods use texture elements to describe textures. It is good for image synthesis applications. Statistical methods use gray-level relationship between neighboring pixels to describe to local texture property in first-order, second-order, or higher-order statistics. The methods are good for invariant texture analysis and classification. Model-based methods model images as different probability or linear combination models (Zhang & Tang 2002) and use model parameters to describe their texture features, such as autoregressive models, fractal models (Kaplan 1999), Gaussian-mixture models (GMM) (Nguyen & Wu 2012), hidden Markov models (HMM) (Chen & Kundu 1993, Najmi & Gray 2000), Markov random fields (MRF) (Krishnamachari & Chellappa 1997) and so on. The transform methods transfer images into a frequency domain to describe textures. The methods usually use Fourier, Gabor, or wavelet transform. An overview about older methods such autocorrelation and other is given in Haralick (1979) and van Gool et. al (1985).

Often the texture descriptors are compared on standard texture data sets but recently appeared work of texture description for real world problems such as description of objects in medical images, microscopic images for different purposes such as e.g. in system biology and for environmental applications, food inspection and so on. Texture became valuable information about images. Researcher tries to develop many new texture descriptors that take into account the variances of the texture, the spectral influences and so on. At lot of different methods exist and it is not easy to do a categorization of all these methods. We want to describe in brief the recent developments. They are often variants of the above-described categories that have been evaluated on standard data sets. However nowadays, more work on real world applications appear.

Din-Chang Tseng et. al(2015) developed a multiscale texture segmentation approach based on contextual hidden Markov tree (CHMT) model and boundary refinement. A hidden Markov tree (HMT) model is a probabilistic model for capturing persistence properties of wavelet coefficients without considering clustering properties. They have proposed the CHMT model to enhance the clustering properties by adding extended coefficients associated with wavelet coefficients in every scale.

Wesley Nunes Goncalves et. al(2014) developed a method that can capture the details richness of the image surface. They estimated the fractal dimension by the Bouligand- Minkowski method due to its precision in quantifying structural properties of images. They validated their method on two standard texture datasets and the experimental results reveal that the methods are good enough to describe different data sets.

R. Mukundan (2014) use orthogonal moment functions based on Tchebycheff polynomials. They claim that the method is good because of their superior feature representation capabilities. They construct feature vectors from orthonormal Tchebycheff moments evaluated on 5x5 neighborhoods of pixels, and encoding the texture information as a Lehmer code that represents the relative strengths of the evaluated moments. The features will be referred to as Local Tchebycheff Moments (LTMs). The encoding scheme provides a byte value for each pixel, and generates a gray-level _LTM-image_ of the input image. The histogram of the LTM-image is then used as the texture descriptor for classification.

YuhuiQuan et. al(2014) developed a statistical approach to static texture description, which combines a local pattern coding strategy with a robust global descriptor to achieve highly discriminative power, invariance to photometric transformation and strong robustness against geometric changes. They called their method pattern fractal spectrum that characterizes the self-similar behavior of the local pattern distributions by calculating fractal dimension on each type of pattern. Compared with other fractal-based approaches, the proposed descriptor is compact, highly distinctive and computationally efficient. The evaluation was done on a standard benchmark set.

Aujol et. al(2006) explored in their paper various aspects of the image decomposition problem using modern variational techniques. They aim at splitting an original image f into two components u and v, where u holds the geometrical information and v holds the textural information. The modeling uses the total-variation energy for extracting the structural part and one of four of the following norms for the textural part: L2, G, L1 and a new tunable norm, suggested there for the first time, based on Gabor functions. They design tools for the TV -Gabor model.

Champion et. al(2014) do texture modelling on a real-world application for forest stand age from SAR images. The texture descriptors are calculated from statistics generated by the gray-level co-occurrence matrix for varying distance d, and orientation α, values used to calculate the matrix. It is found that texture descriptors such as contrast, inverse-difference moment, homogeneity, and correlation are strongly influenced by the parameters (d, α) related to forest stand structure (forest rows, stand density) and image resolution. In contrast, the calculated energy and entropy from the co-occurrence matrix are observed to be highly correlated to stand age and displayed a stable performance whatever the distance and orientation parameters (d, α), thus rendering them a good contender.

Dharmagunawardhana et. al(2014) proposed a novel robust texture descriptor based on Gaussian Markov random fields (GMRFs). A spatially localized parameter estimation technique using local linear regression is performed and the distributions of local parameter estimates are constructed to formulate the texture features. The inconsistencies arising in localized parameter estimation are addressed by applying generalized inverse, regularization, and an estimation window-size selection criterion. The texture descriptors are named as local parameter histograms (LPHs) and are used in texture segmentation with the k-means clustering algorithm. The segmentation results on general texture datasets demonstrate that LPH descriptors significantly improve the performance of classical GMRF features and achieve better results compared to the state-of-the-art texture descriptors based on local feature distributions.

Madzin et. al(2014) deal with medical application, where the usage of multiple medical images generated by computer tomography such as x-ray, Magnetic Resonance Imaging (MRI) and CT-scan images is a standard tool of medical procedure for physicians. The major problems in analyzing various modality of medical image are the inconsistent orientation and position of the body-parts of interest. In this research, local descriptor of texture, shape and color are used to extract features from multi-modality medical image in patches and interest point's descriptor.

Palanivel et. al (2015) use a Markov process with Bayesian Approach to analyze textures in the image and that are identified and distinguished from untextured regions with edges. The parameters of the model are estimated based on the Bayesian approach. They use two types of classification namely supervised and unsupervised classification.

Massich et. al (2014) use Self-Invariant Feature Transform (SIFT), both as low-level and high-level descriptors, applied to differentiate the tissues present in breast US images. For the low-level texture descriptors case, SIFT descriptors are extracted from a regular grid. The high-level texture descriptor is built as a Bag-of-Features (BoF) of SIFT descriptors. Experimental results are provided showing the validity of the proposed approach for describing the tissues in breast US images.

Song et. al (2014) presented a noise-robust descriptor by exploring a set of local contrast patterns (LCPs) via global measures for texture classification. To handle image noise, the directed and undirected difference masks are designed to calculate three types of local intensity contrasts: directed, undirected, and maximum difference responses. To describe pixel-wise features, these responses are separately quantized and encoded into specific patterns based on different global measures. These resulting patterns (i.e., LCPs) are jointly encoded to form our final texture representation. The evaluation has been done on two standard data sets and showed superior performance compared too many state-of-the-art methods.

Zhang and Pham (2010) and Pham (2014) tried to recognize the Subcellular Location Features (SLF) by three well-known texture feature descriptions, which are the local binary patterns (LBP), Gabor filtering and Gray Level Co-occurrence Matrix (GLCM), to recognize the cell phenotype images. Using the public benchmark 2D HeLa cell images, high classification accuracy 96% is obtained with rejection rate 21% from the proposed system by taking advantages of the complementary strengths of feature construction and majority-voting based classifiers' decision fusions.

Marcos et. al (2015) use Gray-Level Co-occurrence Matrices (GLCM), Log-Gabor Filters (LGF), Local Binary Patterns (LBP) and Discrete Tchebycheff Moments (DTM) for pollen identification in microscopic images. Fisher's discriminant analysis and k-nearest neighbor were subsequently applied to perform dimensionality reduction and multivariate classification, respectively. They found that the combination of all the texture features resulted in the highest performance, yielding an accuracy of 94.83%.

Olveres et. al (2014) use texture image segmentation for medical images. The noise inherent to images and the lack of contrast information between adjacent regions hamper the performance of the algorithms. The characterizations of regions as statistical parametric models to handle level set evolution have been proposed. In this paper, they study the influence of texture on a level-set-based segmentation and propose the use of Hermite features that are incorporated into the level set model to improve organ segmentation that may be useful for quantifying left ventricular blood vessel. The proposal was also compared against other texture descriptors such as local binary patterns, Image derivatives, and Hounsfield low attenuation values.

Cai et. al(2015) propose a novel phase-based texture descriptor for efficient and robust classifiers to discriminate benign and malignant tumors in breast cancer images. The phased congruency-based binary pattern (PCBP) is an oriented local texture descriptor that combines the phase congruency (PC) approach with the local binary pattern (LBP). The proposed PCBP texture descriptor achieves the highest values (i.e. 0.894) and the least variations in respect of the AUC index, regardless of the gray-scale variations.

Cheng et. al (2008) propose a texture method based on the co-occurrence matrix to detect colorectal polyps in colonoscopy images. They used support vector machines for classification and achieve a sensitivity of 86, 2%.

We have developed our own texture descriptor based on statistics that model the texture by a Poisson process after the image is processed by a morphological operation. The remaining areas in the images can be described by first-order and second-order statistics as well as higher-order statistics if the numbers of remaining areas are large enough. The texture descriptor can be easily and fast computed and can handle different medical textures very well (Perner 1999, Perneret. al 2002). These medical textures are often not easy to describe as it is in case of the Brodatz texture data set[1]. Our method has also explanation capability. A human can understand the differences in the texture by looking up the remaining images. If necessary, a symbolic description of the different textures can be found. Our texture descriptor has still some other properties that are of interest but here in this paper, we want to compare our texture descriptor to the co-occurrence matrix since it is from the category of statistic texture descriptors. The co-occurrence matrix is still the most used texture descriptor and we want to explore the differences between our texture descriptors and the co-occurrence matrix.

III. THE CO-OCCURRENCE TEXTURE DESCRIPTOR

The co-occurrence texture feature descriptor is comprised of fourteen statistical features (Haralick et. al 1973) derived from the co-occurrence matrix.

A co-occurrence matrix $C_{(\Delta x,\Delta y)}$ with the offset $(\Delta x,\Delta y)$ is defined over an *nxm* Image *I*:

$$C_{\Delta x,\Delta y}(i,j)=\sum_{p=1}^{n}\sum_{q=1}^{m}\begin{cases}1, & I(p,q)=i\ and\ I(p+\Delta x,q+\Delta y)=j\\ 1, & I(p,q)=j\ and\ I(p-\Delta x,q-\Delta y)=i\\ 0, & otherwise\end{cases} \tag{1}$$

The co-occurrence matrix can be interpreted as a matrix of frequency from neighboring pixels in image *I* with an offset $(\Delta x,\Delta y)$ where a pixel has the gray level *i* and the other pixel a gray level *j*. Note that this matrix is symmetric.

We can define the normalized co-occurrence matrix from $C_{(\Delta x,\Delta y)}$ as:

$$P_{(\Delta x,\Delta y)}=\frac{1}{R}C_{(\Delta x,\Delta y)} \tag{2}$$

with $R=\sum_{i=1}^{N_g}\sum_{j=1}^{N_g}C_{(\Delta x,\Delta y)}(i,j)$ being the normalized factor.

Let p_{ij} be the (*i, j*)-th element of matrix $P_{(\Delta x,\Delta y)}$, with N_g being the number of distinct gray levels in the image *I*. The *i-th* entry in the marginal probability matrix obtained by summing the rows of p_{ij} is for the line respectively.

$$p_x(i)=\sum_{j=1}^{N_g}p_{ij} \quad \text{and} \quad p_y(i)=\sum_{i=1}^{N_g}p_{ij} \tag{3}$$

Further, we are calculating:

$$p_{x+y}(k)=\sum_{\substack{i=1\\ i+j=k}}^{N_g}\sum_{j=1}^{N_g}\ p_{ij} \tag{4}$$

With k=2, 3,. . . .2 N_g

Since $P_{(\Delta x,\Delta y)}$ is also a symmetric matrix $p(i)=p_x(i)=p_y(i)$.

This results in:

$$\mu = \mu_x = \mu_y = \sum_{k=1}^{N_g} kp(k) \tag{6}$$

$$\sigma^2 = \sum_{k=1}^{N_g} p(k)(k-\mu)^2 \tag{7}$$

Now we can define our co-occurrence texture features by well-known discreet chance dimensions such as the average, moments, and variants, measures that describe the dependence of two random variables such as the correlation (Dreyer & Sauer 1982), and the measure of the mess such as the entropy:

1. Angular Second Moment:

$$f_1 = \sum_{i=1}^{N_g}\sum_{j=1}^{N_g} p_{ij}^2 \tag{8}$$

2. Contrast

$$f_2 = \sum_{k=0}^{N_g} k^2 \left(\sum_{\substack{i=1 \\ |i-j|=k}}^{N_g} \sum_{j=1}^{N_g} p_{ij} \right) \tag{9}$$

3. Correlation

$$f_3 = \frac{1}{\sigma_x \sigma_y}\left(\sum_{i=1}^{N_g}\sum_{j=1}^{N_g} ijp_{ij} - \mu_x \mu_y \right) = \frac{1}{\sigma^2}\left(\sum_{i=1}^{N_g}\sum_{j=1}^{N_g} ijp_{ij} - \mu^2 \right) \tag{10}$$

4. Sum of Squares Variance

$$f_4 = \sum_{i=1}^{N_g}\sum_{j=1}^{N_g} (i-\mu)^2 p_{ij} \tag{11}$$

5. Inverse Difference Moment

$$f_5 = \sum_{i=1}^{N_g}\sum_{j=1}^{N_g} \frac{1}{1+(i-j)^2} p_{ij} \tag{12}$$

6. Sum Average

$$f_6 = \sum_{k=2}^{2N_g} kp_{x+y}(k) \tag{13}$$

7. Sum Variance

$$f_7 = \sum_{k=2}^{N_g} (i-f_6)^2 p_{x+y}(k) \tag{14}$$

8. Sum Entropy

$$f_8 = -\sum_{k=2}^{2N_g} p_{x+y}(k) \log p_{x+y}(k) \tag{15}$$

9. Entropy

$$f_9 = -\sum_{i=1}^{N_g}\sum_{j=1}^{N_g} p_{ij}\log p_{ij} \tag{16}$$

10. Difference Variance

$$f_{10} = \text{variance of } p_{x-y} \tag{17}$$

11. Difference Entropy

$$f_{11} = -\sum_{k=0}^{N_g-1} p_{x-y}(k)\log p_{x-y}(k) \tag{18}$$

12.

and

13. Information Measure of Correlation

$$f_{12} = \frac{f_9 - HXY1}{H} \tag{19}$$

$$f_{13} = \sqrt{1-\exp[-2(HXY2 - f_9)]\}} \tag{20}$$

Where

$$HXY1 = -\sum_{i=1}^{N_g}\sum_{j=1}^{N_g} p_{ij}\log\left(p_x(i)p_y(j)\right) \tag{21}$$

$$HXY2 = -\sum_{i=1}^{N_g}\sum_{j=1}^{N_g} p_x(i)p_y(j)\log\left(p_x(i)p_y(j)\right) \tag{22}$$

$$H = \sum_{k=1}^{N_g} p(k)\log p(k) \tag{23}$$

For our tests, we compute four co-occurrence matrixes $C_{(\Delta x,\Delta y)}$ with the offsets shown in Table 1.

TABLE 1
USED OFFSETS $(\Delta x,\Delta y)$ AND THEIR NEIGHBORHOOD RELATIONS

Angle	$(\Delta x,\Delta y)$
0°	(1,0)
45°	(1,-1)
90°	(0,-1)
135°	(-1,-1)

First, we compute for the four matrixes the thirteen co-occurrence texture features of formula (8)-(20). Thus, we obtain four values for each feature. To reduce the feature set, we compute analog to Haralicket. al (1973) the mean and rank of each feature so that we finally get twenty-six features. This feature set is named COO-1.
Another method to compute the texture features that saves computation time is to sum over the four matrixes CT

$$CT_{ij} = C_{(0,1)}(i,j) + C_{(-1,1)}(i,j) + C_{(-1,0)}(i,j) + C_{(-1,-1)}(i,j) \tag{24}$$

The matrix CT is normalized per formula 2. From the normalized matrix PT, we calculate the thirteen texture features of co-occurrence descriptor. This feature set is named COO-2.

In addition to the above described features, is defined the maximal correlation coefficient as feature number fourteen. However, we are not using this coefficient in our study because of the high computation time.

IV. TEXTURE DESCRIPTOR BASED ON RANDOM SETS

Boolean sets were invented by Matheron (1975). An in-depth description of the theory can be found in Stoyan et al(1987). The Boolean model allows to model and simulate a huge variety of textures e.g. for crystals, leaves, etc. The texture model *X* is obtained by taking various realizations of compact random sets, implanting them in Poisson points in R^n, and taking the supremum. The functional moment $Q(B)$ of *X*, after Booleanization, is calculated as:

$$P(B \subset X^{c}) = Q(B) = \exp(-\theta \overline{Mes}(X^{'} \oplus \check{B})) \qquad \forall B \in \kappa \tag{25}$$

where κ is the set of the compact random set of R^n, θ the density of the process and $\overline{Mes}(X^{'} \oplus \check{X})$ is an average measure that characterizes the geometric properties of the remaining set of objects after dilation. Relation (25) is the fundamental formula of the model. It completely characterizes the texture model. $Q(B)$ does not depend on the location of B, i.e., it is stationary. One can also provide that it is ergodic so that we can peak the measure for a specific portion of the space without referring to the particular portion of the space.

Formula 25 show us that the texture model depends on two parameters:

- the density θ of the process and
- a measure $\overline{Mes(X^{`}} \oplus \check{B})$ that characterizes the objects. In the one-dimensional space, it is the average length of the lines and in the two-dimensional space $\overline{Mes(X^{`}} \oplus \check{B})$ are the average measure of the area and the perimeter of the objects under the assumption of convex shapes.

We consider the two-dimensional case and develop a proper texture descriptor.

Suppose now that we have a texture image with 8 bit gray levels. Then we can consider the texture image as the superposition of various Boolean models, each of them having a different gray level value on the scale from 0 to 255 for the objects within the bit plane.

To reduce the dimensionality of the resulting feature vector, the gray levels ranging from 0 to 255 are now quantized into S intervals t. Each image f(x,y) is classified according to the gray level into t classes, with t={0,1,2,..,S}. For each class a binary image is calculated containing the value "1" for pixels with a gray level value falling into the gray level interval of class t and value "0" for all other pixels. The resulting bit plane *f(x,y,t)* can now be considered as a realization of the Boolean model. The quantization of the gray level into *S* intervals was done at equal distances. In the following, we call the image *f(x,y,t)* a class image. In the class image we can see a lot of different objects. These objects get labeled with the contour following method (Klette & Zamperoni 1996). Afterwards, features from the bit-plane and from these objects are calculated. Since it does not make sense to consider the features of every single object due to the curse of dimensionality, we calculate the mean and standard deviation for each feature that characterizes the objects such as the area and the contour. In addition to that, we calculate the number of objects and the areal density in the class image.

The list of features and their calculation are shown in Table 2. The first one is the areal density of the class image *t* which is the number of pixels in the class image, labeled by "1", divided by the area of the image. If all pixels of an image are labeled by "1", then the density is one. If no pixel in an image is labeled, then the density is zero.

TABLE 2
TEXTURE FEATURES BASED ON RANDOM SET

Description	Name	Type	Formula
Area in class image *t*	***Area_t***	num	$Area_t = \begin{cases} Area_t = Area_t + 1 & \text{if } f(x,y,t) = 1 \\ Area_t = Area_t & \text{if } f(x,y,t) = 0 \end{cases}$
Density in class image *t*	***Dens_t***	num	$Dens_t = \begin{cases} Dens_t = Dens_t + \frac{1}{A} & \text{if } f(x,y,t) = 1 \\ Dens_t = Dens_t & \text{if } f(x,y,t) = 0 \end{cases}$ with $A = \sum_{t=1}^{S} Area_t$
Number of objects	***Count_t***	num	$n(t)$
Mean area of objects in class image *t*	***AreaMean_t***	num	$\overline{A(t)} = \frac{1}{n(t)} \sum_{i=1}^{n(t)} A_i(t)$
Standard deviation of the area of the objects in class image *t*	***AreaStdDev_t***	num	$S(t) = \sqrt{\frac{1}{n(t)} \sum_{i=1}^{n(t)} (A_i(t) - \overline{A(t)})^2}$
The contour length of a single object is $u = l + \sqrt{2} \cdot m$ with *l* being the number of contour pixels having odd chain coding numbers and *m* being the number of contour pixels having even chain coding numbers.			
Mean contour length of objects in class image *t*	***ContMean_t***	num	$\bar{u}(t) = \frac{1}{n(t)} \sum_{i=1}^{n(t)} u_i(t)$
Standard deviation of the contour length of objects in class image *t*	***ContStdDev_t***	num	$S(t) = \sqrt{\frac{1}{n(t)} \sum_{i=1}^{n(t)} (u_i(t) - \overline{u(t)})^2}$

From the objects in the class image *t*, the area, a simple shape factor, and the length of the contour are calculated. Per the model, not a single feature of each object is taken for classification due to the curse of dimensionality, but the mean and the standard deviation of each feature are calculated over all the objects in the class image t. We also calculate the frequency of the object size in each class image t.

Depending on the number of slices S we get a feature set of 42(S=6), 84(S=12), 112(S=16).

V. MATERIAL OF THE APPLICATION AND THE DATA-MINING TOOL *DECISION MASTER®*

We studied the performance of the two texture descriptors based on a data set of 344 images. These images come from an endoscope video system used for colon examination (Cheng et. al 2008). The data set contains 283 normal tissue images and 61 polyp images (see Figure 1) in the form of sub-images of a size 33x33 that are derived from 37 original colonoscopy images. The polyps in the 37 original colonoscopy images were identified and selected by a "well-trained" medical expert. A polyp is split into as many as possible sub-images.

The 283 normal images consist of dark regions, reflections etc. of the 37 original colonoscopy images.

This presents a two-class problem; one must decide if the image shows a polyp or not. The texture descriptions were calculated from these images. The resulting data set was used to train a decision tree based on the C4.5 algorithm (Perner 2002). Cross-validation was used to estimate the error rate.

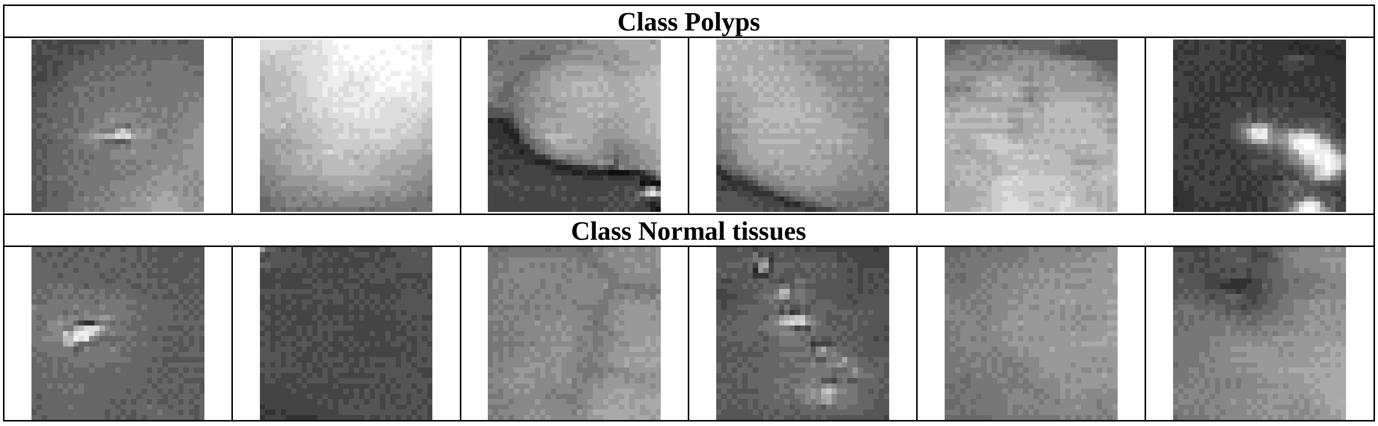

FIG. 1. SOME EXEMPLARY IMAGES

The tool ***Decision Master***® (Perner 1994-2017) is a data mining tool based on decision tree induction. It contains binary and n-ary decision tree induction methods such as standard algorithm like C4.5, ID3 and n-ary decision-tree induction methods developed by the Institute of Computer Vision and applied Computer Sciences ***IBaI*** (Perner & Trautzsch 1998).It is a commercial tool now and sold worldwide. It allows comparing the learnt models based on standard algorithms and special developed algorithms. N-ary trees get usually more compact than binary trees. The explanation capability of the trees is then better than for binary trees. However, it cannot be said from scratch which decision tree induction method is best based on the error rate for the desired data set. Therefore, it should be easy for the user to check out several decisions tree induction methods. The tool ***Decision Master***® allows that in an excellent manner. It has functions for dealing with missing values, erroneous values, and outliers such as the box-plot method and others. N-fold cross-validation or test-and-train can evaluate the learnt model. Several error rates are calculated such as the overall error rate, the class-specific error rate, and the classification quality (Perner et. al 2001). The tool has a nice user interface so that a non-computer expert can easy handle it. The other option is to integrate the software as OEM component in larger systems for example in E-commerce suites for on-line user profiling or for learning other information from the trace of the online-user (Perner & Fiss 2002).

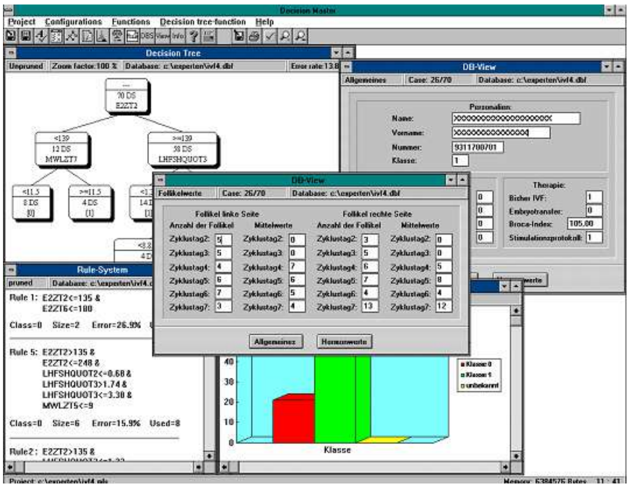

Name: XXXXXXXXXXXXXXXXXXXX
Vorname: XXXXXXXXXXXXXXXX
Nummer: 9311700701
Klasse: 1

Bisher IVF: 1
Embryotransfer: 0
Broca-Index: 105,00
Stimulationsprotokoll: 1

	Follikel linke Seite: Anzahl der Follikel	Follikel linke Seite: Mittelwerte	Follikel rechte Seite: Anzahl der Follikel	Follikel rechte Seite: Mittelwerte
Zyklustag2:	5	0	3	0
Zyklustag3:	5	0	5	0
Zyklustag4:	4	7	6	5
Zyklustag5:	6	6	7	8
Zyklustag6:	7	5	4	4
Zyklustag7:	3	4	13	12

```
Rule 1:  E2ZT2<=135 &
         E2ZT6<=180

Class=0   Size=2   Error=26.9%

Rule 5:  E2ZT2>135 &
         E2ZT2<=248 &
         LHFSHQUOT2<=0.68 &
         LHFSHQUOT3>1.74 &
         LHFSHQUOT3<=3.30 &
         MWLZT5<=9

Class=0   Size=6   Error=15.9%   Used=8

Rule2 :  E2ZT2>135 &
```

FIG. 2 SCREENSHOT OF THE DATA-MINING TOOL DECISION MASTER®

VI. RESULTS

For the texture descriptor based on random sets the choice of S is important. On the one hand, we need a sufficiently large *S* to separate the classes. On the other hand, with increasing S also the number of features increases and we run into the curse-of-dimensionality problem.

Figure 3 shows the class images for some polyp images and some normal tissue images for *S=6*. Figure 4 shows the class images for some polyp images and some tissue images for *S=12*. Figure 4 shows that most pixels of normal tissue images are located in only a few lower 1-3 class images. In contrast to this, in the polyp images the pixels are distributed more across the class images.

For our tests, we used S=6, S=12 and S=16. We have not yet developed a good procedure to estimate the number of S. The determination of the right number of S is still heuristic but in most of our applications S=12 turned out to be a good choice

(Perner et. al 2002).

In the first test (test_1), we used 30 polyp images and 30 normal tissue images as a data base. The results are shown in Figure 6. In the second tests (test_2), we used all 344 images as a data base. The results are shown in Figure 7.

In both tests the texture descriptor based on random sets with S=12 is the best texture descriptor. The test shows that the choice of *S=6*is too small and the choice of *S=16* is already too large. This observation might already demonstrate the effect of the curse of dimensionality.

The texture descriptor based on random sets for S=12 has an error rate of 1.67% for the data set with 60 images (see Figure 6) with equally distributed number of polyps and normal tissue. Compared to this, the texture descriptor COO-1 has an error rate of 3.33% and COO-2 has an error rate of 10% (see Figure 6).

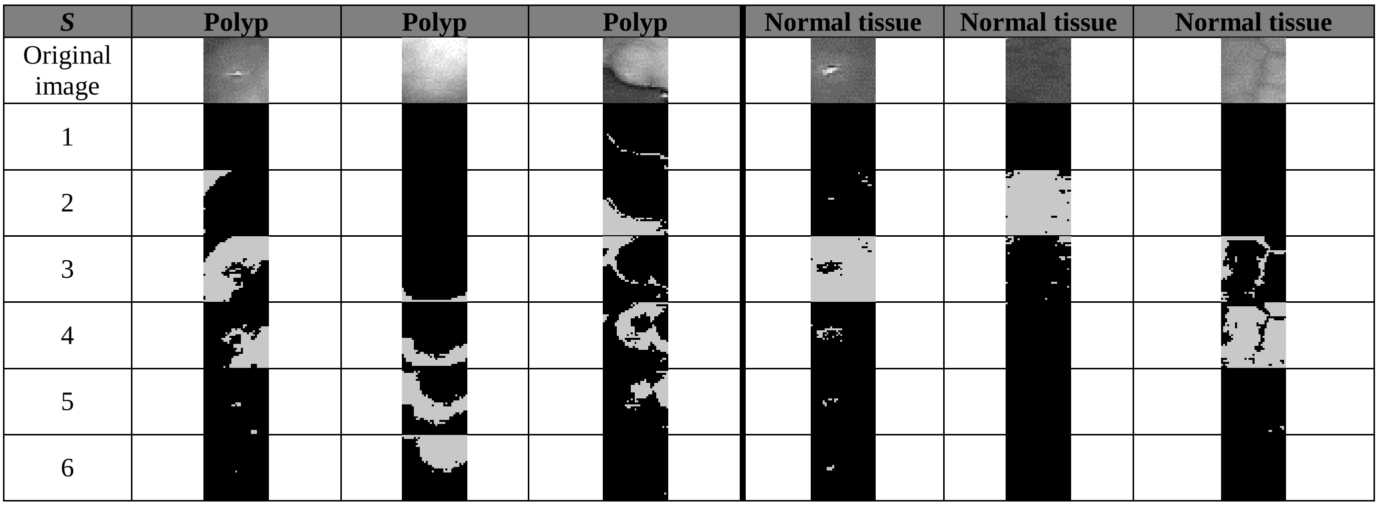

FIG. 3. THE IMAGES f(x,y,t) WITH S=6

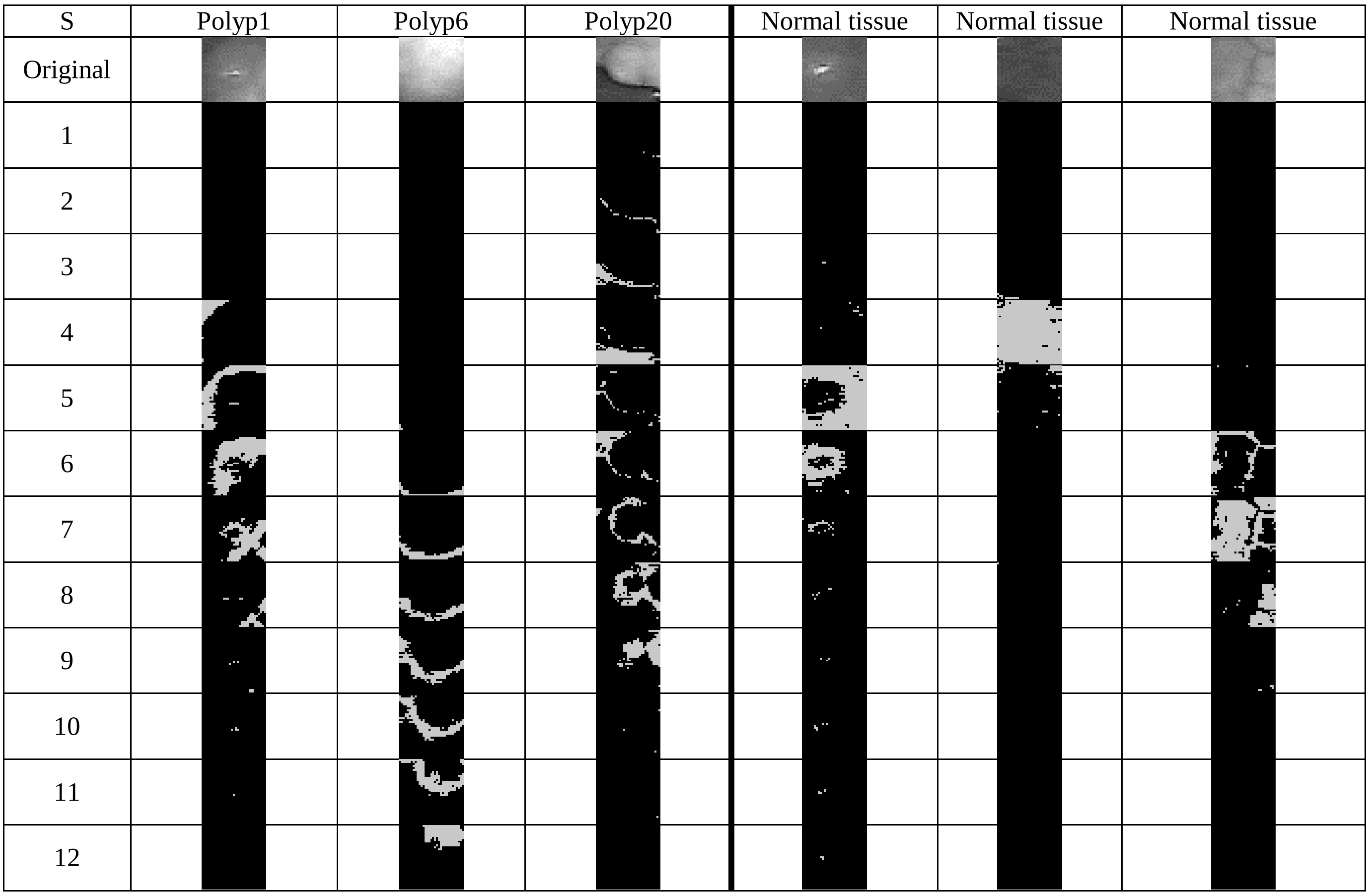

FIG. 4. THE IMAGES f(x,y,t) WITH S=12

The texture descriptor based on random sets for S=12 has an error rate of 9.88% for the data set with 334 images (see Figure 7) with 283 normal tissues and 61 polyps. Compared to this, the texture descriptor COO-1 has an error rate of 13.37% and COO-2 has an error rate of 18.89% (see Figure 7).

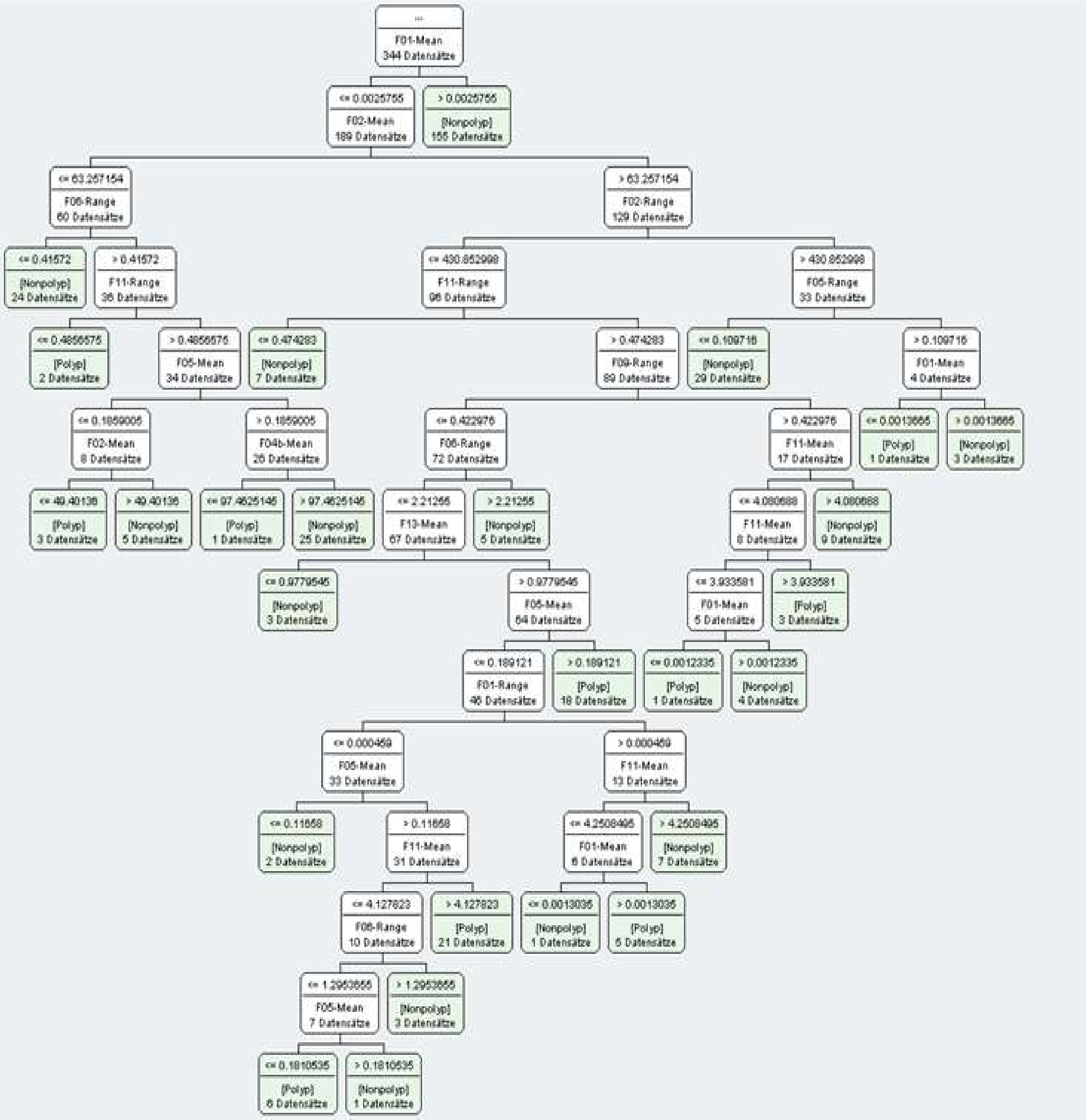

FIG. 5. DECISION TREE FOR COO FEATURE DESCRIPTOR

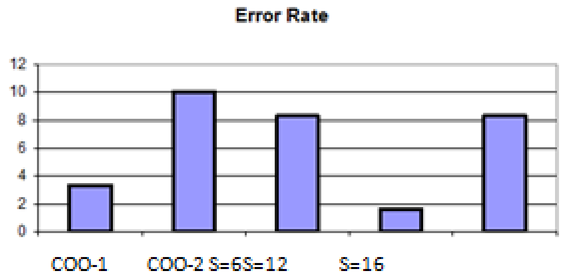

FIG. 6. ERROR RATE (IN PERCENT) FOR TEST 1

FIG. 7. ERROR RATE (IN PERCENT) FOR TEST 2

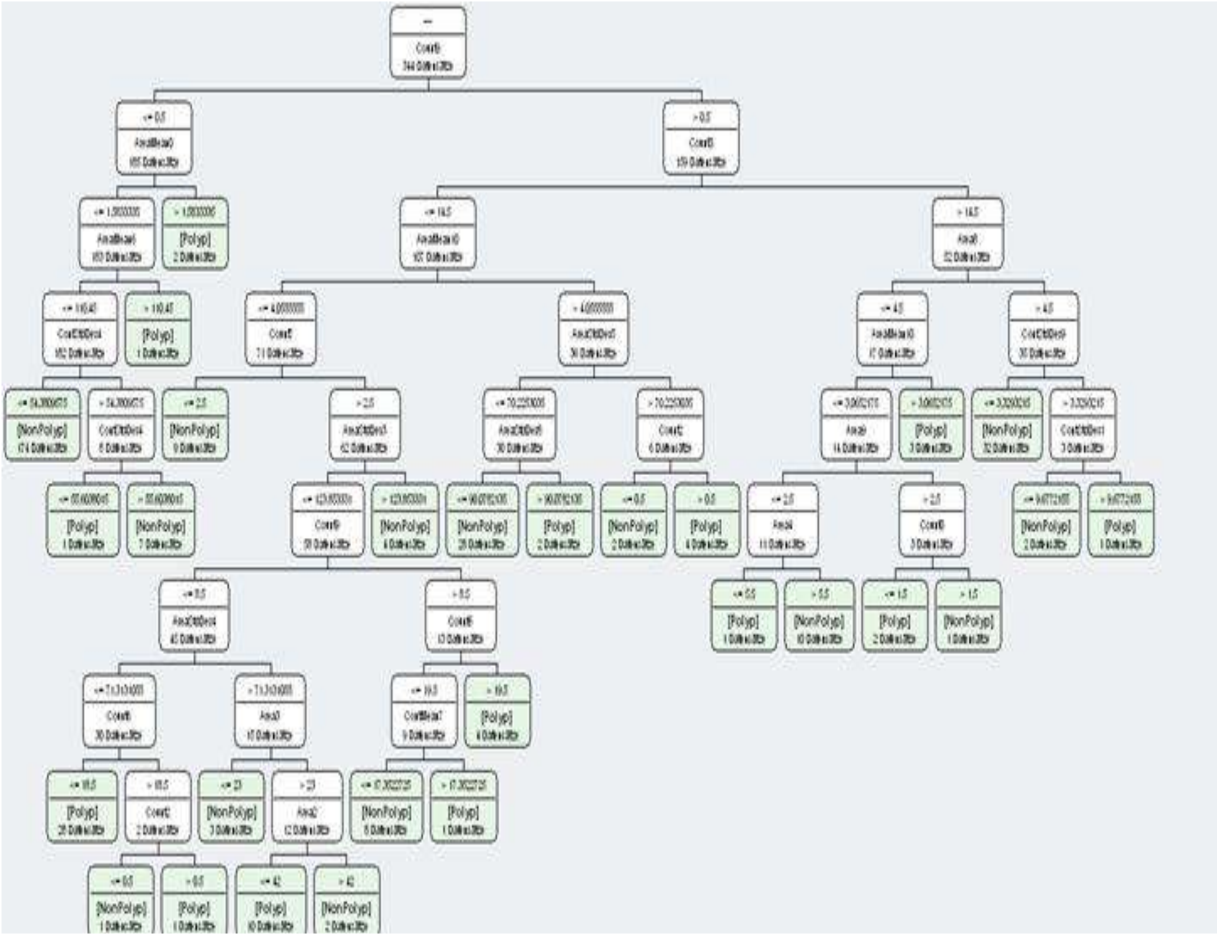

FIG. 8. DECISION TREE FOR TEXTURE FEATURES BASED ON RANDOM SETS

The resulting decision trees are shown in Figure 5 for COO feature descriptor and in Figure 8 for the texture features based on random sets.

The comparison of the two trees shows that the feature selection method during decision tree induction selects only 12 features from 26 features for COO texture descriptor and 22 features from 84 features for the texture descriptor based on random sets (see Table 2). The tree expands more in depth for the COO feature descriptor than for the texture descriptor based on random sets. The runtime of the program for the calculation of COO texture descriptor is 7-times longer than for the texture descriptor based on random sets (see Table 3).The runtime of the program for the calculation of COO-2 texture descriptor is not as long but the error rate is much higher than that for COO-1.

TABLE 3

RUN TIME

Runtime	COO-1	COO-2	Texture Descriptor based on Random Sets
	91.03s	83.22s	13.75s

VII. DISCUSSION

We have studied the behavior of the well-known co-occurrence texture descriptor to our novel random set texture descriptor. Both are statistical-based texture descriptors.

In this application, the texture descriptor based on random sets outperformed the COO texture descriptor. The accuracy is 3.49 % higher than that of COO texture descriptor in case of COO-1 and 9.01% higher in case of COO-2.

Decision trees are sensitive to unbalanced class distribution. Therefore, the error rate in the second experiment rises since the ratio of the two classes is 1/5 in the data set. Nonetheless, the tendency of the error rate of the three descriptors is the same.

A further advantage of the texture descriptor based on random sets over COO texture descriptor is the reduced time required for computing the features. In addition, we can understand the semantics behind the numerical texture description. The texture features based on random sets have a semantic meaning and give an expert an understanding about texture (see Table 2).

The choice of the number of slices *S* emerges to S=12 in all the applications we have done until now. The number S=12 provides a feature set of 84 features. It might be that this is a compromise between a rich description of texture and the large feature set problem (curse-dimensionality). Besides that, our observations showed that the objects in the slice images converges to single points in case of S=16. If this happens then there is no information in the shape or contour anymore.

The Random-Set texture descriptor has a nice feature besides the co-occurrence texture descriptor. Semantic labels depending on the application can describe the texture and therefore the meaning of the texture is understandable by a human. In case of Figure 4 we can say for poly_1-image, it has objects in the higher slices. In case of poly_20-image, it is a homogenous texture since objects are distributed over all slices, and in case of normal tissue, the objects are in the middle of the slices. The semantic label helps the human to understand the texture and to talk about the texture in a common way. The medical texture objects such as for the polyp images and for cell images (Perner et. al 2002) are often not large objects. That limits the statistics we can use. We stayed on the first-order statistics. Higher-order statistics make no sense for small objects since the number of objects gets low and no sufficient static can be calculated.

The run-time of the random-set texture descriptor is seven times lower than as for the co-occurrence texture descriptor. This is a big advantage of the random-set texture descriptor over the co-occurrence texture descriptor. It helps to speed up the calculation of the image processing methods. The random-set texture descriptor can be given out a standard module for texture calculation. The input to the module is only the object points and the outputs of the module are the calculated features for the slices.

The decision tree induction method performs nicely on texture classification. The decision tree induction method is also a feature selector. Therefore, the method can as a learning method for the classification model as well as a feature selector. The number of features selected for COO texture descriptor is always lower than the number selected for the texture descriptor based on random sets. The texture descriptor based on random sets may provide a richer description of texture. Features from almost all slices are included in the decision.

The data set contains 283 normal tissue images and 61 polyp images. This is a two-class problem. The unequal number of the data in the two classes makes our problem to an unbalanced data set problem. The polyps in the images were identified and selected by a “well-trained” medical expert. The 283 normal images consist of dark regions and reflection. For the full unequally distributed data set, we achieved an error rate of 9.88% based on cross-validation. We achieved an error rate of 1.67% by cross-validation when we created a data set with equally distributed data in each class. To sample the data into two equally distributed data sets is our strategy to deal with the unbalanced data set problem for decision tree induction.

VIII. CONCLUSION

Many texture descriptors are known from the literature (Rao 1990). The most used texture descriptor is the texture descriptor based on the co-occurrence matrix. We proposed a texture descriptor based on Random sets (Perner et. al 2002a). In this paper, we compared both texture descriptors based on a medical-image data set for colon examination. The image should be classified into normal tissue images and into polyp images. We choose a medical application since the appearance of many medical objects can often be nicely described by texture. We learnt a classifier model based on decision tree induction. Then we compared the classification results for both texture descriptors.

We have found that the texture descriptor based on Random sets outperforms the co-occurrence texture descriptor based on the error rate, tree properties and the runtime. Co-occurrence texture descriptor uses fewer features from the set of calculated texture features than the texture descriptor based on Random sets. However, this might only demonstrate that the co-occurrence texture descriptor has limited description power since the error rate is much higher than that for the texture descriptor based on random sets. One reason might be that the medical objects are not so large and the higher-order statistics fail due to the limited number of pixels. The run-time of the Random-set texture descriptor is seven times lower than as for the co-occurrence texture descriptor. This is a big advantage of the Random-set texture descriptor over the co-occurrence texture descriptor since the large computation time of image analysis algorithm is still a problem. The Random-set texture descriptor can form a software module that can be used for different applications and different sizes of the objects.

In addition, the texture descriptor based on Random sets has semantic meanings. An expert can understand the properties of the texture when looking at the slices produced during the calculation of the texture features. Therefore, the different appearances in the slices can be labeled by semantic terms that would give us explanation capability of the different textures.

The unbalanced data set problem as it often appears for medical data sets is handled in our study by sampling two equally distributed data sets together for the two-class problem. If we use this data set we can achieve a higher accuracy for the classification for both texture descriptors but still the Random-set texture descriptor outperforms the co-occurrence matrix-texture descriptor.

ACKNOWLEDGMENT

This work has been sponsored under the grant title “Study of the Cognitive Aspects of Human Vision” CogVision under the grant number IS 2012-4.

REFERENCES

[1] Rao A. R (1990).: A Taxonomy for Texture Description and Identification, Springer Verlag, Berlin.

[2] Haralick, R.H., Shanmugam, K., Dingstein, I. (1973), Textural Features for Image Classification. IEEE Transactions on Systems, Man and Cybernetics 3(6), 610-621.Perner P., Perner H., Müller B. (2002a), Mining Knowledge for Hep-2 Cell Image Classification, Journal Artificial Intelligence in Medicine (26), 161-173.

[3] M. H. Bharati, J. J. Liu, and J. F. MacGregor (June 2004), “Image texture analysis: methods and comparisons,” Chemometrics and Intelligent Laboratory Systems, vol. 72, pp. 57-71.

[4] G. Castellano, L. Bonilha, L. M. Li, and F. Cendes (Dec. 2004), “Texture analysis of medical images,” Clinical Radiology, vol. 59, no. 2, pp. 1061-1069.

[5] J. G. Zhang and T. N. Tan (Mar. 2002), “Brief review of invariant texture analysis methods,” Pattern Recognition, vol. 35, pp. 735-747.

[6] L. M. Kaplan (Nov. 1999), “Extended fractal analysis for texture classification and segmentation,” IEEE Trans. Image Processing, vol. 8, no. 11, pp. 1572-1585.

[7] T. M. Nguyen and Q. M. J. Wu (Feb. 2012), “Gaussian-mixture-model-based spatial neighborhood relationships for pixel labeling problem,” IEEE Trans. Systems, Man, and Cybernetics Part B-Cybernetics, vol. 42, no. 1, pp. 193-202.

[8] J.-L. Chen and A. Kundu (1993), “Automatic unsupervised texture segmentation using hidden Markov model,” in Proc. IEEE Int. Conf. Acoustics, Speech and Signal Processing, Minneapolis, Minnesota, Apr. 27-30, pp. 21-24.

[9] J. Li, A. Najmi, and R. M. Gray (Feb. 2000), “Image classification by a two-dimensional hidden Markov model,” IEEE Trans. Signal Processing, vol. 48, no. 2, pp. 517-533.

[10] H. Dreyer and W. Sauer, Prozeßanalyse – ElementarestochastischeMethoden, VEB VerlagTechnik Berlin, 1982

[11] S. Krishnamachari and R. Chellappa (Feb. 1997), “Multiresolution Gauss-Markov random field models for texture segmentation,” IEEE Trans. Image Processing, vol. 6, no. 2, pp. 251-267.

[12] R. Haralick (May 1979), Statistical and Structural Approaches to Texture, IEPEREO, C EETDHINEG S OF VOL. 67, NO. 5, p. 786-804

[13] Luc van Gool, P. Deweale, A Oosterlink (1985), Survey – Texture Analysis Anno 1983, Computer Vision, Graphics, and Image Processing, 29, p. 336-357.

[14] Din-Chang Tseng, Member, IACSIT and Ruei-Lung Chen (June 2015), Multiscale Texture Segmentation Using Contextual Hidden Markov Tree Models, International Journal of Machine Learning and Computing, Vol. 5, No. 3, p. 198- 205.

[15] Wesley NunesGon_calves, Bruno Brandoli Machado, and Odemir Martinez Bruno (Febr. 2014), Texture descriptor combining fractal dimension and artificial crawlers, Physica A: Statistical Mechanics and its Applications, Volume 395, Pages 358–370

[16] R. Mukundan (2014), Local Tchebycheff Moments for Texture Analysis, In: G.A. Papakostas, Moments and Moment Invariants - Theory and Applications, GCSR Vol. 1, Science Gate Publishing, p. 127- 142.

[17] YuhuiQuan , Yong Xu, , Yuping Sun (April 2014), A distinct and compact texture descriptor, Image and Vision Computing, Volume 32, Issue 4, Pages 250–259

[18] J.-F. Aujol, G. Gilboa, T. Chan, St. Osher (April 2006), Structure-Texture Image Decomposition - Modeling, Algorithms, and Parameter Selection, International Journal of Computer Vision, Volume 67, Issue 1, pp 111-136

[19] I. Champion, Chr. Germain, J. P. Da Costa, A. Alborini, and P. Dubois-Fernandez (January 2014), Retrieval of Forest Stand Age From SAR Image, Texture for Varying Distance and Orientation Values of the Gray Level Co-Occurrence Matrix, IEEE GEOSCIENCE AND REMOTE SENSING LETTERS, VOL. 11, NO. 1, p. 5-9.

[20] Ch. Dharmagunawardhana, S. Mahmoodia, M. Bennettb, M. Niranjana (Nov. 2014), Gaussian Markov random field based improved texture descriptor for image segmentation, Image and Vision Computing, Volume 32, Issue 11, Pages 884–895.

[21] H. Madzin, R. Zainuddin, and Nur-Sabirin Mohamed (Nov. 2014), Analysis of Visual Features in Local Descriptor for Multi-Modality Medical Image, The International Arab Journal of Information Technology, Vol. 11, No. 5, p. 468- 475.

[22] N.Palanivel, P.Keerthika, K.Yazhini, P.Thamizhini (April 2015), Texture Analysis using Markov process with Bayesian Approach, International Journal of Advanced Research in Computer and Communication Engineering, Vol. 4, Issue 4, p. 101-104.

[23] J. Massich, F. Meriaudeau, M. Sent´ıs, S. Ganau, E. P´erez, D. Puig, R. Mart´i, A. Oliver, and J. Mart´I (2014), SIFT Texture Description for Understanding Breast Ultrasound Images In: H. Fujita, T. Hara, and C. Muramatsu (Eds.): IWDM 2014, LNCS 8539, pp. 681–688, 2014, Springer International Publishing Switzerland.

[24] Tiecheng Song, Hongliang Li, Senior Member, IEEE, FanmanMeng, Qingbo Wu, Bing Luo, Bing Zeng (2014), Noise-Robust Texture Description Using Local Contrast Patterns via Global Measures, Signal Processing Letters, IE Volume:21 Issue:1, p. 93 - 96

[25] B. Zhang, Tuan D. Pham (2010), Multiple Features Based Two-stage Hybrid Classifier Ensembles for Subcellular Phenotype Images Classification, International Journal of Biometrics and Bioinformatics, (IJBB), Volume (4): Issue (5) 176-193.

[26] Tuan D. Pham, (January 10, 2014) Automated identification of mitochondrial regions in complex intracellular space by texture analysis, Proc. SPIE 9069, Fifth International Conference on Graphic and Image Processing (ICGIP 2013), 90690G; doi:10.1117/12.2050102

[27] J. V. Marcos,, R. Nava, G. Cristobal, R. Redondo, B. Escalante-Ramrez, G. Bueno, O. Deniz, A. Gonzalez-Porto, C. Pardo, F. Chung, T. Rodriguez (2015), Automated pollen identification using microscopic imaging and texture analysis, Micron, Volume 68, January 2015, Pages 36–46

[28] J. Olveres, R. Nava, E. Moya-Albor, B. Escalante-Ramirez, J. Brieva, G. Cristobal and E. Vallejo (2015), Texture descriptor approaches to level set segmentation in medical images, Optics, Photonics, and Digital Technologies for Multimedia Applications III, edited by Peter Schelkens, TouradjEbrahimi, Gabriel Cristóbal, FrédéricTruchetet, PasiSaarikko, Proc. of SPIE Vol. 9138, p. 1-12

[29] L. Cai, X. Wang, Y. Wang, Y. Guo, J. Yu and Y. Wang (2015), Robust phase-based texture descriptor for classification of breast ultrasound images, BioMedical Engineering OnLine (2015) 14:26, p. 1-21

[30] Da-Chuan Cheng, Wen-Chien Ting, Yung-Fu Chen, Qin Pu, Xiaoyi Jiang (2008), Colorectal Polyps Detection Using Texture Features and Support Vector Machine, In: P. Perner, Advances in Mass Data Analysis of Images and Signals in Medicine, Biotechnology, Chemistry and Food Industry Lecture Notes in Computer Science Volume 5108, 2008, pp 62-72

[31] P. Perner (1998), Classification of HEp-2 Cells Using Fluorescent Image Analysis and Data Mining,14th Intern. Conference on Pattern Recognition, Brisbane Austr., IEEE Computer Society Press 1998, Vol. II, pp. 1677-1679

[32] Matheron, G. (1975), Random Sets and Integral Geometry. J. Wiley&Sons, New York, London (1975)

[33] Stoyan, D., Kendall, W.S., Mecke, J. (1987), Stochastic Geometry and Its Applications. AkademieVerlag (1987)

[34] Perner P. (1994-2017), Data Mining Tool *Decision Master*, ibai-solutions www.ibai-solutions.de

[35] Klette, R., Zamperoni, P. (1996), Handbook of image processing operators, Chichester; New York: Wiley, 1996.

[36] Perner P. (2002b), Data Mining on Multimedia Data, lncs 2558, Springer Verlag, 2002.

[37] Perner P. and Trautzsch S. (1998), Multinterval Discretization for Decision Tree Learning, In: Advances in Pattern Recognition, A. Amin, D. Dori, P. Pudil, and H. Freeman (Eds.), Springer Verlag 1998, LNCS 1451, pp. 475-482.

[38] P. Perner, U. Zscherpel, C. Jacobsen (2001), A Comparision between Neural Networks and Decision Trees based on Data from Industrial Radiographic Testing, Pattern Recognition Letters 22 (2001), pp. 47-54.

Experimental Study of Problem of Estrangement of AR. Drone Four Rotor Helicopter Velocity Parameter Calculated by the Internal IMU

Hideki Toda

Department of Electric and Electronic Engineering, University of Toyama, 3190 Gofuku, Toyama, 930-8555, Japan

Abstract**—***For four rotor helicopter system, the velocity parameter is important for stable real-time control, and the velocity is calculated by the IMU (Internal Measurement Unit) from the three-axis acceleration and gyro sensors.*

Since the IMU unit developed and designed for multi-purpose use, high-frequency range of the acceleration/gyro sensors information was used for estimating the velocity and it is afraid to do overestimation of the velocity especially when the drone collision against the wall (even with a slight contact) and the impact due to blasts. The result shows that the IMU unit calculated velocity was divergent 20 times from the real velocity measured from the camera on the ceiling even when low speed contact with a wall (25 cm/sec speed). When the estimated velocity parameter would be used for the position control and stabilizing of AR. Drone helicopter, it will be necessary to consider the problem of the estrangement of the velocity to develop the drone system for inspection at infrastructure equipment such as the bridge or tunnel.

Keywords**—Four rotor helicopter, AR. Drone 1.0, Velocity estimation, IMU, Investigation of bridge or tunnels.**

I. INTRODUCTION

In this paper, the velocity parameter obtained from the IMU (Internal Measurement Unit) in AR. Drone four rotor helicopter 1.0 was measured and analyzed, and it was found that the velocity parameter was calculated as an estrangement fashion when the drone touch against a wall with a slight impact. The IMU is one of the standard equipment of the drone system, since the information of acceleration and gyro sensors is indispensable for real-time stable posture controlling [1-7]. In addition, the velocity parameter is also estimating at the same time in the IMU, and it was typically used for the "space position" controlling and stabilizing process for drone controlling [1,8-16]. Since the IMU is developed and designed for multi-purpose use, high-frequency range of the acceleration and gyro sensors information was used for estimating the velocity parameter and it is afraid to do overestimation of the velocity especially when the drone collides against object such as wall or tree branches (Fig.1).Also, impacts from wind flow blasts would be afraid to do overestimation of the velocity. The main object of this paper is to compare the real velocity value measured from the camera on the ceiling with the IMU output estimated velocity parameter in the $x-y$space in the room (Fig.2) to confirm the effect of the overestimation of the velocity parameter by the IMU.

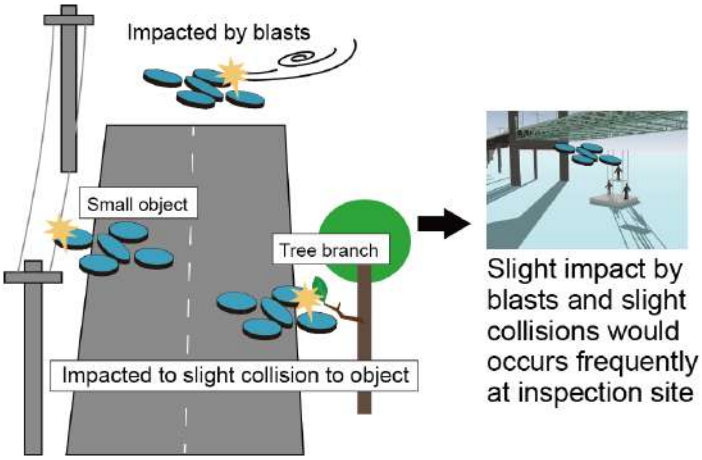

FIG.1. IMPACTED BY BLASTS AND SLIGHT COLLISION TO OBJECT WOULD OCCURS FREQUENTLY WHILE INSPECTING BRIDGE OR TUNNEL BY USING A DRONE SYSTEM.

Twenty percent of currently 730,000 bridges are under construction for more than 50 years in Japan [8].Many business operations of periodic inspection of the under bridge, inside tunnels and buildings are beginning to be tried [17-19]. Even if the drone would be controlled by a human being, the flight by visual confirmation of man is difficult in the over 10 m long distance flight [2,3,8-10,20-23].In many cases, the periodic inspection of a bridge is necessary to operate in a place 200 m away, and it is impossible to remove the influence of contact and blasts around the four rotor machine that cannot be visually observed [1, 14, 17,18].

II. PREVIOUS STUDY AND THE MATHEMATICAL BACKGROUND

Four rotor helicopter system would not be included autonomous position controlling way as itself, and the positioning control is necessary for the space using InfraRed 3D cameras [3,12] or GPS sensor system [14, 18] to control the drone position [3, 13-15, 24-27].In the InfraRed 3D camera, the precision of the position measurement is 1 mm order. However, the area of the using this method is within 10 m and the indoor situation only [2].On the other hand, if the drone would be controlled in the outdoor situation, the GPS signal can be used that there is no obstacles upper direction (sky) and movement direction. However, to use the drone for the periodic inspection of under the bridge or inside tunnels, the two approaches cannot be adopted since the instability of the GPS signal under these sites [17]. Also, in such situations of the long distance periodic inspection (such a case 200 m distance from the base), camera image feedback control (or by visual confirmation of man from the base point) is necessary.

To realize stable flight control at the long-distance situation (over 10 m), the camera image feedback control would become important, on the other hand, autonomous flight stabilizing process using the IMU information would be more indispensable since slight touching to thin tree branches and impacts from wind flow blasts could not correctly confirm from the base point visually [3].To suppress the deviation of trajectory due to the disturbances such as wind flow, one of the main factors of the feedback control is velocity parameter $\vec{v}$. Equation of motion of the drone while floating was described as (not included four rotors depend on complex dynamics, simple one-mass equation of motion).

$$m\vec{a} = \vec{F} = -k\vec{v} + \vec{f} \tag{1}$$

where m is a mass, $\vec{a}$ is the acceleration, $\vec{v}$ is the velocity, k is friction coefficient by air and $\vec{f}$is the external control input. In Eq.1, the term $-k\vec{v}$ has movement vibration suppression influence as the friction, and it can stabilize the drone movement, but the effect is limited small since the k is very small and unstable.

To realize the stabilization, the effect of the D (differential) gain is typically used as below,

$$\vec{f} = -k_d\overrightarrow{v^e} \tag{2}$$

where k_d is constant feedback differential gain parameter, $\overrightarrow{v^e}$is estimated velocity calculated by the IMU. Generally, the real velocity $\vec{v}$ and the estimated velocity $\overrightarrow{v^e}$(calculated value by the IMU) take same value under normal flight situation, and the term $-k_d\overrightarrow{v^e}$ affects the movement vibration suppression. The effect is typically large comparing with the air friction$-k$.

On the other hand, to calculate the estimated velocity$\overrightarrow{v^e}$, the IMU have to estimate$\overrightarrow{v^e}$ by using two sensor outputs - the internal acceleration and gyro sensor. Since the IMU is developed and designed for multi-purpose use, high-frequency range of the acceleration and gyro sensors information is used for precise estimating of$\overrightarrow{v^e}$. Especially, the high-frequency (few hundred hertz) information is indispensable to estimate it. But when the drone would collide with some slight touching to thin tree branches or impacts from blasts in the outdoor inspection works, there is a possibility that an unpredictable high-frequency change of the acceleration and gyro sensors would distort the$\overrightarrow{v^e}$. As a result, it is afraid to shift the velocity value especially when the drone collides against some object or would be impacted by blasts.

III. METHOD

In this experiment, AR. Drone 1.0 quad rotor model helicopter developed by Parrot Co. [28] was used. In Fig. 2, the aircraft is positioned at the center of the room (5×6 m square room, height is 2.4 m) and it flows automatically with the height of 0.6 m from the ground. To control the movement of the aircraft, AR. Drone library for Processing named ARDroneForP5 as developed by Y.Shigeo [28] was used and it was connected to a PC with Wi-Fi network. The basic period of movement command transmission between the aircraft and the PC was about 99.6 msec (18.4 msec standard deviation S.D.). The estimated velocity $\overrightarrow{v^e}$can be measured from the internal IMU of the drone via the control library ARDroneForP5 with about 10 Hz speed.

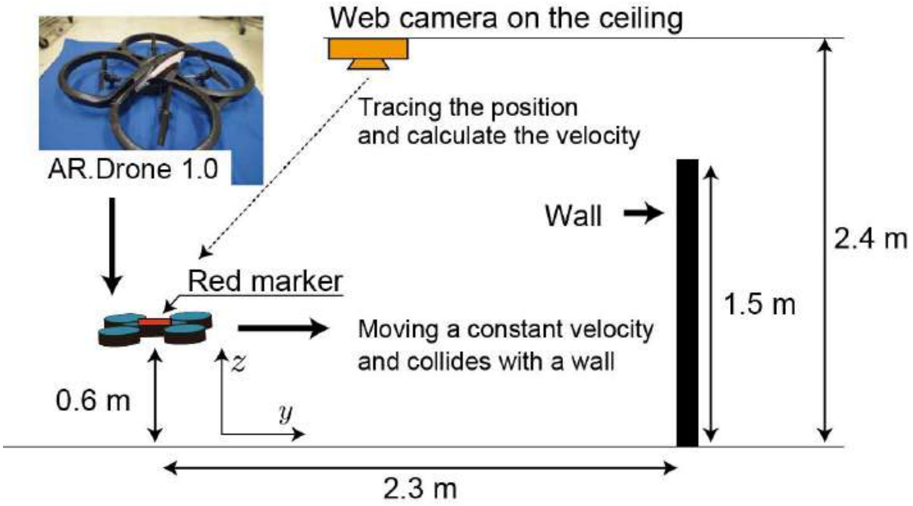

FIG.2. SIDE VIEW OF THE EXPERIMENTAL SETUP. AR.DRONE WAS CONTROLLED TO A CONSTANT VELOCITY MOVEMENT, AND COLLIDED WITH A WALL AT THE CONSTANT VELOCITY. THE REAL DRONE MOVEMENT VELOCITY WAS MEASURED BY A WEB CAMERA AT THE CEILING.

Fig.3 shows a top view of the experimental setup. The real drone position in the $x-y$ space (Fig.3) was measured by a web camera (BSW20KM11, 640×480, 60 fps, 130 deg visual angle, iBUFFALO Co.) attached to the ceiling of the room. The position discrimination was about 2 mm. To reduce measurement noise of the real velocity, a low pass filter was applied to the real velocity value calculated from the position data obtained at 60 Hz. Time constant was defined about 100 msec (10 Hz).From the result of the drone position, the real velocity $\vec{v}$ can be calculated.

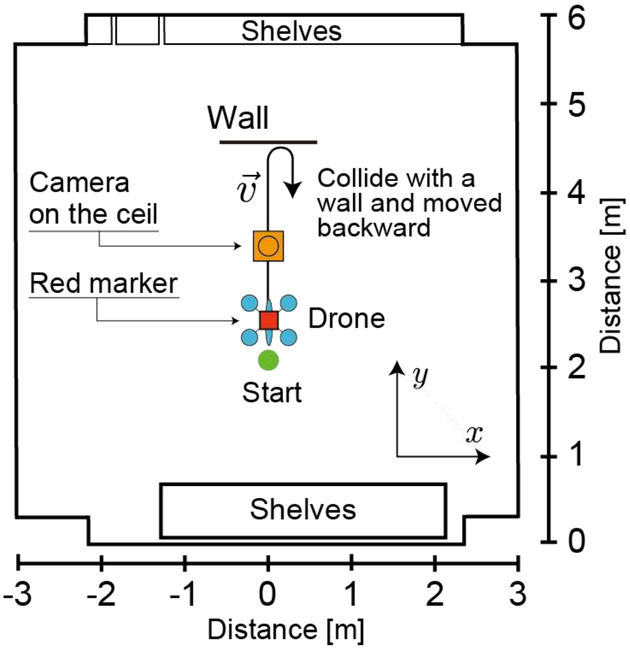

FIG.3. SETUP OF AR. DRONE COLLIDING EXPERIMENT TO A WALL WITH A CONSTANT VELOCITY $\vec{v}$ (TOP VIEW).

To compare the two velocity values while the collision, y axis values of the velocity $\vec{v}$ and $\overrightarrow{v^e}$ were used in Fig.3. It were denoted as v_y and v_y^e respectively. The drone's movement roll and pitch speed commands $V_{command}^r$ = $x$axis, $V_{command}^p$ =$y$axis and the yaw (spin) control command $V_{command}^s$ are determined.

$$\begin{cases} V_{command}^r & = 0 \\ V_{command}^p & = \gamma_p \\ V_{command}^s & = 0 \end{cases} \tag{3}$$

Where γ_p is constant value [2, 10, 20-22].

IV. EXPERIMENT

There are two phases of the movement control in the experiment. (1) Take off and 5 sec fixed point floating phase: The γ_p set as 0 before the drone take off. After the take-off, 5 sec normal flight (without any control of the drone) is implemented to stabilize the posture. Since the phase (1) was totally within 10 sec, there is slight yaw change (< 0.5 deg) and slight movement (< 15 cm) by the drone implemented posture control system. From the reason, we do not send any control commands to the drone while phase (1).

(2) Constant velocity and backward (slowdown) control phase: Firstly, the$\gamma_p$set as 30 or 100 (max 100 in the ARDroneForP5 library) as constant velocity movement ($+y$ axis direction) after the phase (1). Next, when the drone is crossed the position of the camera on the ceiling, the constant velocity parameter γ_p is changed to -100, and the drone was tried to backward movement ($-y$ axis direction) with the inertial motion continued. Since the positive velocity v_y of the drone is continuously reducing while the backward control phase, the v_y would pass through 0 and take negative value. In this phase (2), the drone would collide with the wall at a collision velocity, and the collision velocity v_y^cmainly depends on the firstly set γ_p value (30 or 100%).

V. RESULT

Figure 4 represents the result of comparison between the real velocity $v_y$of $y$axis in Fig.3 and the estimated velocity$v_y^e$of y axis obtained from the AR.Drone's IMU. Horizontal axis means elapsed time t [sec].In this experiment, the standard deviation (S.D.) of the real position of x was measured as 6.7 cm while 2.3 m flight, and it means that there was little movement of $x$axis while the movement. Filled Square mark means the real velocity v_y measured from the camera on the ceiling, and the white square mark is the estimated velocity v_y^e obtained from the AR.Drone's IMU in each time period [sec]. Two velocity transitions vary in coincidence, and the deviation (S.D. of $v_y - v_y^e$) was calculated as 23.4 cm/sec.

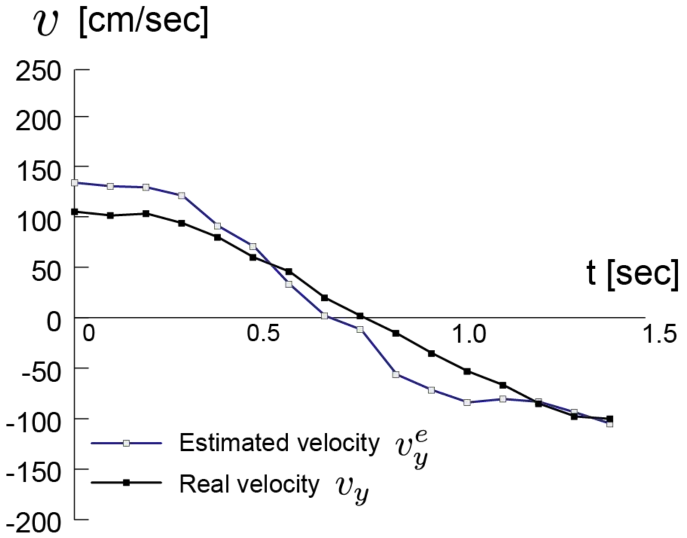

FIG.4. COMPARISON BETWEEN THE REAL VELOCITY v_y OF y AXIS AND THE ESTIMATED VELOCITY v_y^eOBTAINED FROM THE AR.DRONE'S IMU. THERE IS NO COLLISION CASE WITH THE WALL. HORIZONTAL AXIS REPRESENTS TIME [sec]

Figure 5 represents the result of comparison between the real velocity v_y of y axis and the estimated velocity v_y^e of y axis obtained from the AR.Drone's IMU when there is a slight collision with a wall. Even in this experiment, the two velocity transitions vary in coincidence, but in the timing of vertical dotted line (collision timing), the estimated velocity v_y^e suddenly transitioned to a high positive value (205 cm/sec) and it was decreasing and approaching to real velocity value v_y with a large delay. Immediately after the collision, the real velocity was v_y=-10.0 cm/sec.In the timing of the collision, the real velocity v_y takes about 25 cm/sec, and this velocity estrangement phenomenon was observed in almost all collisions. There is an over 20 times difference between the v_y^e and v_y when the collisions ($v_y^e/v_y = \frac{205\ cm/sec}{10.0\ cm/sec}$ = 20.5).

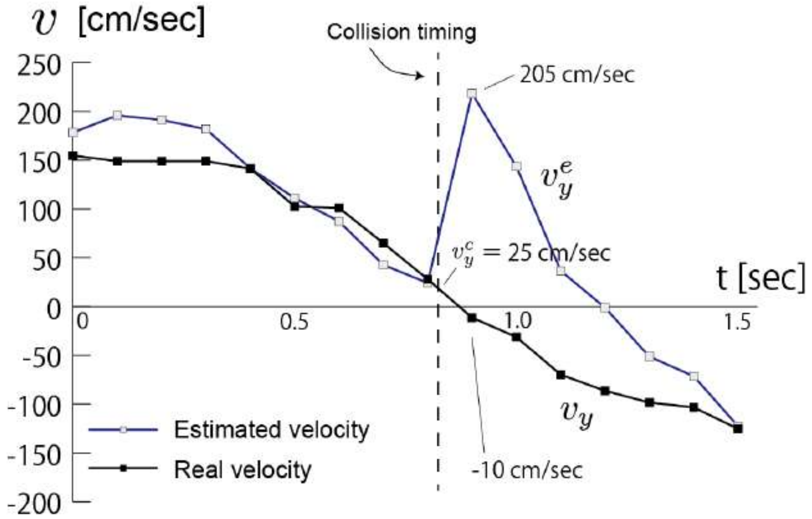

FIG.5. COMPARISON BETWEEN THE REAL VELOCITY v_yOF y AXIS AND THE ESTIMATED VELOCITY v_y^e OBTAINED FROM THE AR.DRONE'S IMU WHEN THE DRONE COLLIDES WITH THE WALL SOFTLY (ABOUTv_y^c =25 CM/SEC)

Figure 6 represents the result of comparison between the real velocity $v_y$and the estimated velocity v_y^e when the drone was collided to a wall with a high velocity (about v_y^c=60 cm/sec). The two velocity transitions vary in coincidence basically until the collision timing (vertical dotted line), the estimated velocity v_y^e suddenly transitioned to a positive high value (maximum 425 cm/sec) and it was decreasing and approaching to real velocity value v_y with a large delay. The real velocity was measured as -5 cm/sec in the above timing. In the timing of the collision, the real velocityv_y takes about 60 cm/sec.

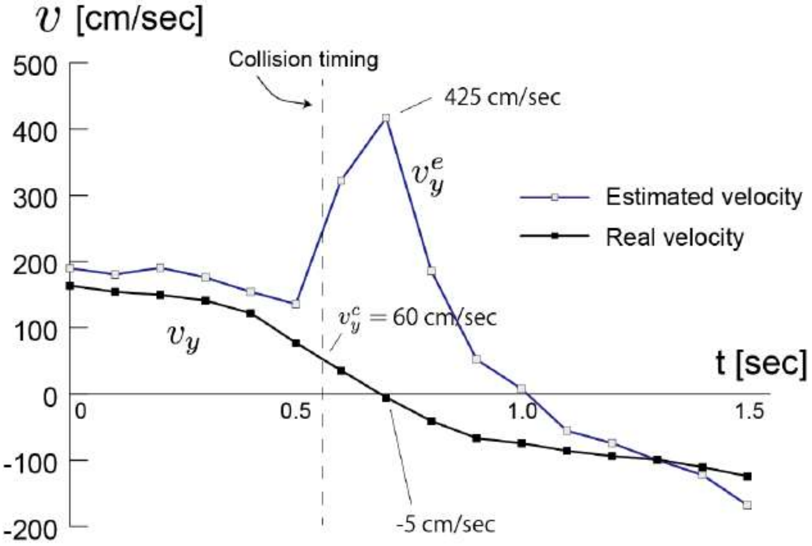

FIG.6COMPARISON BETWEEN THE REAL VELOCITY v_y OF y AXIS AND THE ESTIMATED VELOCITY v_y^e OBTAINED FROM THE AR.DRONE'S IMU WHEN THE DRONE COLLIDES WITH THE WALL HARDLY (ABOUTv_y^c =60 CM/SEC)

From above three experiments, the estimated velocity v_y^e was estranged from the real velocity $v_y$after the collision timing with the wall. Maybe multiple causes are considerable to explain the phenomenon, however, if the drone use the v_y^e to stabilize the position movement that was discussed in section 2, the estrangement of the velocity would affect incorrect D gain feedback as denoted by Eq.2.

VI. DISCUSSION

The reason for the estrangement of the estimation velocity v_y^e would be induced by the velocity estimating algorithm implemented in the IMU. Since IMU is generally developed and designed for multi-purpose use, it would use high-frequency range of the acceleration and gyro sensors information to estimate the velocity, and there is a problem that the influence of high-frequency information affecting to the velocity estimation would be unstable especially when the IMU is impacted by small tree branches collision or blasts to four rotors system. If the IMU does not use the high-frequency information, the precision of the estimated velocity would be reduced, and imprecision in the velocity estimation would make control of the spatial position of the four rotors system inaccurate (see Eq.2). To improve the accuracy of the spatial position control, high precision velocity estimation is necessary, the two factors are in a trade-off relationship and it would be difficult to analyze this trade-off problem. The estrangement of the estimation velocity is necessary to take care when the subject uses the estimation velocity factor to stabilize the AR. Drone 1.0 helicopter at least.

VII. CONCLUSION

In this paper, the velocity parameter obtained from the IMU (Internal Measurement Unit) in AR. Drone four rotor helicopter 1.0 was measured and analyzed, and it was found that the velocity parameter was calculated as an overestimated fashion when the drone touch against the wall with a slight impact. For four rotors helicopter system, the velocity parameter is important for stable real-time control, and the velocity is generally calculated by the IMU (Internal Measurement Unit) from the three-axis acceleration and gyro sensors. The result shows that the IMU estimating velocity v_y^e was divergent 20 times from the real velocity $v_y$measured from the camera on the ceiling even when low speed contact with a wall (25 cm/sec speed). When the estimated velocity parameter would be used for the position control and stabilizing of AR. Drone helicopter, it will be necessary to consider the problem of the estrangement of the velocity to develop the drone system for inspection at infrastructure equipment such as the bridge or tunnel.

ACKNOWLEDGEMENTS

This work was supported by JSPS KAKENHI Grant Number JP15K12598.

REFERENCES

[1] K. Nonami, F. Kendoul, S. Suzuki andW. Wang, D. Nakazawa, “Autonomous flying robots: unmanned aerial vehicles and micro aerial vehicles”, Springer Japan, 2010.

[2] H. Takano andH. Toda, “Roll movement realized by yaw and roll command combination method of AR Drone 4 rotor helicopter for improving stability of automatic position stop”, International Conference on Advanced Mechatronics (ICAM 2015), Waseda University, Tokyo, Japan, Dec.5-8, 2015, p.53.

[3] S. Azrad, F. Kendoul andK. Nonami, “Visual Servoing of Quadrotor Micro-Air Vehicle Using Color-Based Tracking Algorithm”, Journal of System Design and Dynamics (JSME), Vol. 4, No. 2, 2010,pp. 255-268.

[4] T. K. Roy, M. Garratt, H. R. Pota andM. K. Samal, “Robust altitude control for a small helicopter by considering the ground effect compensation", Intelligent Control and Automation (WCICA), 10th World Congress, DOI:10.1109/WCICA.2012.6358168, 2010, pp. 1796-1800.

[5] A. C. Satici, H. Poonawala andM. W. Spong, “Robust Optimal Control of Quadrotor UAVs”, IEEE Access, Vol. 1, DOI:10.1109/ACCESS.2013.2260794, 2013, pp. 79-93.

[6] J. Toledo, L. Acosta, M. Sigut, J. Felipe, “Stability Analisys of a Four Rotor Helicopter”, Automation Congress, WAC '06. World, 2006, pp. 1-6.

[7] P. Castillo, A. Dzul, R. Lozano, “Real-time stabilization and tracking of a four-rotor mini rotorcraft”, IEEE Transactions on Control Systems Technology, Vol.12,Issue: 4, DOI:10.1109/TCST.2004.825052, 2004, pp. 510-516.

[8] E. Altug, J. P. Ostrowski, C. J. Taylor, “Control of a quadrotor helicopter using dual camera visual feedback”, International Journal of Robotics Research, Vol.24, No.5, 2005, pp. 329-341.

[9] B. Ludington, E. Johnson, G. Vachtservanos, “Augmenting UAV autonomy: vision-based navigation and target tracking for unmanned aerial vehicles”, IEEE Robotics and Automation Magazine, Vol.13, No.3, 2006, pp. 63-71.

[10] H. Toda, H. Takano, “Effect of Discrete Yaw Direction Setting for 4 Roter Helicopter Control: Computer Simulation and AR. Drone Model Implementation”, International Journal of Innovative Research in Advanced Engineering, Vol. 3, Issue 7, Paper ID JYAE10086, doi:10.17632/cj8f3v6csr.1, 2016.

[11] J. Engel, J. Sturm, D. Cremers, “Camera-based navigation of a low-cost quadrocopter”, IEEE/RSJ International Conference on Intelligent Robots and Systems (IROS), DOI: 10.1109/IROS.2012.6385458, 2012.

[12] O. Andrisani, E. T. Kim, J. Schierman, F. P. Kuhl, “A nonlinear helicopter tracker using attitude measurements”, IEEE Transactions on Aerospace and Electronic Systems, Vol. 27, Issue 1, DOI:10.1109/7.68146, 1991, pp. 40-47.

[13] L. Garcia-Delgado, A. Dzul, V. Santib, M. Llama, “Quad-rotors formation based on potential functions with obstacle avoidance”, Control Theory and Applications, Vol. 6, Issue. 12, DOI:10.1049/iet-cta.2011.0370, 2012, pp. 1787-1802.

[14] F. Kendoul, Z. Yu, K. Nonami, "Embedded autopilot for accurate waypoint navigation and trajectory tracking: Application to miniature rotorcraft UAVs", IEEE International Conference on Robotics and Automation, ICRA '09., DOI:10.1109/ROBOT.2009.5152549, 2009, pp. 2884-2890.

[15] E. Altu, J. P. Ostrowski, R. Mahony, "Control of a Quadrotor Helicopter Using Visual Feedback", Proceedings of the 2002 IEEE International Conference on Robotics and Automation, Washington DC, 2002, pp. 72-77.

[16] Y. Yoshihara, K. Watanabe, T. Iwatani, K. Hashimoto, "Image-based visual servo control for a micro helicopter under partial occlusions", Proceedings of 2007 JSME Conference on Robotics and Mechatronics, 2A2-A06, Akita, Japan, 2007.

[17] Ministry of Land (Japan), Liang maintenance technology site verification and evaluation of the results 2015, https://www.mlit.go.jp/road/ir/ir-council/pdf/yobo3_1_6.pdf (accessed on Aug. 2 2017)

[18] K. Nomura, "Industrial applications type electric multi-rotor helicopter, introduction of mini-surveyor and flight demonstration", Mini-surveyor consortium 2016, http://mec2.tm.chiba-u.jp/~nonami/consortium/outline.html/ (accessed on Aug.2 2017)

[19] (2016) Ministry of Land (Japan), "Results of on-site verification and evaluation of bridge maintenance technology", https://www.mlit.go.jp/common/001083014.pdf (accessed on Aug.2 2017)

[20] H. Toda, S. Honda, H. Takano, "Effectiveness of Fast Speed Yaw and Roll Control Switching Instead of Normal Roll Control for AR Drone 4 rotor Helicopter", International Journal of Innovative Research in Advanced Engineering, Vol. 3, Issue 7, Paper ID JYAE10081, doi:10.17632/y52bmbgtkg.1, 2016.

[21] S. Honda, H. Toda, M. Kitani, G. Capi, "Development of small size 4 rotor helicopter automatic position control algorithm", 32nd Annual Conference of the Robotics Society of Japan, 1D3-01, 2013.

[22] S. Honda, H. Toda, M. Kitani, G. Capi,"Development of 4 rotor automatic flight control system using image processing filters that can be self-position estimation in natural objects with the aim of the reactor building search", ROBOMECH2014, March, Toyama, 2014.

[23] K. Nonami, "Rotary Wing Aerial Robotics", Journal of Robotics Society of Japan, Vol. 24 (8), 2006, pp. 890-896.

[24] R. Mahony, T. Hamel, "Image-based visual servo control of aerial robotic systems using linear image features", IEEE Trans. on Robotics, Vol.21, No.2, 2005, pp. 227-239.

[25] K. Watanabe, Y. Iwatani, N. Kenichiro, K. Hashimoto, "A vision-based support system for micro helicopter control", Proceedings of Conference on Robotics and Mechatronics, 1P1-F13, Nagano, Japan, June 5-7, 2008.

[26] Y. Kubota, T. Iwatani, "Dependable visual servoing of a small-scale helicopter with a wireless camera", Proceedings of Conference on Robotics and Mechatronics, 1A2-O15, Okayama, Japan, May 26-28, 2011.

[27] O. Meister, N. Frietsch, C. Ascher, G. F. Trommer, "Adaptive path planning for a VTOL-UAV", IEEE International Coference on Position, Location and Navigation Symposium, DOI:10.1109/PLANS.2008.4570046, 2008, pp. 1252-1259.

[28] S. Yoshida, "Engneering navi", library of ARDroneForP5, http://kougaku-navi.net/ARDroneForP5/ (accessed on Aug.2 2017).

AD Publications
Sector-3, MP Nagar, Bikaner,
Rajasthan, India
www.adpublications.org, info@adpublications.org